



Fakultät für Medizin

Klinik und Poliklinik für Innere Medizin II

A Dietary-Shaped Gut Microbiome Accelerates Progression From Barrett's Esophagus To Adenocarcinoma via Systemic Bile Acids

Theresa Baumeister

Vollständiger Abdruck der von der Fakultät für Medizin der Technischen Universität München zur Erlangung des akademischen Grades eines

Doctor of Philosophy (Ph.D.)

genehmigten Dissertation.

Vorsitz: Priv.-Doz. Dr. Christian Sorg

Betreuer: Prof. Dr. Michael Quante

Prüfer der Dissertation:

1. Prof. Dr. Roland Schmid
2. Prof. Dr. Dirk Haller
3. Prof. Dr. Bärbel Stecher

Die Dissertation wurde am 21.06.2021 bei der Fakultät für Medizin der Technischen Universität München eingereicht und durch die Fakultät für Medizin am 13.10.2021 angenommen.

Dedicated to my family and my chosen family, the people who decided to always love and support me in all phases of my life.

Table of Content

Table of Figures and Tables	7
Abstract	10
Zusammenfassung	11
1. Introduction	12
1.1. The Gastro-Intestinal Tract: an anatomical and physiological overview	12
1.1.1. Esophagus	12
1.1.2. Stomach	13
1.1.3. Small Intestine.....	13
1.1.4. Large Intestine.....	14
1.1.5. The Role of Liver and Gall Bladder as Accessory Digestive Organs.....	14
1.2. Pathophysiology of the Esophagus and the Upper Gastro-Intestinal Tract.....	14
1.2.1. Motility Disorders.....	14
1.2.2. Gastro-esophageal Reflux Disease.....	15
1.2.3. Reflux Esophagitis.....	15
1.2.4. Barrett’s Esophagus.....	16
1.2.5. Esophageal Cancer.....	16
1.3. Characterization of Barrett’s Esophagus (BE) and Esophageal Adenocarcinoma (EAC)	17
1.3.1. Hypotheses of the Origin.....	17
1.3.2. Prevalence and Incidence of GERD, BE and EAC.....	19
1.3.3. Risk Factors	20
1.3.4. Disease Models.....	21
1.4. The Impact of Dietary Intake on the Pathophysiology of the Gastro-Intestinal Tract.....	23
1.4.1. Western Diet and Obesity.....	23
1.4.2. Dietary Fat.....	24
1.5. The Impact of the Microbiome on the Pathophysiology of the Gastro-Intestinal-Tract	26
1.5.1. The Microbiome of the Gastro-Intestinal Tract	26
1.5.2. Dietary Adaptation.....	26
1.5.3. Inflammatory Effects of the Dietary Shaped Gut Microbiome	27
1.6. The Impact of Bile Acids on the Pathophysiology of the Gastro-Intestinal-Tract.....	28
1.6.1. Bile Acid Synthesis and Enterohepatic Circulation	28
1.6.2. Bile Acid Metabolization by the Gut Microbiome	28
1.6.3. Bile Acid Signaling via the Nuclear Receptor Farnesoid X Receptor (FXR)	30
1.6.4. The Role of Bile Acids in Diseases of the Gastro-Intestinal Tract	33
1.7. Aims of This Thesis.....	35
1.7.1. Aim 1: Characterization of the of the L2-IL1B mouse model with a whole-body knockout of the BA receptor FXR.....	35
1.7.2. Aim 2: Investigation of the Impact of a High-Fat-Diet (HFD) on the Bile Acid (BA) modulating Microbiome and BA levels of the L2-IL1B Mouse Model.....	35
1.7.3. Aim 3: Investigation of the Effect of OCA Treatment on BA treated Organoids <i>In Vitro</i> and on L2-IL1B Mice Fed CD and HFD In Vivo.....	35
1.7.4. Aim 4: Assessment of the Microbiome and Bile Acid Profile in Patients with BE, Dysplastic BE and EAC	35
2. Materials and Methods	36
2.1. Human BarrettNET Study Cohort.....	36
2.2. Sample Collection and Overview – Murine Studies.....	37
2.2.1. Transgenic Mouse Strains.....	37

2.2.2.	Holding and Husbandry	37
2.2.3.	Weaning, DNA extraction and Genotyping	38
2.2.4.	Dietary Treatment.....	40
2.2.5.	Diet composition	40
2.3.	Euthanasia, Preparation and Sample collection from mice	42
2.4.	Macroscopic scoring	44
2.5.	Flow-Cytometry for Analysis of Immune Cell Levels	45
2.6.	Histological analysis.....	48
2.6.1.	Preparation of Formalin-Fixed Paraffin-Embedded (FFPE) Tissue Samples and Sections.....	48
2.6.2.	Hematoxylin and Eosin (HE) Staining.....	50
2.6.3.	Histologic Scoring.....	51
2.6.4.	Periodic-Acid-Schiff (PAS) reaction with and without Alcian Blue Staining.....	51
2.6.5.	Immunohistochemistry.....	53
2.6.6.	In-Situ-Hybridization (ISH).....	57
2.6.7.	Quantification of Immunohistochemistry	57
2.7.	RNA and Extraction and Downstream Applications	58
2.7.1.	RNA Extraction.....	58
2.7.2.	Reverse Transcription Polymerase Chain Reaction (RT-PCR)	58
2.7.3.	Quantitative Real Time PCR (qRT-PCR).....	58
2.8.	16S-Sequencing for Microbiome Analysis.....	61
2.8.1.	Sample Collection	61
2.8.2.	Sample Preparation.....	61
2.8.3.	Quality Control of DNA Samples for 16S RNA Gene Sequencing.....	63
2.8.4.	High Throughput 16S- ribosomal RNA (rRNA) Gene Sequencing and Microbiome Profiling .	64
2.8.5.	Analysis of 16S Sequencing Data	64
2.9.	Mass Spectrometry for targeted and untargeted Metabolomic analysis.....	65
2.9.1.	Sample Collection and Overview.....	65
2.9.2.	Sample Preparation.....	65
2.9.3.	Untargeted Metabolomic Analyses	66
2.10.	Targeted Metabolomic analyses for BA	68
2.10.1.	Performance of Targeted Metabolomic Analyses	68
2.10.2.	Analysis and Statistical Evaluation of Targeted Metabolomic Analyses.....	71
2.11.	Cell Culture (Organoid Culture from L2-IL1B mice)	72
2.11.1.	Preparation of Conditioned Medium for Organoid Maintenance	72
2.11.2.	Isolation and Maintenance of Organoids.....	74
2.11.3.	Freezing and Thawing of Organoids	75
2.11.4.	Treatment of L2-IL1B Mouse Cardia Organoids with Bile Acids	76
2.11.5.	Histological Analysis of Organoids	79
2.12.	RNA Extraction and Downstream Applications	80
2.12.1.	qRT-PCR	80
2.12.2.	DNA Damage ELISA.....	80
2.13.	Statistical Analysis.....	80
3.	Results	81
3.1.	Characterization of the Pathophysiologic and Metabolic Profile of the L2-IL1B Mouse Model with a Whole-body Knockout of the BA Receptor FXR	81
3.1.1.	FXR Expression Potentially Acts Protectively Against Malignant Progression in BE.....	81

3.1.2.	Knockout of FXR in L2-IL1B Mice Leads to Aggravation of the Dysplastic Phenotype	83
3.1.3.	Knockout of FXR Leads to a Reduction of Mucus Production in L2-IL1B mice	85
3.1.4.	Knockout of FXR Leads to Increased Smooth Muscle Differentiation in L2-IL-1B Mice	86
3.1.5.	Knockout of FXR Leads to Increased Caspase 1 Activation in L2-IL1B Mice.....	87
3.1.6.	Knockout of FXR Leads to Increased DNA Damage in L2-IL1B Mice	88
3.1.7.	Knockout of FXR Causes Increasing Lgr5+ Stem Cell Numbers in L2-IL1B Mice.....	89
3.1.8.	The L2-IL1B Mouse Model Harbors Lgr5 FXR Double Positive Cells	90
3.1.9.	Knockout of FXR does not Influence Proliferation in L2-IL1B Mice	91
3.1.10.	Knockout of FXR does not Influence TGR5 Expression in L2-IL1B Mice.....	92
3.1.11.	Knockout of FXR in the L2-IL1B Mouse Model Induces Changes in the SCJ Tissue on RNA Level	93
3.1.12.	The Serum Bile Acid Pool of L2-IL1B Mice Changes in Response to FXR Knockout	99
3.2.	Impact of a High-Fat-Diet on the Bile Acid Modulating Microbiome and BA Levels of the L2-IL1B Mouse Model	101
3.2.1.	Treatment with HFD Changes the Fecal Metabolome of L2-IL1B Mice.....	101
3.2.2.	Treatment with HFD Changes the Gut Microbiome of L2-IL1B Mice – with Focus on Bile Acid Modulating Bacteria	103
3.2.3.	Treatment with HFD Causes Enrichment of Bile Acids in the Gut Metabolome of L2-IL1B Mice	105
3.2.4.	Treatment with HFD Changes the Serum and Tissue BA Profile of L2-IL1B Mice	109
3.3.	Impact of the FXR Receptor Agonist Obeticholic Acid on L2-IL1B Organoids and on CD and HFD Treated L2-IL1B Mice	111
3.3.1.	Treatment of L2-IL1B SCJ Organoids with Bile Acids and OCA.....	112
3.3.2.	Treatment of a Cohort of L2-IL1B Mice Raised in NYC with CD, HFD or HFD+OCA.....	118
3.3.3.	Treatment of a Second Cohort of L2-IL1B mice Raised in Munich with CD, CD+OCA, HFD or HFD+OCA.....	140
3.4.	Assessment of the Microbiome and Bile Acid Profile in Patients with BE, Dysplastic BE and EAC ...	164
3.4.1.	The BA Pool in the Stool of Patients Shifts with the Disease State	164
3.4.1.	The BA Pool in the Serum of Patients Shifts with the Disease State.....	166
3.4.2.	BA Metabolizing Bacteria Levels in the Stool of Patients do not Change with Disease Progression	168
3.4.3.	Disease Severity in Patients Correlates Positively with Potentially BA Metabolizing Gut Microbiota and BA Levels	169
3.4.4.	BA Metabolizing Bacteria Levels Extracted From Patient Biopsies Increase With Disease Progression.....	170
4.	Supplementary Figures	171
5.	Discussion.....	183
5.1.	The Protective Role of FXR Expression on the Phenotype in the L2-IL1B Mouse Model	184
5.1.1.	The Impact of FXR Knockout on Disease Development on Cellular Level.....	185
5.1.2.	The Impact of FXR Knockout on the BA Pool, with Possible Implications for Disease Progression	186
5.2.	HFD Treatment Leads To Increasing Numbers of BA Metabolizing Bacteria and of BA Levels in the L2-IL1B Mouse Model.....	187
5.2.1.	The Gut Microbiome and Metabolome in Response to HFD	188
5.2.2.	The Serum and Tissue Metabolome in Response to HFD	190
5.3.	Treatment of L2-IL1B Mice Fed CD or HFD with OCA Shifts the BA Metabolizing Microbiome and BA Pool, Reduces Levels of Specific BA, and Acts Protective on Disease Progression	192
5.3.1.	The Impact of OCA Treatment on Disease Development on Cellular Level.....	193
5.3.2.	The Impact of OCA Treatment on the Microbiome and BA Profile in L2-IL1B HFD Mice in Context with other Systemic Effects	194

5.4.	The BA Profile of Patients Shifts with Disease Progression, with Specific BA Increasing with Higher Disease Stage	199
5.4.1.	The BA Profile in the Stool of Patients Shifts With Increasing Disease Severity in Correlation with an Increased Potential of Microbial Secondary BA Synthesis	200
5.4.2.	The BA Profile in the Serum of Patients Shows Distinct Shifts Towards Taurine-Conjugated and Secondary BA in Correlation with Disease Progression, in Association with Enrichment of Potentially BA-Metabolizing Bacteria in the Esophagus	201
5.5.	Conclusion	202
5.6.	Limitations	204
5.7.	Future Perspectives	205
5.7.1.	Impact of Environmental Factors on Inflammation and Progenitor Cells in the L2-IL1B Mouse Model.....	205
5.7.2.	A Fructose Enriched Diet Study to Examine the Effects of Excessive Consumption of Sweeteners on L2-IL1B Mice.....	206
5.7.3.	A Fiber Enriched Diet Study to Examine Potential Beneficial Effects of Dietary Intervention on Disease Progression in L2-IL1B Mice	206
5.7.4.	Summary of Future Perspectives	206
6.	References	207
7.	List of Abbreviations	223
8.	Acknowledgements	229

Table of Figures and Tables

Figure 1: Hypotheses of the origin of BE	17
Figure 2: Bile acid synthesis, modulation and metabolization pathways in humans and mice	30
Figure 3: FXR mediated bile acid circulation and transporters	31
Figure 4: Downstream pathways of FXR	32
Table 1: Genotyping Primer Sequences	39
Table 2: Composition of Experimental Diets	40
Table 3: Overview over tissue collection procedure for each experimental mouse	43
Table 4: Macroscopic scoring system for stomach and esophagus of L2-IL1B mice	44
Table 5: Composition of Digestion Buffers for tissues subjected to flow cytometry	46
Table 6: Composition of Krebs-Ringer Buffer for preparation of Digestion Buffers	46
Table 7: Composition of FACS Washing Buffer	47
Table 8: Composition of staining solutions for tissues subjected to flow cytometry	47
Figure 5: schematic representation of the dissection of the opened and flattened murine stomach for embedding in paraffin	49
Table 9: Protocol for Hematoxylin and Eosin (HE) Staining	50
Table 10: Histologic scoring system for stomach and esophagus of L2-IL1B mice	51
Table 11: Protocol for Periodic Acid Schiff Staining with Alcian Blue	51
Table 12: Standard protocol for immunohistochemistry	53
Table 13: Specifications of antibodies used	56
Table 14: Primers for quantitative Real Time - PCR	59
Table 15: Comparison of DNA quality after DNA extraction	62
Figure 6: DNA samples run on agarose gel for DNA quality and integrity assessment	63
Table 16: Bile Acids Measured in Targeted Bile Acid Metabolomic Analysis	70
Table 17: Compositions of growth medium and complete growth medium with selection markers for L-WRN producing cells (ATCC® CRL3276™)	73
Table 18: Composition of L-WRN conditioned media supplemented with growth factors for organoid culture	74
Table 19: Composition of the Click-iT® EdU reaction cocktail	78
Figure 7: FXR is expressed in BE but not in EAC tissue in human patients and L2-IL1B mice	82
Figure 8: FXR knockout increases macroscopic scores in 12m old L2-IL1B mice	83
Figure 9: FXR knockout increases dysplasia scores and decreases goblet cell (GC) ratio in 12m old L2-IL1B mice	84
Figure 10: Coverage with PAS positive mucus producing cells decreases in L2-IL1B-FXR ^{-/-} compared to L2-IL1B mice	85
Figure 11: αSMA expression increases in L2-IL1B-FXR ^{-/-} compared to L2-IL1B	86
Figure 12: Caspase1 expression increases in L2-IL1B-FXR ^{-/-} compared to L2-IL1B mice	87
Figure 13: γ-H2AX expression increases in L2-IL1B-FXR ^{-/-} compared to L2-IL1B mice	88
Figure 14: Lgr5 expression increases in L2-IL1B-FXR ^{-/-} compared to L2-IL1B	89
Figure 15: FXR and Lgr5-In-situ-hybridization on serial sections of cardia tissue shows coexpression of both markers in L2-IL1B mice	90
Figure 17: TGR5 expression does not change between L2-IL1B and L2-IL1B-FXR ^{-/-} mice	92
Figure 18: Venn-diagram comparing significantly up- and downregulated annotatable genes in L2-IL1B-FXR ^{-/-} compared to L2-IL1B mice	94
Figure 19: Significantly enriched (A) Gene Ontology and (B) Hallmark gene sets in L2-IL1B-FXR ^{-/-} compared to L2-IL1B mice	95
Table 20: Significantly regulated genes in BE tissue of L2-IL1B-FXR ^{-/-} compared to L2-IL1B mice, detected by microarray analysis	96
Table 21: Significantly regulated genes in BE tissue of L2-IL1B-FXR ^{-/-} compared to L2-IL1B mice, detected by microarray analysis	97
Figure 20: Selected GSEA enrichment plots	98
Figure 21: Untargeted metabolomic analysis of the Serum of L2-IL1B-FXR ^{-/-} compared to L2-IL1B mice	99
Figure 22: Targeted metabolomic and microarray gene expression analyses of the serum of L2-IL1B and L2-IL1B-FXR ^{-/-} mice	100
Figure 23: Targeted metabolomic analyses of fecal BA levels in L2-IL1B mice fed chow, CD and HFD	102
Figure 24: Changes in Bacterial groups with bile acid metabolizing capacities in the stool of L2-IL1B mice fed CD or HFD	104
Figure 25: Untargeted metabolomic analysis of cecal content from mice fed CD vs HFD via RP chromatography	106
Figure 26: Untargeted metabolomic analysis of cecal content from mice fed CD vs HFD via HILIC	107
Figure 27: Untargeted metabolomic analysis of fecal content from mice fed CD vs HFD via HILIC	108
Figure 28: Targeted BA analysis in serum and tissue of L2-IL1B mice fed CD or HFD	110
Figure 29: OCA treatment ameliorates the damage induced by BA in L2-IL1B BE Organoids	113
Figure 30: OCA treatment reduces proliferation induced by BA in L2-IL1B BE Organoids	115
Figure 31: OCA treatment reduces DNA Damage induced by cytotoxic DCA in L2-IL1B BE Organoids	117
Figure 32: HFD increases the dysplastic phenotype in L2-IL1B mice, while OCA treatment in L2-IL1B mice fed HFD ameliorates the dysplastic phenotype	119

Figure 33: FXR expression is significantly increasing in small intestinal (SI) tissue of L2-IL1B mice upon OCA treatment	120
Figure 34: OCA treatment in L2-IL1B mice fed HFD significantly decreases proliferation analyzed by Ki67 compared to CD and HFD	121
Figure 35: OCA treatment in L2-IL1B mice fed HFD does not reduce DNA damage compared to CD and HFD	122
Figure 36: Lgr5 stem cell numbers are decreasing in L2-IL1B HFD mice upon treatment with OCA.	124
Figure 37: Expression of the BA receptor Tgr5 does not change between intervention groups	125
Figure 38: OCA treatment changes the fecal bile acid profile in L2-IL1B mice fed HFD.....	127
Figure 39: Beta diversity comparison for fecal microbial profiles: meta-Normalized Multidimensional Scaling (metaNMDS) plots of feces from 6- and 9-month-old L2-IL1B mice fed CD, HFD or HFD+OCA	130
Figure 40: OCA treatment changes the BA metabolizing microbial profile in the cecum of L2-IL1B mice fed HFD	131
Figure 41: Beta diversity comparison for fecal microbial profiles: meta-Normalized Multidimensional Scaling (metaNMDS) plots of feces from 6- and 9-month-old L2-IL1B mice fed CD, HFD or HFD+OCA	132
Figure 42: OCA treatment changes the BA metabolizing microbial profile in the feces of L2-IL1B mice fed HFD.....	133
Figure 43: Correlation analysis between fecal BA levels and the abundance of fecal microbial genera.....	136
Figure 44: OCA treatment changes the bile acid profile in L2-IL1B mice fed HFD	138
Figure 45: Macroscopic scores do not differ between treatment groups in L2-IL1B mice treated with CD or HFD with or without OCA.....	140
Figure 46: OCA treatment in L2-IL1B mice fed HFD ameliorates the dysplastic phenotype and increases differentiation represented by goblet cell (GC) ratio.	142
Figure 47: Obeticholic acid levels in the cecum of OCA treated L2-IL1B mice on CD and HFD mice are significantly elevated compared to untreated mice	143
Figure 48: Untargeted metabolomic analysis of cecal content from mice fed CD vs CD+OCA via RP chromatography.....	144
Figure 49: Untargeted metabolomic analysis of cecal content from mice fed HFD vs HFD+OCA via RP chromatography.....	145
Figure 50: Untargeted metabolomic analysis of cecal content from mice fed CD vs CD+OCA via HILIC.....	146
Figure 51: Untargeted metabolomic analysis of cecal content from mice fed HFD vs HFD+OCA via HILIC.	147
Figure 52: Untargeted metabolomic analysis of fecal content from mice fed CD vs CD+OCA via HILIC.	148
Figure 53: Untargeted metabolomic analysis of fecal content from mice fed HFD vs HFD+OCA via HILIC.	149
Figure 54: OCA treatment changes the cecal bile acid profile in L2-IL1B mice fed CD or HFD	151
Figure 55: OCA treatment changes the fecal bile acid profile in L2-IL1B mice fed CD or HFD	153
Figure 56: Fecal bile salt hydrolase (BSH) expression decreases in L2-IL1B mice fed CD or HFD upon treatment with OCA	154
Figure 57: Beta diversity comparison for fecal microbial profiles: meta-Normalized Multidimensional Scaling (metaNMDS) plots of feces from 6- and 9-month-old L2-IL1B mice fed CD, HFD, CD+OCA or HFD+OCA	156
Figure 58: Beta diversity comparison for fecal microbial profiles: meta-Normalized Multidimensional Scaling (metaNMDS) plots of feces from 6- and 9-month-old L2-IL1B mice fed CD, HFD, CD+OCA or HFD+OCA	156
Figure 59: OCA treatment changes the BA metabolizing microbial profile in the cecum of L2-IL1B mice fed CD and HFD	157
Figure 60: Correlation of the relative abundance of bacteria from kingdom (k) to genus level in the cecum of L2-IL1B mice.....	158
Figure 61: Correlation of the relative abundance of bacteria from kingdom (k) to genus level in the stool of L2-IL1B mice	159
Figure 62: The influence of OCA treatment on tissue morphology of CD or HFD fed mice	161
Figure 63: OCA treatment decreases neutrophil infiltration in the cardia and increases cardia NK and blood NKT cell levels.....	163
Figure 64: The human fecal BA profile changes in BE and EAC compared to control patients	165
Figure 65: Bacterial bile salt hydrolase (BSH) expression in the stool of human patients increases with disease severity	165
Figure 66: The human serum BA profile changes in diseased (BE, dysplasia, EAC) compared to control patients	167
Figure 67: The gut microbial profile in human patients with focus on BA metabolizing bacteria	168
Figure 68: Correlation of the relative abundance of bacteria genera in the stool of human patients with disease severity and fecal BA levels.....	169
Figure 69: Bacterial groups with potential BA modulating capacities are increasing in abundance in correlation with disease severity in the esophageal microbiome.....	170
Supplementary Fig. 1: Histological scores are not changing significantly between L2-IL1B and L2-IL1B-FXR ^{-/-} mice at 6 months of age	171
Supplementary Fig. 2: Histological scores are not changing significantly between L2-IL1B and L2-IL1B-FXR ^{-/-} mice at 9 months of age	172
Supplementary Fig. 3: The amount of PAS positive mucus producing cells is not changing significantly between L2-IL1B and L2-IL1B-FXR ^{-/-} mice at 6 and 9 months of age.....	173
Supplementary Fig. 4: The amount of αSMA positive cells is not changing significantly between L2-IL1B and L2-IL1B-FXR ^{-/-} mice at 6 and 9 months of age.....	174
Supplementary Fig. 5: The amount of Caspase1 positive cells is not changing significantly between L2-IL1B and L2-IL1B-FXR ^{-/-} mice at 6 and 9 months of age.....	175

Supplementary Fig. 6: The amount of γ -H2AX positive cells is not changing significantly between L2-IL1B and L2-IL1B-FXR ^{-/-} mice at 6 and 9 months of age	176
Supplementary Fig. 7: Bile Acid concentrations in Small Intestinal, Colon and BE tissue	177
Supplementary Fig. 8: The macroscopic tumor percentage in the SCJ of L2-IL1B mice at 6 months of age is decreasing significantly in mice fed HFD and CD+OCA compared to CD	178
Supplementary Fig. 9: OCA treatment decreases dysplasia scores and increases the goblet cell (GC) ratio in 6m old L2-IL1B mice fed HFD	179
Supplementary Fig. 10: OCA treatment in L2-IL1B mice fed CD or HFD does not change cecal primary to secondary BA ratios	180
Supplementary Fig. 11: OCA treatment in L2-IL1B mice fed CD or HFD does not change fecal primary to secondary BA ratios	181
Supplementary Fig. 12: Correlation Fecal Microbiome targeted BA metabolome	182
Figure 70: Schematic graphical overview over the effects of Diet and OCA treatment on Disease Progression from BE to EAC (Created with BioRender.com)	203

Abstract

The main precursor condition of esophageal adenocarcinoma (EAC) is Barrett's esophagus (BE). The onset and progression of BE is mainly attributed to inflammation and cellular damage due to chronic reflux of gastric and bile acid. Risk of progression from BE to EAC correlates with increasing obesity incidence and intake of western-style diet in westernized countries, but the exact role of dietary intake in disease development is still unclear. Until now, it could be shown that dietary intake high in fat, often consumed in westernized countries and leading to obesity in humans leads to increased bile acid (BA) levels and changes the gut microbiome. Only recently our group showed that high fat diet (HFD) changes the gut microbiome and inflammatory environment in L2-IL1B-mice, thereby promoting carcinogenesis. The aim of this thesis was to better understand the impact of a westernized diet on the microbiome–metabolome axis on disease onset and progression in the L2-IL1B mouse model and in human patients. One focal point of this study was the influence of high fat consumption on bile acid metabolizing bacteria, bile acid production, metabolization and distribution and their effects on disease progression.

We found that the nuclear bile acid sensitive Farnesoid-X-Receptor (FXR) had protective effects on the BE phenotype in L2-IL1B mice, with knockout of FXR promoting a pro-tumorigenic tissue microenvironment and disease progression and shifting serum BA levels. In L2-IL1B mice, treatment with HFD increased the abundance of BA-metabolizing bacteria along with gut, serum, and intestinal as well as BE tissue BA levels in correlation with disease progression. Obeticholic acid (OCA), a selective FXR agonist, had protective functions in L2-IL1B organoids treated with BA. In L2-IL1B mice fed HFD, OCA induced differentiation and decreased Leucine-rich repeat-containing G-protein coupled Receptor 5 (Lgr5) stem cell numbers in the metaplastic tissue, ameliorating the dysplastic phenotype and tumor microenvironment and reducing BA levels in correlation with reduced abundance of BA-metabolizing gut bacteria. These findings provided evidence for a functional diet–microbiome–metabolome chain affecting disease progression in BE in the L2-IL1B mouse model, with a direct role of BA. Microbiome and Metabolome data from tissue and stool of patients shows systemic increases of specific BA and increases in BA-metabolizing microbiota in the BE tissue in correlation with disease progression, thereby supporting this theory. Thus, we provide evidence for a novel mechanism explaining how the diet-microbiome-metabolome axis might be able to accelerate esophageal carcinogenesis. In conclusion, more effort should be undertaken to examine the patients' lifestyle and dietary intake more comprehensively, and to treat patients not only locally with drugs or using endoscopic techniques, but to include dietary and serum bile acid surveillance and potentially bile acid regulating treatments in new treatment approaches.

Zusammenfassung

Die wichtigste Vorläufererkrankung des Ösophagus-Adenokarzinoms (AEG) ist Barrett-Ösophagus (BE). Die Entstehung und das Fortschreiten von BE wird hauptsächlich auf Entzündungen und Zellschäden durch chronischen Reflux von Magen- und Gallensäuren zurückgeführt. Das Risiko der Progression von BE zu AEG korreliert mit der zunehmenden endemischen Verbreitung von Übergewicht und dem Verzehr von sogenannter „western diet“ in westlichen Ländern. Die genaue Rolle der Nahrungsaufnahme bei der Krankheitsentwicklung ist bis dato unklar. Bisher konnte gezeigt werden, dass fettreiche Ernährung, wie sie oft in westlich geprägten Ländern konsumiert wird und die zu Übergewicht führt, zu erhöhten Gallensäurespiegeln führt und das Darmmikrobiom verändert. Erst kürzlich konnte unsere Arbeitsgruppe zeigen, dass eine fettreiche Ernährung das Darmmikrobiom und das entzündliche Milieu in L2-IL1B-Mäusen verändert und dadurch die Karzinogenese fördert. Ziel dieser Arbeit war es, den Einfluss diätischer Komponenten auf die Mikrobiom-Metabolom-Achse und somit auf den Krankheitsverlauf im L2-IL1B-Mausmodell und bei Patienten besser zu verstehen. Der Fokus dieser Studie lag dabei auf der Auswirkung hohen Fettkonsums auf Gallensäure-metabolisierende Bakterien im Darm, auf Produktion und Metabolismus von Gallensäuren, deren Anreicherung im Körper und deren Auswirkungen auf die Krankheitsprogression.

Wir fanden heraus, dass der nukleäre Gallensäure-sensitive Farnesoid-X-Rezeptor (FXR) protektive Effekte auf den Phänotyp in L2-IL1B-Mäusen hat, wobei der Knockout von FXR die Krankheitsprogression fördert und sich auf den Serum Gallensäure Spiegel auswirkt. Bei L2-IL1B-Mäusen erhöhte die Behandlung mit HFD das Vorkommen Gallensäure-metabolisierender Bakterien und Gallensäurespiegel im Darm, Serum und BE-Gewebe in Korrelation mit der Krankheitsprogression. Obeticholsäure (OCA), ein selektiver FXR-Agonist, wirkte sich in L2-IL1B-Organoiden, die mit BA behandelt wurden protektiv aus. In L2-IL1B-Mäusen, die mit HFD gefüttert wurden, induzierte OCA Differenzierung und verringerte die Anzahl Lgr5 positiver Stammzellen im metaplastischen Gewebe, wodurch das Fortschreiten des Phänotyps inhibiert wurde. Auch Gallensäurespiegel wurden in Korrelation mit dem Mikrobiom reduziert.

Die Ergebnisse dieser Studie zeigen die Existenz einer funktionellen Achse zwischen Diät, Mikrobiom und Metabolom, die die Krankheitsprogression bei BE im L2-IL1B-Mausmodell beeinflusst. Auch Mikrobiom- und Metabolom-Daten aus Gewebe und Stuhl von menschlichen Patienten zeigen eine systemische Erhöhung spezieller Gallensäuren und Gallensäure-metabolisierender Mikrobiota im BE-Gewebe in Korrelation mit dem Krankheitsverlauf.

1. Introduction

1.1. The Gastro-Intestinal Tract: an anatomical and physiological overview

The term Gastro-Intestinal (GI) tract comprises all organs of the digestive system from the oral cavity to the anus, including the esophagus, stomach, and intestines, each fulfilling specific functions in food digestion and the alimentation of the body with energy and nutrients.

1.1.1. Esophagus

The esophagus is a muscular tube of approximately 25 cm length in adult humans, that transports pre-comminuted and predigested solid food and liquids from the oral cavity via the pharynx into the stomach¹⁻⁴. Particle transport into the stomach is supported by peristaltic contractions of the muscular walls of the esophagus^{1,5}. The esophagus is anatomically beginning at the end of the oral cavity and passes the mediastinum behind the trachea and the heart before it passes through the diaphragm and enters the stomach²⁻⁴. At both ends of the esophagus there are esophageal sphincters, muscular rings helping to control the transport of particles along the esophagus⁴. While the upper esophageal sphincter (UES) between pharynx and cervical esophagus is partially under voluntary control and prevents particles and secretions from entering the trachea, the lower esophageal sphincter (LES) between esophagus and stomach is not under voluntary control and is primarily preventing stomach contents and acids from regurgitation into the esophagus, as its inner wall is not designed for repetitive acid exposure^{1,6-9}. The esophageal wall comprises four different tissue compartments: most lumenally the mucosa with the submucosa, muscularis propria and adventitia arranged in layers below, while a serosa is missing^{3,10,11}. The mucosa of the esophagus consists of nonkeratinized stratified squamous epithelium with lamina propria and the muscularis underneath^{4,11,12}. The submucosa consists of connective tissue containing plasma- and vascular cells, nerves, and mucosal glands^{4,11,12}. The muscularis propria comprises muscles with a transition of skeletal muscles into smooth muscles along the esophagus^{4,11,12}. The adventitia consists of loose connective tissue including nerves, blood- and lymph vessels. The adventitia is attached to neighboring structures like trachea or diaphragm via elastic fibers^{4,11,12}. Near to the LES, the esophageal mucosa with its squamous epithelium segues into gastric columnar epithelium at the squamous-columnar junction (SCJ)¹³. The intrinsic part of the LES is controlled by hormonally influenced esophageal muscle fibers, while extrinsically the diaphragm muscle assisting respiration is connected⁴. Dysfunctions of the esophageal peristalsis or the LES are also called esophageal motility disorders, often manifesting in gastro-esophageal reflux^{8,14,15}. Esophagus and stomach of animal models like rats and mice are anatomically similar to the human stomach, although their esophagus does not contain submucosal glands¹⁶. Also, the SCJ of both rodents lies

anatomically in the stomach, between a squamous lined stomach compartment called forestomach and the glandular columnar lined rest of the stomach¹⁶. Importantly, the forestomach does not fulfill digestion purposes and is anatomically differently. It acts as storage pocket for food ingested in bulk, and slowly releases the food to the rest of the stomach, where it is then digested^{17,18}. The forestomach is thought to react to exposure of xenobiotics in the food similarly as the human esophagus¹⁷, making studies on the BE and EAC at the SCJ in mouse and rat models comparable to human disease progression despite anatomical differences.

1.1.2. Stomach

The stomach is a distensible muscular organ lying between esophagus and small intestine. The stomach is responsible for storage and digestion of food via secretion of gastric acid and digestive enzymes such as pepsin and agitation of the food through peristalsis^{4,11}. Although absorption of nutrients is a main function of the small intestine, the stomach can also absorb molecules such as caffeine, ethanol, water, or medication to a certain extent^{11,19-21}. The stomach consists of four anatomical regions: the cardia, the fundus, the corpus and the pylorus^{4,11,22}. The gastric cardia is located adjacent to the squamous-columnar junction and the LES and contains a substantial number of mucosal glands (cardiac glands)^{4,11}. The fundus is located at the superior part of the stomach, while the corpus comprises the main and most central part of the stomach and contains monoclinal gastric glands^{4,11}. The pylorus is the most distal part of the stomach, with the pyloric antrum, the pyloric canal, and the pyloric sphincter, a hormonally controlled muscular ring directing the passage of food particles from the stomach to the duodenum as first part of the small intestine^{11,23,24}. The stomach wall comprises five different layers: most lumenally the gastric mucosa with the submucosa, muscularis externa, subserosa and serosa arranged underneath^{11,12}. The mucosa of the stomach consists of columnar epithelium with a lamina propria and the mucosa muscularis underneath^{4,11}.

1.1.3. Small Intestine

The small intestine lies between stomach and the cecum of the large intestine. The small intestine is responsible for further enzymatic digestion, production of gastrointestinal hormones and active absorption of nutrients and other molecules from the digested food mass¹². It can be divided into three different compartments called duodenum, jejunum, and ileum. In the duodenum, secreted enzymes further digest food particles from the stomach¹². In the jejunum, nutrients and particles predigested in the duodenum are reabsorbed, while in the ileum mainly bile salts, vitamin B12 and leftover molecules from the jejunum are absorbed^{11,12,25-27}. Similar to the stomach, the small intestine is composed of mucosa, submucosa, muscularis propria and serosa¹². The mucosa of the intestine also lies lumenally on top of a lamina propria and the

mucosa muscularis¹². Circular folds and the dense arrangement of millions of villi maximize the absorptive surface area of the mucosa^{11,12}.

1.1.4. Large Intestine

The large intestine has a length of approximately 150 cm and lies between the distal part of the small intestinal ileum and the anus, where stool is excreted. The large intestine is mainly responsible for absorption of water and remaining nutrients, production and absorption of vitamins as well as for formation and excretion of stool²⁷. The large intestine also has different compartments beginning with cecum, appendix, ascending-, transverse-, descending- and sigmoid colon, rectum and the anus¹¹. The large intestine is composed of mucosa, muscularis mucosa, submucosa, muscularis propria and serosa¹¹. The mucosa consists of columnar epithelium organized in hollow tube formed crypts with minimal surface area instead of villi luminally covering of lamina propria and the muscularis mucosa²⁸.

1.1.5. The Role of Liver and Gall Bladder as Accessory Digestive Organs

Both liver and gall bladder, besides teeth, tongue, salivary glands and pancreas belong to the accessory digestive organs, having functions important to digestion¹². The liver consists of parenchymal cells, mainly hepatocytes and non-parenchymal cells, including stellate, Kupffer and sinusoidal endothelial cells¹². It is essential in a variety of metabolic processes, in glycogen and vitamin activation and storage and primary bile acid synthesis as end-product of cholesterol catabolism^{11,29}. The liver secretes approximately one liter of bile per day, partially for molecule secretion purposes and partially for emulsification and digestion of dietary fats and lipid soluble vitamins in the gut^{11,30}. Bile mainly consists of water mixed with bile salts, cholesterol, lecithin, proteins, ions and bile pigments such as bilirubin^{11,31}. Bile is stored in the gallbladder and released into the small intestine upon fat ingestion^{11,31}. High levels of bile acids accumulating in other tissues are toxic, tissue damaging and contributing to a variety of diseases of the gastrointestinal tract, wherefore it is highly important to control bile acid production and maintain constant bile acid levels in the body³⁰.

1.2. Pathophysiology of the Esophagus and the Upper Gastro-Intestinal Tract

1.2.1. Motility Disorders

Disturbed peristaltic movement of the esophagus or of the function of the LES lead to esophageal motility disorders with symptoms such as dysphagia, heartburn, or non-cardiac chest pain^{4,15,32}. There are diverse primary and secondary esophageal motility disorders, with secondary disorders being caused by other primary diseases or malfunctions of the body. They include nonspecific esophageal motility disorder, achalasia, diffuse esophageal spasm,

nutcracker esophagus, hypertensive LES or Gastro-Esophageal Reflux Disease (GERD), with GERD being the predominant disorder^{4,32}.

1.2.2. Gastro-esophageal Reflux Disease

Gastro-Esophageal Reflux Disease is highly prevalent in industrialized western countries such as the United States³³⁻³⁵. GERD has been defined as “ *the effortless movement of stomach contents into the esophagus...causing troublesome symptoms or complications*”³³. Thereby, the esophagus is repeatedly exposed to acidic reflux of gastric juice including hydrochloric acid and gastro-duodenal content including bile acids, with gastro-duodenal content damaging the esophageal wall more than gastric juice alone³⁶⁻³⁸. Due to increased intra-abdominal pressure, unhealthy dietary habits and other co-morbidities, obese individuals are more likely to develop GERD³⁹. Symptoms of GERD typically comprise heartburn, acid regurgitation and chest pain³³. Chronic reflux leads to inflammation and damage of the esophageal tissue and is considered the main risk factor of BE, a metaplastic transformation of esophageal squamous to columnar epithelium beginning at the squamous-columnar junction^{40,41}.

1.2.3. Reflux Esophagitis

Other than eosinophilic, drug-induced or infectious esophagitis caused by allergies, medications or bacterial, viral or fungal infections, reflux esophagitis is caused by chronic acidic reflux containing noxious agents⁴². By reflux-induced inflammation, the esophageal squamous epithelium is damaged. Whether the damage is caused by direct caustic acid injury or by secretion of cytokines and subsequent creation of an inflammatory microenvironment, characterized by attraction of immune cells and proliferation of basal cells, or whether unknown factors also play a role is not completely clear⁴³. Interestingly, in a study by Souza et al. 2009, inflammatory cells were recruited early to the lower esophageal mucosa due to cytokine secretion by epithelial cells exposed to reflux, long before epithelial damage^{43,44}. Accordingly, following lymphocytic infiltration, basal cell hyperplasia in the squamous epithelium occurred several weeks before surface epithelial damage. Inflammatory conditions have been shown to correlate with tumorigenesis in general and to be one of the main factors of malignant progression in diseases of the digestive system, including reflux esophagitis causing BE as subsequent complication^{45,46,47}.

1.2.4. Barrett's Esophagus

Barrett's Esophagus (BE) is the most relevant precursor lesion of EAC. Its main risk factor is chronic reflux (GERD)⁴⁸. Although only 0.1-0.3 % of patients with BE develop EAC and a majority of EAC patients do not have any clinical history of BE before diagnosis, patients with diagnosed BE have a 30-50x increased risk to develop EAC compared to persons without BE⁴⁹⁻⁵⁴. Anatomically, Barrett esophagus emanates from the gastroesophageal junction (GEJ) and expands into the distal esophagus in the form of tongue-shaped metaplastic islets⁵⁵. The stratified squamous epithelium of the distal esophagus is replaced with a metaplastic columnar epithelium resembling classical intestinal metaplasia with goblet cells, or with non-goblet, columnar lined esophagus resembling intestinal and cardia metaplasia^{40,56,57}. Interestingly, even though endoscopic techniques to treat BE are effective, and together are able to ablate the complete abnormal BE tissue in the esophagus, reoccurrence of Barrett esophagus cannot be circumvented in all of the patients^{58,59}. This leads to the suspicion that BE is originally emanating from other regions through migration of progenitor cells.

1.2.5. Esophageal Cancer

Esophageal cancer is not a very common, but one of the deadliest types of cancer, being among the leading causes of cancer-caused death worldwide in reports since the 1990s⁶⁰⁻⁶³. Only lately, combined overall survival of 19 % was postulated for esophageal cancer which renders it among the deadliest cancers together with pancreatic, lung, and liver cancer⁶⁴. The big majority of esophageal cancers can be characterized as esophageal squamous cell carcinoma (ESCC) or as esophageal adenocarcinoma (EAC)⁶⁵. While ESCC mainly develop in the middle to lower third of the esophagus, EAC is located in the most distal part of the esophagus^{65,66}. Both types of esophageal cancers are differentially abundant in different regions of the world. The main type of cancer in the high incidence regions in Asia and the Middle East is ESCC, most probably caused by poor nutritional status, low consumption of vegetables and fruits and high consumption of extremely hot beverages⁶⁷⁻⁷⁰. ESCC in western countries is mainly caused by smoking and high alcohol consumption^{67,71}. The main type of esophageal cancer in western and westernized countries such as the United States and Europe is EAC, most probably caused by smoking, overweight, obesity and GERD triggering BE^{67,72-74}. Interestingly, there is a strong link between obesity and resulting onset of GERD and BE then developing to EAC⁷²⁻⁷⁴.

1.3. Characterization of Barrett's Esophagus (BE) and Esophageal Adenocarcinoma (EAC)

1.3.1. Hypotheses of the Origin

As patients diagnosed with BE have a highly increased risk to develop EAC during their clinical history⁵³, it is plausible that BE and EAC develop from the same progenitor. To date, there are several theories of how BE develops.

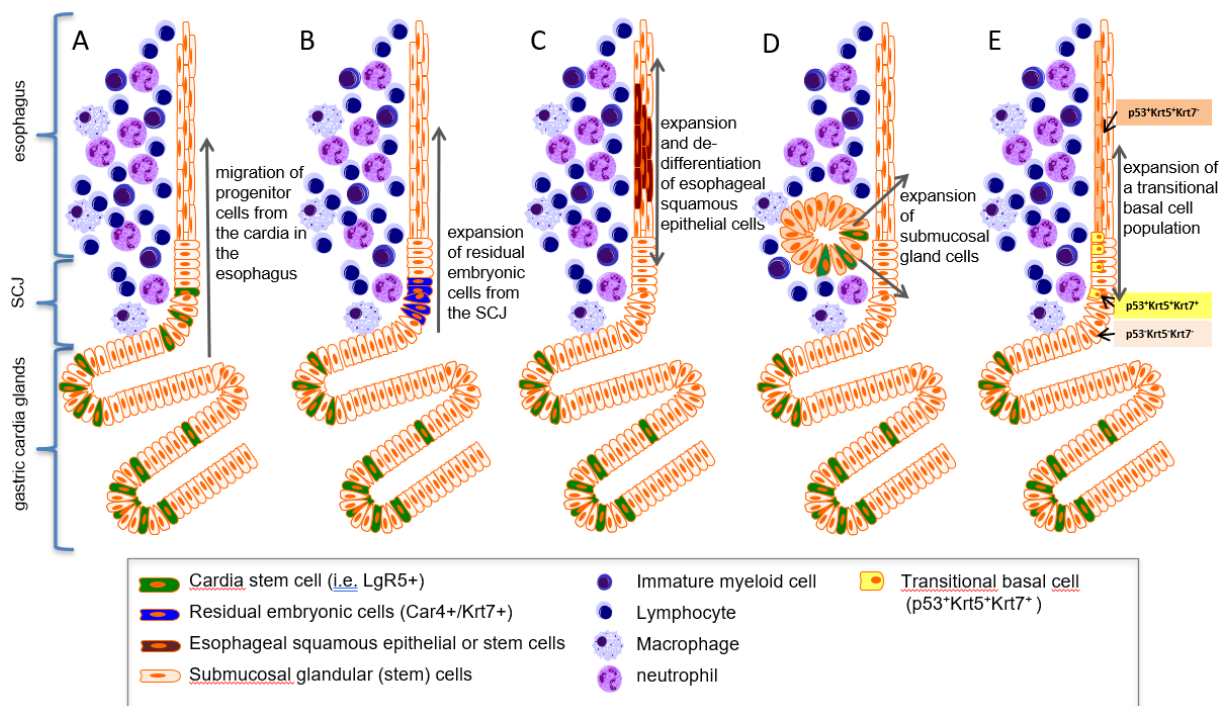


Figure 1: Hypotheses of the origin of BE. The hypotheses suggest the migration of (A) progenitor (stem) cells or (B) residual embryonic stem cells from the SCJ towards the esophagus, (C) transdifferentiation of squamous epithelium or expansion of (D) submucosal glands or (E) a transitional basal cell population as origin of BE.

Early clinical studies of BE described the histological resemblance of columnar epithelium of BE with gastric epithelium^{75,76}. Thus, it was assumed that gastric epithelium from the cardia close to the GEJ migrates and expands into the esophagus. To date there are different highly efficient approaches to treat patients with BE endoscopically, but still BE not unusually reoccurs at the GEJ^{58,59}. Recurrence rates of BE were shown to be proportional to the extent of endoscopic ablation towards the GEJ^{59,77}. Yet, BE still develops in patients after esophagogastrostomy, where the GEJ is often surgically removed⁷⁸. Interestingly, the gastric cardia region has properties of a transitional epithelium characterized by absence of parietal cells and concurrent presence of different progenitor cell markers such as Lgr5 and Cholecystinin B Receptor (CCKBR), pointing towards a potential origin of BE in the gastric cardia⁷⁹⁻⁸² (Fig.1 A). The work of this thesis was based on a mouse model in which overexpression of *Interleukin 1 beta* (*IL1B*) in esophagus and forestomach shows expansion

of *Lgr5* stem cells and progression from cardiac glands to metaplastic epithelium representing intestinal metaplasia at and above the SCJ resembling human BE⁸².

There is one more hypothesis that also suspects expansion of stem cells from the GEJ, in this case remnant embryonic stem cells, to be the cause of BE (Fig.1 B). Tumor protein p63 (p63) plays a role in epithelial development and while p63 deficient mice suffer from loss of their stratified epithelia leading to prenatal death, the p63 deficient mouse embryos develop metaplasia similar to human BE^{83,84}. Contradicting this hypothesis, gene expression studies on human tissue showed p63 expression rather in ESCC than in EAC, with no similarity to BE gene sets^{84,85}.

One of the hypotheses describes that BE arises by the transition of squamous into columnar epithelial cells via transdifferentiation, meaning via transformation between differentiated cell types without cellular division⁸⁶ (Fig.1 C). Transdifferentiation of columnar to squamous epithelium naturally happens during embryonic development of mice, and could be partially inversed artificially in cell culture experiments and mouse models^{87,88,89}. Still, until today, no study could show transdifferentiation of squamous to columnar cells in the esophagus.

Another hypothesis focuses on submucosal glands as potential origin of BE⁹⁰ (Fig.1 D). Submucosal glands consist of columnar epithelium in the basal part, while they are lined by squamous epithelium in the luminal part. Studies on the histological representation of BE in human tissue and animal models with submucosal glands suggested a transition of cells of the gland ducts to columnar epithelium^{91,92}. While submucosal glands are similar to and potentially contribute to the development of metaplastic BE epithelium, the idea that they present as exclusive progenitors of BE is strongly contradicted by the fact that rodent models without submucosal glands are also able to develop BE metaplasia and that BE originates from a heterogenous population of progenitors⁹³⁻⁹⁵.

The most recent hypothesis on BE development was published by Jang et al. in 2017, suggesting transitional basal cells as the potential origin of BE⁹⁶ (Fig.1 E). Based on lineage tracing experiments, the authors identified a basal p63+, Keratin 5+, Keratin 7+ "p63+KRT5+KRT7+" cell population in a transitional zone of squamous epithelium near the GEJ, which is able to form metaplastic intestinal type epithelium with goblet cells upon ectopic expression of *Caudal type homeobox 2 (CDX2)*. Interestingly, exposure to BA caused expansion of *Cdx2* expressing cells at the GEJ.

There is one more hypothesis about the origin of BE suspecting circulating bone marrow cells as progenitors of BE (not depicted). This hypothesis is based on findings describing their ability to migrate across and differentiate to different tissues upon injury, suggesting their contribution

to cancer development⁹⁷⁻¹⁰¹. It has been shown that in rat and mouse models of BE as well as in a human case, transplantation of bone marrow and stem cells resulted in migration and participation of bone marrow derived stem cells in formation of BE and EAC^{102,103}.

Although there exists a multitude of studies on most of these hypotheses supporting or rejecting them, the ultimate proof of a single cellular origin of BE is still missing. Due to the highly heterogenic nature of BE and due to the various research findings on this topic, it seems rather plausible that the different hypotheses all have their reason for existence. The latest research highlights the GEJ and gastric cardia as likely areas of origin for the expansion of progenitor cells, highly probably stem cells of one or different types, leading to development of metaplasia.

1.3.2. Prevalence and Incidence of GERD, BE and EAC

As previously discussed, EAC is not ranging amongst the most common cancers but amongst the cancers with the poorest survival rates⁶⁰⁻⁶³. Of note, while the incidence of ESCC is constantly decreasing, EAC incidence is increasing steadily in many western or westernized countries and exceeded that of ESCC in the past decades¹⁰⁴⁻¹⁰⁷. Although there are studies reporting a stagnation in the increasing trend in the US mainly in men^{105,108,109}, stimulating a debate on the realistic change of prevalence of EAC over time, there are other studies reporting a continuous increase in incidence rates¹⁰⁴. Also, in other countries such as Japan or Finland, steadily increasing incidences of EAC are reported in recent studies^{106,107,110}, and there exist studies predicting further increase of EAC incidence in the next years¹¹¹. Increasing incidences were repeatedly attributed to changes in the prevalence of GERD and BE, dietary habits, and obesity^{104,106,110,112}. Although true incidence rates of GERD and BE are harder to analyze than those of EAC as it is assumed that many cases remain unreported, available information suggests increasing rates of GERD comparable to those of EAC¹¹³. Studies analyzing EAC incidence in individuals with or without GERD or previously diagnosed BE consistently agree on the fact that chronic reflux and prior diagnosis with BE, especially dysplastic BE, increases the risk of development of EAC significantly¹¹⁴⁻¹¹⁹, while there is a study associating progression free years of BE with an again decreasing risk for final progression to EAC¹¹⁴. Importantly, reported differences in disease progression rates between Europe and north America might be a result of different treatment guidelines and strategies between countries¹¹⁶.

1.3.3. Risk Factors

As mentioned before, incidence rates of EAC were associated to prevalence of GERD and BE, which compose the main risk factors for EAC¹¹⁴⁻¹¹⁹. GERD leads to damage of the esophageal squamous epithelium, hence predisposing the tissue for development of BE⁴⁸. Thereby, reflux containing bile acids damages the tissue more compared to acidic reflux only⁴⁸. The study from Rantanen et al., analyzing data from the Finnish cancer registry differentiates EAC and Adenocarcinoma of the esophagogastric junction (EGJAC). Interestingly, while risk for EAC in the Finnish study was significantly associated with previously diagnosed BE, EGJAC was strongly associated with previous Cholecystectomy, a procedure in which the gallbladder, storing bile acids between meals, preventing continuous secretion into the GI tract, is removed¹⁰⁷. Reflux is also influenced in part by *Helicobacter pylori* infection. Being strongly associated with gastric cancer and thus being eradicated in many countries over the past decades, *H. pylori* is inversely correlated with GERD and EAC¹²⁰⁻¹²². *H. pylori* infection can lead to atrophic gastritis with loss of gastric glandular cells, in which the secretion of gastric acid and pepsin in the stomach and thus in gastro-esophageal reflux are decreasing, which is proposedly the cause of the protective effect of *H. pylori* on EAC¹²³⁻¹²⁵.

Chronic reflux is especially promoted by central obesity, or a high Body-Mass-Index (BMI) or waist circumference, caused by consumption of a diet high in fat and other processed components, often also referred to as western diet¹²⁶⁻¹³¹. Central obesity is also a direct risk factor of BE and EAC^{128,132,133}. Interestingly, in mice, an association between the gut microbiome and western diet induced obesity was found. Removal of the gut microbiome or microbial reprogramming was able to inhibit obesity caused by intake of western diet^{134,135}. These results together suggest a close interconnection between diet, obesity, GERD, the gastrointestinal microbiome, and BE and EAC development.

1.3.4. Disease Models

Different disease models, both *in vitro* and *in vivo* have been established to analyze the development and progression and possible prevention or treatment of BE and EAC.

In vitro disease models include 2D cell lines, organotypic culture (OTC) models, and 3D organoids. There are different established esophageal cell lines, representing different types of esophageal cancer, with at least three lines being frequently used in studies: OE19, -21 and -33¹³⁶. While the cell line OE19 represents esophageal gastric junction and cardia adenocarcinoma, OE21 represents ESCC and OE33 represents EAC¹³⁶. 2D cell culture models have limitations in terms of representing a 3D *in vivo* disease system, wherefore efforts were made to establish *in vitro* models mimicking the disease more closely.

OTC models with epithelial cells being cultured on collagen with fibroblasts were a 3D cell culture model established to be able to study cellular interactions between epithelium and stroma more closely^{137,138}. A limitation of this model is that it still lacks other cell types such as immune or stem cells. Another 3D culture model to study BE and EAC is organoid culture, which reproduces the architecture of the epithelium more closely, consisting of the major cell types of the tissue¹³⁹. Organoids can be generated from primary murine and human cells and grown in matrigel with medium supplemented with growth factors¹³⁹. Organoids can be used for multiple experimental settings and downstream applications, such as coculture experiments, drug testing, lentiviral transfection or Crispr-Cas9 experiments, therefore making them an attractive study model.

In vivo disease models mimic the disease in a living organism and are important to study the genetic, anatomical, and pathophysiologic components of BE and EAC in a more holistic approach. There exists a wide variety of *in vivo* disease models of BE and EAC in different mammals which were all based on surgical methods.

The first surgical model to study acute esophagitis via ligation of the pylorus was already developed 1938 by Selye et al. Pyloric ligation caused very severe reflux, which lead to death of the mice within days and was not mimicking human disease sufficiently¹⁴⁰. Omura et al. created a more sophisticated model of chronic reflux via gastric obstruction, whereas this model did not further develop BE or EAC¹⁴¹.

In a canine model of BE, surgical removal of mucosal tissue lead to columnar metaplasia due to reflux and wound healing in the distal esophagus¹⁴². Larger mammals like dogs have an anatomical structure of the esophagus, which is very similar to humans, also containing submucosal glands. The main limitation of this approach was the - with 1.5-3 years - extremely

long timespan until development of disease. Certainly, this disease model would also cause high costs and be increasingly difficult to be ethically approved.

Faster and more cost-effective rat models of BE, undergoing different surgical procedures to connect esophagus or the gastro-esophageal junction to different parts of the intestine were created¹⁴³⁻¹⁴⁶. With these models, gastro-duodenal reflux could be shown to induce severe BE and EAC, which even worsened after treatment with nitrosamines, iron, or high-fat diet^{144,147-149}.

Due to their small size, mouse models showed limited suitability for surgical approaches to create BE. Still, there also were successful murine surgical reflux models to study BE and EAC^{150,151}. In these studies, similar to rat models, mice, partially with genetic mutations, were undergoing esophagojejunostomy¹⁵⁰⁻¹⁵². Limitations of both surgical rat and mouse models were that the models were highly artificial, had high mortality rates and surgically induced reflux contained high amounts of bile and less acidic gastric reflux as in patients with GERD, leading to severe disease development.

Also, different approaches for genetically engineered mouse models to study BE and EAC were made. There were different models with genetic alterations such as *Thrombospondin 1* (*THBS1*) or *p63* deletion, or hedgehog pathway activation, all leading to development of columnar metaplasia mimicking BE, but no progression to EAC. Partially those models are highly artificial such as the *p63* knockout model leading to prenatal death^{84,152,153}. In this thesis, the first genetic mouse model to study BE and its progression to EAC was used. It is characterized by development of metaplasia, dysplasia, and tumor development at the SCJ. Metaplastic changes are a result of inflammation induced by overexpression of human *IL1B* in the squamous esophagus and forestomach of C57BL/6J mice under the EBV promoter⁸². Treatment of the mice with high fat diet, the bile acid deoxycholic acid in the drinking water or with bile acids and nitrosamine accelerated disease progression in these mice.

1.4. The Impact of Dietary Intake on the Pathophysiology of the Gastro-Intestinal Tract

It is well known that a diet rich in fat, sugar and animal derived products as consumed in western countries correlates with high rates of certain cancers, many of them in the gastrointestinal tract. In comparison, populations in developing countries, typically consuming a diet with low amounts of these products have low incidence rates of the respective cancer types¹⁵⁴. Already in the 1980s, an article in the journal of the national cancer institute proposed that up to 35 % of all cancers could potentially be attributed to dietary intake¹⁵⁵. Especially intake of carcinogens, affected formation of carcinogens and downstream signaling, for example via the bacterial gut flora or interference with bile acid metabolism and overnutrition are discussed as potential causes for tumor promotion through diet¹⁵⁵. Vice versa, caloric restriction and fasting are thought to be cancer preventive and adjuvant in cancer treatment¹⁵⁶. As the exact mechanisms underlying the causality between diet and cancer are often not clear until today, research on this topic is still highly important.

1.4.1. Western Diet and Obesity

Obesity has been linked to various cancers, including those of the gastrointestinal tract, such as colon, gastric and also esophageal cancer¹⁵⁷. The respective study from the American cancer society conducted in 1997 already attributed 14-20 % of all cancer deaths in the U.S. to overweight and obesity¹⁵⁷. Importantly, obesity has become endemic in the western world, with constantly increasing obesity rates in western and especially in westernized countries in the last decades¹⁵⁸. Hence, it cannot be excluded that the influence of obesity on cancer deaths is increasing steadily together with its prevalence in the world population.

In the industrial era, technical advances in the food production industry led to massively increased low-cost availability of food products from animal origin, high in fat, salt, high caloric and artificial sweeteners, and of highly processed foods¹⁵⁹. As it was initially consumed in industrialized western countries, a diet rich in these dietary components is typically defined by the term western (style) diet. In parallel with the massive and rapid changes in food availability and thus increasingly high caloric dietary intake, the incidence of obesity and certain diseases such as cardiovascular diseases and cancer rose in those countries, most probably due to a parallel decrease in physical activity and the practical impossibility to evolutionarily adapt in to the dietary changes in the given time-frame^{158,159}.

The study on which this thesis is based is focusing on the impact of a diet high in fat on an IL-1B overexpressing genetic mouse model for esophageal adenocarcinoma. Therefore, the potential mechanisms on how both dietary components of a western diet are acting on tumorigenesis are presented in more detail in the following.

1.4.2. Dietary Fat

Within the last 100 years, the time in which dietary intake in the western population changed markedly, also consumption of refined vegetable oils and fat from domestic animal products, often high in animal derived fat, increased dramatically¹⁵⁹. Fat is predominantly digested in the small intestine, where bile, containing bile acids and other lipases secreted by the gallbladder emulsifies and cleaves fat into glycerin and fatty acids¹⁶⁰. Those particles are then absorbed by the intestinal mucosa and fed into the blood circulation, where they are transported to the cells of the body as energy source. Excess energy not used in the lipid catabolism of the cells is stored as storage lipids in the adipocytes of the body¹⁶¹. Lipid digesting bile acids, which are originally produced in the liver, undergo so-called enterohepatic circulation. They are mainly reabsorbed in the terminal ileum, the most distal part of the small intestine and transported back to the liver for reuse via blood circulation¹⁶².

High fat diet and resulting accumulation of fat and obesity act on tumorigenesis mainly via alterations in hormone secretion and establishment of chronic inflammatory conditions.

In overweight individuals, chronically elevated insulin levels lead to disturbed insulin signaling¹⁶³. Hyperinsulinemia resulting from dietary intake and overweight leads to high circulating levels of insulin growth factor 1 (IGF1), supporting tumor cell growth and influencing proliferation and apoptosis via JNK pathway activation¹⁶³. There is also evidence that insulin resistance and type 2 diabetes are related to increased oxidative DNA damage¹⁶⁴. It was shown that adipocytes are directly able to influence cellular proliferation and apoptosis, most probably via changes in adipokine secretion. For instance, secretion of the adipokine adiponectin decreases in the adipose tissue upon ingestion of high fat diet and in the whole circulation in obese individuals^{165,166}. Adiponectin has antiproliferative and antiangiogenic properties, increases insulin sensitivity, decreases IGF1 and mechanistic target of rapamycin (mTOR) signaling via activation of AMP activated protein kinase (AMPK) and suppression of signal transducer and activator of transcription 3 (STAT3) and vascular endothelial growth factor (VEGF) signaling and inhibits inflammatory Nuclear Factor κ B (NF- κ B) signaling^{166,167}. Vice versa, serum levels of the adipokine leptin, which primarily regulates appetite and satiety, are generally increased in obese individuals. Leptin is associated to colon cancer malignancy and was shown to be able to increase proliferation and decrease apoptosis in in diverse cell types, by affecting phosphoinositid-3-kinase (PI3K)/ AKT serine/threonine kinase (AKT)/ mTOR signaling¹⁶⁸.

Obesity is also able to induce systemic inflammatory conditions via increased fatty acid deposition in different organs, via activation of inflammatory pathways such as the JNK or NF- κ B pathway and increased levels of proinflammatory cytokines and markers such as toll like

receptor 4 (TLR-4), inducible nitric oxide synthase (iNOS), cyclooxygenase-2 (COX-2), tumor necrosis factor alpha (TNF- α) or monocyte chemoattractant protein 1 (MCP-1)¹⁶⁹⁻¹⁷¹. Overweight and obesity are characterized by an accumulation of adipose tissue in the body. Especially visceral adipose tissue is associated to comorbidities, potentially due to its central position with its blood circulation being connected to the portal vein directly leading to the liver¹⁷². Adipose tissue itself can trigger inflammation, as enlarged adipocytes produce increased amounts of inflammatory cytokines and trigger macrophage infiltration in the tissue¹⁷³. The underlying mechanisms inducing systemic inflammation are not completely clear but evidence exists that at least partially, diet induced shifts of the microbiome and subsequent decreases in the epithelial barrier function are responsible for creation of an inflammatory environment^{169,174}. In addition, it was also proven that obesity is transmissible via fecal microbiota transplantation (FMT), providing evidence for a profound role of the diet-shaped intestinal microbiome on development of obesity and its metabolic effects, potentially also on its comorbidities¹⁷⁵.

1.5. The Impact of the Microbiome on the Pathophysiology of the Gastro-Intestinal-Tract

1.5.1. The Microbiome of the Gastro-Intestinal Tract

The “microbiome” of a human body describes all microorganisms colonizing a specific local habitat, including bacteria, viruses, eukaryota and archaea, interacting with each other and the host¹⁷⁶⁻¹⁷⁸. Bacterial abundance increases in the GI tract from proximal (esophagus) to distal along with decreasing oxygen availability and fluctuating PH values^{179,180}. The GI microbiota consists of up to 10^{13} bacteria only in the colon¹⁸¹. Functional insights into the microbiome remained hidden for many years due to limited technical abilities. Cultivation methods used for microbiome characterization were not able to realistically map complex microbial communities due to growth limitations^{182,183}. Since it is possible to study microbes using culture independent sequencing techniques, the characterization of microbial communities rapidly gathered pace¹⁸⁴.

The genes of the microbiome encode for innumerable functions, with some pathways affecting body homeostasis and human health substantially. Microbes in the gut are living in symbiosis with the gut mucosa and the immune system¹⁸⁵. A healthy microbiome is characterized by colonization with commensal microbiota, which prevents potential opportunistic pathogen overgrowth¹⁸⁶. The gastrointestinal microbial community is greatly contributing to food digestion, energy recovery and metabolism, for example fermentation of polysaccharides to short-chain fatty acids (SCFA) or metabolization of primary to secondary BA¹⁸⁷⁻¹⁸⁹. The gut microbial community and its functional potential are shaped by diet composition. Adaptive immunity maintains healthy microbial homeostasis and functional host barriers under the influence of microbial communities of a healthy microbiome¹⁹⁰⁻¹⁹². In response to increased fat intake the microbial profile shifts, triggering immune system activation and contributing to the development of obesity and other metabolic disorders, which can be prevented when artificially suppressing the microbiota by antibiotics^{174,188,193}.

1.5.2. Dietary Adaptation

Upon intake of a diet high in fat, the gut microbiome typically shifts. Upon HFD treatment, a decrease in *Bacteroidetes* and an increase in *Firmicutes*, changing the so called Firmicutes to Bacteroidetes ratio often associated with obesity was reported, similarly to studies in genetically obese mouse strains¹⁹³⁻¹⁹⁵. It could be demonstrated that in HFD mice, these changes are directly induced by diet and not conveyed by developing obesity¹⁹⁴. Changes in diverse other bacterial families upon HFD ingestion were also reported, such as increases in abundance of *Rikenellaceae* and decreases in the abundance of *Proteobacteria*, *Lactobacillaceae*, *Bifidobacteriaceae* or *Ruminococaceae*^{174,194,196}. Microbial changes in the

different studies were mostly not uniform, but were even shown to be mouse strain dependent¹⁹⁷. These findings arise the question if, in many cases, it is the combined metabolic ability profile of the bacterial community favoring disease development rather than a certain bacterial family. Importantly, in obese individuals the presence of a distinct microbiome capable of harvesting an increased amount of energy from the diet was detected¹⁹³. The weight of lean mice transplanted with these microbiota also increased¹⁹³. Nevertheless, also single bacterial strains were proven to contribute to mediation of diet induced effects on inflammation, metabolism, and obesity. As an example, both *Akkermansia muciniphilia* or *Clostridium cluster XIVa* containing *Roseburia spp.* are decreasing in abundance and capable of changing the metabolic profile during HFD feeding and diet induced obesity^{198,199}.

1.5.3. Inflammatory Effects of the Dietary Shaped Gut Microbiome

Upon HFD treatment, low-grade systemic inflammation is typically detected along with the described microbial changes. The inflammatory condition is likely to be mediated through those microbial changes, characterized by increased intestinal permeability along with decreased expression of tight junction proteins, increased TLR4 activation, decreased intestinal alkaline phosphatase and increased serum lipopolysaccharide (LPS) levels, also termed metabolic endotoxemia^{174,200}. LPS is a bacterial endotoxin which is part of the outer membrane of Gram-negative bacteria. TLR-4 is the receptor activated by LPS, while intestinal alkaline phosphatase is an enzyme detoxifying LPS, which is normally expressed in intestinal cells²⁰⁰. Treatment of HFD treated mice with antibiotics ameliorated metabolic endotoxemia and inflammatory conditions, proving the role of the diet-induced microbiome in onset of systemic inflammation¹⁷⁴. In both HFD but also in High Fructose Diet mice, increased levels of IL1B, TNF- α and MCP-1 were detected, and hepatic lipid accumulation led to TLR-4 signaling resulting in onset of cytokine and apoptotic signaling in the liver. The upregulation of CD36, FAS (FAS cell surface death receptor) and sterol response element binding protein 1 (SREBP1) further contributed to development of a fatty liver and thus inflammatory signaling²⁰¹.

1.6. The Impact of Bile Acids on the Pathophysiology of the Gastro-Intestinal-Tract

1.6.1. Bile Acid Synthesis and Enterohepatic Circulation

Bile acids are produced by the liver as a pathway of cholesterol catabolism, and secreted via the canaliculi, where they are mixed with water, cholesterol, bile pigments and other components to form bile^{11,30,31}. Bile is then stored in the gallbladder and secreted upon food consumption^{11,31}. After their release in the upper intestinal tract, the detergent properties of bile acids enable them to support emulsification and digestion of fat, cholesterol, and lipid soluble vitamins^{11,30}.

There exist two different highly complex bile acid synthesis pathways in the liver, the classical synthesis pathway controlled by cholesterol 7 α -hydroxylase (Cyp7A1) as rate-limiting enzyme, resulting in cholic acid (CA) and partially chenodeoxycholic acid (CDCA) production, and the alternative bile acid synthesis pathway controlled by sterol 27-hydroxylase (Cyp27A1), resulting in CDCA production only²⁰²⁻²⁰⁴ (Fig.2). While humans produce similar amounts of CA and CDCA, the exact ratio between the produced bile acids is determined by sterol 12 α -hydroxylase (Cyp8B1), as Cyp8B1 is an essential enzyme for CA production²⁰³. Bile acids are further conjugated to glycine or taurine at C₂₄ in the liver to increase their amphipaticity for secretion and digestion purposes²⁰⁴. After conjugation, bile acids are actively secreted from the liver into bile via the bile salt export pump (BSEP) and stored in the gallbladder until release upon food consumption²⁰³. 95 % of the secreted, mostly conjugated bile acids are reabsorbed in the small intestinal ileum via the apical sodium dependent bile acid transporter (ASBT, IBAT or SLC10A2), fed into the portal vein, and transported back to the liver in a process called enterohepatic circulation^{202,203}. Only approximately 5 % of bile acids escape the reabsorption process and undergo metabolism by the gut microbiota in the distal intestine.

1.6.2. Bile Acid Metabolization by the Gut Microbiome

Bacteria in the gut microbiome are able to modify secreted bile acids, most probably for energy harvesting or detoxification purposes³⁰. In the small intestine, specific microbiota expressing a gene called bile salt hydroxylase (BSH) deconjugate the conjugated bile acids by cleavage of the bond to glycine or taurine^{30,205} (Fig.2). BSH activity was found mainly in gram-positive bacteria, such as in the major bacterial genera *Bacteroides*, *Bifidobacterium*, *Clostridium*, *Lactobacillus* and *Enterococcus*, but also in pathogenic bacteria such as *Listeria monocytogenes*²²⁹. Deconjugated bile acids cannot be actively transported back to the liver by ASBT and are further transported to the colon, where they undergo bacterial driven 7 α -dehydroxylation and other microbial bile acid metabolism²⁰³ (Fig.2, Fig.3). CA and CDCA and their conjugates are defined under the term “primary bile acids” and are actively

reabsorbed in the small intestine, whereas bile acids that underwent 7α -dehydroxylation and comparable metabolism by bacterial species in the gut are defined as “secondary bile acids” and passively diffuse into blood circulation across the colonic epithelial surface³⁰. The ability of bacteria to perform and regulate primary to secondary bile acid metabolism is conveyed by so called bile acid inducible (*bai*) genes^{30,203}. 7α -dehydroxylation is restricted to unconjugated bile acids and leads to generation of the two main secondary bile acids Deoxycholic Acid (DCA) from CA and Lithocholic Acid (LCA) from CDCA in humans^{203,206}. Only little is known about the bacterial species exerting 7α -dehydroxylation function. The only bacterial strains with confirmed 7α -dehydroxylation capacity have been identified in the genus *Clostridium* and *Eubacterium*^{203,206}, but *bai* gene activity and 7α -dehydroxylation were computationally predicted also in other bacterial species²⁰⁷. Importantly, there also exists a broad network of other bacterial bile acid metabolism processes, such as dehydrogenation, oxidation, reduction or epimerization processes, mainly guided by different hydroxysteroid dehydrogenases (HSDHs)²⁰⁶ (Fig. 2). HSDHs have been identified in a broader spectrum of bacterial species, such as in the genera *Clostridium* and *Ruminococcus*, in certain strains of *Peptostreptococcus* (e.g., *Peptostreptococcus productus*), *Egerthella* (e.g., *Egerthella lenta*), *Eubacterium*, *Bacteroides* (e.g., *Bacteroides fragilis*, *Ba. Thetaiotaomicron*), etc.²⁰⁶. In the liver, CDCA can be endogenously metabolized to the primary bile acids ursodeoxycholic acid (UDCA), or to muricholic acids (MCA) in mice, whereas in humans, MCAs are not detected and UDCA is only found as secondary bile acid generated via $7\alpha/\beta$ isomerization of CDCA^{202,203}. The murine MCAs alpha-MCA (α MCA) and beta-MCA (β MCA) can undergo bacterial 7α -dehydroxylation and form murideoxycholic acid (MDCA), while ω MCA is produced solely from β MCA via 6β -epimerization²⁰³. Further metabolites that are mainly formed from MCAs are hyodeoxycholic acid (HDCA) and hyocholic acid (HCA)²⁰³. Additional isomerization processes performed by bacteria can also lead to formation of so called iso- and allo- bile acids²⁰³. Secondary bile acids are passively reabsorbed by the colon, also undergo enterohepatic circulation, and contribute to diversification of the bile acid pool as they cannot be transformed back to primary bile acids in the liver.

The structural diversity of the bile acid pool is mirrored by its functional diversity, as bile acids are not only capable of lipid digestion but also exert other functions such as antimicrobial activity, regulation of bile acid metabolism or of cellular signaling pathways.

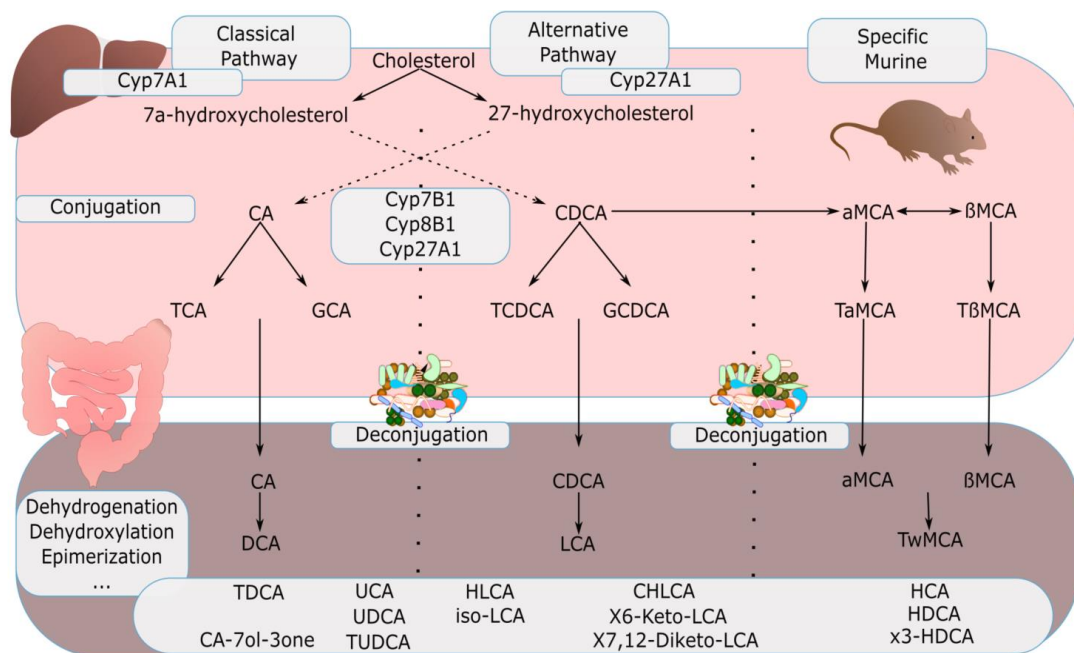


Figure 2: Bile acid synthesis, modulation and metabolism pathways in humans and mice (Created by BioRender.com)

1.6.3. Bile Acid Signaling via the Nuclear Receptor Farnesoid X Receptor (FXR)

There is a subset of receptors, including nuclear FXR, vitamin-D-receptor (VDR) and membrane-bound takeda G protein-coupled receptor (TGR5, also G protein-coupled bile acid receptor, GPBAR1) which showed to be responsible to bile acids^{202,208,209}. While TGR5 is thought to be mainly involved in Glucose metabolism, insulin signaling and other metabolic pathways²³², VDR is involved in calcium and phosphate homeostasis and detoxification of its ligand LCA^{226,210}. FXR is a nuclear orphan receptor and the main bile acid receptor regulating primary bile acid transport and de-novo synthesis. The receptor is primarily expressed in the small intestine and the liver but can also be found in various other tissues, such as kidney or spleen, where it's exact function is not yet clear. FXR is activated by excess bile acids, mainly CDCA and CA and their conjugates, while tauro-MCAs (TMCAs) are natural antagonists of the receptor^{203,209}. Upon activation FXR forms a heterodimer with retinoid-x-receptor (RXR) is internalized, regulates the expression of downstream targets, and inhibits primary bile acid synthesis via a negative feedback loop²⁰³ (Fig.3). In the ileum, activation of FXR leads to induction of fibroblast growth factor (*Fgf15* in mice (or *Fgf19* in humans), with subsequent translocation to the liver where *Fgf15* (*Fgf19*) triggers JNK and extracellular signal-regulated kinase 1 (ERK) signaling, further inhibiting *Cyp7A1* expression^{203,204}(Fig.3). In the liver itself, activated FXR induces the expression of small heterodimer partner (SHP) which binds and inhibits liver receptor homolog 1 (LRH-1), a gene responsible for activation of *Cyp7A1* gene expression^{203,204}. FXR activation is also proposed to inhibit *Cyp8B1* expression in the liver, thereby restricting production of CA²⁰³. Inhibition of both *Cyp7A1* and *Cyp8B1* gene expression

mainly downregulates CA generation and bile acid synthesis via the classical synthesis pathway.

FXR also regulates the activation of bile acid transporters, including Ileal bile acid binding protein (IBABP) in the intestine, bile salt export pump (BSEP) and Na-taurocholate cotransporting polypeptide (NTCP or SLC10A1) in the liver and organic solute transporter (Ost- α or SLC51A and Ost- β or SLC51B) in both tissues²¹¹(Fig. 3). IBABP, a transporter involved in apical to basolateral bile acid transport in enterocytes, and *FXR* gene expression mutually activate each other and stimulate IBAT activity as a downstream target²¹². Also, BSEP, a hepatic bile export pump and Ost- α and Ost- β , which are bile acid transporters expressed in enterocytes and hepatocytes are stimulated by FXR, while NTCP, which regulates bile acid uptake in hepatocytes is repressed by FXR²¹¹. Regulation of bile acid transport is also a critical factor for repression of *Cyp7A1* expression.

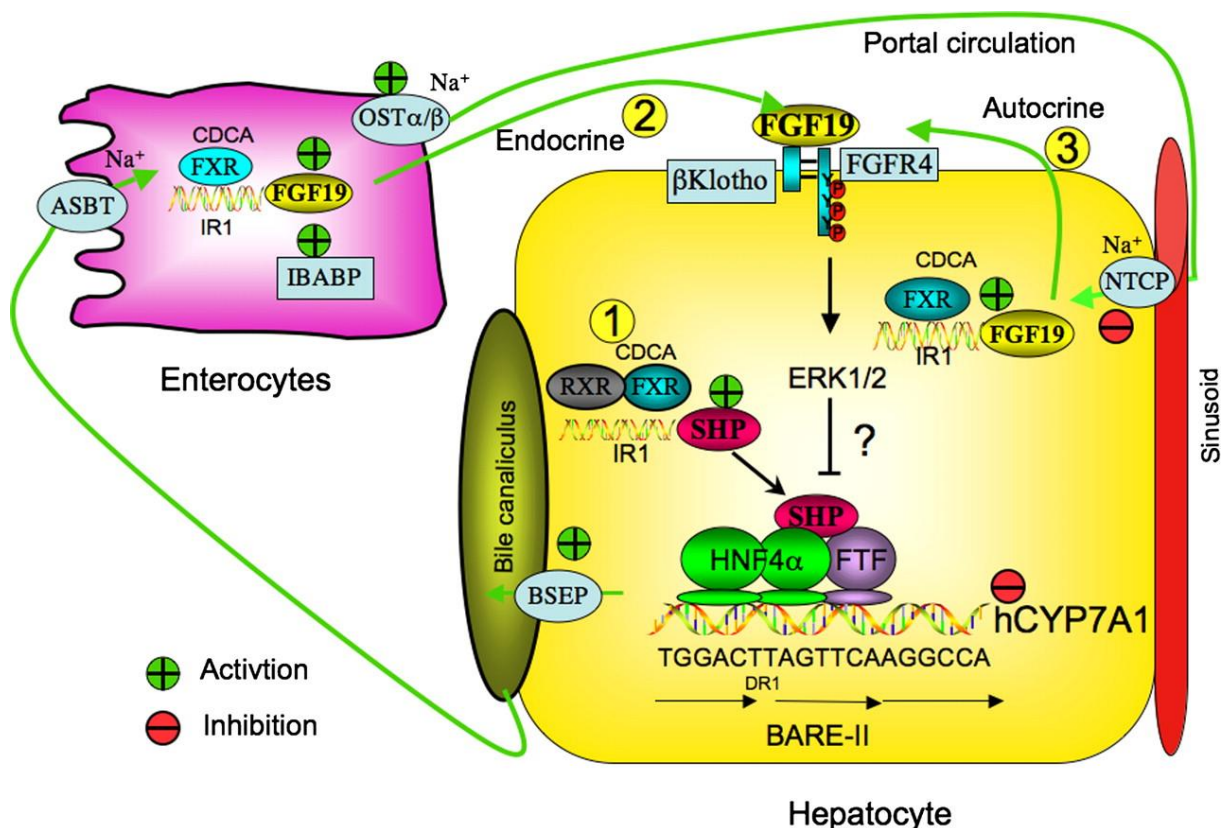
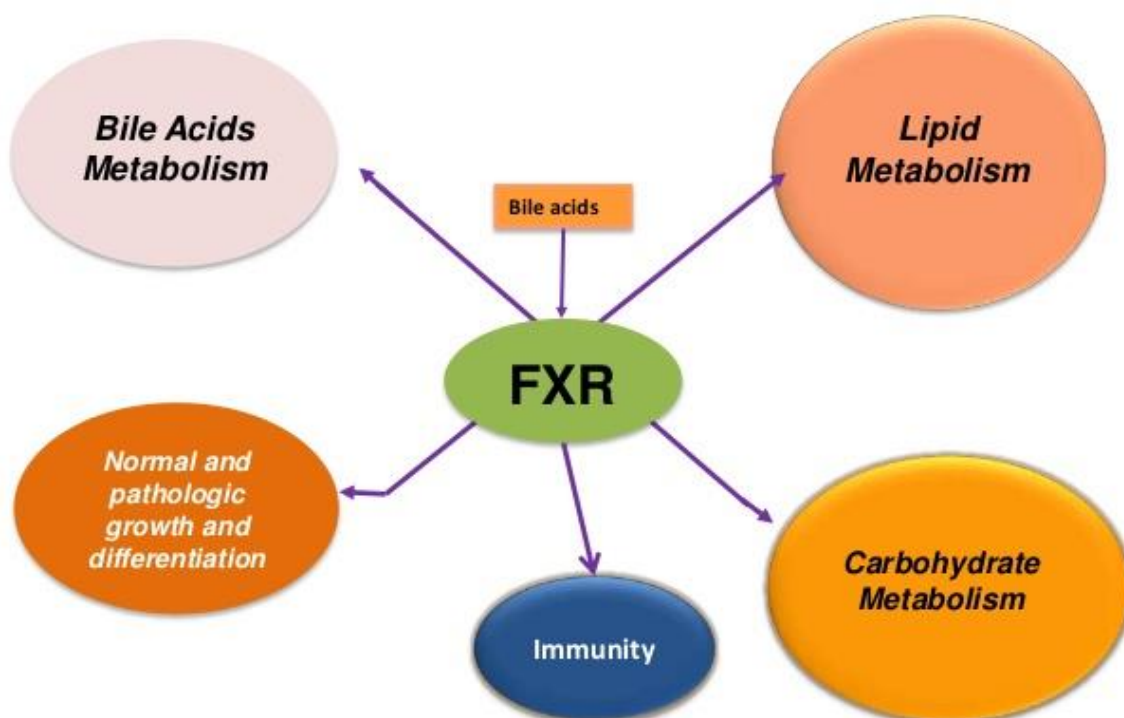


Figure 3: FXR mediated bile acid circulation and transporters, from²¹¹. Copyright © 2009 by the American Society for Biochemistry and Molecular Biology, Inc.

FXR not only plays a role in bile acid metabolism and homeostasis. FXR activation can not only reverse insulin resistance in obese individuals²¹³, but was shown to inhibit fibrosis²¹⁴, intestinal tumorigenesis²¹⁵ and hepatic tumor cell proliferation, dedifferentiation and migration²¹⁶, as well as inflammatory signaling via NF- κ B by reducing IL1 β , interleukin 2 and 6 (IL2 and IL6), TNF- α and interferon γ (IFN- γ) expression²¹⁷(Fig.4). A recent publication by Ting et al. (2019) showed that FXR expression in colorectal cancer (CRC) mice fed HFD was downregulated, and treatment with an FXR agonist could ameliorate the phenotype by changing the bile acid pool, inhibiting cancer stem cell proliferation and protecting from cellular damage²¹⁸. The manifold functions of FXR intervening in metabolic and tumorigenic signaling make FXR an attractive therapeutic target for treatment of bile acid mediated metabolic and gastrointestinal diseases²¹⁹. As first drug targeting FXR, obeticholic acid (OCA), a semisynthetic, highly specific FXR agonist was approved for treatment of primary biliary cholangitis in combination with the secondary bile acid UDCA, an endogenous FXR agonist²²⁰.

FXR is central to bile acids signaling



Fiorucci S., et al. Prog Lipid Res. 2010 Apr;49(2):171-85

Figure 4: Downstream pathways of FXR

1.6.4. The Role of Bile Acids in Diseases of the Gastro-Intestinal Tract

The impact of bile acids on gastrointestinal diseases is complex and tightly interwoven with the microbiome, as (especially secondary) bile acid levels and growth of (especially bile acid sensitive or metabolizing) bacteria in the gut are mutually dependent on each other^{206,221}. While bile acids regulate metabolism and bile acid homeostasis mainly via bile acid receptor signaling in liver and gastrointestinal tract^{202,208,209}, the dietary shaped gut microbiota influence metabolic pathways such as insulin and glucose homeostasis via induction of metabolic signaling pathways²²². Alterations in the bile acid–gut microbiome axis can favor onset of inflammation and insulin resistance and are not only correlating with metabolic diseases such as obesity and type 2 diabetes but also with gastrointestinal disorders such as inflammatory bowel disease (IBD), non-alcoholic fatty liver disease (NAFLD) and liver and intestinal cancer^{221,223-226}. Physiological bile acid levels have no negative impact on gastrointestinal health, while lowered bile acid levels can lead to bacterial overgrowth²²⁷, and vice-versa increased bile acid levels can exert damaging functions in the GI tract^{228,229}. Upon intra- or extracellular accumulation, bile acids can exert cytotoxic effects due to their chemical structure. The more hydrophobic the structure of bile acids, the more cytotoxic they are, ranging CDCA and DCA amongst the most and UDCA amongst the least cytotoxic bile acids²³⁰. In both intestinal and hepatic diseases, FXR was shown to have an impact on disease progression, and treatment with FXR agonists could protect from cellular damage and disease progression, therefore making FXR an interesting drug target for gastrointestinal diseases triggered by bile acid accumulation^{218,231-233}.

1.6.4.1. Intestinal Diseases

In the intestine, increased levels of bile acids as occurring due to bile acid malabsorption or intake of a western diet can have damaging effects on epithelial barrier function and intestinal tissue and cause dysbiosis in the gut^{228,229}. Importantly, different bile acids exert different functions depending on their structure and cytotoxicity. While CA, CDCA, DCA and its glycine and taurine conjugates were shown to increase intestinal permeability, UDCA did not^{234,235}. Disruption of the epithelial barrier function favors bile acid and bacterial translocation from the intestinal lumen into tissue and blood circulation, with bacterial compounds triggering metabolic endotoxemia^{174,200}. While DCA was shown to further promote inflammatory processes via NF- κ B and Reactive Oxygen Species (ROS) activation²³⁶, LCA and UDCA protect against intestinal inflammation²³⁷. Especially UDCA reduces dextran sodium sulfate (DSS) induces colitis and restores anti-inflammatory bacterial species in the gut, which are typically decimated in inflammatory bowel disease (IBD)²³⁷⁻²³⁹. The impact of bile acids on carcinogenesis was most extensively researched in colon cancer. In colon carcinoma, FXR

was proven to be downregulated and especially secondary bile acids cause tumorigenesis^{240,241}. In general, accumulating toxic bile acids, especially CA, DCA and Taurodeoxycholic acid (TDCA) promote carcinogenesis in the intestine, while Taurocholic acid (TCA) was shown to promote neoplasia in the stomach²⁴². DCA evidently also causes dysbiosis in the gut which further promotes intestinal carcinogenesis²²⁹.

1.6.4.2. Hepatic Diseases

As previously stated, the bile acid-microbiome axis has been associated with non-alcoholic fatty liver disease onset and progression (NAFLD) and liver cancer^{221,225,226}. Development of NAFLD is characterized by massive lipid accumulation in the liver, can be seen as hepatic manifestation of metabolic disorders such as obesity and describes a spectrum of diseases from liver steatosis progressing to non-alcoholic steatohepatitis (NASH) and liver cirrhosis²⁴⁸. In both NAFLD and NASH patients, systemic bile acid levels are increased. In cholestatic liver diseases such as primary biliary cholangitis (PBC) and primary sclerosing cholangitis (PSC), local bile acid levels in the liver are increased due to impaired bile acid secretion of the liver and can lead to development of liver cirrhosis²³¹. Although all of these diseases are caused by multiple factors, accumulating bile acids in the liver tissue are thought to cause or promote inflammation and liver injury, driving disease development and progression^{248,243}. In NAFLD and NASH as well as PBC and PSC, FXR agonists such as UDCA or OCA ameliorated the disease phenotype via reducing bile acid levels and conveying anti-inflammatory and anti-cytotoxic properties²³¹⁻²³³. To date, as first FXR targeting therapy, treatment of PBC with a combination of UDCA and OCA is approved by the American Food and Drug Association²²⁰.

1.6.4.3. Esophageal and Gastric Diseases

It was shown that GERD, the main risk factor of BE has more severe tissue damaging effects if the refluxed juices contain gastric juice with gastro-duodenal content including bile acids, compared to gastric juice alone³⁶⁻³⁸. In BE cells, exposure to acid and bile acids promotes progression to EAC²⁴⁴. Treatment with excess bile acids in a mouse model increased histological scores, tissue damage and progenitor cell expansion in BE, showing bile acids to accelerate and aggravate BE development and progression⁸². Although it is widely accepted that the damaging effect of bile acids on BE is conveyed via chronic reflux, Souza et al. (2009) showed that, in a surgical esophagoduodenostomy rat model, cellular alterations preceded reflux mediated tissue damage. These findings support a concept of a more holistic approach explaining disease development in BE, with bile acid exposure rather triggering inflammatory signaling and cytokine secretion than causing direct tissue erosion via the reflux⁴⁴. Of note, especially DCA was shown to trigger inflammation and apoptosis resistance in BE and EAC via activation of ROS/NF- κ B signaling^{236,245}.

1.7. Aims of This Thesis

1.7.1. **Aim 1:** Characterization of the of the L2-IL1B mouse model with a whole-body knockout of the BA receptor FXR

The aim of the first part of this work was to thoroughly characterize the phenotype of L2-IL1B mice with a full body knockout of the nuclear bile acid receptor FXR. The main focus was to evaluate phenotype severity and cellular characteristics occurring with the phenotype. Also, metabolomic analysis of the serum bile acid profile and microarray analysis of the tumors at the squamous columnar junction was performed. The findings were aimed to be brought into context with the molecular mechanisms FXR is involved in.

1.7.2. **Aim 2:** Investigation of the Impact of a High-Fat-Diet (HFD) on the Bile Acid (BA) modulating Microbiome and BA levels of the L2-IL1B Mouse Model

Previously the effect of a life-long treatment of L2-IL1B mice with HFD and its impact on the inflammatory and gastrointestinal microbial environment was evaluated in our lab. The second aim of this work was to analyze the impact of HFD treatment on the fecal bile acid modulating microbiome as well as on the fecal, seral and tissue associated metabolome; especially on BA in the L2-IL1B mouse model.

1.7.3. **Aim 3:** Investigation of the Effect of OCA Treatment on BA treated Organoids *In Vitro* and on L2-IL1B Mice Fed CD and HFD *In Vivo*

The third focus of this work was to evaluate the effect of bile acids and the FXR agonist OCA on the phenotype of 3D organoids from the BE region of our L2-IL1B mouse model *in vitro*. After assessment of the effects *in vitro*, we aimed to characterize the effect of OCA treatment on L2-IL1B mice fed CD or HFD, including the fecal microbiome and the fecal, seral and tissue associated bile acid pool and metabolome.

1.7.4. **Aim 4:** Assessment of the Microbiome and Bile Acid Profile in Patients with BE, Dysplastic BE and EAC

To draw conclusions about the applicability of our findings in human patients, we analyzed the fecal microbiome and fecal and seral metabolome of patients in different disease states to evaluate the association of the specific bile acid profile with disease progression.

2. Materials and Methods

2.1. Human BarrettNET Study Cohort

Samples and data from a prospective study of 49 patients with non-dysplastic BE (BE), low grade dysplasia (LGD), high grade dysplasia (HGD), or EAC, as well as non-BE controls; a subset of patients from the BarrettNET study at Klinikum Rechts der Isar were analyzed for changes in bile acid metabolizing bacteria or serum bile acids with disease progression²⁴⁶.

Inclusion criteria in the study included an age between 18-80 years, surveillance endoscopy in patients with already diagnosed BE without previously known occurrence of low-grade or high-grade dysplasia or EAC and no presence of contraindications.

Per patient and visit 4-6 endoscopic biopsies (1 from esophageal squamous epithelium, 1 from cardia, 1 up to 4 biopsies from BE for embedding), blood, saliva and fecal samples were collected from each of the patients in the cohort. Biopsies, blood, and saliva specimen were collected in line with the endoscopy.

All biopsies (Preanalytics, PAXgene Tissue Container, Cat 765112), blood (PAXgene blood DNA tubes 2,5 ml Cat 761165; Sarstedt S-Monovette® 5 ml 9NC, Cat. 05.1071) and Saliva (Sarstedt, Stratec Saliva Gene collector, Cat. 1035211200) were collected at the Klinikum Rechts der Isar, TUM, in Munich, Germany.

Fecal samples were collected by the patients (Sarstedt, Stool Collection Tubes with Stool DNA Stabilizer, Cat. 1038111300). Biopsies were sent to the clinical pathology department and upon arrival there processed according to manufacturer's protocol. Paraffin embedded samples were stored at -20 °C in the pathology department to ensure the preservation of DNA and RNA integrity as recommended by the manufacturer. Stabilized blood samples were stored at -80°C or room temperature while saliva and fecal samples, both with DNA stabilizer, were stored at -80 °C at appropriate storage conditions.

For this thesis, tissue and stool samples were analyzed via 16S-sequencing for microbial changes and stool and blood serum samples were analyzed via metabolomic analysis.

2.2. Sample Collection and Overview – Murine Studies

2.2.1. Transgenic Mouse Strains

All animal experimental work performed in Germany was carried out under the approval of the district government of Upper Bavaria (Regierung Oberbayern), according to the animal experimental permits (Tierversuchsanträge) 55.2.1.54-2532-125-12 and 55.2-1-54-2532-24-2016. All animal experiments were conducted in accordance with German Federal Animal Welfare and Ethical Guidelines of the Klinikum Rechts der Isar, TUM, Munich and the Columbia University, New York, NY, USA

2.2.1.1. L2-IL1B Strain

All animal experimental work in this study was based on the first genetic mouse model (L2-IL1B) of BE and EAC generated and previously described by Quante et al.²⁴⁷. L2-IL1B mice express human IL-1B under the control of the Epstein-Barr virus (EBV-L2) promoter, specifically targeting the oral cavity, the esophagus and forestomach lined by squamous epithelium. Resulting continuous inflammation in the esophagus and forestomach leads to metaplastic transformation of the epithelium at the SCJ resembling BE in humans.

2.2.1.2. L2-IL1B FXR^{-/-} Strain

L2-IL1B Mice were backcrossed to C57BL/6J mice and crossed with FXR^{-/-} mice, which have a loxP-Cre based full-body knockout of FXR²⁴⁸. to obtain L2-IL1B-FXR^{-/-} mice. All mice were fed a standard chow diet and water *ad libitum*. Mouse breeding, maintenance and sample collection were performed by the former PhD student Andreas Nuber.

2.2.2. Holding and Husbandry

For microbiome and metabolome characterization of L2-IL1B Mice on Control- or High-Fat-Diet (CD, HFD) L2-IL1B Mice were backcrossed to C57BL/6J mice and bred and maintained under specific pathogen free (SPF) conditions in the animal facility of the ZIEL institute for food and health at the Wissenschaftszentrum Weihenstephan (WZW), TUM.

L2-IL1B-FXR^{-/-} mice were bred and kept under specific pathogen free (SPF) conditions in the animal facility of Klinikum Rechts der Isar, TUM.

For the OCA treatment studies in Germany, L2-IL1B Mice were backcrossed to C57BL/6J mice and bred in a mouse facility from Charles River in Italy under specific pathogen free (SPF) conditions. Following weaning and genotyping, mice were sent back to Germany at an age of

6-8 weeks. In Germany, all mice were kept under specific pathogen free (SPF) conditions in the animal facility of Klinikum Rechts der Isar, TUM.

For the OCA treatment studies in New York, L2-IL1B Mice were backcrossed to C57BL/6J mice and bred and maintained under specific pathogen free (SPF) conditions in an animal facility of the Irving cancer research center, Columbia University, NY.

Mice were kept in specific-pathogen-free (SPF) facilities in individually ventilated cages fulfilling the FELASA criteria in groups up to six animals. The mice were maintained in 12 hours day to night cycle and fed a standard chow diet and water *ad libitum* unless stated otherwise.

2.2.3. Weaning, DNA extraction and Genotyping

Mice were weaned at an age of approximately three weeks after birth and numbered consecutively. Mouse numbers were tagged via ear punch biopsies. Tissue from the ear punch biopsies was subsequently used for genotyping.

The tissue was lysed in 200 μ l DirectPCR® Lysis Reagent Tail (31-102-T, Peqlab) supplemented with 2 μ l Proteinase K (03115828001, Roche Diagnostics) over night for up to sixteen hours at 55°C and 400-500 rpm in a heating block. Enzymatic tissue lysis was stopped by heating the samples for 60 min at 85°C. After heating, lysates were quickly centrifuged and stored at 4°C.

Fresh tissue lysates were used for Polymerase Chain Reaction (PCR) applications to determine the genotype of the mice. For PCR, 1 μ l tissue lysate each was transferred to a new PCR reaction tube, mixed with 5 μ l ReadyMix™ REDTaq® PCR Reaction Mix (R2523, Sigma) or GoTaq® Green Master Mix (M7422, Promega), 1 mM of the respective primers for genotyping and filled up with PCR grade dH₂O to a final reaction volume of 10 μ l. PCR was then performed in a Thermal Cycler (T100, Biorad).

Genotyping primers (Eurofins Genomics) were ordered as High Purity Salt Free (HPSF) purified lyophilizates. Primers were quickly centrifuged, dissolved with PCR grade water to 100 mM stock solutions and stored long-term at -20°C. For use in PCR reactions, primers were diluted 1:10 to working solutions of 10 mM and stored short-term at 4°C. Genotyping primer sequences are presented in Table 1.

Thermocycler settings were programmed as follows for a multistep PCR reaction: Initial denaturation (95°C, 3min) followed by 35-40 cycles of denaturation (95°C, 30 sec), annealing (primer specific usually 55°C for IL8, 57°C for L2-IL1B and FXR, 30 sec) and elongation (30 sec at 72°C) and cooling until storage at 4°C.

PCR product size was visualized via agarose gel electrophoresis on a 1.5-2 % agarose gel in TAE solution (840004, Biozym) blended with ethidium bromide (2218.1, Roth). Therefore 7.5-10g Agarose were dissolved in a glass beaker with 500 ml TAE buffer by boiling in a microwave. After cooling the solution to 60-70°C, 12.5 µl ethidium bromide solution was blended into the solution and the gel was poured in gel chambers with combs to form gel pockets (Bio-Rad). After complete cool down the combs were carefully removed and the gel was transferred into electrophoresis gel chambers (Bio-Rad) filled with TAE buffer. Gel pockets were loaded with 10 µl of PCR reaction solution each. For band size estimation a 100 bp ladder (N0467L, BioLabs) was run on the gel with the samples. Gels were run at constant voltages of 120-150V for approximately 60 minutes until fragment sizes were distinguishable. PCR Fragment Bands were visualized and photographed under UV light on a Gel Doc™ XR system (Bio-Rad) using Quantity One software (Bio-Rad) for analysis. PCR fragment band sizes and resulting genotypes were evaluated manually. Results were updated in the group intern mouse list as well as the Python-based animal facility software PyRAT.

Table 1: Genotyping Primer Sequences

Target		Sequence	Annealing Temp.	Elongation Time	Amplicon Size
L2-IL1B	forward	5'- CTT CCT GTT CCA TTC AGA GAC GAT - 3'	57°C	30sec	277bp
	reverse	5'-CTC CAG CTG TAG AGT GGG CTT ATC - 3'			
IL8	forward	5'-TGA GGT CAA GGG CTA GGA GA-3'	55°C	30sec	300 bp
	reverse	5'-AAA TTT GGG GTG GAA AGG TT-3			
FXR	forward	5'-TCT CTT TAA GTG ATG ACG GGA ATC T-3'	57°C	30sec	WT 250 bp Mut 291 bp
	mutant forward	5'-GCT CTA AGG AGA GTC ACT TGT GCA-3'			
	reverse	5'-GCA TGC TCT GTT CAT AAA CGC CAT-3'			

2.2.4. Dietary Treatment

For dietary treatment studies in Germany, starting at 8-9 weeks of age, mice were randomly distributed in treatment groups and fed standard lab chow diet, high fat diet (HFD, Ssniff, S5745-E712), a matching control diet (CD, Ssniff, S5745-E702) or high fat diet / control diet + obeticholic acid (HFD+OCA, S0615-E710; CD+OCA, Ssniff, S0615-E705). All diets were pretreated with γ radiation by the manufacturer before fumigation / disinfection and introduction into the animal facility.

For dietary treatment studies in New York, starting at 8-9 weeks of age, mice were randomly distributed in treatment groups and fed high fat diet (HFD), a matching control diet (CD), or high fat diet + obeticholic acid (dietary composition analogous to german diets). All diets were pretreated with γ radiation by the manufacturer before fumigation / disinfection and introduction into the animal facility.

2.2.5. Diet composition

Exact diet composition of lab chow diet and the experimental diets used for treatment of mice in Germany for microbiome and metabolome evaluation is presented in Table 2

Table 2: Composition of Experimental Diets

Diets Purchased at Ssniff	V1124-000	S5745-E712 +obeticholic acid S0615-E710	S5745-E702 +obeticholic acid S0615-E705
Dietary components	Standard Chow	High fat diet Palm oil +/- obeticholic acid (60mg/kg)	Control Palm oil +/- obeticholic acid (60mg/kg)
Gross Energy (GE)	16.7 MJ/kg	21.9 MJ/kg	16.9 MJ/kg
Metabolizable Energy (ME)	14.0 MJ/kg	19.7 MJ/kg	15.3 MJ/kg
Protein [kJ%]	27	18	23
Fat [kJ%]	12	48	13
Carbohydrates [kJ%]	61	34	64

Crude Nutrients [%]			
Protein	22.0	21.2	21.2
Fat	4.5	25.1	5.1
Fiber	3.9	5.0	5.0
Ash	6.2	5.3	5.3
Starch	34.2	26.7	45.9
Sugar	5.1	6.1	6.1
N free extracts	51.2	37.7	56.8
Amino Acids [%]			
Lysine	1.5	1.8	1.8
Methionine	0.5	0.8	0.8
Met + Cys	0.4	1.1	1.1
	V1124-000	S5745-E712	S5745-E702
Dietary components	Standard Chow	High fat diet Palm oil	Control
Amino Acids [%]			
Threonine	0.9	0.9	0.9
Tryptophan	0.3	0.3	0.3
Minerals [%]			
Calcium	1.0	0.9	0.9
Phosphorus	0.7	0.7	0.7
Sodium	0.2	0.2	0.2
Magnesium	0.2	0.2	0.2
Vitamins [IU/kg]			
Vitamin A	25,000.00	18,000.00	18,000.00
Vitamin D ₃	1,500.00	1,800.00	1,800.00
Vitamin E	135	180	180
Fatty acids [%]			

C 12:0	-	0.01	0.01
C 14:0	0.01	0.21	0.02
C 16:0	0.54	9.18	0.58
C 18:0	0.14	1.11	0.18
C 20:0	0.02	0.1	0.02
C 16:1	0.02	0.05	0.01
C 18:1	1.03	9.19	1.29
C 18:2	2.42	4.67	2.65
C 18:3	0.28	0.35	0.29

2.3. Euthanasia, Preparation and Sample collection from mice

Mice were euthanized by an isoflurane (798-932, cp-pharma) overdose and cervical dislocation at specific timepoints between 6-15 months. Blood was drawn by cardiac puncture, partially subjected for downstream applications, and partially used for preparation and storage of serum (Microvette, 20.1344, Sarstedt). Mice were adequately dissected; organs were removed, washed with PBS, and subjected to downstream applications. The collected organs included liver, pancreas, spleen, lung, heart, stomach and esophagus, small and large intestine, and kidneys as well as two tail pieces for re-genotyping. Feces and cecal content were collected and snap frozen. Downstream applications included preparation of single cells for flow cytometry, collection of tissue pieces for snap freezing in liquid nitrogen and storage in RNAlater™ (AM-7020; Invitrogen) as well as collection of small tissue in 4 % Paraformaldehyde (PFA; MRI Apotheke) for dehydration and histological evaluation. An overview over the tissue collected and stored for further processing is presented in Table 3. Dissection information, weight of spleen and liver as well as apparent macroscopic abnormalities of the organs were noted on a mouse necropsy record sheet, which was stored together with mouse room scoring sheets of the respective mice. The stomach with the esophagus attached was opened along the long curvature, cleaned with PBS, transferred to, and spread on an absorbent piece of paper with a ruler for size evaluation. The esophagus was also opened and flattened on the paper. Camera pictures of the stomach and eventual other abnormalities were taken for macroscopic evaluation.

Table 3: Overview over tissue collection procedure for each experimental mouse

Tissue	2 Samples DNA/RNA and Protein	Histology (1/2)	Flow Cytometry (1/2)	Comments
Esophagus	x	x	x	
Forestomach	x	x	x	
SCJ	x	x	x	
Rest of Stomach	x	x	x	
Liver	x	x	x	
Spleen	x	x	x	
Duodenum	x	x		Swiss roll
Jejunum	x	x		Swiss roll
Ileum	x	x		Swiss roll
Colon	x	x	x	Swiss roll, for flow cytometry cut in half along the colon
Lung	x	x		
Heart	x	x		
Kidney	x	x		
Feces / Cecum				Freeze Pellets & Cecum Content at -80°C
Blood	x	x	x	Collect in Sarstedt microvettes – spin 5 min at full speed for serum Use fresh for FC

2.4. Macroscopic scoring

Photos taken from stomach and esophagus during dissection were evaluated for tumor size and tumor coverage in percent using the freely available software ImageJ²⁴⁹. Macroscopic scores were determined as mean of tumor size and tumor coverage score based on the criteria presented in Table 4.

Table 4: Macroscopic scoring system for stomach and esophagus of L2-IL1B mice

Tumor size		Tumor coverage	
0	No abnormalities	0	No abnormalities
1	<0.5mm	1	Focal tumors (<20%)
2	<1.0mm	2	Partial tumors (20-50%)
3	<2.0mm	3	Increased tumors (>50-80%)
4	<3.0mm	4	Continuous tumors (>80%)

2.5. Flow-Cytometry for Analysis of Immune Cell Levels

For flow-cytometry, blood collected by cardiac puncture and a piece of spleen, which was passed through a 40 μm cell strainer were lysed in Red Blood Cell Lysing Buffer (07664163, BD). After 10 min., cells were centrifuged for 10 min. at 4 °C and 400g. The supernatant was discarded. Lysis, centrifugation, and disposal of supernatant were repeated once. Half of the stomach was dissected in esophagus, forestomach + cardia and rest of stomach. Also, half of the colon and liver pieces were collected, and all tissues were placed in Petri dishes (628161, Greiner) with 1 ml 0.5M EDTA (Ethylenediaminetetraacetic acid; AM9260G, Invitrogen) on ice until further processing. After dissection, all tissues were cut into small pieces and transferred to 50 ml tubes (227261, Greiner) with 5 ml of the freshly prepared appropriate digestion buffer for each tissue. Composition of the digestion buffers is presented in Table 5 and 6. Tissues were digested for 30 min. at 37 °C and 150-250 rpm in a shaking incubator (TH15, Edmund Bühler GmbH). After incubation, tissues were passed through 40 μm cell strainers (352340, Falcon) with the sterile end of syringe plungers (4606108V, B Braun). Cells were centrifuged for 10 min. at 4 °C and 400g. Supernatants were discarded, all samples were resuspended in 200-300 μl FACS (Fluorescence Activated Cell Sorting) washing buffer each and transferred to a round-bottom 96 well plate (Thermo Scientific™ 163320) in 2 wells per sample. Composition of the flow cytometry buffer is presented in Table 7. All following steps were performed on ice. The samples in the 96 well plate were centrifuged for 10 min. at 4 °C and 400g and the supernatant was discarded. Samples were again washed by resuspension in 150 μl flow cytometry buffer with following centrifugation for 10 min. at 4 °C and 400g and disposal of supernatant. One well per sample was stained with 50 μl of the appropriate staining solutions for analysis of T- and myeloid cells for 30 min. in the dark. Compositions of the staining solutions are presented in Table 8. After staining, cells were again washed twice with flow cytometry buffer as described before. Cell pellets were then resuspended in 200 μl flow cytometry buffer each and transferred to 1.4 ml flow cytometry tubes (MP32022, MICRONIC). Before measuring fluorescent intensities of the samples at the flow cytometer (Gallios, Beckman Coulter), 5 μl of 7-AAD life-dead cell staining solution (00-6993-50, eBioscience) was added to each sample. After data acquisition data was transferred to the FlowJo software (BD). Immune cell populations were identified after applying compensation and after gating according to established methods in our laboratory.

Table 5: Composition of Digestion Buffers for tissues subjected to flow cytometry

(Solutions freshly prepared before starting tissue preparation for flow cytometry)

Targeted tissue	Buffer	Additives
Esophagus	Krebs-Ringer-Solution	BSA 40 mg/ml (9418, Sigma) + Collagenase P (11213873001, Roche) 2 mg/ml
Cardia and forestomach + Rest of stomach	RPMI (11875-093, Invitrogen)	Collagenase P 2 mg/ml (11213873001, Roche) + Pronase 2 mg/ml (10165921001, Roche)
Liver + Colon	RPMI (11875-093, Invitrogen)	Collagenase P 2 mg/ml (11213873001, Roche)

Table 6: Composition of Krebs-Ringer Buffer for preparation of Digestion Buffers

(Stock of 1000 ml prepared and stored at 4°C)

Compound	Concentration	g/L	Article number	Manufacturer
NaCl	118 mM	6.9	S3014-1KG	Sigma
NaHCO ₃	24.8 mM	2.08	1.06329.0500	Merck
KH ₂ PO ₄	1.2 mM	0.16	3904.1	Roth
KCl	4.8 mM	0.358	1.04936.1000	Merck
CaCl ₂	1.25 mM	0.139	CN93.1	Roth
MgSO ₄	1.2 mM	0.14	208094-500G	Sigma
HEPES	10 mM	2.383	9105.3	Roth

Table 7: Composition of FACS Washing Buffer

(Stock of 500 ml prepared and stored at 4°C)

Purpose	Buffer	Additives
Washing Buffer ("FACS Buffer")	DPBS (14190-094, Life Technologies)	BSA 2% (9418, Sigma) + 2mM EDTA

Table 8: Composition of staining solutions for tissues subjected to flow cytometry

(0.5 µl of each Antibody (all anti-mouse; eBioscience) per sample filled to a total volume of 50 µl staining solution with FACS Buffer)

Myeloid cell staining solution		T-cell staining solution	
Antibody, Reference number		Antibody, Reference number	
CD11c FITC	11-0114-85	NK1.1 APC-eFluor 780	47-5941-82
F4/80 APC	17-4801-82	CD3e FTIC	11-0033-82
CD11b APC-eFluor 780	47-0112-82	CD8a APC	17-0081-82
CD45 eFluor 450	48-0451-82	CD4 eFluor 450	48-0041-82
Ly-6C PE	12-5932-82	γδ TCR PE	12-5711-82
Ly-6G Alexa Flour 700	56-5931-82		

2.6. Histological analysis

2.6.1. Preparation of Formalin-Fixed Paraffin-Embedded (FFPE) Tissue Samples and Sections

Mice were sacrificed and dissected as described in Section 5. After collection of small tissue pieces for snap freezing and storage in RNAlater™ (AM-7020; Invitrogen), organs were placed in histology cassettes (7-0014, neoLab) and transferred to freshly prepared 4% Paraformaldehyde (PFA) solution (MRI, Apotheke) for overnight fixation. Intestines, separated into duodenum, jejunum, ileum, and colon were cleaned by flushing with PBS using a syringe with a gavaging needle and then fixed overnight in 4% PFA. After fixation, intestines were opened longitudinally with scissors and rolled as swiss rolls before transferring them into histology cassettes.

After overnight fixation, PFA was discarded and histology cassettes containing tissues were washed in 70% ethanol before overnight dehydration in ethanol (increasing concentrations), xylene and paraffin in a S300 tissue processing unit (Leica). On the following day, the tissues were embedded into paraffin, cooled, and stored at room temperature. Figure 5 schematically shows the dissection of the stomach for embedding in paraffin.

For preparation of paraffin sections, Formalin-Fixed Paraffin-Embedded (FFPE) tissue blocks were precooled at -20 °C for at least 60 min. Blocks were then removed from the freezer and cut into 2-3 µm sections with a MICROM HM 355S microtome (ThermoFisher), transferred to a 45°C warm water bath and mounted on SUPERFROST® (ULTRA) PLUS microscope slides (ThermoFisher). Sections were air dried over night at room temperature and stored in light protecting slide boxes until further usage. Before staining, immunohistochemistry or in-situ hybridization, slides were heated to 60 °C for 60 min. to increase tissue attachment of the sections to the glass slides.

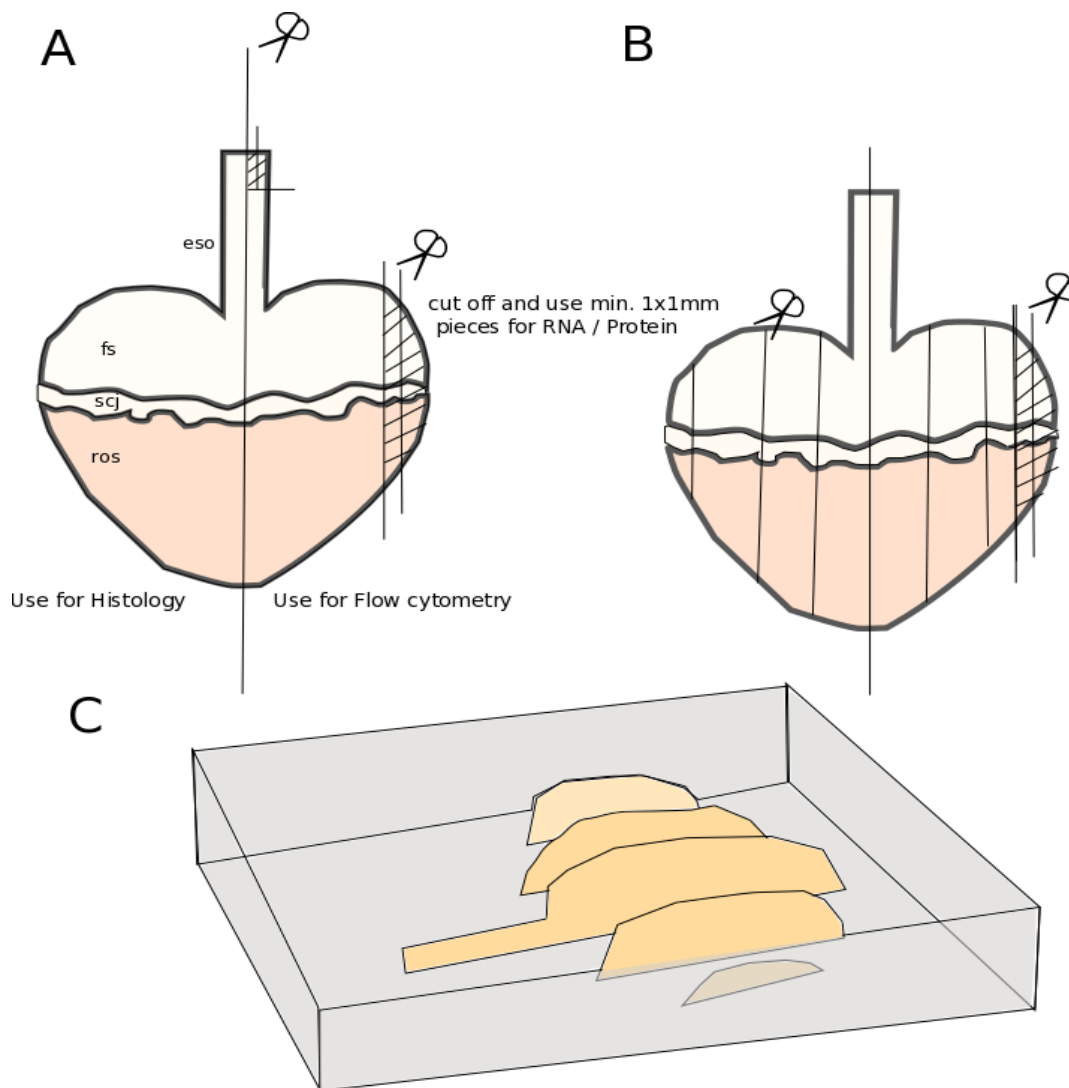


Figure 5: schematic representation of the dissection of the opened and flattened murine stomach for embedding in paraffin (eso = esophagus; fs = forestomach scj = squamous-columnar junction; ros = rest of stomach)

2.6.2. Hematoxylin and Eosin (HE) Staining

HE staining was performed for basic microscopic evaluation of the tissue structure and for microscopic histologic scoring. Staining was performed in glass containers for staining as described in Table 9. After staining, slides were mounted in Pertex embedding medium (41-4012-00, Medite) and covered with coverslips (MENZEL-Gläser, e.g., BB024032A1, ThermoFisher).

Table 9: Protocol for Hematoxylin and Eosin (HE) Staining

	Reagent	Time	Manufacturer	Article number	Purpose
1	Roti-Histol	>10 min	Roth	6640.4	Deparaffinization
2	Roti-Histol	>10 min	Roth	6640.4	Deparaffinization
3	100% Ethanol	2x 5 min	MRI Apotheke		Rehydration
4	96% Ethanol	2x 2 min	MRI Apotheke		Rehydration
5	70 % Ethanol	2x 2 min	MRI Apotheke		Rehydration
6	dH ₂ O (running)	5 min	-		Rehydration
7	Mayer Hämalaun	3 min	Merck	1.09249.2500	Staining basophilic structures
8	Tap water (running)	10 min	-		Washing
9	0.33 % Eosin	3.5 min	MRI Apotheke		Staining acidophilic structures
10	96 % Ethanol	25 sec	MRI Apotheke		Dehydration
11	2-Propanol	25 sec	MRI Apotheke		Dehydration
12	Roti-Histol	>5 min	Roth	6640.4	Dehydration
13	Roti.Histol	>5 min	Roth	6640.4	Dehydration

2.6.3. Histologic Scoring

HE stained sections were scored for inflammation, metaplasia, dysplasia, and goblet cell (GC) ratio by an experienced gastroenterologist. Histologic scores were determined based on the criteria presented in Table 10.

Table 10: Histologic scoring system for stomach and esophagus of L2-IL1B mice

Score	Inflammation	Metaplasia	Dysplasia
0	no inflammation	no metaplasia	no dysplasia
1	mild inflammation	rare mucus cells	superficial epithelial atypia
2	moderate inflammation	single metaplastic glands	atypia in glandular complexity
3	severe inflammation	multiple metaplastic glands	low grade dysplasia
4			high grade dysplasia

2.6.4. Periodic-Acid-Schiff (PAS) reaction with and without Alcian Blue Staining

PAS (Alcian blue) staining detects glycoproteins, polysaccharides, and mucins and thus mucus producing cells in the tissue. Alcian blue as optional step especially stains for acidic mucins in the tissue. Staining was performed in glass containers for staining as described in Table 11.

Table 11: Protocol for Periodic Acid Schiff Staining with Alcian Blue

	Reagent	Time	Manufacturer	Article number	Purpose
1	Roti-Histol (Xylene replacement)	>10 min	Roth	6640.4	Deparaffinization
2	Roti-Histol	>10 min	Roth	6640.4	Deparaffinization
3	100% Ethanol	2x 5 min	MRI Apotheke		Rehydration

4	96% Ethanol	2x 2 min	MRI Apotheke		Rehydration
5	70% Ethanol	2x 2 min	MRI Apotheke		Rehydration
6	dH ₂ O (running)	5 min	-		Rehydration
7	Alcian Blue	20 sec	Merck	101647	Staining acidic mucins
8	Tap water (running)	3 min	-		Washing
9	Periodic Acid	5- 10 min	Roth	HP00.1	Oxidation
10	Tap water (running)	3 min	-		Washing
11	Schiff's Reagent	15 min	Roth	X900.2	Staining mucins
12	Tap water (running)	3 min	-		Washing
13	Hematoxylin (Gill III)	1 min	Merck	1.05175.2500	Counterstaining
14	Tap water (running)	5 min	-		Washing
15	70 % Ethanol	2x 2 min	MRI Apotheke		Dehydration
16	96 % Ethanol	2x 2 min	MRI Apotheke		Dehydration
17	100 % Ethanol	2x 5 min	MRI Apotheke		Dehydration
18	Roti-Histol	>5 min	Roth	6640.4	Dehydration
19	Roti.Histol	>5 min	Roth	6640.4	Dehydration

2.6.5. Immunohistochemistry

Immunohistochemistry (IHC) on sections from FFPE tissue was performed for detection of specific antigens in the tissue. IHC was performed in glass containers and in a humidified, light protected chamber according to the protocol presented in Table 12. Steps were performed at room temperature unless stated otherwise. Washing buffer TBST (TBS; 1244.1, Roth with 0.025 % Triton X-100; T8787, Sigma-Aldrich) and 3% BSA (0163.2, Roth) in TBST were prepared before starting the IHC protocol. Antibodies and Antibody specific protocol adjustments are presented in Table 13. For incubation steps in the humidified chamber, tissue on the slides was overlaid completely with 200 µl of the respective solutions. After completing IHC, slides were mounted in Pertex embedding medium (41-4012-00, Medite) and covered with coverslips (MENZEL-Gläser, e.g., BB024032A1, ThermoFisher).

Table 12: Standard protocol for immunohistochemistry

	Reagent	Time	Manufacturer	Article number	Purpose
1	Roti-Histol (Xylene replacement)	>10 min	Roth	6640.4	Deparaffinization
2	Roti-Histol	>10 min	Roth	6640.4	Deparaffinization
3	100% Ethanol	2x 5 min	MRI Apotheke		Rehydration
4	96% Ethanol	2x 2 min	MRI Apotheke		Rehydration
5	70% Ethanol	2x 2 min	MRI Apotheke		Rehydration
6	dH ₂ O (running)	1 min	-		Rehydration
7	Citrate Buffer (Bring to boil 5 min at 900 W)	15 min 450 W	Merck	1.00244.1000	Antigen retrieval in heat stable closed cuvette

	in a microwave before)				
8	Citrate Buffer (cooling)	10 min	-		Cool down
8	Tap water (running)	10 min	-		Cool down
Transfer slides to humidified chamber and circle tissue with PAP-pen (Dako, S2002); prevent slides from drying at any time by overlaying tissue with a minimum of 200 µl of the respective solution					
9	3 % H ₂ O ₂ in PBS	15 min	Merck	1.08597.1000	Endogenous peroxidase block
10	Buffer TBST (TBS + 0.025 % Triton-X-100)	3x 5 min	-		Washing
11	3 % BSA in TBST + 5 % Serum (specific) + Streptavidin (4 drops/ml)	60 min	Streptavidin/Biotin blocking kit, Serum: Vector Labs	SP-2002, S-1000 (Goat serum)	Endogenous receptor block
12	Primary antibody in 3 % BSA in TBST + Biotin (4 drops /ml)	O/N 4°C or 1h RT	-		Binding of Antibody
13	Buffer TBST (TBS + 0.025 % Triton-X-100)	3x 5 min	-		Washing

14	Biotinylated Secondary antibody in 3 % BSA in TBST	Specific	Vector Labs	BA-1000 (Goat anti-rabbit)	Binding of Antibody
15	Buffer TBST (TBS + 0.025 % Triton-X-100)	3x 5 min	-		Washing
16	ABC – treatment (prepare 30 min before use)	30 min	ABC kit: Vector Labs	PK-6100	Avidin-Biotin-Complex to increase signal intensity
17	Buffer TBST (TBS + 0.025 % Triton-X-100)	3x 5 min	-		Washing
18	DAB (prepare freshly)	Specific	DAB peroxidase substrate kit: Vector Labs	SK-4100	Signal detection
Transfer slides back to glass rack for following steps					
19	dH ₂ O	1 min	-		Washing
20	Hematoxylin (Gill III)	30 sec	Merck	1.05175.2500	Counterstaining
21	Tap water (running)	1 min	-		Washing, pH adjustment
22	70 % Ethanol	2x 2 min	MRI Apotheke		Dehydration
16	96 % Ethanol	2x 2 min	MRI Apotheke		Dehydration

17	100 % Ethanol	2x 5 min	MRI Apotheke		Dehydration
18	Roti-Histol	>5 min	Roth	6640.4	Dehydration
19	Roti-Histol	>5 min	Roth	6640.4	Dehydration

Table 13: Specifications of antibodies used

Antigen	Purpose	Manufacturer	Article number	Secondary Antibody and Blocking Serum
γ-H2AX 1:750	DNA Damage	Cell Signaling	γ-H2AX (ser139) #9718	Goat-anti-rabbit 1:1000 Goat Serum
Ki67 1:1000	Proliferation	Abcam	AB15580	Goat-anti-rabbit 1:1000 Goat Serum
Caspase1 1:50 30 min at RT	Inflammasome activation	eBioscience	E910	Goat-anti-rabbit 1:1000 Goat Serum
αSMA 1:400	Fibroblast infiltration	Abcam	AB5694	Goat-anti-rabbit 1:1000 Goat Serum
TGR 5 1:500	TGR5 receptor expression	Abcam	AB72608	Goat-anti-rabbit 1:1000 Goat Serum

2.6.6. In-Situ-Hybridization (ISH)

ISH was used to detect antigen expression on RNA levels for Lgr5 and FXR. For the Lgr5 in Situ Hybridization the RNAscope 2.5 HD assay – Detection reagent BROWN (ACD) and all related reagents from ACD were used. The procedure was performed according to the manufacturer's protocol using the Mm-Lgr5 target probe (ACD, Cat. No. 312171), the Hs-Lgr5 target probe (ACD, Cat. No 311021) and the Mm-NR1H4 target probe (ACD, Cat. No 484491) for detection of FXR expression.

2.6.7. Quantification of Immunohistochemistry

For PAS staining and α SMA, caspase1, γ -H2AX and Ki67 IHC in BE tissue, the percentage of positive (DAB stained) cells compared to the size of the BE region was analyzed. FXR and Lgr5 ISH in BE tissue the percentage of positive cells compared to the size of the BE region in percent was analyzed. In serial section analysis, additionally the ratio of double positive versus single positive cells was analyzed. TGR5 IHC was performed to confirm stable expression amongst intervention groups and was not quantified.

2.7. RNA and Extraction and Downstream Applications

2.7.1. RNA Extraction

Tissue for RNA isolation was collected from forestomach, cardia, rest of stomach, esophagus, liver, spleen, colon, and small intestine and stored overnight in 250 µl RNAlater™ (AM-7020; Invitrogen) at 4°C before long-term storage at -80°C. All working areas were cleaned with RNase Away™ (10328011; ThermoFisher) before starting RNA extraction.

Total RNA was isolated from the tissues of interest. RNA isolation was performed using the RNeasy Mini Kit (74104; Qiagen). Tissues were thawed at room temperature and homogenized in RLT-buffer (Lysis buffer; 1015762; Qiagen) supplemented with 1 % beta-mercaptoethanol (4227.3, Roth) for approximately 30 sec. or until no remaining residuals were visible using a SilentCrusher M (Heidolph). Before homogenization and between different samples the SilentCrusher was cleaned using Tubes filled with RNase Away™ (10328011; ThermoFisher) and then 2 tubes filled with dH₂O. Subsequently RNA was extracted from the homogenate according to the manufacturer's protocol. RNA was eluted in 20 µl PCR-grade water. RNA concentration and quality were measured on a Nano-Drop 2000 spectrophotometer (Thermo Scientific). RNA was directly subjected to reverse transcription or stored at -80°C until further use in downstream applications.

2.7.2. Reverse Transcription Polymerase Chain Reaction (RT-PCR)

Reverse transcription of 250-1000ng RNA to cDNA was performed using the QuantiTect Reverse Transcription Kit (205314, Qiagen) according to manufacturer's instructions. Elimination of genomic DNA was ensured by incubation of the sample in gDNA wipeout buffer for 2 min. at 42 °C. Subsequently RNA was incubated with Quantiscript Reverse Transcriptase, Quantiscript RT buffer and RT Primer Mix and incubated at 42°C. To obtain optimal results, elongation time was prolonged to 30 min. as suggested in the manufacturer's protocol. The reaction was stopped by heat inactivation for 3 min. at 95 °C.

2.7.3. Quantitative Real Time PCR (qRT-PCR)

Target gene expression levels were evaluated by qRT-PCR on a LightCycler® 480 (Roche). PCR reactions were performed in a total volume of 10 µl per reaction using the QuantiFast SYBR Green PCR Kit (4000) (204057, Qiagen). For each reaction 10-25 ng RNA were used in a volume of 1-2 µl, reactions were performed in triplicates. Glyceraldehyde 3-phosphate dehydrogenase (GAPDH), Cyclophilin A and beta-Actin were used as standard housekeeping genes, 16S-RNA and bacterial GAPDH were used as housekeeping genes for determination of fecal bacterial gene expression. PCR conditions used for all reactions were 95°C for 3

minutes, followed by 40 cycles of 95°C for 30 seconds, 55°C for 30 seconds, and 72°C for 30 seconds. Primers and primer sequences were retrieved from the existing internal primer stock, from papers, collaborators, or designed via Primer-Blast (<https://www.ncbi.nlm.nih.gov/tools/primer-blast/>; NCBI). All primer pairs were re-evaluated for self-complementation and gene specificity. Gene specificity was ensured by blasting all primers on Primer-Blast (NCBI). Primer amplification efficiencies were tested by creating a standard curve from PCR reactions of serial dilutions of cDNA of positive control tissues. Also, the melting curve of the primers was checked for quality control. All primer sequences used in qRT-PCR are listed in Table 14.

Table 14: Primers for quantitative Real Time - PCR

Target		Sequence	Melting Temp.	Notes
FXR	forward	5'-GGCTGCAAAGGTTTCTTCCG-3'	67.9	
	reverse	5'-ACATTCAGCCAACATCCCCA-3'	67.6	
FXR	forward	5'-GCACGCTGATCAGACAGCTA-3'	64.4	
	reverse	5'-CAGGAGGGTCTGTTGGTCTG-3'	64.8	
IBABP	forward	5'-CACCATTGGCAAAGAATGTG-3'	65.7	
	reverse	5'-AACTTGTCACCCACGACCTC-3'	66.7	
SHP	forward	5'-AGCTGGGTCCCAAGGAGTAT-3'	63.7	
	reverse	5'-CTTGAGGGTAGAGGCCATGA-3'	64.1	
PPAR α	forward	5'-ACGTTTGTGGCTGGTCAAGT-3'	64.6	
	reverse	5'-TGGAGAGAGGGTGTCTGTGAT-3'	63.8	
PPAR γ	forward	5'-TGTCGGTTTCAGAAGTGCCTTG-3'	68.4	ppar-y
	reverse	5'-TTCAGCTGGTCGATATCACTGGA-3'	68.4	
PPAR γ	forward	5'-CGGTTTCAGAAGTGCCTTG-3'	67.5	ppar-y1-2
	reverse	5'-GGTTCAGCTGGTCGATATCAC-3'	65	
PPAR γ	forward	5'-ATGCACTGCCTATGAGCACT-3'	67.5	ppar-y2

	reverse	5'-CAACTGTGGTAAAGGGCTTG-3'	65	
ALPI	forward	5'- CTGTCAAAGCATCAGGGAGC - 3'	63.8	
	reverse	5'- GGAAGGGTCTACTGAGGGGT - 3'	54.2	
CTGF	forward	5'- AGCGGTGAGTCCTTCCAAAG - 3'	65.5	
	reverse	5'- TTCCAGTCGGTAGGCAGCTA - 3'	64.7	
mGAPDH	forward	5'- GACATCAAGAAGGTGGTGAAGCA G-3'	68	
	reverse	5'- ATACCAGGAAATGAGCTTGACAAA -3'	64.5	
βactin	forward	5'-CCGTGAACCCTAAGGCCAACC- 3'	72.7	
	reverse	5'-ACCCCGTCTCCGGAGTCCATC- 3'	69.5	
BSH	forward	5'-ATGGGCGGACTAGGATTACC-3'	63.8	Working conc. 100 μM
	reverse	5'-TGCCACTCTCTGTCTTC-3'	54.2	
16S-RNA	forward	5'-TGATCCTGGCTCAGGACGAA-3'	68.3	Working conc. 100 μM
	reverse	5'-TGCAAGCACCAATCAATACCA- 3'	66.2	

2.8. 16S-Sequencing for Microbiome Analysis

16S-sequencing from patients' stool, saliva and PAXgene tissue samples was performed to characterize the gut, oral and local esophageal microbial microenvironment of the human patient cohort in different disease states. 16S-sequencing from experimental mice on different diets and treatments was performed from cecal content and fecal samples to characterize the diet and treatment dependent microbial microenvironment in the mice. Therefore, DNA was extracted from the samples using different extraction methods.

2.8.1. Sample Collection

Human Study specimen from the human BarrettNET study were used for 16S-sequencing analysis. Human PAXgene tissue, saliva and stool samples which were processed and stored as previously stated were removed from storage and submitted to downstream processing. For this study, only 16S-sequencing data from human stool and PAXgene tissue were further analyzed, information on downstream processing of human saliva is thus not further explained. For 16S-sequencing analysis of cecal and fecal content of L2-IL1B mice on experimental diets snap frozen samples collected in the mouse room (fresh feces only) or after dissection were used for downstream processing.

2.8.2. Sample Preparation

2.8.2.1. Human Stool, Murine Fecal and Cecal Samples

DNA from human fecal samples was extracted using a short modified version of the previously published Godon-protocol²⁵⁰. Feces were already frozen with DNA stabilizer (Sarstedt, Stool Collection Tubes with Stool DNA Stabilizer, Cat. 1038111300). To 700 µl of the feces-DNA stabilizer mix, 250 µl 4M Guanidinium thiocyanate and 500 µl 5% N-lauroylsarcosine were added. The probes were incubated for 1h at 70 °C. Sterile silica beads (0.1 mm, Biospec products) were used for bacterial cell lysis in a FastPrep-24 bead beater (MP biomedical). Then 15 mg Polyvinylpyrrolidone was added, and the suspension was centrifuged at 15.000g at 4 °C for 3 min. The supernatant was collected and again centrifuged at 15.000g at 4 °C for 3 min. 500 µl of clear supernatant was collected. 5 µl RNase (10 mg/ml) were added to the samples followed by an incubation step for 20 min at 37 °C and shaking at 700 rpm. Subsequently, DNA was extracted with the NucleoSpin gDNA Clean-up kit following the manufacturers protocol.

2.8.2.2. Human PAXgene-Fixed Paraffin-Embedded (PFPE) Samples (Tissue)

DNA from human PAXgene biopsy samples was extracted using the PAXgene® tissue DNA-Kit (Preanalytix), following the manufacturers protocol for purification of Genomic DNA from sections of PAXgene treated, paraffin-embedded tissue.

For all extracted DNA samples, a Sodium acetate precipitation was performed for purification and concentration of the samples. DNA samples were mixed 1:10 with a sodium acetate solution (3M). Then 4 volumes of 100 % ethanol were added, mixed thoroughly, and incubated over night at -20 °C. All samples were centrifuged at top speed for 30 min at 4 °C and the supernatant was discarded. The pelleted DNA was washed with 500 µl ice-cold 80 % ethanol. The samples were centrifuged at top speed for 10 min at 4 °C and the supernatant was discarded. If needed, the washing step was repeated once. The DNA pellet was air-dried and resuspended in 10 µL nuclease free dH₂O.

After precipitation, concentration and purity of all samples was measured on a Nanodrop™ 1000 Spectrophotometer (Thermo Scientific). In a test-sequencing experiment, it could be shown that DNA probes from all three origins with values similar to the average purity values shown in Table 15 obtained DNA integrity and could be sequenced without problems.

Table 15: Comparison of DNA quality after DNA extraction in PAXgene fixed tissue and Stool samples of participants with BE, Dysplasia and EAC. Mean ± SD of DNA ratios at 260, 280 and 230 nm, representing purity of extracted DNA (determined by NanoDrop).

Tissue	BE			Dysplasia			EAC		
	<i>n</i>	260 /280	260 /230	<i>n</i>	260 /280	260 /230	<i>n</i>	260 /280	260 /230
Tissue	17	1.92 ± 0.06	1.64 ± 0.32	5	1.91 ± 0.06	1.44 ± 0.18	14	1.87 ± 0.09	1.45 ± 0.24
Stool	14	1.69 ± 0.26	0.92 ± 0.28	5	1.76 ± 0.15	1.00 ± 0.40	13	1.70 ± 0.26	0.98 ± 0.31

2.8.3. Quality Control of DNA Samples for 16S RNA Gene Sequencing

After DNA extraction and purification from the human specimen, quality control of the DNA samples was performed in the ZIEL – Institute for Food & Health, CF Microbiome/NGS in the WZW Weihenstephan, TUM School of Life Science, TUM. The V3/V4 region of 16S rRNA genes was amplified (25 cycles for fecal samples, 15 cycles for tissue biopsies) from 12 ng of metagenomic DNA using the bacteria-specific primers 341F and 785R following a two-step procedure to limit amplification bias²⁵¹. Amplicons were purified using the AMPure XP system (Beckmann).

Amplified DNA samples were run on agarose gels together with mock community and Zymo DNA positive controls and dH2O negative controls (Fig. 6). The applied DNA storage conditions, extraction and purification methods were all suitable for the implementation of 16S rRNA gene sequencing. In most cases DNA yields were high enough to perform 16S sequencing.

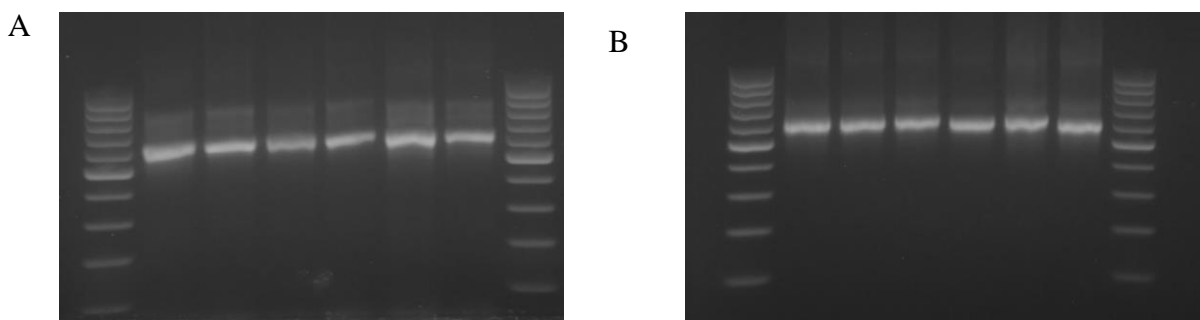


Figure 6: DNA samples run on agarose gel for DNA quality and integrity assessment (A) before purification and (B) after purification. Exemplary presentation of a subset of purified samples (17-21: Saliva DNA samples from Dysplasia and EAC patients; M6: Mock community sample for positive control; ZymoDNA positive and dH2O negative control not shown in the exemplary picture)

In a low number of samples, the DNA yield after extraction and purification was very low, but this resulted in all cases from a very low material input at the beginning of the DNA extraction. Low material inputs again resulted from the incorrect usage of the collection tubes provided for the patients.

2.8.4. High Throughput 16S- ribosomal RNA (rRNA) Gene Sequencing and Microbiome Profiling

The V3/V4 region of 16S rRNA genes was amplified (25 cycles for fecal samples, 15 cycles for tissue biopsies) from 12 ng of metagenomic DNA using the bacteria-specific primers 341F and 785R following a two-step procedure to limit amplification bias²⁵¹. Amplicons were purified using the AMPure XP system (Beckmann), pooled in an equimolar amount, and sequenced in paired-end modus (PE275) using a MiSeq system (Illumina, Inc.) following the manufacturer's instructions.

2.8.5. Analysis of 16S Sequencing Data

16S Sequencing Data was analyzed using IMNGS, a web-based pipeline for processing of 16SRNA amplicon datasets²⁵², and RHEA, an R-based pipeline for data analysis and visualization. Beginning with the IMNGS workflow, resulting sequences were remultiplexed with a Perl script provided by the creators of IMNGS called remultiplexor²⁵². The IMNGS workflow itself is based on the UPARSE pipeline²⁵³. In the IMNGS workflow, pairing, quality filtering and clustering of zero radius operational transcriptional units (zOTUs) were performed, wherefore USEARCH 8.0 was used²⁵⁴. Therefore, all reads were trimmed to the position of the first base with a quality score smaller than three and then paired. The resulting sequences were size filtered and sequences with assembled size <300 and >600 nucleotides were excluded. Paired reads with an expected error bigger than three were also excluded. Remaining sequences were trimmed by five nucleotides on each side to avoid GC bias and nonrandom base composition. After processing of the remultiplexed data by the IMNGS workflow, a zOTU-table with associated sequences and taxonomic information for further analysis was generated. Further analyses, including normalization, analysis of alpha- and beta-diversity, taxonomic abundance and correlation analyses were performed using the Rhea-pipeline created for the R-interface RStudio²⁵⁵⁻²⁵⁷.

2.9. Mass Spectrometry for targeted and untargeted Metabolomic analysis

2.9.1. Sample Collection and Overview

Serum samples from the L2-IL1B and L2-IL1B-FXR^{-/-} mouse cohort, CD, HFD and HFD+OCA treated L2-IL1B mice and human control patients, and patients diagnosed with BE, dysplasia and EAC from the BarrettNET study were used for metabolomic analyses. Also, cecal content and feces from CD, HFD and HFD+OCA treated L2-IL1B mice and stool of human patients were submitted for metabolomic analysis. Untargeted metabolomic analyses and targeted metabolomic analyses for BA were performed on the submitted samples. On SCJ, small intestinal (SI) and colon tissue, only targeted metabolomic analyses for BA were performed.

2.9.2. Sample Preparation

The same sample extraction protocol was used for untargeted and targeted metabolomic analyses. Cecal and fecal/stool content or tissue were weighed in 2 ml bead beater tubes (CKMix 2 ml, Bertin Technologies, Montigny-le-Bretonneux, France) filled with ceramic beads (1.4 mm and 2.8 mm ceramic beads i.d.). Samples were later normalized to input weight. For mouse originated samples, 1 ml methanol-based dehydrocholic acid extraction solvent ($c=1.3 \mu\text{mol/L}$) as an internal standard for work-up losses was added. For human originated samples, 5 ml methanol-based dehydrocholic acid extraction solvent was added. Samples were homogenized using a bead beater (Precellys Evolution, Bertin Technologies) supplied with a Cryolys cooling module (Bertin Technologies, cooled with liquid nitrogen). (3x20 seconds at 10.000rpm, 15 seconds breaks). The suspension was centrifuged (10 min, 8000 rpm, 10 °C) using an Eppendorf Centrifuge 5415R (Eppendorf, Hamburg, Germany). 100 μl clear supernatant was mixed with 20 μl deuterated internal standard solution ($c=7 \mu\text{mol/L}$) for ionization losses and injected into the LC-MS/MS system for targeted bile acid analysis. 0.5 ml clear supernatant was transferred to a LC-MS/MS vial for untargeted measurement. Depending on the sample size 10-100 μl of each sample was pooled to prepare a QC-sample. For metabolomic analysis of the serum samples, steps for breakdown of cells and content were unnecessary and thus excluded. The leftover supernatant was stored at -80°C for potential further analysis.

2.9.3. Untargeted Metabolomic Analyses

2.9.3.1. Performance of Untargeted Metabolomic Analyses

The untargeted analysis was performed using a Nexera UHPLC system (Shimadzu) coupled to a Q-TOF mass spectrometer (TripleTOF 6600, AB Sciex). Separation of the samples was performed using a HILIC UPLC BEH Amide 2.1x100, 1.7 μm analytic column (Waters Corp.) with 400 $\mu\text{l}/\text{min}$ flow rate and a reversed phase Kinetex XB-C18, 2.1x100, 1.7 μm analytic column (Phenomenex). The mobile phase for the HILIC separation was 5 mM ammonium acetate in water (eluent A) and 5 mM ammonium acetate in acetonitrile/water (95/5, v/v) (eluent B). The gradient profile was 100% B from 0 to 1.5 min, 60% B at 8 min and 20% B at 10 min to 11.5 min and 100% B at 12 to 15 min. The mobile phase for the reversed phase separation was 0.1% formic acid (eluent A) and 0.1% formic acid in acetonitrile (eluent B) with 300 $\mu\text{l}/\text{min}$ flow rate. The gradient profile was 0.2% B from 0 to 0.5 min to 100% B at 10 min which was hold for 3.25 min, afterwards the column was equilibrated to starting conditions. A volume of 5 μl per sample was injected for both chromatographic methods. The autosampler was cooled to 10°C and the column oven heated to 40°C. Every tenth run a quality control (QC) sample which was pooled from all samples was injected. The fecal samples were measured in a randomized order. The samples have been measured in Information Dependent Acquisition (IDA) mode. MS settings in the positive mode were as follows: Gas 1 55, Gas 2 65, Curtain gas 35, Temperature 500°C, Ion Spray Voltage 5500, declustering potential 80. The mass range of the TOF MS and MS/MS scans were 50 - 2000 m/z and the collision energy was ramped from 15 - 55 V. MS settings in the negative mode were as follows: Gas 1 55, Gas 2 65, Cur 35, Temperature 500°C, Ion Spray Voltage -4500, declustering potential -80. The mass range of the TOF MS and MS/MS scans were 50 - 2000 m/z and the collision energy was ramped from -15 - -55 V.

2.9.3.2. Analysis and Statistical Evaluation of Untargeted Metabolomic Analyses

Untargeted metabolomic analysis were performed via reverse phase (RP) chromatography and hydrophilic interaction chromatography (HILIC) in negative and positive ionization mode. Metabolomic analyses were performed in collaboration with Dr. Karin Kleigrewe and Dr. Chen Meng from the Bavarian Center for Biomolecular Mass Spectrometry (BayBioMS) at TUM. While RP chromatography demonstrates a better separation for non-polar compounds (including most BA), HILIC is more profound for polar compounds. In the positive ionization mode molecules are well detectable which are able to accept protons like for example amines, while the negative ionization mode compounds are detectable which can easily loose a proton like for example acids well, and some compounds can be ionized in both modes like amino acids. After the feces of the mice were analyzed via HILIC only, further untargeted metabolomic analyses were performed via both RP and HILIC to obtain optimal detection of all types of metabolites between groups. Results were visualized via the web-based analysis tool "XCMSViewer" (in-house data analysis pipeline of the BayBioMS) as well as the web-based tool "VolcanoseR" for publishable graphical visualization of volcano-plots²⁵⁸.

Preprocessing of data via the XCMSViewer was performed as explained in the following: raw data were converted to mzXML format to facilitate downstream processing via the ProteoWizard platform using msconvert²⁵⁹. Subsequently, peak-picking, alignment, correspondence performed using published R-package "xcms" available via the Bioconductor website for bioinformatic processing²⁶⁰⁻²⁶². Peak detection was performed using the built-in matchedFilter algorithm^{260,261} with parameters of 7.5 seconds for fwhm (specifying peaks' full width half maximum of matched filtration Gaussian model peak) and 25 ppm for mass tolerance (maximum expected deviation of m/z values). Chromatographic peak detection on the full data set was performed, chromatograms identified by less than three peaks with intensities higher than 1000 were excluded as noise. Then the retention time alignment was performed based on the chromatographic peaks presented in more than half of the total samples. Correspondence, defined as matching of detected chromatographic peaks between samples was performed using the peak density algorithm²⁶⁰, with grouping of peaks that were abundant in more than 40 % of the samples. Results were extracted as assay matrix containing feature abundance, feature definition including m/z, retention time and additional metadata and row annotations. The area under the chromatographic peaks was used to quantify the relative abundance of metabolites.

Quality of the data was inspected by visualization of the chromatographic peaks, clustering of similarity between chromatograms and distribution of total ion currents. The frequency of

identified chromatographic peaks along the retention time axis and peak intensity distribution per sample were reviewed for quality control purposes.

For feature annotation, the ion mass of the features was compared to different databases (MS1 annotation), including the MS-DIAL DB, HFDB, PubChem and in-house reference DBs at BayBioMS, allowing some common modifications and a tolerance window of mass (15 ppm). MS2 comparison was done by calculating the cosine distance between measured and reference spectra. N/A values in which single BA could not be detected in a sample due to the detection limit were replaced with LOD (limit of detection) values which were defined as one half of the minimal measured value of the BA amongst all analyzed samples. For statistical analysis, unpaired, two-tailed t-tests were performed between two groups. Significant enrichment of the compounds between groups was defined as a mean difference (mean diff.) $-2 \leq$ and ≥ 2 ; represented as \log_{10} mean diff. $-0.3 \leq$ and ≥ 0.3 with a p-value of ≤ 0.05 , represented as \log_{10} p-value of ≥ 1.3 . For this study, analysis of the untargeted metabolomic data was mainly focused on significant changes in BA levels between groups. Detected metabolites were evaluated for correct annotation by reviewing chromatographic characteristics between predicted and measured metabolite or by availability of data of previously measured reference standards, which were available for most BA measured.

2.10. Targeted Metabolomic analyses for BA

2.10.1. Performance of Targeted Metabolomic Analyses

Targeted BA analyses were performed in collaboration with Dr. Sina Reiter and Andreas Dunkel from the Leibniz institute for food and health at TUM and with Dr. Karin Kleigrewe and Dr. Chen Meng from the Bavarian Center for Biomolecular Mass Spectrometry (BayBioMS) at TUM. Targeted serum BA analyses comparing CD with HFD mice were performed with Dr. Sama Sayin in the working group of Prof. Dr. Timothy Wang at Columbia University.

Briefly, 20 μ l of isotopically labeled bile acids (ca. 7 μ M each) were added to 100 μ l of sample extract. Targeted bile acid measurement was performed using a QTRAP 5500 triple quadrupole mass spectrometer (Sciex, Darmstadt, Germany) coupled to an ExionLC AD (Sciex, Darmstadt, Germany) ultrahigh performance liquid chromatography system. A multiple reaction monitoring (MRM) method was used for the detection and quantification of the bile acids. An electrospray ion voltage of -4500 V and the following ion source parameters were used: curtain gas (35 psi), temperature (450 $^{\circ}$ C), gas 1 (55 psi), gas 2 (65 psi), and entrance potential (-10 V). The MS parameters and LC conditions were optimized using commercially available standards of endogenous bile acids and deuterated bile acids, for the simultaneous quantification of selected 34 analytes. For separation of the analytes a 100×2.1 mm, 100 \AA ,

1.7 μm , Kinetex C18 column (Phenomenex, Aschaffenburg, Germany) was used. Chromatographic separation was performed with a constant flow rate of 0.4 ml/min using a mobile phase consisted of water (eluent A) and acetonitrile/water (95/5, v/v, eluent B), both containing 5 mM ammonium acetate and 0.1% formic acid. The gradient elution started with 25% B for 2 min, increased at 3.5 min to 27% B, in 2 min to 35% B, which was hold until 10 min, increased in 1 min to 43% B, held for 1 min, increased in 2 min to 58% B; held 3 min isocratically at 58% B, then the concentration was increased to 65% at 17.5 min, with another increase to 80% B at 18 min, following an increase at 19 min to 100% B which was hold for 1 min, at 20.5 min the column was equilibrated for 4.5 min at starting. The injection volume for all samples was 1 μL , the column oven temperature was set to 40 $^{\circ}\text{C}$, and the auto-sampler was kept at 15 $^{\circ}\text{C}$. Data acquisition and instrumental control were performed with Analyst 1.7 software (Sciex, Darmstadt, Germany). Targeted metabolomic analyses were analyzed as BA intensities, or respectively, if correlated to input weight and dilution, in nmol/g feces. Targeted Serum BA analysis comparing CD with HFD mice were visualized as heatmaps showing primary and secondary BA intensities between samples, as well as a correlation heatmap of BA levels with dysplasia scores and inversely with goblet cell ratio, representing differentiation status. Bile acids detected via targeted BA analysis are listed in Table 16.

Table 16: Bile Acids Measured in Targeted Bile Acid Metabolomic Analysis

5 β -Cholic acid-3 α -ol-7-one, 7-Ketolithocholic acid, (7-KLCA)	3-Dehydrocholic acid (3-DHCA)
5 β -Cholic acid-3 α -ol-12-one, 12- Ketolithocholic acid, (12-KLCA)	5 β -Cholic acid-3 α -ol-6,7-dione, (6,7-DKLCA)
α -Muricholic acid, (α -MCA)	5 β -Cholic acid-3 α -ol-6-one, (6-KLCA)
β -Muricholic acid, (β -MCA)	7-Dehydrocholic acid, (7-DHCA)
5 β -Cholen-24-oic acid-3,12-diol, Apocholic acid, (ApCA)	Cholic acid-7-sulphate, (7-SCA)
Chenodeoxycholic acid, (CDCA)	12-Dehydrocholic acid, (12-DHCA)
Cholic acid, (CA)	5 β -Cholic acid-7 α -ol-3-one, (Ca-7ol3one)
Deoxycholic acid, (DCA)	Glycocholic acid, (GCA)
Glycochenodeoxycholic acid, (GCDCA)	Glycoursodeoxycholic acid, (GUDCA)
Glycodeoxycholic acid, (GDCA)	Isolithocholic acid, (ILCA)
Hyodeoxycholic acid, (HDCA)	Taurocholic acid, (TCA)
Lithocholic acid, (LCA)	Taurohyodeoxycholic acid, (THDCA)
Tauro- α -Muricholic acid, (T- α -MCA)	Taurolithocholic acid, (TLCA)
Taurochenodeoxycholic acid, (TCDCA)	Tauro- ω -Muricholic acid, (T- ω -MCA)
Taurodeoxycholic acid, (TDCA)	Allocholic acid, (ACA)
Tauroursodeoxycholic acid, (TUDCA)	Ursocholic acid, (UCA)
Ursodeoxycholic acid, (UDCA)	5 β -Cholic acid-3 α -ol-7,12-dione, (7,12-DKLCA)
Glycolithocholic acid, (GLCA)	Dehydrolithocholic acid, (DHLCA)
Murideoxycholic acid, (MDCA)	Glycohyocholic acid, (GHCA)
Allolithocholic acid, (ALCA)	Lithocholenic acid, (LGenA)
Glycohyodeoxycholic acid, (GHCA)	Obeticholic acid, (OCA)
Isodeoxycholic acid, (IDCA)	γ -Muricholic acid/Hyocholic acid, (γ MCA)

2.10.2. Analysis and Statistical Evaluation of Targeted Metabolomic Analyses

For single BA analyses, data were normalized by log₁₀ transformation for scaling purposes. N/A values in which single BA could not be detected in a sample due to the detection limit were replaced with LOD (limit of detection) values which were defined as one half of the minimal measured value of the BA amongst all analyzed samples. For statistical analysis, unpaired, two-tailed t-tests were performed between two groups. For total BA analysis, pooled BA intensities/concentrations of primary / secondary or total BA were compared between groups. Primary compared to secondary BA levels are depicted as pie charts for visualization of changes between groups and did not undergo further statistical analyses. Pooled levels were compared between groups to assess changes between intervention cohorts. For statistical analysis of two groups, unpaired, two-tailed t-tests were used, for analysis of three or more groups, ordinary one-way ANOVA with Tukey test to correct for multiple comparisons was used. For further statistical analysis and visualization, including 3D PLS-DA (Partial Least Squares – Discriminant Analysis), selection of important features by VIP (variable importance in projection) scores and clustered heatmap analyses, the web-based tool metaboanalyst was used²⁶³. Data with BA intensities / concentrations were uploaded as excel files. N/A values in which single BA could not be detected in a sample due to the detection limit were replaced with LOD values which were defined as one half of the minimal measured value of the BA amongst all analyzed samples. Data was normalized by log₁₀ transformation and autoscaling (mean-centering and dividing by SD of each variable). Sample distribution between classes was visualized by PLS-DA analysis. PLS is a supervised clustering method. It uses multivariate regression techniques to extract the information that can predict class membership (Y) via linear combination of original variables (X). For measuring variable importance in PLS-DA, variable importance in projection (VIP) scores or correlation coefficients were used. VIP scores are a weighted sum of squares of the PLS loadings considering the amount of Y-variation in each dimension. Correlation coefficients are based on the weighted sum of PLS-regression. The weights are a function of the reduction of the sums of squares across the number of PLS components. The averages of the feature coefficients are used to indicate the overall coefficient-based importance. Hierarchical clustering of Samples and / or detected BA was performed using Euclidean distance matrix and ward clustering algorithm and was presented as heatmap. Heatmaps show results of the top 20 regulated BA as single values per sample for murine derived samples and as mean values for human derived samples.

2.11. Cell Culture (Organoid Culture from L2-IL1B mice)

2.11.1. Preparation of Conditioned Medium for Organoid Maintenance

L-WRN (LWnt3A, R-spondin 3 and Noggin) conditioned medium with additional growth factors was used as growth medium for organoid culture. Media was conditioned with L-WRN producing cells (ATCC® CRL3276™) according to the manufacturer's protocol. Cells were thawed in a water bath at 37 °C and transferred to a cell culture flask containing prewarmed growth medium. Cells are maintained in an incubator 37 °C. After 24 hours, medium was exchanged with complete growth medium containing selection markers. The exact compositions of growth medium and complete growth medium are presented in Table 17. When confluent, cells were splitted in selection media. After selection for 7-10 days, cells were splitted up to 1:10. Cells were then seeded in T150 cell culture flasks until desired number of flasks was reached in growth medium without selection markers to prevent carryover of drugs into conditioned medium. 25 ml of cell suspension were seeded per T150 flask. Flasks were incubated for 3-4 days until cells become overconfluent. Medium was exchanged with 25 ml fresh medium and incubated for 24 hours for conditioning. Conditioned medium was removed from the flasks and centrifuged at 2000g for 5 minutes to remove cellular contamination. The supernatant was collected and stored at 4 °C. Conditioning of medium over 24 hours was repeated for a total of 4 times and the centrifuged supernatant was pooled. All L-WRN conditioned media was sterile filtered, mixed 1:1 with fresh growth media and aliquoted into 50 ml tubes for long-term storage at -20 °C until further use. For organoid culture, L-WRN conditioned media was supplemented with additional growth factors. The composition of the L-WRN media with growth factors is presented in Table 18.

Table 17: Compositions of growth medium and complete growth medium with selection markers for L-WRN producing cells (ATCC® CRL3276™)

Buffer	Concentration	Manufacturer and Article Number
For growth medium		
advanced DMEMF12	Basis for medium	12634010, Gibco™ via ThermoFisher
FBS	10 %	10500064, Gibco™ via ThermoFisher
Penicillin/Streptomycin	1%	15140122, Gibco™ via ThermoFisher
HEPES	1%	15630080, Gibco™ via ThermoFisher
GLUTAMAX	1%	35050061, Gibco™ via ThermoFisher
Selection markers for complete growth medium		
G-418	0.5 mg / ml	10131035, Gibco™ via ThermoFisher
Hygromycin B	0.5 mg / ml	10687010, Gibco™ via ThermoFisher

Table 18: Composition of L-WRN conditioned media supplemented with growth factors for organoid culture

Buffer	Concentration	Manufacturer and Article Number
For L-WRN conditioned growth medium with growth factors		
L-WRN conditioned medium	Basic medium	-
B27 (100x conc.)	1x	17504044, ThermoFisher
N2 (50x conc.)	1x	17502048, ThermoFisher
Human EGF	50 ng/ml	AF-100-15, Peprotech
N-acetyl cysteine (NAC)	1 mM	A7250, Sigma Aldrich

2.11.2. Isolation and Maintenance of Organoids

Mouse organoid culture was performed according to the procedure published by Pastula et al. 2016 with minor adjustments¹³⁹. After euthanasia of the mouse, the cardia region of the stomach was resected and washed in dPBS (14190144, Gibco™ via ThermoFisher) to remove remaining food particles and other contaminants. In case that stomach tissue was also needed for histology and storage for RNA and Protein extraction, only half of the stomach and cardia region were used for organoid isolation. Resected cardia tissue was cut into small pieces using surgical scissors and transferred to an Eppendorf tube containing 200-300 µl Accutase® cell detachment solution (A6964, Sigma-Aldrich). The tissue was incubated in Accutase® on a shaker for 15 min. for enzymatic tissue digestion. Tissue pieces were transferred to a 50 ml collection tube containing 20 ml of ice-cold dPBS (14190144, Gibco™ via ThermoFisher) supplemented with 2mM EDTA (AM9260G, Invitrogen™ via ThermoFisher) and EGTA (3054.2, Roth) each. All following steps were performed on ice. The tissue was incubated on a shaker on ice for 45 min. for chemical tissue digestion. Supernatant was removed from sedimented tissue pieces and tissue was washed and mechanically disintegrated by pipetting up and down in 10 ml of cold dPBS (14190144, Gibco™ via ThermoFisher) + 10 % FBS (10500064, Gibco™ via ThermoFisher). The tissue suspension was passed through a 70 µm cell strainer into a 50 ml tube. The tissue was removed from the strainer by washing it with 10 ml of fresh dPBS + 10 % FBS back into the old collection tube. Mechanical disintegration, filtration, and recovery of the tissue from the strainer as described was repeated for a total of four times. The final volume of 40 ml cell suspension was centrifuged at 4°C for 10 min. at 400g. The supernatant was removed from the cell pellet and the cells were resuspended in

150-300 µl Matrigel® (354230, Corning®) depending on the pellet size. 50 µl ice-cold Matrigel® per well were plated in a 24 well plate prewarmed to 37°C. The plate was incubated for approximately 10 minutes in an incubator at 37°C to let the Matrigel® solidify. Then, 500 µl L-WRN media with growth factors was added to each well containing Matrigel. The Plate was incubated at 37 °C. Media was changed every 2-3 days and organoids were passaged every 7-10 days depending on the growth rate of the organoids. For passaging, media was removed from the wells and the 24 well plate was incubated on ice to accelerate disintegration of Matrigel®. 500 µl of ice-cold dPBS + 10 % FBS were pipetted into each well. Matrigel® was disrupted by pipetting the ice-cold buffer and the suspension from each well was transferred to and pooled in a 15 ml collection tube. The washing step was repeated with another 500 µl of ice-cold dPBS + 10 % FBS. Matrigel® and organoids were gently further disrupted by pipetting the suspension in the 15 ml collection tube up and down 10-20 times. The tube was then centrifuged at 4°C for 10 min. at 400g. supernatant and potential Matrigel® residuals forming a gelatinous mass on top of the cell pellet were carefully removed. The cell pellet was resuspended in fresh Matrigel®, plated into a new prewarmed 24 well plate and overlaid with media as previously described. Wells were expanded 1:2-1:4 per passage depending on the growth rate of the organoids.

2.11.3. Freezing and Thawing of Organoids

For preservation and storage purposes, organoids were treated and pooled as described for passaging in section 11.2 The resulting cell pellet was suspended in Crypt Freezing Medium (12648010, Gibco) and transferred into Cryo- tubes (72.380, Sarstedt), which were frozen at -80°C. For long term storage samples were transferred to liquid nitrogen the next day.

Frozen organoids were thawed briefly in a water bath at 37 °C. The cell suspension was centrifuged at 4 °C for 10 min. at 400g and resuspended in Matrigel. ROCK-Inhibitor (1254, Tocris) was added to the conditioned media to reduce cell stress in the first growth phase.

2.11.4. Treatment of L2-IL1B Mouse Cardia Organoids with Bile Acids

2.11.4.1. Titration of Drug Concentrations for Treatment

According to the literature and previous research, treatment of the organoids was tested with five different drug concentrations per drug. For OCA, concentrations of 0.5, 1, 2, 5 and 10 μM , and for T β MCA and DCA, concentrations of 1, 10, 50, 100 and 200 μM of drug in the medium were tested. Each concentration was tested in triplets. The drugs were mixed into the media and media was changed every 24 h, the organoids were treated with media + drug for 120 h. Organoids were counted and photographed for size measurements every 24h beginning from 0h before treatment. After 120 h, RNA was extracted from the wells which still contained living organoids.

2.11.4.2. Treatment of Organoids with Bile Acids

Mouse cardia organoids were isolated from L2-IL1B mice. Treatment was started two days after 3rd - 4th passage of the organoids. The organoid treatment was performed for 72 h with OCA, DCA or T β MCA or OCA + DCA or OCA + T β MCA in concentrations of 10 and 100 μM diluted in the medium. Every 24 h cell numbers were counted and photographed, and medium was changed subsequently. Every 24 h, 2-3 wells with organoids were pooled and RNA was extracted using the RNeasy Micro Kit (Qiagen, Germany) and conditioned media from every treatment condition was collected and stored.

2.11.4.3. Evaluation of Organoid Growth and Size

Beginning from timepoint 0 right before starting the treatment, organoids were counted, and pictures were taken every 24 h before changing the media. For size measurements, pictures of a representative number of organoids of each well were taken at 5x. The diameter of every organoid was measured from 3 different angles.

2.11.4.4. Flow-Cytometry of Organoids

Different protocols for flow cytometry-based proliferation and cell cycle analysis using MTT and PI staining and the Click-iT™ EdU (5-ethynyl-2'-deoxyuridine) Alexa Fluor™ 488 Flow Cytometry Assay Kit (C10425, Invitrogen™ via ThermoFisher) for evaluation of cell proliferation were tested for organoid culture, with the most reliable and reproducible results obtained by the optimized protocol of the Click-iT™ EdU Flow Cytometry Assay Kit.

2.11.4.5. Click-iT EdU Flow Cytometry Assay Kit for Evaluation of Cell Proliferation

Cell proliferation rates in treated organoids were evaluated using the Click-iT™ EdU Alexa Fluor™ 488 Flow Cytometry Assay Kit (C10425, Invitrogen™ via ThermoFisher). The nucleoside analog EdU (5-ethynyl-2'-deoxyuridine) is used for evaluation of cell proliferation as it is incorporated into DNA instead of thymidine during active DNA synthesis. A copper catalyzed reaction between the ethynyl moiety of EdU and a fluorescent dye coupled azide (click reaction) enables fluorescent based analysis via flow cytometry. Cells were labeled, fixed and permeabilized according to the manufacturer's protocol with minor modifications. All reagents were prepared according to the manufacturer's protocol.

Organoid cells were treated with 50 µM EdU in fresh conditioned medium for two hours in an incubator at 37 °C. The concentration of 50 µM EdU was determined by testing different EdU concentrations and incubation times to obtain optimal results during flow cytometry. Depending on organoid growth, cells from approximately 6 wells of organoids per condition were treated with EdU for flow cytometry. After two hours, organoids were harvested with 500 µl of ice-cold dPBS + 10 % FBS per well, pooled and centrifuged for 10 min. at 4 °C and 400 rcf as described for passaging. The cell pellet was then incubated in 1 ml of 0.25 % Trypsin-EDTA (25200056, Gibco™ via ThermoFisher) for 15 min. on a rotation wheel in an incubator at 37 °C with occasional vortexing to obtain single cells. The reaction was stopped with 9 ml of dPBS + 10 % FBS and the cells were again centrifuged for 10 min. at 4 °C and 400 rcf and the supernatant was discarded. After single cell isolation, cells were washed with 3 ml of 1% BSA (9418, Sigma) in dPBS and centrifuged as described before. Supernatant was discarded and the pellet was thoroughly resuspended in 100 µl of Click-iT® fixative (Component D). Cells were incubated for 15 min. at RT on a rotation wheel under exclusion of light. Cells were washed with 3 ml of 1% BSA in dPBS and pelleted by centrifugation as described before. The cell pellet was resuspended in 100 µl of 1X Click-iT® saponin-based permeabilization and wash reagent. The Click-iT® EdU reaction cocktail was prepared according to the manufacturer's protocol. The exact composition of the Click-iT® EdU reaction cocktail is presented in Table 19. 0.5 ml of freshly prepared reaction cocktail were added to the organoid cells in 1X Click-iT® saponin-based permeabilization and wash reagent and incubated for 30 min. at RT on a rotation wheel under exclusion of light. Cells were again washed with 3 ml of 1% BSA in dPBS and pelleted by centrifugation as described before. The supernatant was removed, and the cells were resuspended in 100 µl of 1X Click-iT® saponin-based permeabilization and wash reagent. Cells were stained for DNA content and analyzed on a Gallios flow cytometer (Beckman Coulter), using an excitation laser at 488nm, and measuring emission using a green bandpass emission filter (530/30 nm). Results were analyzed using FlowJo software (TreeStar).

Table 19: Composition of the Click-iT® EdU reaction cocktail

Reaction Components	Amount per reaction	Manufacturer and Article Number
For Click-iT® EdU reaction cocktail		
dPBS	438 µl	14190144, Gibco™ via ThermoFisher
CuSO ₄ (Component F)	10 µl	Supplied with Click-iT™ EdU Alexa Fluor™ 488 Flow Cytometry Assay Kit
Fluorescent dye azide (prepared according to manufacturer's protocol)	2.5 µl	Supplied with Click-iT™ EdU Alexa Fluor™ 488 Flow Cytometry Assay Kit
1X Click-iT® EdU reaction buffer additive (prepared according to manufacturer's protocol)	50 µl	Supplied with Click-iT™ EdU Alexa Fluor™ 488 Flow Cytometry Assay Kit
Total reaction volume	500 µl	

2.11.5. Histological Analysis of Organoids

2.11.5.1. Preparation of PFPE Samples and Sections

For fixation and embedding of organoids for PFPE sections, Organoids were grown on disinfected round glass cover slips inserted into a 24-well plate after passaging. Organoids were passaged and maintained as described.

For fixation, the medium was aspirated, and organoids were washed with 500 μ l of PBS⁺ (dPBS + 0.9mM CaCl₂ and 0.493 mM of MgCl₂) per well. Organoids were incubated at RT on a shaker for one minute. Afterwards PBS⁺ was aspirated and the washing step was repeated twice. After the third washing step, 500 μ l of 4 % PFA (Apotheke, Klinikum Rechts der Isar) were added to each well and organoids were fixed in PFA for 30 min. at RT on a shaker. For short-term storage, organoids were then kept in 500 μ l 0.1 % PFA in PBS per well at 4 °C for up to one week. After fixation, organoids were again washed three times in 500 μ l of PBS⁺ as described before. Subsequently, glass plates were removed from the 24-well plate using forceps or injection needles and transferred to Bio-Net histology cassettes (09-0403, Langenbrinck GmbH). Histology cassettes containing glass plates with organoids attached were washed in 70% ethanol before overnight dehydration in ethanol (increasing concentrations), xylene and paraffin in a S300 tissue processing unit (Leica). On the following day, the organoids were scratched from the glass plates into embedding forms using a scalpel, embedded into paraffin, cooled, and stored at room temperature. Depending on the amount of organoids per well, organoids from two to three wells were pooled. Paraffin blocks were cooled and cut like normal blocks containing tissue, with a section thickness of 2-3 μ m. Sections were checked for organoid content under a light microscope.

2.11.5.2. Staining and Immunohistochemistry of Organoids

Staining and IHC were performed as previously described for tissue sections.

2.11.5.3. Quantification of Immunohistochemistry of Organoids

γ -H2AX and Ki67 IHC in organoids were quantified as the percentage of positive (DAB stained) cells relative to all cells per organoid. All organoids from one mouse, which were treated with the same treatment conditions were counted as technical replicates. Organoids from different mice were defined as biological replicates. Organoids from n=3 mice per condition were treated for statistical analysis. For statistical analysis, ordinary one-way ANOVA with Tukey test to correct for multiple comparisons was performed.

2.12. RNA Extraction and Downstream Applications

Depending on organoid growth, 3-6 wells of organoids were harvested with 500 μ l of ice-cold dPBS + 10 % FBS per well, pooled and centrifuged for 10 min. at 4 °C and 400 rcf as described for passaging. Subsequently the supernatant was removed, and the pellet was resuspended in 500 μ l collagenase/ dispase (1 mg/ml) and incubated at 37 °C for 1 hour to digest matrigel residuals enzymatically. The reaction was stopped with 500 μ l 5 mM EDTA (AM9260G, Invitrogen™ via ThermoFisher) in dPBS. The tube was filled up to 10 ml with dPBS, again centrifuged at 10 min. at 4 °C and 400 rcf and the supernatant was removed. The remaining cell pellet was lysed in 600 μ l RLT-buffer (Lysis buffer; 1015762; Qiagen) supplemented with 1 % beta-mercaptoethanol (4227.3, Roth). RNA isolation was performed using the RNeasy Mini Kit (74104; Qiagen) according to the manufacturer's protocol.

2.12.1. qRT-PCR

Reverse transcription PCR and qRT-PCR were both performed as described for tissue samples.

2.12.2. DNA Damage ELISA

OxiSelect Oxidative DNA Damage ELISA, 8'OhdG Quantitation (Cell Biolabs, Inc. STA-320) was performed using conditioned media from the different treatments according to the manufacturer's protocol to detect oxidative DNA damage in the organoids. Conditioned media from 12m L2-IL1b mouse organoids treated with OCA, DCA, T β MCA, OCA+DCA or OCA+T β MCA and without treatment were analyzed after 48h and 72h treatment. Data was acquired on a multiskan FC microplate reader (Thermo Scientific) and analyzed using Microsoft Excel and GraphPad Prism version 8

2.13. Statistical Analysis

Statistical analyses were performed using GraphPad Prism version 8.00 for Windows (GraphPad Software). Data was usually presented as mean \pm standard deviation (SD). Targeted metabolomic data was usually presented as mean. Comparison of two groups were performed by unpaired t-tests. For comparison of more than two normally distributed groups ordinary one-way ANOVA with Tukey's multiple comparison test was performed. If the values were not normally distributed Mann-Whitney-U tests or Kruskal-Wallis test with Dunn's multiple comparison test was performed. Histological scores - being ordinal values - were compared using Kruskal-Wallis tests and Dunn's post-hoc test. Statistical significance is indicated by asterisk. A p-value of ≤ 0.05 and was assumed to be statistically significant ($p \leq 0.05$ *, $p \leq 0.01$ **, $p \leq 0.001$ ***, $p \leq 0.0001$ ****).

3. Results

3.1. Characterization of the Pathophysiologic and Metabolic Profile of the L2-IL1B Mouse Model with a Whole-body Knockout of the BA Receptor FXR

3.1.1. FXR Expression Potentially Acts Protectively Against Malignant Progression in BE

It is assumed that BAs damage the esophageal tissue, create an inflammatory microenvironment, and thus promote tumorigenesis^{47,82,242,264}. In accordance with previous studies, we found FXR, a nuclear BA receptor central to metabolic and inflammatory BA signaling^{217,219}, to be expressed in BE of patients and L2-IL1B mice^{265,266}. Its expression was lost over the course of tumor progression, pointing to a protective effect (Fig.7 A-C)^{267,268}. To evaluate the function of FXR in the development of BE and EAC we induced a full body knockout of FXR on the background of the L2-IL1B mouse model by crossing L2-IL1B transgenic mice with FXR^{-/-} mice (L2-IL1B-FXR^{-/-}).

The following results section contains data from a previously generated mouse model. All experiments and analyses shown were newly performed from data and material collected from the mouse model by Andreas Nuber, a former doctoral student of the laboratory.

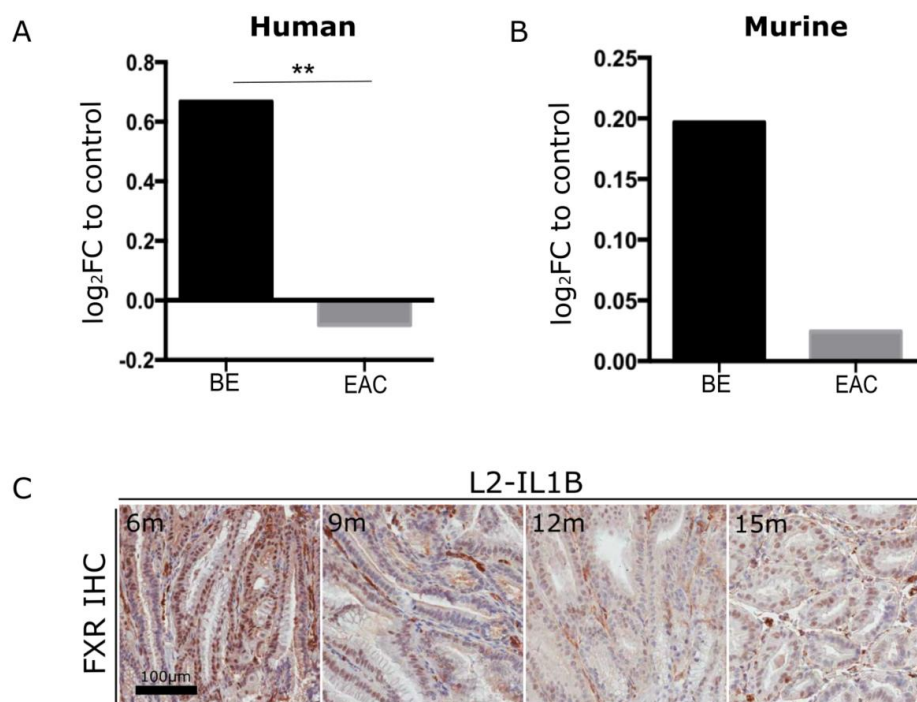


Figure 7: FXR is expressed in BE but not in EAC tissue in human patients and L2-IL1B mice (A) Analysis of publicly available gene expression data generated by Kim et al., 2010²⁶⁹ for FXR in normal, BE or EAC tissue samples. Expression of FXR in BE is significantly higher compared to normal and EAC tissue (Data available on NCBI gene expression omnibus database (GSE13898); Data analysis with Geo2r tool from Gene Expression Omnibus public database; upregulation of FXR in BE vs. esophageal control tissue log₂FC=0.6673 p= 6.38x10⁻⁰⁶ padj. = 5.60x10⁻⁰⁵; downregulation of FXR in EAC vs. esophageal control tissue log₂FC= -0.0818 p= 2.01x10⁻⁰¹ padj. = 2.39x10⁻⁰¹; upregulation of FXR in BE vs. EAC log₂FC=-0,533 p= 1,93x10⁻⁰⁶ padj. = 1,24x10⁻⁰³). **(B)** FXR expression data of RNA microarray (GSE24931) in adult BE mice and EAC mice. Gene expression data is displayed as log₂FC to control. Expression of FXR in BE treated with bile acids is higher and EAC is lower compared to normal tissue (Data available on NCBI gene expression omnibus database (GSE13898); Data analysis with Geo2r tool from Gene Expression Omnibus public database; upregulation (not significant) of FXR in BE vs. esophageal control tissue log₂FC=0,2 p= 0,82; padj. = 0,91; no regulation of FXR in EAC vs. esophageal control tissue log₂FC= 0,03 p= 0,98; padj. = 0,99). **(C)** Representative FXR Immunohistochemistry of the squamocolumnar junction of L2-IL1B mice at 6, 9, 12and 15 months, showing decreasing nuclear FXR expression with increasing age and phenotype of the mice. Bar 100 µM.

3.1.2. Knockout of FXR in L2-IL1B Mice Leads to Aggravation of the Dysplastic Phenotype

L2-IL1B-FXR^{-/-} mice were bred and aged. Mice were sacrificed at 6, 9 and 12 months of age to evaluate disease progression by analyzing the phenotype histologically and macroscopically. Macroscopic pictures of the opened and cleaned stomach were taken from every mouse after euthanasia. HE staining of sections of the FFPE stomach tissue blocks of all mice was prepared for histologic scoring. Macroscopically, tumor size and the percentage of tumors covering the SCJ were measured, while histologically, a previously developed scoring system adapted to the L2-IL1B mouse model was applied for scoring^{270,271}. At 12 months of age, the histologic and macroscopic phenotype at the SCJ of L2-IL1B-FXR^{-/-} mice diverged significantly from L2-IL1B mice. Macroscopically (Fig.8 A), tumor percentage in the cardia and tumor size increased in 12-month-old L2-IL1B-FXR^{-/-} compared to L2-IL1B mice (Fig.8 B, C), while changes were not apparent in 6- or 9-month-old mice.

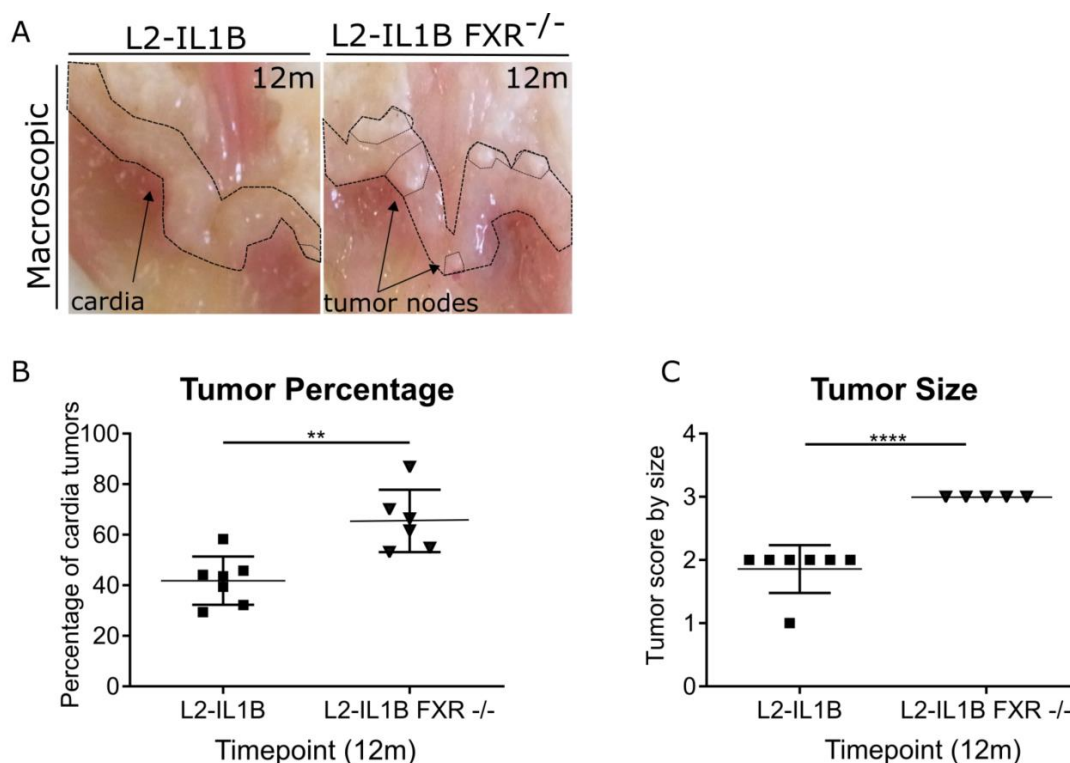


Figure 8: FXR knockout increases macroscopic scores in 12m old L2-IL1B mice (A) Representative macroscopic image of the SCJ region of L2-IL1B and L2-IL1B-FXR^{-/-} mice at 12 months of age, with the SCJ and tumor nodes in the SCJ being outlined (B) Tumor percentage (p=0.0025) and (C) Tumor size (p exact=0.0013) of 12-month-old L2-IL1B vs L2-IL1B-FXR^{-/-} mice are both significantly higher in 12-month-old L2-IL1B compared to L2-IL1B-FXR^{-/-} mice (L2-IL1B n=7; L2-IL1B-FXR^{-/-} n=5). Data are presented as mean with SD. For statistical evaluation of (B, C) unpaired two-tailed t-tests were used.

Also, histologically no significant phenotypic changes between L2-IL1B and L2-IL1B-FXR^{-/-} mice could be detected at 6 and 9 months of age (Supplementary Fig. 1,2). Evaluation of HE staining (Fig.9 A) showed, that at 12 months of age, FXR knockout in L2-IL1B mice caused increased inflammation and dysplasia scores (Fig.9 B, C) with decreased differentiation represented by the percentage of goblet-like cells in the BE region (Fig.9 D). Mucus producing cells of a goblet-like phenotype (further referred to as “goblet cells”) are characterizing the differentiation status of the metaplastic BE region at the SCJ of L2-IL1B mice and a high goblet cell ratio is associated with BE rather than EAC²⁷². Goblet cells were detected in all L2-IL1B and L2-IL1B-FXR^{-/-} mice. Metaplasia scores did not change significantly between cohorts (Fig.8 C). Histologic scoring was performed by an experienced gastroenterologist.

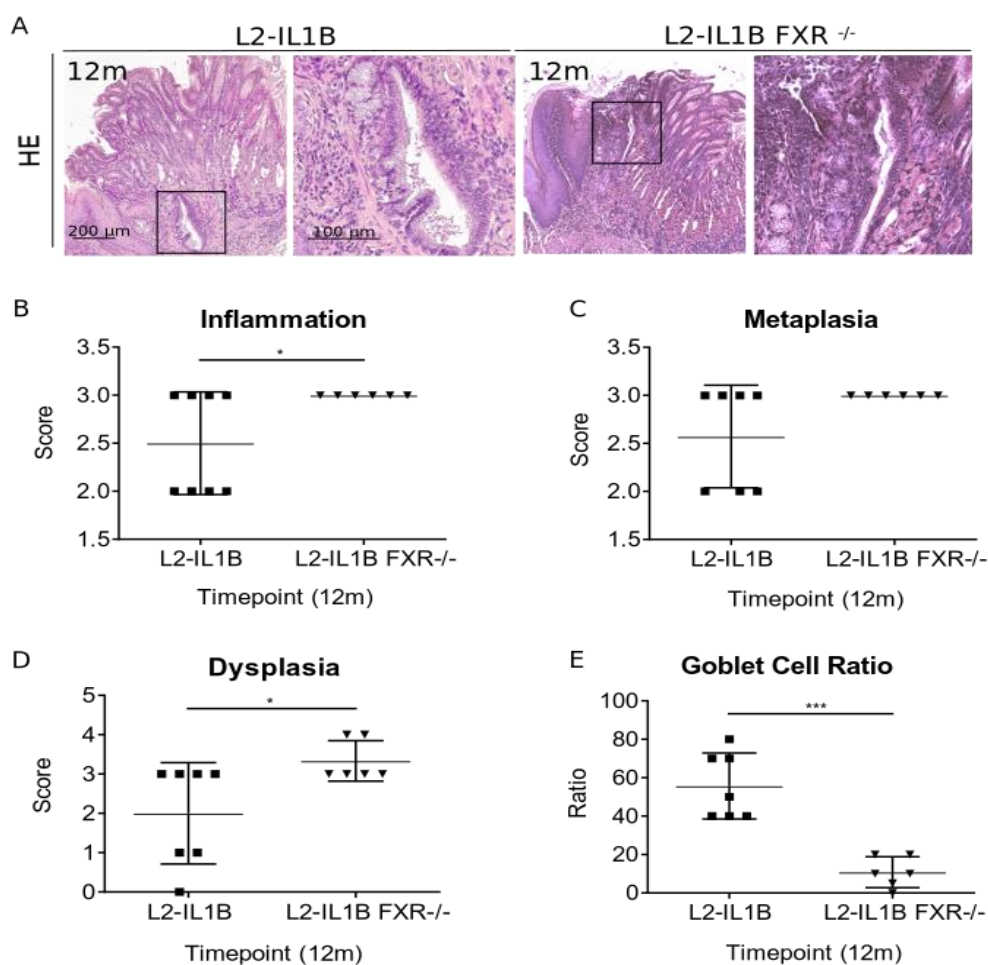


Figure 9: FXR knockout increases dysplasia scores and decreases goblet cell (GC) ratio in 12m old L2-IL1B mice (A) Representative Hematoxylin & Eosin (HE) staining of cardia tissue of L2-IL1B and L2-IL1B-FXR^{-/-} mice at 12 months of age. Bars 200 and 100 μ m. (B) Inflammation (C) Metaplasia and (D) Dysplasia scores as well as (E) Goblet cell ratio in 12-month-old L2-IL1B-FXR^{-/-} mice. Inflammation and Dysplasia scores are significantly higher than in 12-month-old L2-IL1B mice ($p_{inflammation}=0.0426$; $p_{dysplasia}=0.0409$). Goblet Cell Ratio as a marker for differentiation is significantly lower in L2-IL1B-FXR^{-/-} compared to L2-IL1B mice ($p=0.0001$). Data are presented as mean with SD. For statistical evaluation of (B-D) unpaired two-tailed t-tests were used.

3.1.3. Knockout of FXR Leads to a Reduction of Mucus Production in L2-IL1B mice

Mucus production by mucinous goblet cells in the SCJ was evaluated by PAS staining. While the ratio of goblet cells is correlated to differentiation in the BE region²⁷², mucus production by these cells has a protective effect on epithelial damage and subsequently malignant transformation in BE. Evaluation of PAS staining (Fig.10 A) showed, that at 12 months of age, FXR knockout in L2-IL1B mice led to decreased mucus production (Fig.10 B), while no significant phenotypic changes between L2-IL1B and L2-IL1B-FXR^{-/-} mice could be detected at 6 and 9 months of age (Supplementary Fig. 3).

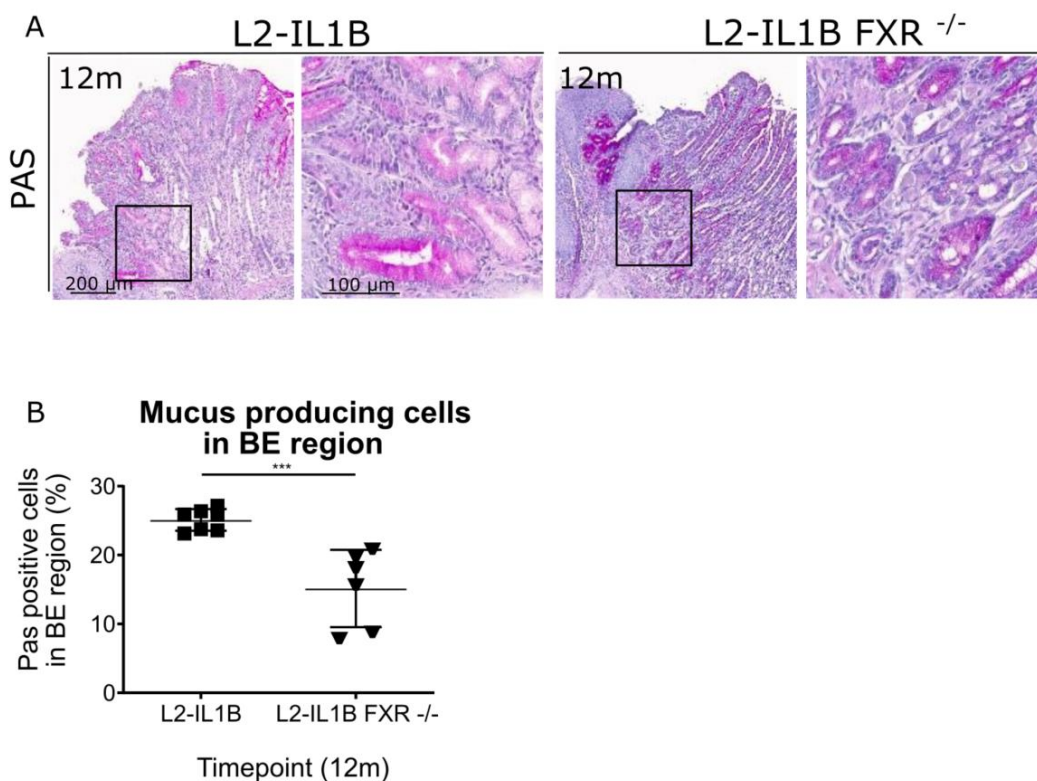


Figure 10: Coverage with PAS positive mucus producing cells decreases in L2-IL1B-FXR^{-/-} compared to L2-IL1B mice (A) Representative Periodic Acid-Schiff (PAS) staining of cardia tissue of L2-IL1B and L2-IL1B-FXR^{-/-} mice at 12 months. Bars 200 μ m and 100 μ m. **(B)** The amount of PAS positive mucus producing Goblet-like cells is significantly lower in 12m old L2-IL1B-FXR^{-/-} mice compared to L2-IL1B mice ($p=0.0009$). Data are presented as mean with SD. For statistical evaluation of **(B)** an unpaired two-tailed t-test was used.

3.1.4. Knockout of FXR Leads to Increased Smooth Muscle Differentiation in L2-IL-1B Mice

Smooth muscle differentiation leads to formation of myofibroblasts, which are supporting matrix reorganization and fibrosis. They are found in increased amounts in inflammation induced cancers such as ESCC²⁷³. Their ratio also increases with disease progression in the L2-IL1B mouse model²⁷⁰. To assess smooth muscle differentiation in L2-IL1B and L2-IL1B-FXR^{-/-} mice, we analyzed immunohistochemistry for alpha smooth muscle actin (α SMA). The percentage of α SMA positive myofibroblasts in the BE region significantly increased in 12-month-old L2-IL1B-FXR^{-/-} compared to L2-IL1B mice (Fig.11), while no significant changes could be detected in 6- and 9-month-old mice (Supplementary Fig.4). The detected increase in the percentage of α SMA positive cells in the BE region indicates formation of a more pro-inflammatory and pro-tumorigenic microenvironment through loss of FXR.

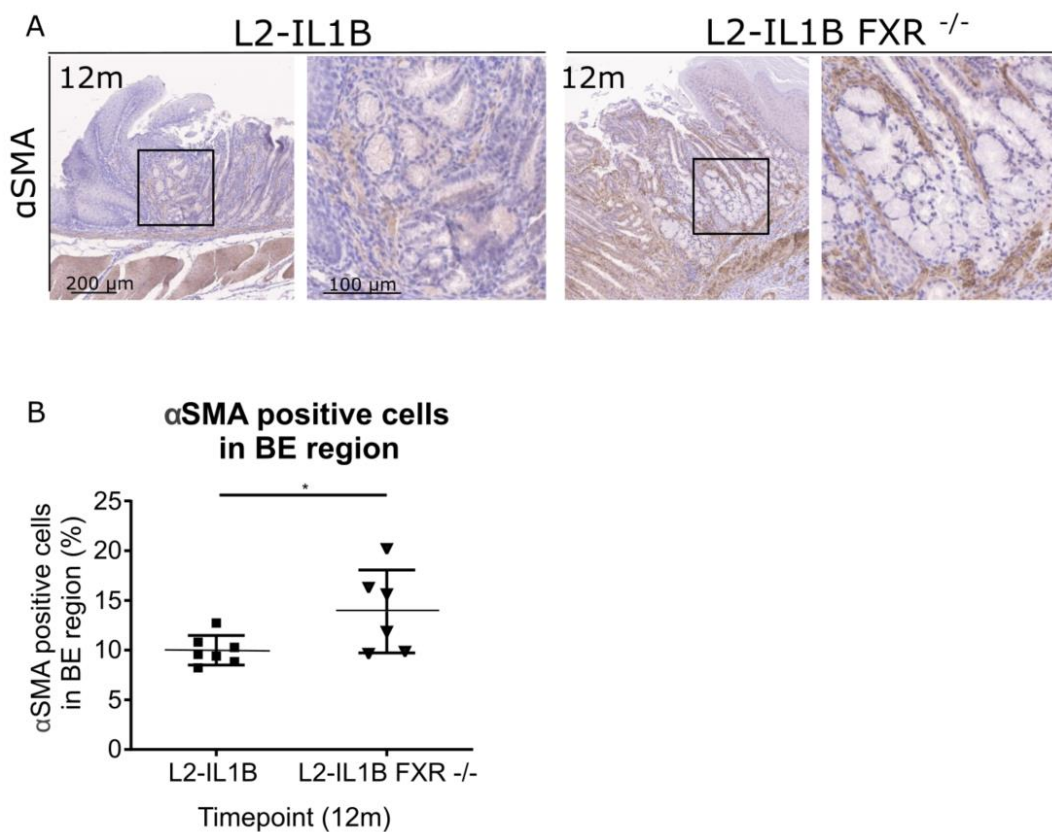


Figure 11: α SMA expression increases in L2-IL1B-FXR^{-/-} compared to L2-IL1B mice (A) Representative α SMA immunohistochemistry of cardia tissue of L2-IL1B and L2-IL1B-FXR^{-/-} mice at 12 months. Bars 200 μ m and 50 μ m. (B) The amount of α SMA positive cells is significantly elevated in 12m old L2-IL1B-FXR^{-/-} mice compared to L2-IL1B mice ($p=0.0398$). Data are presented as mean with SD. For statistical evaluation of (B) an unpaired two-tailed t-test was used.

3.1.5. Knockout of FXR Leads to Increased Caspase 1 Activation in L2-IL1B Mice

The inflammasome is a multiprotein platform involved in the activation of inflammatory responses and first line host defense mechanisms against pathogenic triggers including microbial as well as endogenous signaling²⁷⁴. The family of caspases comprises different intracellular cysteine proteases. Caspase 1 is an essential part of the inflammasome, which upon activation further cleaves proinflammatory cytokine precursors, including IL1B, into their active forms²⁷⁴. FXR was proven to play a role in antimicrobial defense and maintenance of epithelial integrity, and knockout of FXR disturbs antimicrobial epithelial barrier functions²⁷⁵, thereby potentially causing increased activation of Caspase 1 and thus IL1B in the tissue. To assess Caspase 1 activation in the tissue of L2-IL1B-FXR^{-/-} compared to L2-IL1B mice we analyzed immunohistochemistry for Caspase 1. While no significant changes could be detected in 6- and 9-month-old mice (Supplementary Fig.5), the percentage of Caspase 1 positive cells in the BE region significantly increased in 12-month-old L2-IL1B-FXR^{-/-} compared to L2-IL1B mice (Fig.12), supporting the concept of the formation of a pro-inflammatory microenvironment in BE tissue upon knockout of FXR.

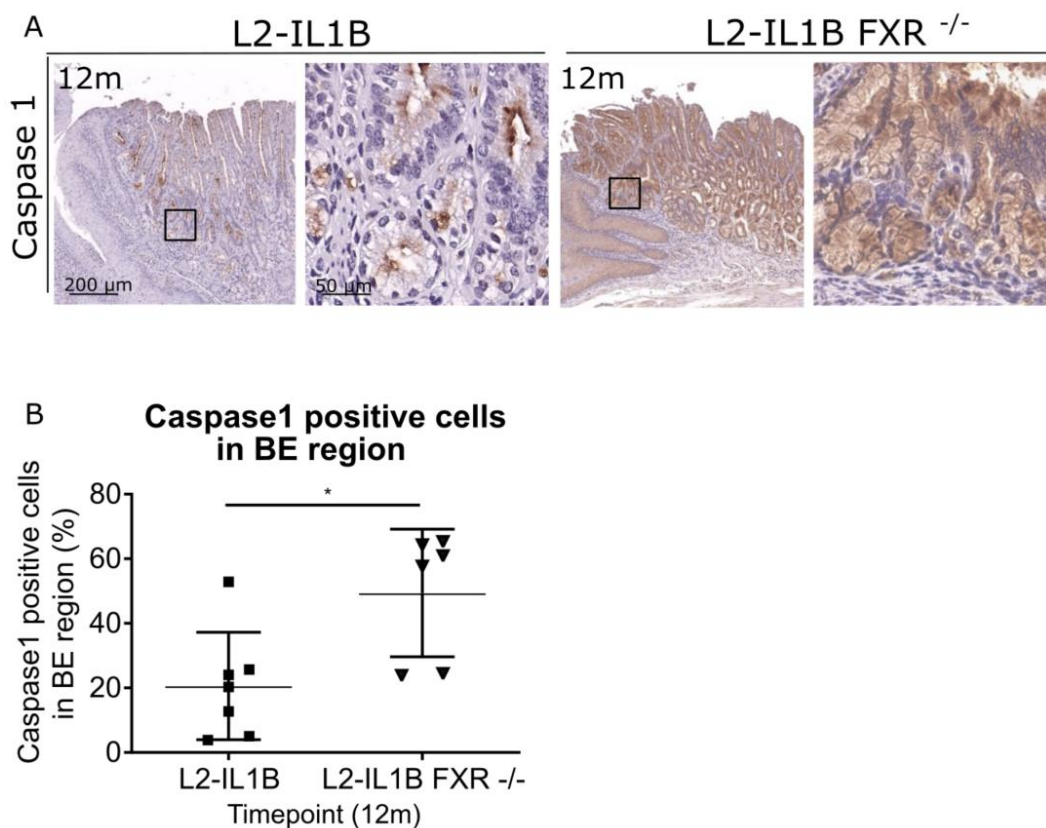


Figure 12: Caspase1 expression increases in L2-IL1B-FXR^{-/-} compared to L2-IL1B mice (A) Representative Caspase 1 immunohistochemistry in the cardia region of 12m old L2-IL1B and L2-IL1B-FXR^{-/-} mice. Bars 200 μM and 50 μM. **(B)** The percentage of Caspase 1 positive cells is significantly higher in 12m old L2-IL1B-FXR mice compared to L2-IL1B mice (p=0.0157). Data are presented as mean with SD. For statistical evaluation of **(B)** an unpaired two-tailed t-test was used.

3.1.6. Knockout of FXR Leads to Increased DNA Damage in L2-IL1B Mice

In 2019, Fu et al. showed that endogenous and dietary factors antagonizing FXR caused increasing cancer stem cell proliferation and DNA damage in a mouse model for intestinal cancer²¹⁸. To examine the appearance of DNA damage in L2-IL1B-FXR^{-/-} mice in comparison to L2-IL1B controls, we analyzed immunohistochemistry for γ -H2AX, a form of H2A histone family member X (H2AX) that forms when double strand breaks in the DNA occur due to induction of DNA damage. The percentage of γ -H2AX positive cells in the BE region significantly increased in 12-month-old L2-IL1B-FXR^{-/-} compared to L2-IL1B mice (Fig.13), while no significant changes could be detected in 6- and 9-month-old mice (Supplementary Fig.6), indicating that FXR knockout leads to loss of protection against DNA damage as induced by microbial or endogenous triggers such as increased bile acid levels.

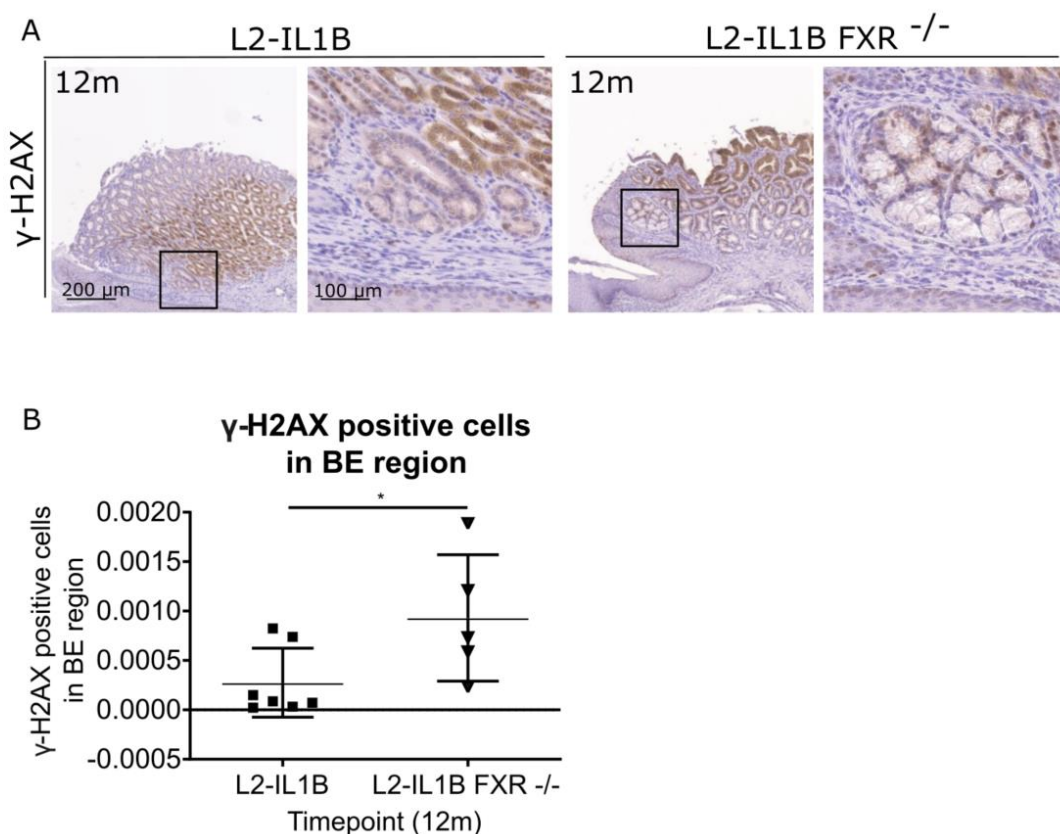


Figure 13: γ -H2AX expression increases in L2-IL1B-FXR^{-/-} compared to L2-IL1B mice (A) Representative γ -H2AX immunohistochemistry of cardia tissue of L2-IL1B and L2-IL1B-FXR^{-/-} mice at 12 months. Bars 200 μ m and 100 μ m. **(B)** The amount of γ -H2AX positive cells is significantly elevated in 12m old L2-IL1B-FXR^{-/-} mice compared to L2-IL1B mice ($p=0.0442$). Data are presented as mean with SD. For statistical evaluation of **(B)** an unpaired two-tailed t-test was used.

3.1.7. Knockout of FXR Causes Increasing Lgr5+ Stem Cell Numbers in L2-IL1B Mice

In 2019, Fu et al. showed that besides increasing DNA damage, antagonizing FXR also increased cancer stem cell proliferation in a mouse model for intestinal cancer²¹⁸. Therefore, we performed and analyzed in-situ hybridization for Lgr5, an intestinal stem cell marker also expressed on stem cells in Barrett's metaplasia, on PFPE slides of 12-month-old L2-IL1B-FXR^{-/-} and L2-IL1B mice (Fig.14 A). The percentage of Lgr5 positive cells in the BE region significantly increased in 12-month-old L2-IL1B-FXR^{-/-} compared to L2-IL1B mice (Fig.14 B). Lgr5 stem cell numbers are associated with accelerated disease progression in the L2-IL1B mouse model²⁷⁰.

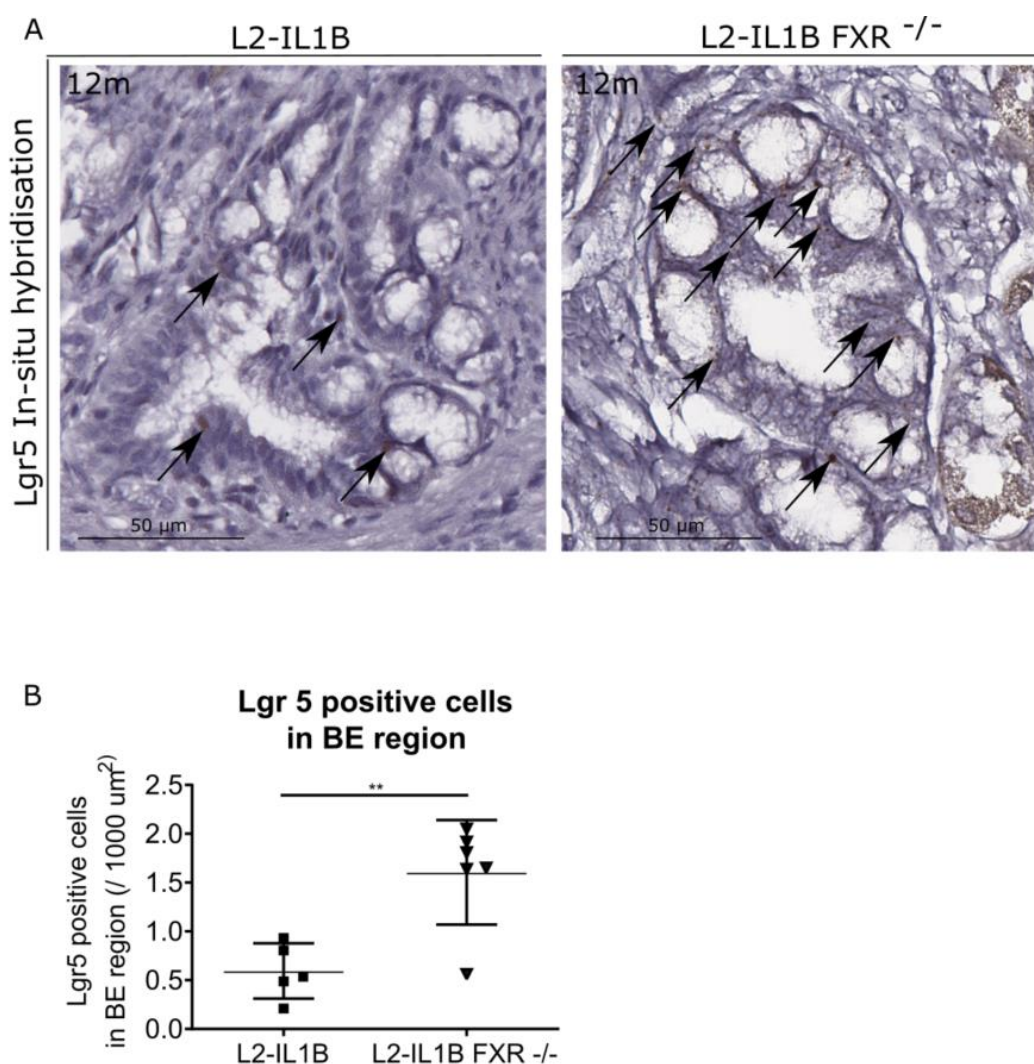


Figure 14: Lgr5 expression increases in L2-IL1B-FXR^{-/-} compared to L2-IL1B mice (A) Lgr5-In-situ-hybridization of the cardia region of 12m old L2-IL1B mice shows expression of Lgr5. Bars 50 μM. **(B)** The number of Lgr5 positive cells is significantly higher in 12m old L2-IL1B-FXR^{-/-} compared to L2-IL1B mice (p=0.0043). Data are presented as mean with SD. For statistical evaluation of **(B)** an unpaired two-tailed t-test was used.

3.1.8. The L2-IL1B Mouse Model Harbors Lgr5 FXR Double Positive Cells

The findings of Fu et al. indicated a regulation of Lgr5 expression and cancer stem cell proliferation via FXR²¹⁸. We therefore performed and analyzed in-situ hybridization for FXR and Lgr5 on serial sections of L2-IL1B mice compared to L2-IL1B-FXR^{-/-} mice. As expected, FXR was not expressed in L2-IL1B-FXR^{-/-} mice. In L2-IL1B mice, we could detect coexpression of FXR and Lgr5 in a subset of cells (Fig.15 A- C).

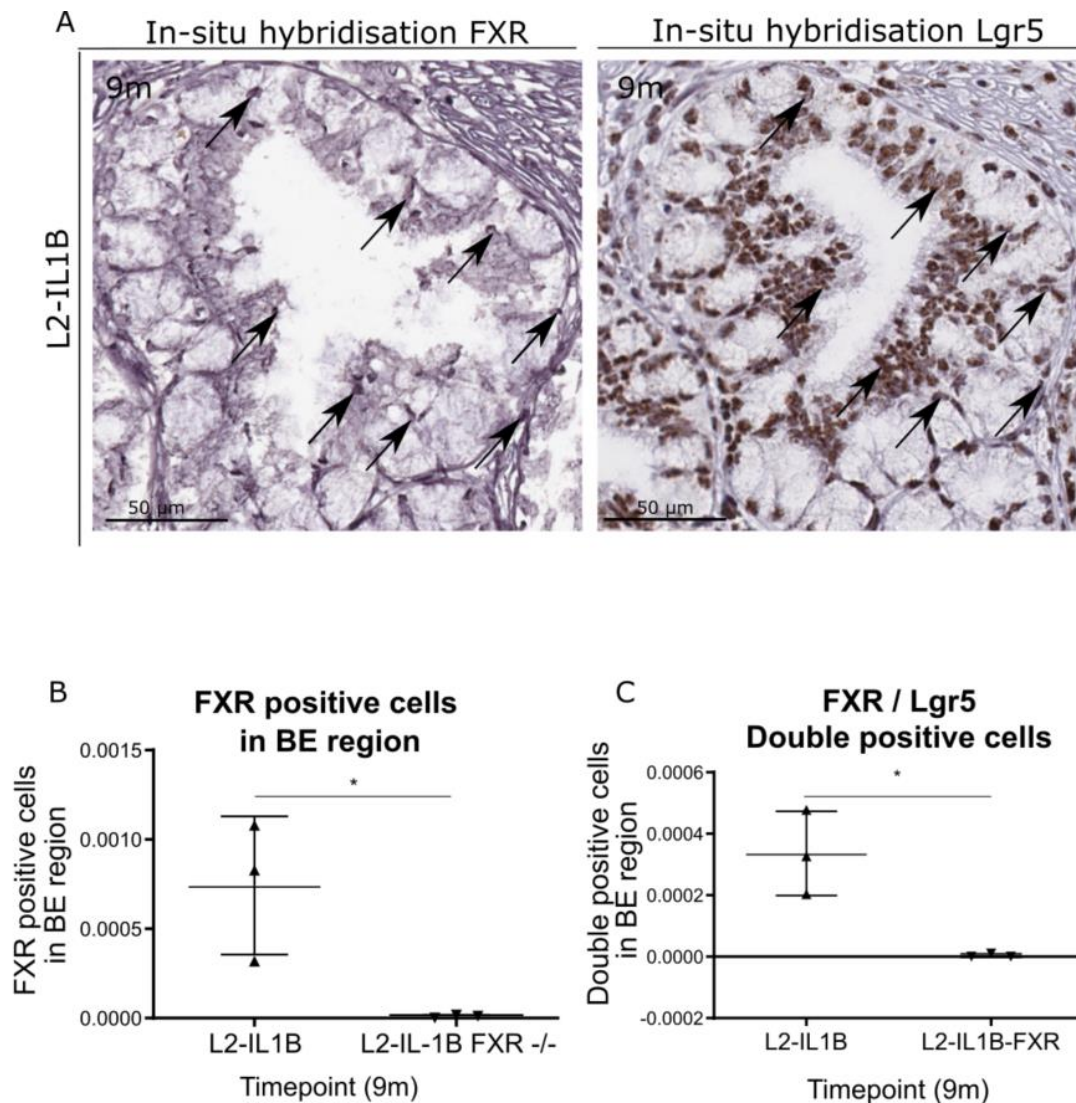


Figure 15: FXR and Lgr5-In-situ-hybridization on serial sections of cardia tissue shows coexpression of both markers in L2-IL1B mice (A) Lgr5-In-situ-hybridization of the cardia region of 9m old L2-IL1B mice shows co-expression of FXR and Lgr5. Bars 50 μ M. **(B)** The number of FXR positive cells is significantly higher in 9m old L2-IL1B-FXR^{-/-} compared to L2-IL1B mice ($p=0.0304$). **(C)** FXR/Lgr5 double-positive cells can be detected in serial sections of L2-IL1B mice. The number of FXR/Lgr5 double-positive cells is significantly higher in L2-IL1B mice as in L2-IL1B-FXR^{-/-} mice ($p=0.0137$), as in the FXR knockout, FXR is not expressed. Data are presented as mean with SD. For statistical evaluation of **(B, C)** unpaired two-tailed t-tests were used.

3.1.9. Knockout of FXR does not Influence Proliferation in L2-IL1B Mice

In models for intestinal or hepatic cancer, modulation of FXR expression regulates cellular proliferation. In general, proliferation of epithelial or carcinoma cells was shown to increase with loss of FXR expression²⁷⁶⁻²⁷⁸. In the L2-IL1B mouse model, we assessed proliferation rates via Ki67 IHC (Fig.16 A). Interestingly, we did not detect significant changes in cellular proliferation in the BE region upon loss of FXR at any timepoint (Fig.16 B), indicating that the main characteristics of loss of FXR in the SCJ tissue are not based on changes in proliferation in general but rather on Lgr5 stem cell expansion in the tissue.

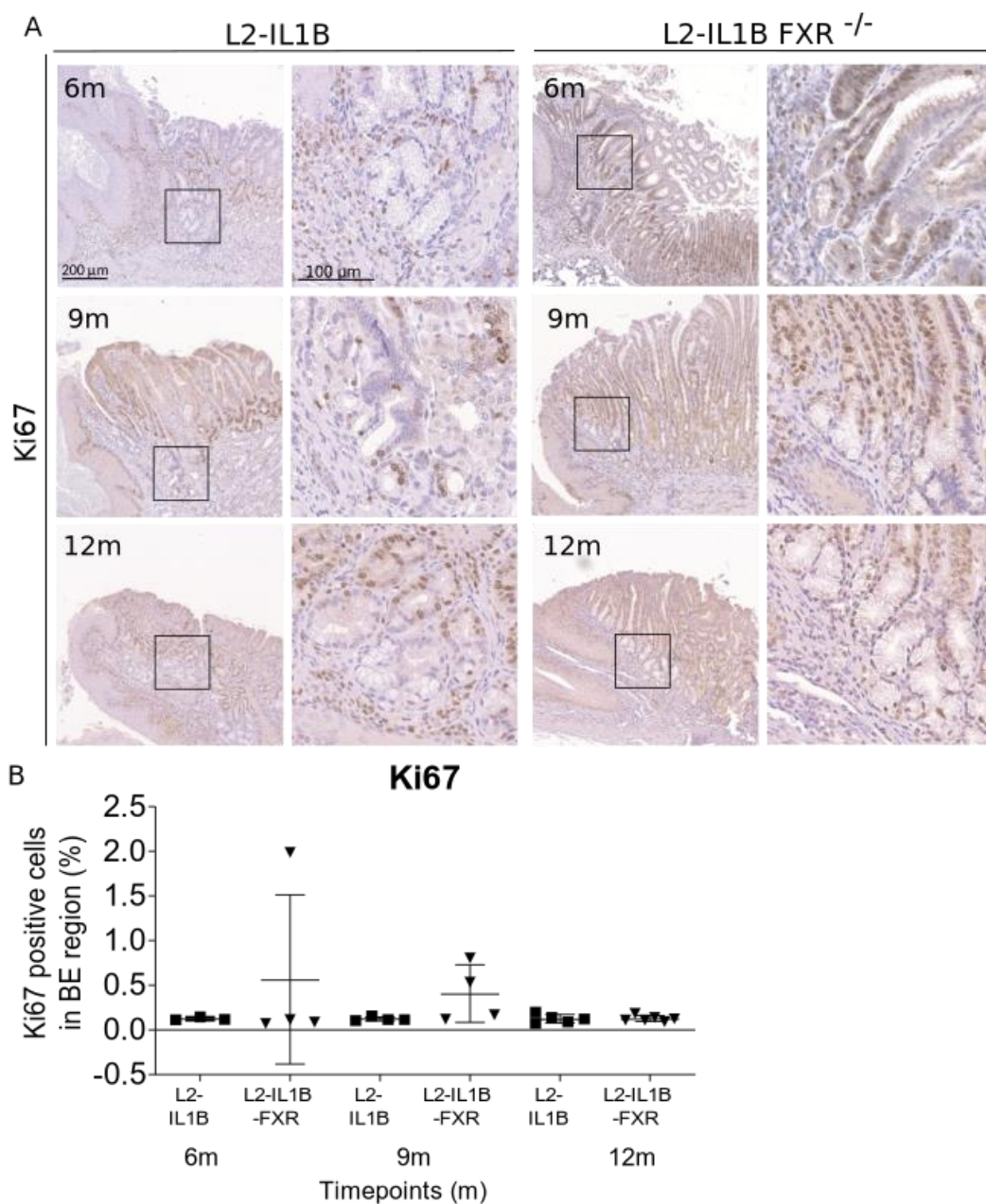


Figure 16: Ki67 expression does not change between L2-IL1B and L2-IL1B-FXR^{-/-} mice (A) Representative Ki67 immunohistochemistry of cardia tissue of L2-IL1B and L2-IL1B-FXR^{-/-} mice at 6,9 and 12 months. Bars 200 μ m and 100 μ m. **(B)** The amount of Ki67 positive cells does not differ significantly between L2-IL1B and L2-IL1B-FXR^{-/-} mice at any assessed timepoint.

3.1.10. Knockout of FXR does not Influence TGR5 Expression in L2-IL1B Mice

Besides FXR, regulation of energy metabolism and other downstream signaling pathways by bile acids is mainly mediated via the G protein coupled receptor 1 (GPBAR1), also known as Takeda G protein-coupled receptor 5 (TGR5). The existence of a dual FXR/TGR5 receptor agonist (INT-767) shows that both receptors can be activated by the same ligands²⁷⁹. To examine potential compensation of signaling by upregulation of TGR5 expression upon loss of FXR, we assessed TGR5 levels in the SCJ tissue of L2-IL1B mice compared to L2-IL1B-FXR^{-/-} mice by analyzing IHC for TGR5 (Fig.17). TGR5 was expressed in the tissue of both L2-IL1B and L2-IL1B-FXR^{-/-} mice, even at a high age with advanced disease state. We could therefore exclude the possibility of compensation of loss of FXR signaling via deregulation of TGR5 expression.

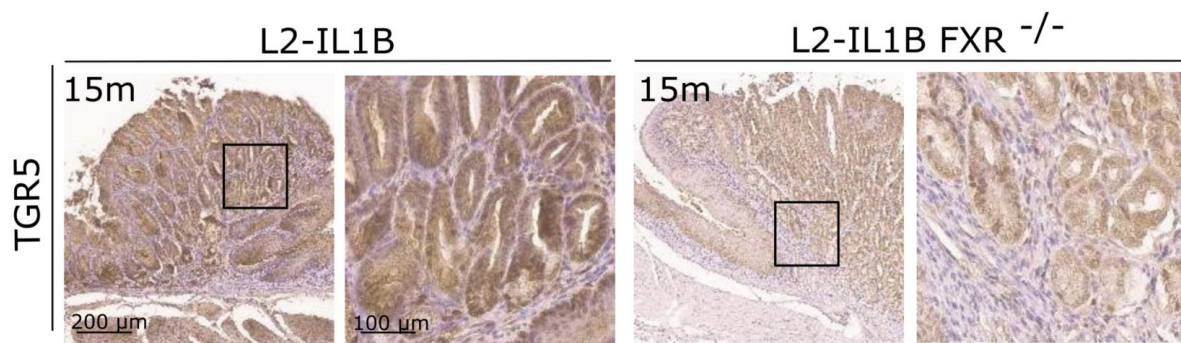


Figure 17: TGR5 expression does not change between L2-IL1B and L2-IL1B-FXR^{-/-} mice Representative TGR5 immunohistochemistry of cardia tissue of L2-IL1B and L2-IL1B-FXR^{-/-} mice at an advanced disease stage at 15months. Do differences in TGR5 expression can be detected between L2-IL1B and L2-IL1B-FXR^{-/-} mice. Bars 200 µM and 100 µM

3.1.11. Knockout of FXR in the L2-IL1B Mouse Model Induces Changes in the SCJ Tissue on RNA Level

Whole-body knockout of FXR in the L2-IL1B mouse model caused aggravation of the dysplastic phenotype at an advanced age, along with severe changes in the phenotype. Loss of FXR at the SCJ led to formation of a more pro-inflammatory and pro-tumorigenic tissue microenvironment along with increasing Lgr5 stem cell numbers while interestingly cellular proliferation in general was not affected. To improve the understanding of the mechanisms underlying the phenotypic aggravation in L2-IL1B-FXR^{-/-} compared to L2-IL1B mice, the transcriptional profile of the mice was evaluated by carrying out microarray analysis of the SCJ tissue of the mice.

Microarray analysis (Affymetrix array) was performed using tissue from the cardia region of 12-month-old L2-IL1B-FXR^{-/-} and L2-IL1B mice, containing typical metaplastic and dysplastic nodes. Initial data processing was carried out by project collaborator and bioinformatician Dr. Richard Friedman (Columbia University, NY, USA). Data sets were further analyzed by gene-set enrichment analysis (GSEA) via the web-based analysis tool offered by UC San Diego and the Broad Institute (www.gsea-msigdb.org) or by filtering for single significantly related genes. Significantly differential gene expression between genotypes was defined as Fold Change (FC) <0.65 and >1.5 with a p-value of ≤0.05. After excluding duplicates, a total of 1362 genes were found to be differentially regulated in L2-IL1B-FXR^{-/-} compared to L2-IL1B mice. A total of 964 genes were upregulated, and 400 genes were downregulated in FXR knockout mice according to microarray analysis (Fig.18). The constant region of the heavy chain of IgM (*IGHM*) gene occurred as both significantly up and downregulated, indicating that potentially different genetic regions of the gene might be differentially expressed.

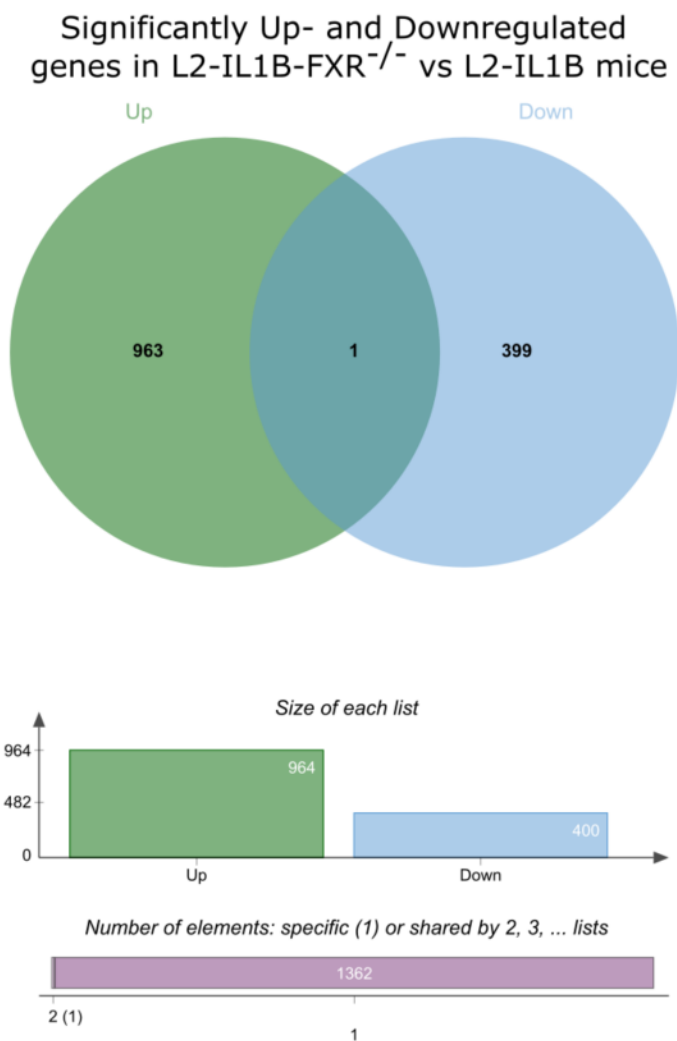
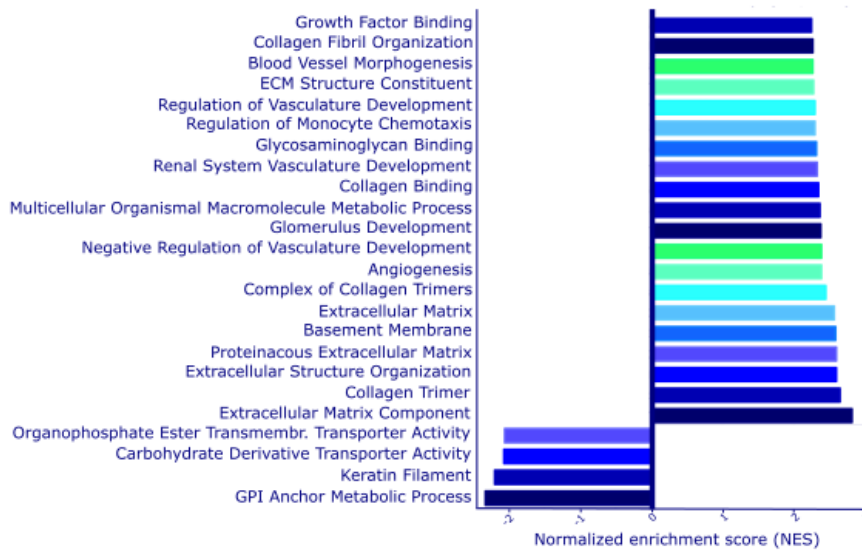


Figure 18: Venn-diagram comparing significantly up- and downregulated annotatable genes in L2-IL1B-FXR^{-/-} compared to L2-IL1B mice. The cutoff was set at Fold Change (FC) <0.65 and >1.5 with a p-value of ≤0.05. Duplicates were excluded. Visualization was realized using the web-based jVenn tool²⁸⁰

GSEA of gene ontology (GO) gene sets (Fig.19 A) was predominated by pathways involved in tissue microenvironment specific changes (Extracellular Matrix, basement membrane, vasculature reorganization and development pathways, collagen fibril organization and binding etc.). Changes in the tissue microenvironment related to tissue reorganization were already detected in histologic analysis. Histologically, the tissue microenvironment of L2-IL1B-FXR^{-/-} mice had proinflammatory properties, and the tissue was found to be more dedifferentiated and fibrotic than in L2-IL1B mice. The enriched gene sets mirrored these findings.

A

GO gene sets enriched in L2-IL1B-FXR vs L2-IL1B mice
(FDR q-value <0.05)



B

Hallmark gene sets enriched in L2-IL1B-FXR vs L2-IL1B mice
(FDR q-value <0.05)

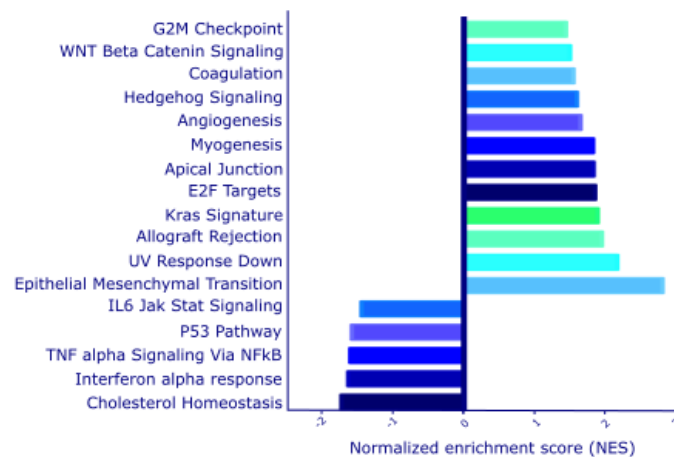


Figure 19: Significantly enriched (A) Gene Ontology and (B) Hallmark gene sets in L2-IL1B-FXR^{-/-} compared to L2-IL1B mice in a tissue microarray of cardia tumor tissue. Data are sorted according to Normalized Enrichment Scores (NES) (Significance cutoff FDR q-value < 0.05)

Table 20 shows significantly regulated single genes associated to changes in the tissue microenvironment. The gene sets and single genes found to be regulated in the tissue microarray support the findings of the histologic analysis of the tissue.

Table 20: Significantly regulated genes in BE tissue of L2-IL1B-FXR^{-/-} compared to L2-IL1B mice, detected by microarray analysis. The Table shows manually assorted genes associated to changes in the tissue microenvironment as detected by histologic analysis.

L2-IL1B-FXR ^{-/-} vs L2-IL1B				
	Symbol	Description	FC	p-value
ECM remodeling	Col1a1	Collagen, type I, alpha 1	3.82	0.00
	Col3a1	Collagen, type III, alpha 1	2.94	0.00
	Fn1	Fibronectin 1	3.72	0.00
	Mmp2	Matrix metalloproteinase 2	2.09	0.00
	Mmp3	Matrix metalloproteinase 3	2.91	0.00
	Mmp10	Matrix metalloproteinase 10	1.74	0.03
	Mmp17	Matrix metalloproteinase 17	1.60	0.04
	Mmp13	Matrix metalloproteinase 13	2.33	0.01
	Mmp19	Matrix metalloproteinase 19	1.62	0.01
	Timp2	Tissue inhibitor of metalloproteinase 2	1.53	0.01
	Timp3	Tissue inhibitor of metalloproteinase 3	3.54	0.00
Fibrosis associated	Ctgf	Connective tissue growth factor	1.98	0.00
	Snai2	Snail family zinc finger 2	1.63	0.01
	Tgfb2	Transforming growth factor, beta 2	1.53	0.00
	Tgfb3	Transforming growth factor, beta 3	1.58	0.01
	Tgfb3	Transforming growth factor, beta receptor III	3.50	0.00
	Tgfb1	Transforming growth factor, beta induced	2.07	0.00
	Tgfb1i1	Transforming growth factor beta 1 induced transcript 1	2.70	0.00
Mesenchymal cell markers	Col1a1	Collagen, type I, alpha 1	3.82	0.00
	Cdh2	Cadherin 2	1.72	0.05
	Vim	Vimentin	2.47	0.00
ER stress	Casp12	Caspase 12	2.06	0.00

GSEA of hallmark gene sets (Fig. 19 B) also showed deregulation of signaling pathways related to the detected changes in the tissue microenvironment (Epithelial Mesenchymal Transition, EMT; Myogenesis; Angiogenesis etc.). Additionally, different signaling pathway gene sets were deregulated in L2-IL1B-FXR^{-/-} compared to L2-IL1B mice. While hallmark gene sets for Kras signaling, Hedgehog- and Wnt- β -catenin signaling and of E2F targets, and G2M checkpoint were enriched in FXR knockout mice, IL6-Jak-Stat signaling, p53, NF κ B and Interferon- α response were downregulated.

Table 21 shows manually assorted, significantly regulated genes of the Wnt, Hedgehog and also Notch signaling pathway in FXR knockout compared to L2-IL1B mice. The three signaling pathways are important in development and embryogenesis and are often deregulated during carcinogenesis. In all three pathways, the majority of associated genes was enriched in L2-IL1B-FXR^{-/-} compared to L2-IL1B mice, indicating pathway activation. Especially concerning Hedgehog and Notch signaling, mainly positive regulators and genes associated to activated signaling were enriched in FXR knockout mice, while in the Wnt signaling pathway, the complexity of differentially regulated genes did not allow to draw conclusions about the exact consequences and the extent of the impact of Wnt pathway deregulation in L2-IL1B-FXR^{-/-} mice without further investigation.

Table 21: Significantly regulated genes in BE tissue of L2-IL1B-FXR^{-/-} compared to L2-IL1B mice, detected by microarray analysis. The Table shows manually assorted genes associated to changes in Wnt, Notch and Hedgehog signaling

L2-IL1B-FXR ^{-/-} vs L2-IL1B				
	Symbol	Description	FC	p-value
WNT signaling upregulated genes	Cdh11	Cadherin 11	1.93	0.00
	Cdh2	Cadherin 12	1.72	0.05
	Cdh5	Cadherin 5	3.65	0.00
	Dchs1	Dachsous Cadherin-Related 1	2.15	0.00
	Dkk2	Dickkopf WNT Signaling Pathway Inhibitor 2	1.88	0.02
	Frzb	Frizzled Related Protein	1.63	0.03
	Fzd2	Frizzled Class Receptor 2	2.29	0.02
	Gnao1	G Protein Subunit Alpha O1	2.90	0.01
	Gnb4	G Protein Subunit Beta 4	2.31	0.01
	Gng2	G Protein Subunit Gamma 2	1.52	0.03
	Gng3	G Protein Subunit Gamma 3	1.94	0.02
	Plcb1	Phospholipase C Beta 1	2.05	0.00
	Plcb4	Phospholipase C Beta 4	1.52	0.05
	Prkcb	Protein Kinase C Beta	1.58	0.02
	Prkce	Protein Kinase C Epsilon	1.50	0.03
	Prkd3	Protein Kinase D3	1.55	0.00
	Pygo1	Pygopus Family PHD Finger 1	1.71	0.01
Tcf21	Transcription Factor 21	2.16	0.00	
Vim	Vimentin	2.47	0.00	
Zeb1	Zinc Finger E-Box Binding Homeobox 1	1.96	0.01	
WNT signaling downregulated genes	Cldn1	Claudin 1	0.53	0.05
	Fosl1	FOS Like 1, AP-1 Transcription Factor Subunit	0.37	0.02
	Plaur	Plasminogen Activator, Urokinase Receptor	0.34	0.02
	Plcd3	Phospholipase C Delta 3	0.57	0.00
	Ptgs2	Prostaglandin-Endoperoxide Synthase 2	0.65	0.02
	Tcf23	Transcription Factor 23	0.64	0.04
	Ubb	Ubiquitin B	0.55	0.00
	Wnt11	Wnt Family Member 11	0.63	0.02
Notch signaling upregulated genes	Dner	Delta/Notch Like EGF Repeat Containing	1.64	0.04
	Dnm1	Dynamin 1	1.55	0.04
	Dnm3	Dynamin 3	1.68	0.01
	Hey1	Hes Related Family BHLH Transcr. Factor With YRPW Motif 1	1.67	0.02
	Hey2	Hes Related Family BHLH Transcr. Factor With YRPW Motif 2	1.92	0.03
	Mfap2	Microfibril Associated Protein 2	1.53	0.02
	Mfap5	Microfibril Associated Protein 5	2.01	0.00
	Ntn1	Netrin 1	1.62	0.00
	Pik3cd	Phosphatidylinositol-4,5-Bisphosphate 3-Kinase Catalytic Subunit Delta	1.51	0.05
Thbs2	Thrombospondin 2	6.57	0.00	
Notch signaling downregulated genes	Epn3	Epsin 3	0.61	0.00
	Notch4	Notch Receptor 4	0.67	0.01
Hedgehog signaling upregulated genes	Boc	BOC Cell Adhesion Associated, Oncogene Regulated	1.51	0.04
	Disp2	Dispatched RND Transporter Family Member 2	1.88	0.05
	Evc	EvC Ciliary Complex Subunit 1	1.85	0.01
	Gas1	Growth Arrest Specific 1	1.88	0.03
	Gli3	GLI Family Zinc Finger 3	2.14	0.00
	Gng2	G Protein Subunit Gamma 2	1.52	0.03
	Hhip	Hedgehog Interacting Protein	4.32	0.00
Hedgehog signaling downregulated genes	Sox18	SRY-Box Transcription Factor 18	2.64	0.00

Figure 20 depicts additional gene sets which were significantly enriched either in L2-IL1B or in L2-IL1B-FXR^{-/-} mice and support previous histologically determined findings in L2-IL1B-FXR^{-/-} mice. There were different highly significantly enriched gene sets for tissue microenvironmental changes, loss of epithelial differentiation and acceleration of the phenotype in L2-IL1B-FXR^{-/-} mice (Fig.20 A). We also found an enrichment of stem cell related pathways in FXR knockout mice, proving increasing stemness of the tissue (Fig.20 B). Additionally, we found cholesterol homeostasis to be deregulated in L2-IL1B-FXR^{-/-} mice (Fig.20 C). As the nuclear bile acid receptor FXR regulates bile acid homeostasis and cholesterol is the chemical precursor for bile acid synthesis, a deregulation of cholesterol and bile acid homeostasis is an expected result of FXR knockout in L2-IL1B mice.

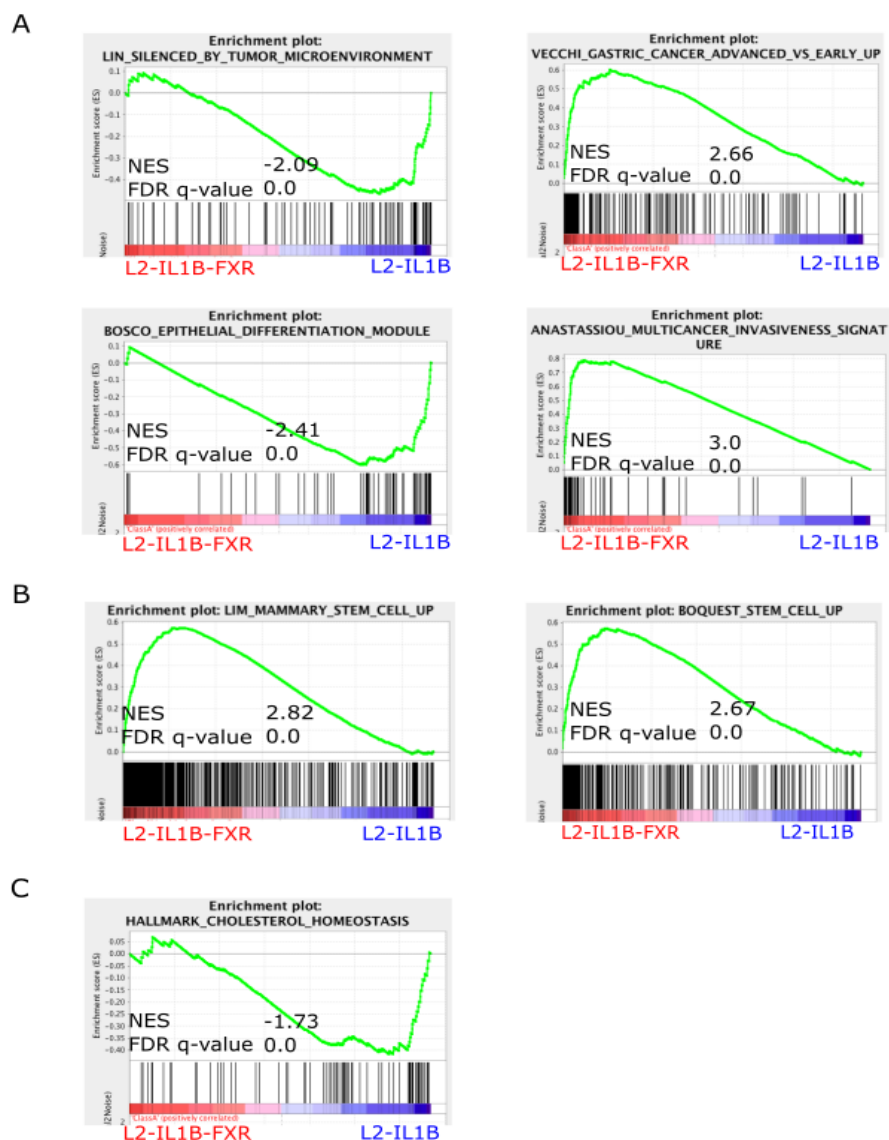


Figure 20: Selected GSEA enrichment plots showing (A) changes in tissue microenvironment, differentiation, and accelerated disease progression (B) increased stemness and (C) deregulation of cholesterol homeostasis in L2-IL1B-FXR^{-/-} compared to L2-IL1B mice

3.1.12. The Serum Bile Acid Pool of L2-IL1B Mice Changes in Response to FXR Knockout

Bile acid homeostasis and de-novo synthesis are regulated by FXR activation via a negative feedback loop involving suppression of Cyp7A1 via SHP. After supporting lipid digestion in the gut, bile acids enter blood circulation to undergo enterohepatic circulation via reuptake through the gut mucosa. As it is plausible that bile acids can also be traced in systemic blood circulation, we expected to be able to detect bile acids in the serum of L2-IL1B mice. We also suspected FXR knockout to have an impact on serum bile acid levels in the mice. Therefore, we performed untargeted and targeted metabolomic analyses of the serum of L2-IL1B and L2-IL1B-FXR^{-/-} mice. We detected a clear separation between serum metabolic profiles of L2-IL1B and L2-IL1B-FXR^{-/-} mice (Fig.21 A). Concerning bile acid levels, especially TCA levels were elevated in the serum of L2-IL1B-FXR^{-/-} mice (Fig.21 B).

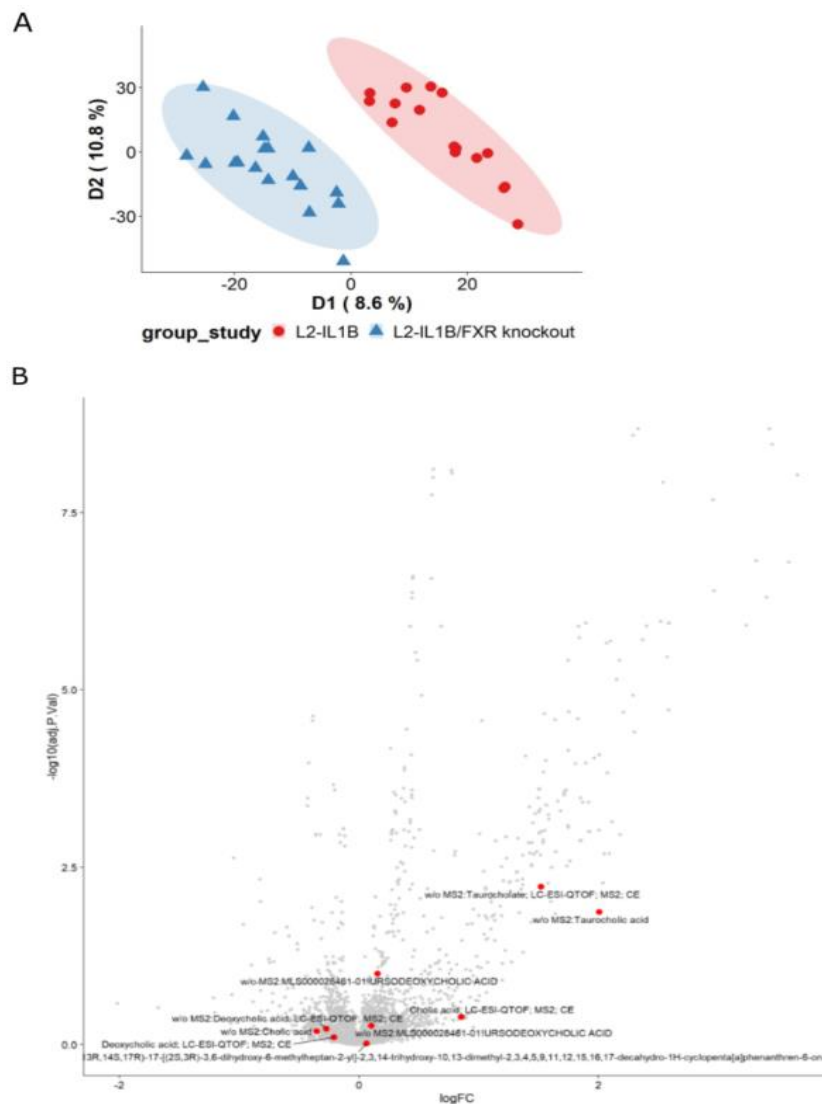


Figure 21: Untargeted metabolomic analysis of the Serum of L2-IL1B-FXR^{-/-} compared to L2-IL1B mice. (A) Supervised PLS-DA analysis shows a clear separation between the metabolic profiles of both groups **(B)** Volcano plot of all metabolites with bile acids marked in red. taurocholic acid and taurochenodeoxycholic acid are significantly enriched in FXR knockout mice compared to controls.

Targeted metabolomic analyses, specifically detecting bile acids in the serum, showed highly significant increases of TCA in the serum of L2-IL1B-FXR^{-/-} mice compared to L2-IL1B controls in conformity with the untargeted analysis results (Fig.22 A). Additionally, also dehydrocholic acid (DHCA) levels increased significantly in the serum of FXR knockout mice, while the amounts of the secondary bile acids LCA, HDCA and UDCA decreased (Fig.22 A). Evaluation of the tissue microarray showed a significant decrease of Cyp27A1 expression, together with an increase in Cyp7B1 gene expression in tumor tissue of L2-IL1B-FXR^{-/-} compared to L2-IL1B mice. Cyp27A1 and Cyp7B1 are the main enzymes involved in the alternative bile acid synthesis pathway.

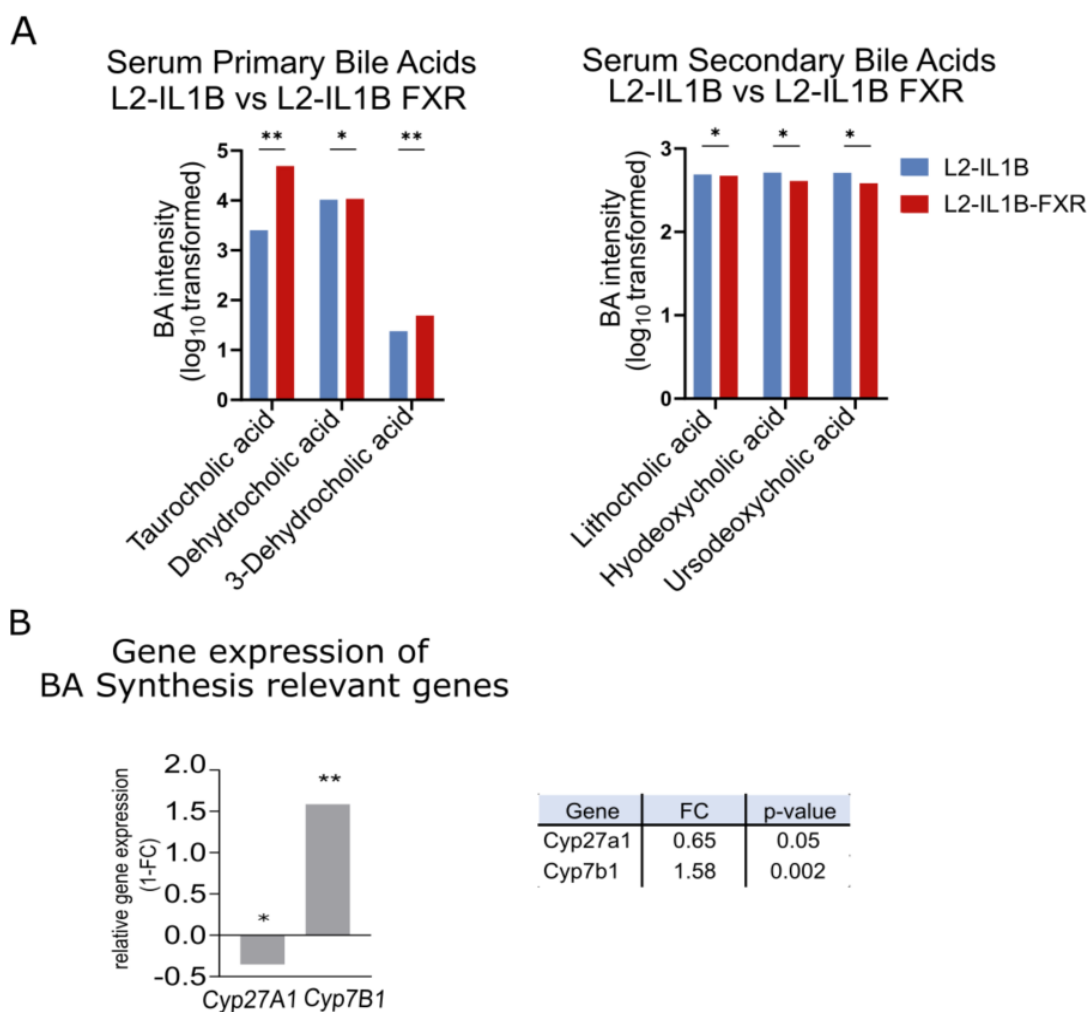


Figure 22: Targeted metabolomic and microarray gene expression analyses of the serum of L2-IL1B and L2-IL1B-FXR^{-/-} mice show a deregulation of the Serum BA profile and BA metabolism upon loss of FXR **(A)** log₁₀ transformed single primary and secondary bile acid intensities in the serum of L2-IL1B mice compared to L2-IL1B-FXR mice shows deregulation of different bile acids, with higher levels of Taurocholic acid (p=0.0010), 3-Dehydrocholic acid (p=0.0084) and Dehydrocholic acid (p=0.0149) and lower levels of Lithocholic acid (p=0.0264), Hyodeoxycholic acid (p=0.0298) and Ursodeoxycholic acid (p=0.0310). **(B)** Microarray analysis from L2-IL1B and L2-IL1B-FXR mice shows significantly decreased expression of Cyp27A1, the rate-limiting enzyme of the alternative bile acid synthesis pathway and, most likely due to feedback regulation upon loss of Cyp27A1 a significantly increase in Cyp7B1 expression, with Cyp7B1 being a bile acid converting enzyme downstream of Cyp27A1 (Cyp27A1 p=0.05; Cyp7B1 p=0.002) (cardia tissue microarray; n=3).

3.2. Impact of a High-Fat-Diet on the Bile Acid Modulating Microbiome and BA Levels of the L2-IL1B Mouse Model

We could recently show that treatment of L2-IL1B mice with HFD alters the gut microbiome of the mice, which together with increasing systemic inflammation leads to accelerated disease progression²⁷⁰. We performed targeted metabolomic analyses for BA in the feces of the mice and reanalyzed the fecal microbiome on zOTU level with focus on BA and BA-modulating bacteria. To further investigate the effect of HFD on L2-IL1B mice, we treated additional mouse cohorts with CD or HFD from two until 6 or 9 months of age and performed untargeted and targeted cecal and fecal as well as targeted serum and tissue BA analyses.

3.2.1. Treatment with HFD Changes the Fecal Metabolome of L2-IL1B Mice

To evaluate the fecal BA profile of the mouse cohorts, targeted BA metabolomic analyses were performed. Comparing HFD mice to chow diet mice, we found fecal primary, secondary, and total BA levels to be significantly increased (Fig.23 A). In detail, the levels of the primary BA alpha and beta-muricholic acid and the secondary BA DCA as well as HDCA and MDCA were significantly increased in HFD mice compared to chow (Fig.23 B). When comparing HFD to CD mice, we also found the primary BA alpha-muricholic and additionally 12-dehydrocholic acid (12-DHCA) and taurochenodeoxycholic acid (TCDCA) and the secondary BA LCA, allo- and iso-lithocholic (ALCA, ILCA) acid and TDCA to be significantly enriched in the feces of HFD mice (Fig.23 C). In PLS-DA analyses of the fecal BA profile measured by targeted BA metabolomic analyses, HFD clustered significantly different from both chow and CD (Fig.23 D, G), and showed a distinct BA profile (Fig.23 E, H). When comparing the main correlating BA in HFD compared to chow and CD, MCAs, taurine-conjugated BA, and secondary DCA and LCA as well as their derivatives appeared to be the main separators between groups (Fig.23 F, I).

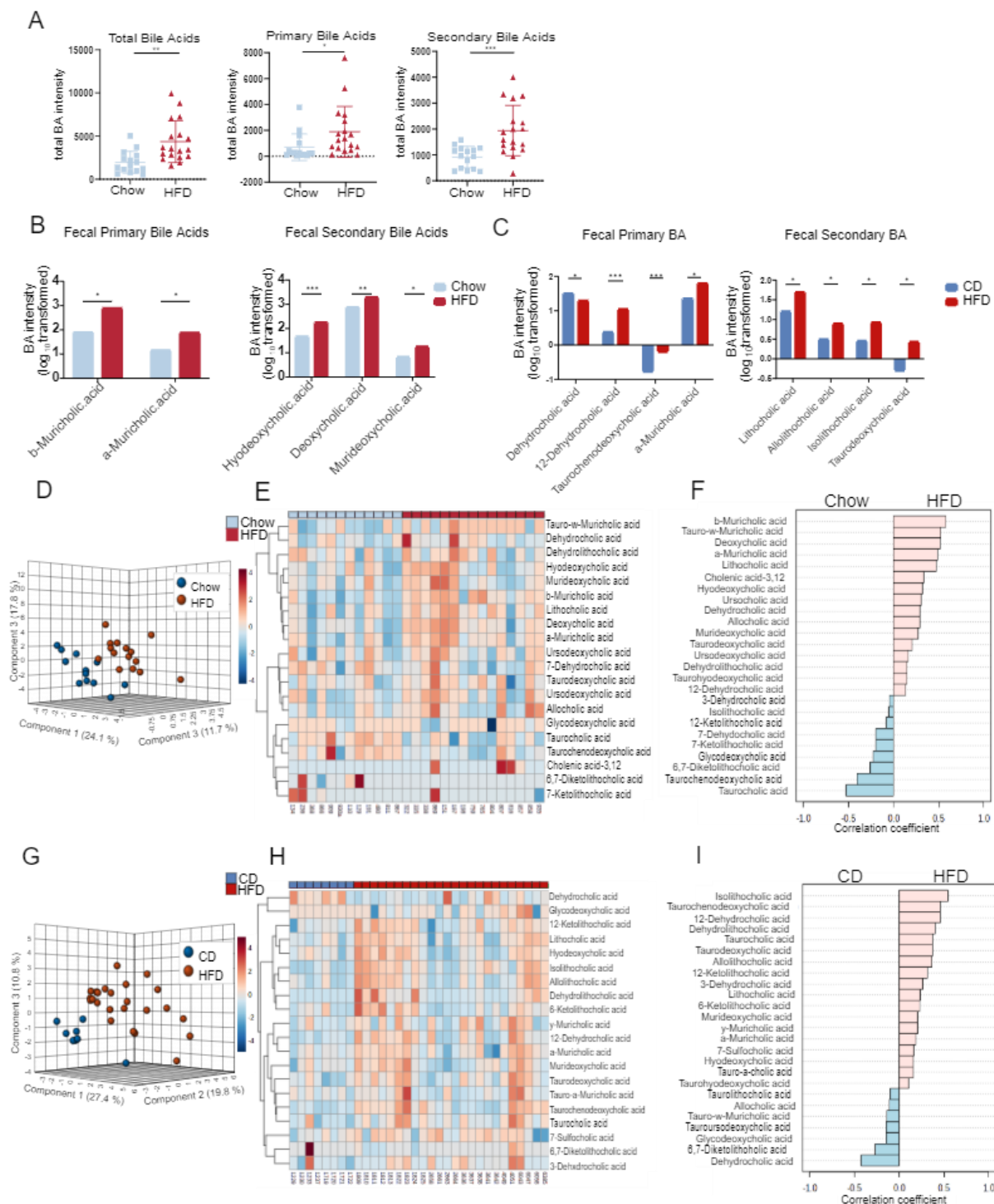


Figure 23: Targeted metabolomic analyses of fecal BA levels in L2-IL1B mice fed chow, CD and HFD show distinct BA profiles between diets, with significantly increased fecal BA levels in HFD mice. (A) Absolute intensities of primary, secondary, and total bile acid levels are increasing in the feces of L2-IL1B mice fed HFD compared to regular chow diet (mice of all timepoints combined; chow n=15; HFD n=17; primary BA p=0.0426; secondary BA p=0.0007; total BA p=0.0016). (B) log₁₀ transformed single bile acid intensities in the feces of L2-IL1B mice fed HFD are increasing compared to mice fed chow diet (comparison of 9-month-old L2-IL1B mice on chow (n=6) or HFD (n=4); beta-muricholic acid p=0.0137; alpha-muricholic acid p=0.0197; hyodeoxycholic acid p=0.0009; deoxycholic acid (DCA) p=0.0039; murideoxycholic acid p=0.0356 (C) log₁₀ transformed single bile acid intensities in the feces of L2-IL1B mice fed HFD are increasing compared to mice fed CD, with only dehydrocholic acid abundance decreasing, for the benefit of increasing abundance of 12-dehydrocholic acid (comparison of 6-9 month old L2-IL1B mice on CD (n=3-8) or HFD (n=20-24) ; dehydrocholic acid (p=0.0239); 12-dehydrocholic acid (p=0.00004); taurochenodeoxycholic acid (p=0.0001); allolithocholic acid (p=0.0195); lithocholic acid (p=0.0217); a-muricholic acid (p=0.0239); taurodeoxycholic acid (p= 0.0357); isolithocholic acid (p=0.0481) (D) Partial least

squares discriminant analysis (PLS-DA) of fecal BA profiles in L2-IL1B mice fed HFD compared to regular chow diet shows a clear separation between chow and HFD treated cohorts (mice of all timepoints combined; chow n=12; HFD n=15). **(E)** Clustering of fecal BAs in L2-IL1B mice fed HFD compared to regular chow diet shown as heatmap. Displayed are the top 20 BAs ranked by t-test (distance measure using euclidean, and clustering algorithm using ward). **(F)** Top 25 BA peaks correlated with L2-IL1B mice fed HFD compared to regular chow diet. **(G)** Partial least squares discriminant analysis (PLS-DA) of fecal BA profiles in L2-IL1B mice fed HFD compared to CD shows a clear separation between CD and HFD treated cohorts (mice of all timepoints combined; chow n=12; HFD n=15). **(H)** Clustering of fecal BAs in L2-IL1B mice fed HFD compared to regular CD shown as heatmap. Displayed are the top25 BAs ranked by t-test (euclidean, distance measure and ward clustering algorithm). **(I)** Top 25 BA peaks correlated with L2-IL1B mice fed HFD compared to CD.

3.2.2. Treatment with HFD Changes the Gut Microbiome of L2-IL1B Mice – with Focus on Bile Acid Modulating Bacteria

We could recently show that treatment of L2-IL1B mice with HFD not only alters the gut microbiome of the mice, but together with increasing systemic inflammation leads to accelerated disease progression²⁷⁰. We re-evaluated the fecal microbiome data from these mice on zOTU level, looking specifically for changes in bacteria with bile acid modulating capacities (Fig. 24 A). We found specific groups of BA modulating bacteria to be differently abundant between different treatment groups. We found a decrease in *Bacteroidota* and an increase in *Firmicutes* as often seen when comparing a HFD with CD. *Clostridia*, the only bacterial class with proven BA 7 α -dehydroxylation and therefore secondary BA production capacities, and the families *Ruminococcaceae* and *Peptostreptococcaceae*, which are capable of BA modulation and were recently suspected to also have strains with 7 α -dehydroxylation properties as a result of computational prediction²⁰⁷ were more abundant in mice fed HFD compared to CD (Fig.24 A). Also, the genus *Blautia* is involved in BA modulation and found to be more abundant in HFD mice (Fig.24 A)²⁸¹. *Clostridia*, but also the families of *Peptostreptococcaceae* and *Lachnospiraceae* and the genus *Blautia*, all involved in BA modulation were positively correlated with dysplasia scores (Fig.24 B). The family of *Ruminococcaceae*, of which certain genera are involved in BA modulation was negatively correlated with dysplasia scores (Fig.24 A). None of the BA modulating genera could be identified to be regulated between disease groups or to be correlated with disease progression, indicating that other genera of the *Ruminococcaceae* family were responsible for this correlation.

3.2.3. Treatment with HFD Causes Enrichment of Bile Acids in the Gut Metabolome of L2-IL1B Mice

To investigate the effect of HFD on the metabolome in L2-IL1B mice more thoroughly, we treated additional mouse cohorts with CD or HFD from two until 6 or 9 months of age and performed untargeted cecal and fecal metabolomic analyses via reverse phase (RP) chromatography and hydrophilic interaction chromatography (HILIC) in negative and positive ionization mode.

Depending on chromatography method and ionization mode, we found different bile acids to be significantly enriched in the cecal content of 6- and 9-month-old mice fed HFD compared to CD. Of note, BA were almost solely enriched in mice treated with HFD in both RP chromatography (Fig.25 A-D) and HILIC (Fig.26. A-D). Mainly MCAs, LCAs and their conjugates but also hydroxycholic acids, DHCAs, different CA derived BA compounds (5 β -Cholic acid-3 α -ol-7-one, 7-KLCA; 5 β -Cholic acid-3 α -ol-7-one, 6-KLCA), CA and its derivatives, CDCA and ursocholic acid (UCA) were enriched in HFD mice (Fig.25, 26). The only exception was glycocholic acid (GCA), which was found to be enriched in 6-month-old CD compared to HFD mice in RP chromatography in the positive ionization mode (Fig.25 B). In RP chromatography of 9-month-old HFD mice, we also found enrichment of palmitic acid, the main fatty acid compound of the diet the mice were treated with (Fig. 25 D). These results showed a general increase of BA pool and levels in the cecal content of mice fed HFD compared to CD mice at both 6 and 9 months of age.

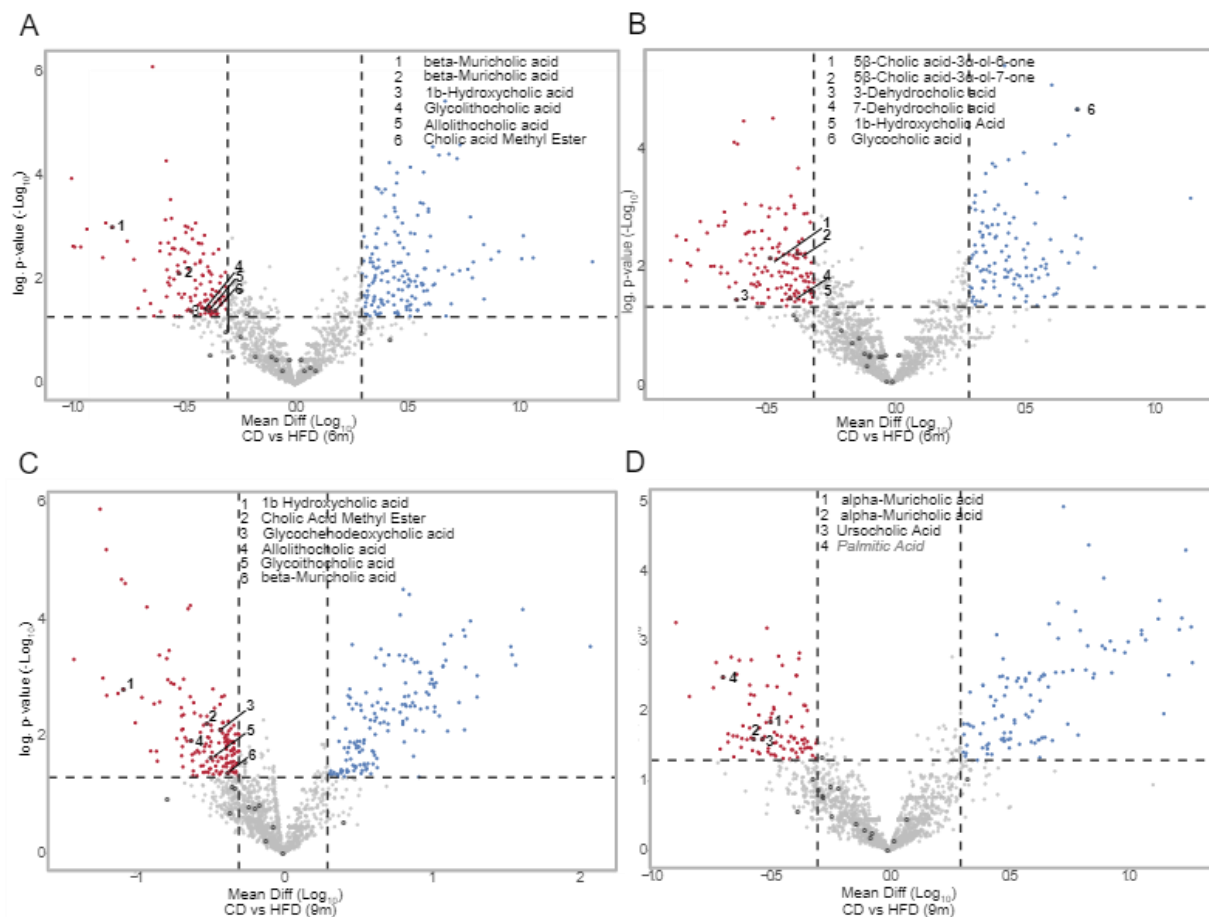


Figure 25: Untargeted metabolomic analysis of cecal content from mice fed CD vs HFD via RP chromatography shows enrichment of BA in the cecal content of HFD mice. For untargeted metabolomic analysis, reversed phase chromatography (RP) was performed in the positive and negative ionization mode. Data is depicted as volcano plots showing metabolites enriched in CD vs HFD fed mice at 6 and 9 months of age, with significantly enriched metabolites ($p \leq 0.05$, Fold Change ≥ 2 ; equals p -value $\log_{10} \geq 1.3$; Meandiff. $\log_{10} \geq 0.3$) being highlighted in red if enriched in HFD and in blue if enriched in CD. Detected bile acid derivatives are marked with circles, significantly enriched BA are numbered. Bile acids are significantly enriched in HFD only, with the exception of glycocholic acid, which is enriched in 6m CD mice. In 9m old HFD mice, also palmitic acid was found to be significantly enriched. **(A)** Significantly enriched BA in 6m L2-IL1B mice fed HFD, reverse phase chromatography in neg. ionization mode: beta-muricholic acid, 1b-hydroxycholic acid, glycolithocholic acid, allolithocholic acid, cholic acid methyl ester. **(B)** Significantly enriched BA in 6m L2-IL1B mice fed HFD, reverse phase chromatography in pos. ionization mode: 5-cholic acid-3-ol-6-one, 5-cholic acid-3-ol-7-one, 3-dehydrocholic acid, 7-dehydrocholic acid, 1b-hydroxycholic acid, glycocholic acid enriched in CD. **(C)** Significantly enriched BA in 9m L2-IL1B mice fed HFD, reverse phase chromatography in neg. ionization mode: hydroxycholic acid derivative, cholic acid derivative, allolithocholic acid, glycolithocholic acid, beta-muricholic acid. **(D)** Significantly enriched BA and SCFA in 9m L2-IL1B mice fed HFD, reverse phase chromatography in pos. ionization mode: alpha-muricholic acid and ursocholic acid.

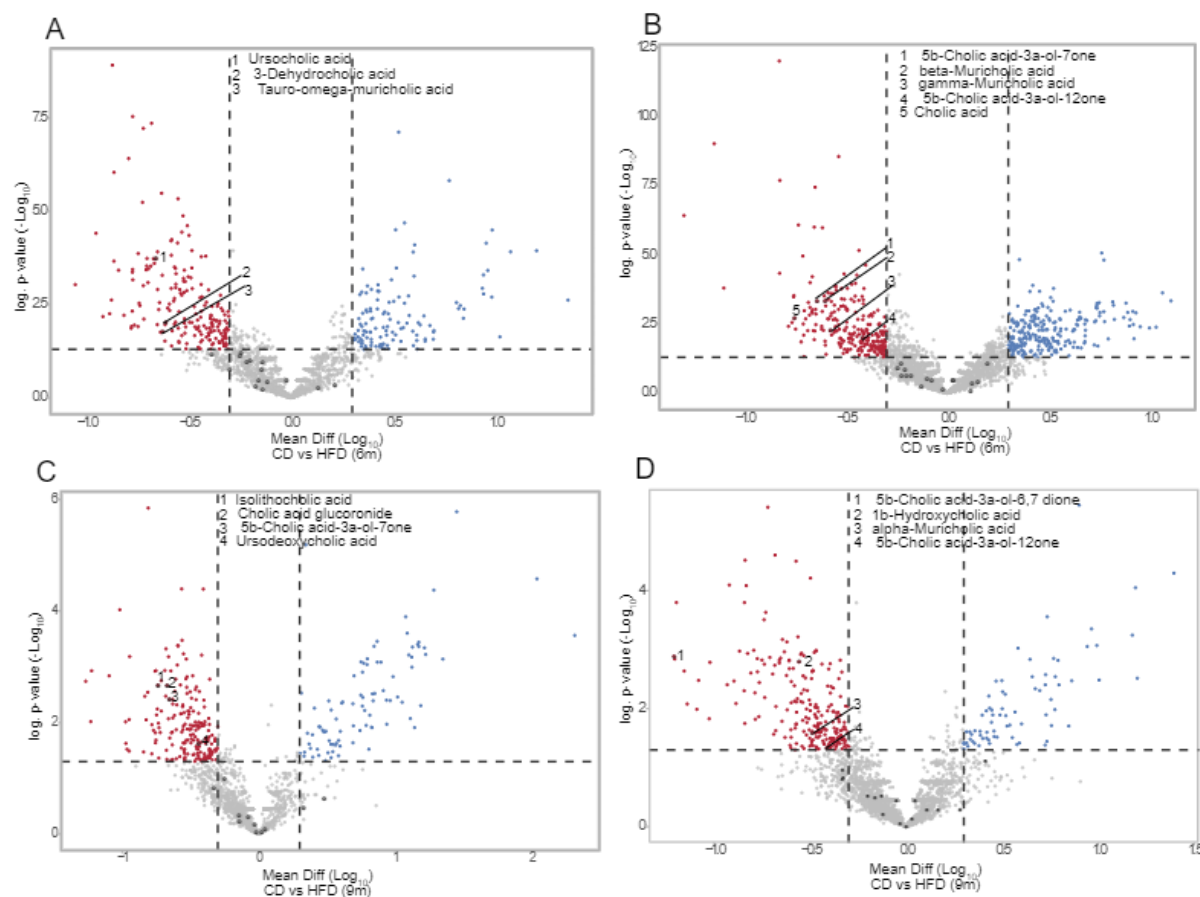


Figure 26: Untargeted metabolomic analysis of cecal content from mice fed CD vs HFD via HILIC shows enrichment of BA in the cecal content of HFD mice. For untargeted metabolomic analysis, hydrophilic interaction chromatography (HILIC) was performed in the positive and negative ionization mode. Data is depicted as volcano plots showing metabolites enriched in CD vs HFD fed mice at 6 and 9 months of age, with significantly enriched metabolites ($p \leq 0.05$, Fold Change ≥ 2 ; equals p -value $\log_{10} \geq 1.3$; Meandiff. $\log_{10} \geq 0.3$) being highlighted in red if enriched in HFD and in blue if enriched in CD. Detected bile acid derivatives are marked with circles, significantly enriched BA are numbered. Bile acids are significantly enriched in HFD. **(A)** Significantly enriched BA in 6m L2-IL1B mice fed HFD, hydrophilic interaction chromatography in neg. ionization mode: ursocholic acid, tauro-omega-muricholic acid, 3-dehydrocholic acid. **(B)** Significantly enriched BA in 6m L2-IL1B mice fed HFD, hydrophilic interaction chromatography in pos. ionization mode: 5b-cholic acid-3a-ol-7-one, beta-muricholic acid, gamma-muricholic acid, 5b-cholic acid-3a-ol-12-one, cholic acid. **(C)** Significantly enriched BA in 9m L2-IL1B mice fed HFD, hydrophilic interaction chromatography in neg. ionization mode: isolithocholic acid, cholic acid glucuronide, 5b-cholic acid-3a-ol-7-one, ursodeoxycholic acid **(D)** Significantly enriched BA in 9m L2-IL1B mice fed HFD hydrophilic interaction chromatography in pos. ionization mode: 5b-cholic acid-3a-ol-6,7-dione, 1b hydroxycholic acid, alpha-muricholic acid, 5b-cholic acid-3a-ol-12-one.

In the fecal content of mice fed CD or HFD at 6 and 9 months of age, which was analyzed via HILIC only, we also found enrichment of BA mainly in HFD mice, with the exception of 3-DHCA, which detected to be enriched in 6-month-old CD mice in positive ionization mode (Fig.27 B). We found CDCA, β MCA acid and cholic acid methyl ester to be enriched in HFD mice at 6 months of age (Fig.27 A, B), and isodeoxycholic acid (IDCA), 7-KLCA, cholic acid methyl ester and lithocholenic acid (LCenA) to be enriched at 9 months of age (Fig.27 C, D). Despite BA still being enriched in HFD, we found less BA to be significantly enriched in the feces compared to the cecal content of HFD mice. These findings correspond to the fact that a high amount of secreted BA is not excreted via the stool but reabsorbed in the intestines, entering the blood flow, and further undergoing enterohepatic circulation.

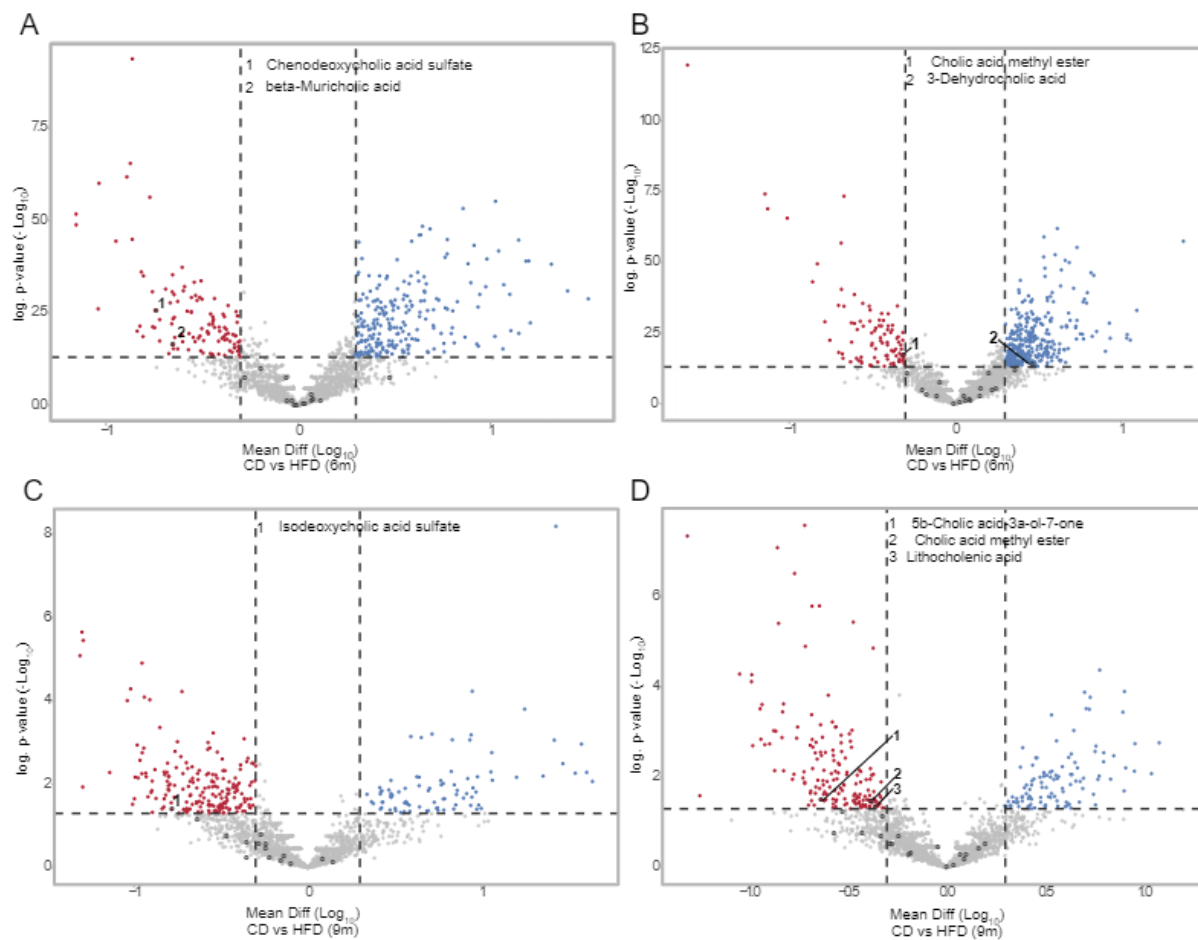


Figure 27: Untargeted metabolomic analysis of fecal content from mice fed CD vs HFD via HILIC shows enrichment of BA in the stool of HFD mice. For untargeted metabolomic analysis, hydrophilic interaction chromatography (HILIC) was performed in the positive and negative ionization mode. Data is depicted as volcano plots showing metabolites enriched in CD vs HFD fed mice at 6 and 9 months of age, with significantly enriched metabolites ($p \leq 0.05$, Fold Change ≥ 2 ; equals p -value $\log_{10} \geq 1.3$; Meandiff. $\log_{10} \geq 0.3$) being highlighted in red if enriched in HFD and in blue if enriched in CD. Detected bile acid derivatives are marked with circles, significantly enriched BA are numbered. Bile acids are significantly enriched in HFD. **(A)** Significantly enriched BA in 6m L2-IL1B mice fed HFD, hydrophilic interaction chromatography in neg. ionization mode: chenodeoxycholic acid sulfate, beta-muricholic acid. **(B)** Significantly enriched BA in 6m L2-IL1B mice fed HFD, hydrophilic interaction chromatography in pos. ionization mode: cholic acid methyl ester, 3-dehydrocholic acid. **(C)** Significantly enriched BA in 9m L2-IL1B mice fed HFD, hydrophilic interaction chromatography in neg. ionization mode: isodeoxycholic acid sulfate **(D)** Significantly enriched BA and SCFA in 9m L2-IL1B mice fed HFD hydrophilic interaction chromatography in pos. ionization mode: 5b-cholic acid-3a-ol-7-one, cholic acid methyl ester, lithocholenic acid.

3.2.4. Treatment with HFD Changes the Serum and Tissue BA Profile of L2-IL1B Mice

Targeted BA analyses showed that, in the serum of L2-IL1B mice fed HFD vs CD, enrichment, mainly of muricholic and taurine-conjugated BA in all mice and of secondary BA with more pronounced effects in male mice could be detected (Fig.28 A). When correlating serum BA levels with dysplasia scores and inversely with goblet cell ratio as measure for differentiation, we found levels of DCA, the most cytotoxic secondary BA to be strongly correlated with disease severity (Fig.28 B).

We also performed targeted analysis of BA levels in the small intestine, colon, and BE tissue at the SCJ of L2-IL1B mice fed CD or HFD (Fig.28 C-E). In the small intestinal tissue, levels of DHCA were lower in HFD compared to CD mice. Also, levels of IDCA and dehydrolithocholic acid (DHLCA) were decreased in HFD compared to CD mice while vice-versa levels of TCDCA, T α MCA, HDCA and tauroursodeoxycholic acid (TUDCA) were enriched. In the colon tissue, the levels of all detected BA were significantly increasing in HFD compared to CD fed mice, including CA, 7- and 12-DHCA, CDCA, α MCA, LCA, DHLCA and TUDCA. In the BE tissue we found significant enrichment of all BA in HFD compared to CD fed mice. We found TCA, CDCA, TCDCA, T α MCA, TDCA, IDCA, DHLCA and TUDCA to be significantly enriched in HFD compared to CD mice.

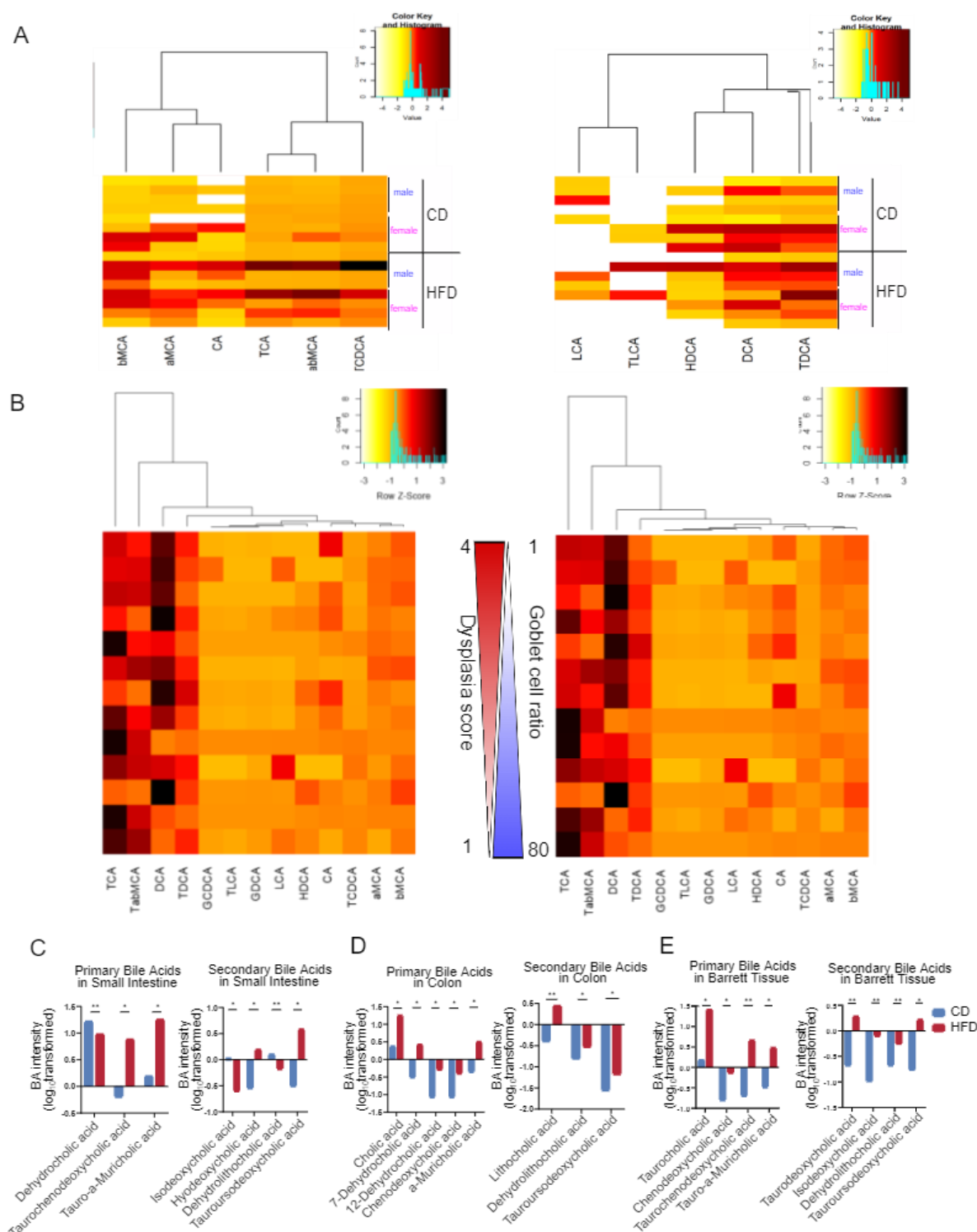


Figure 28: Targeted BA analysis in serum and tissue of L2-IL1B mice fed CD or HFD (A) Primary and secondary serum bile acid levels in male and female mice on CD and HFD. Both secondary and primary bile acid levels are elevated in HFD mice and partially elevated in 3 CD mice. **(B)** Correlation of primary and secondary serum bile acid levels to dysplasia score and goblet cell ratio, with CA and DCA values correlating with dysplasia and inversely with goblet cell ratio as marker for differentiation and less disease severity **(C)** \log_{10} transformed single bile acid intensities in L2-IL1B mice fed HFD are increasing compared to mice fed CD in small intestinal tissue with significant increases of taurochenodeoxycholic acid ($p=0.0208$), tauro-a-muricholic acid ($p=0.0155$), hydoxycholic acid ($p=0.0437$) and tauroursodeoxycholic acid ($p=0.0135$). dehydrolithocholic acid ($p=0.0018$), dehydrocholic acid ($p=0.0049$) and isodeoxycholic acid ($p=0.0213$) levels in the tissue are decreased. **(D)** \log_{10} transformed single bile acid intensities in L2-IL1B mice fed HFD are increasing compared to mice fed CD in colon tissue with significant increases of cholic acid ($p=0.0316$), 7- and 12-dehydrocholic acid ($p=0.0418$; $p=0.0119$), chenodeoxycholic acid ($p=0.0461$), a-muricholic acid ($p=0.0211$) and the secondary BA lithocholic acid ($p=0.0082$),

dehydrolithocholic acid ($p=0.0464$) and tauroursodeoxycholic acid ($p=0.0284$). **(E)** \log_{10} transformed single bile acid intensities in L2-IL1B mice fed HFD are increasing compared to mice fed CD in BE tissue with significant increases of the primary BA taurocholic acid ($p=0.0208$), chenodeoxycholic acid ($p=0.0494$), tauro-CDCA ($p=0.0031$), tauro-a-muricholic acid ($p=0.0133$), and the secondary BA taurodeoxycholic acid ($p=0.0082$), isodeoxycholic acid ($p=0.0013$) dehydrolithocholic acid ($p=0.0022$), tauroursodeoxycholic acid ($p=0.0166$). Data are presented as mean. For statistical evaluation of **(C-E)**, unpaired two-tailed t-tests were used to compare BA levels between the two treatment groups.

3.3. Impact of the FXR Receptor Agonist Obeticholic Acid on L2-IL1B Organoids and on CD and HFD Treated L2-IL1B Mice

Obesity, often caused by intake of a western diet high in fat and processed foods is one of the risk factors for BE and correlates with the risk of progression from BE to EAC^{282,283}. Dietary intake high in fat could be shown to increase BA levels and to change the gut microbiome²⁸⁴⁻²⁸⁶. In the L2-IL1B mouse model, we found BA metabolizing bacteria in the gut and BA levels to be enriched in response to treatment with HFD in correlation with accelerated disease progression and increased disease severity. In the L2-IL1B mouse model and human patients we also found the BA receptor FXR to be expressed in BE tissue, with its expression being lost during disease progression to EAC. A full-body knockout of FXR in L2-IL1B mice increased disease severity. To evaluate the potentially ameliorating effect of an FXR agonist on disease progression in the L2-IL1B mouse model, we studied the effect the semi-synthetic selective FXR agonist OCA first on organoids. After confirmation of the treatment efficacy of OCA in 3D organoid culture, we treated two different cohorts of mice with OCA. The first cohort was treated with CD, HFD or HFD+OCA in the diet from 2 to 6 or 9 months of age. Mice were raised and treated at Columbia University, NYC, USA in collaboration with the working group of Prof. Dr. Timothy Wang. The second cohort was treated with CD, CD+OCA, HFD or HFD+OCA in the diet from 2 to 6 or 9 months of age. The mice of the second cohort were raised and treated at Klinikum Rechts der Isar of TUM in Munich.

The effect of OCA on disease progression was evaluated via histologic analysis, flow cytometry, gene expression analysis and zOTU based microbiome and untargeted and targeted metabolome analyses.

3.3.1. Treatment of L2-IL1B SCJ Organoids with Bile Acids and OCA

3.3.1.1. OCA Treatment acts Protectively on L2-IL1B Organoids Exposed to Bile Acids

To examine FXR as therapeutic target, we treated BE organoids from 12-month-old L2-IL1B mice with 10 μ M OCA, DCA or OCA + DCA or with 10 and 100 μ M OCA, tauro-beta-muricholic acid (T β MCA) or OCA+ T β MCA in the media for 72h after a time of 2 days after passaging. While DCA is known to be the most cytotoxic secondary BA and was correlated with disease severity in the serum of HFD treated mice, T β MCA is an FXR antagonist. Macroscopically, only DCA had an effect on the organoids, causing deformation and accumulation of dead cells in the middle of the organoid (Fig.29 A). Deformation could also be detected in HE stained paraffin embedded organoids (Fig.29 B). Significantly lower organoid numbers were counted in 10 μ M DCA compared to 10 μ M OCA treated samples after 72h treatment, while organoid numbers did not decrease in samples treated with 10 μ M OCA+DCA (Fig.29 C). In T β MCA treatment experiments, organoid numbers increased significantly in T β MCA compared to Ctrl and OCA, with a significant decrease of numbers in OCA+ T β MCA treatment in both 10 μ M and 100 μ M treatments (Fig.29 D). These results indicated a protective effect of OCA on the cytotoxic and pro-proliferative effects of DCA and T β MCA.

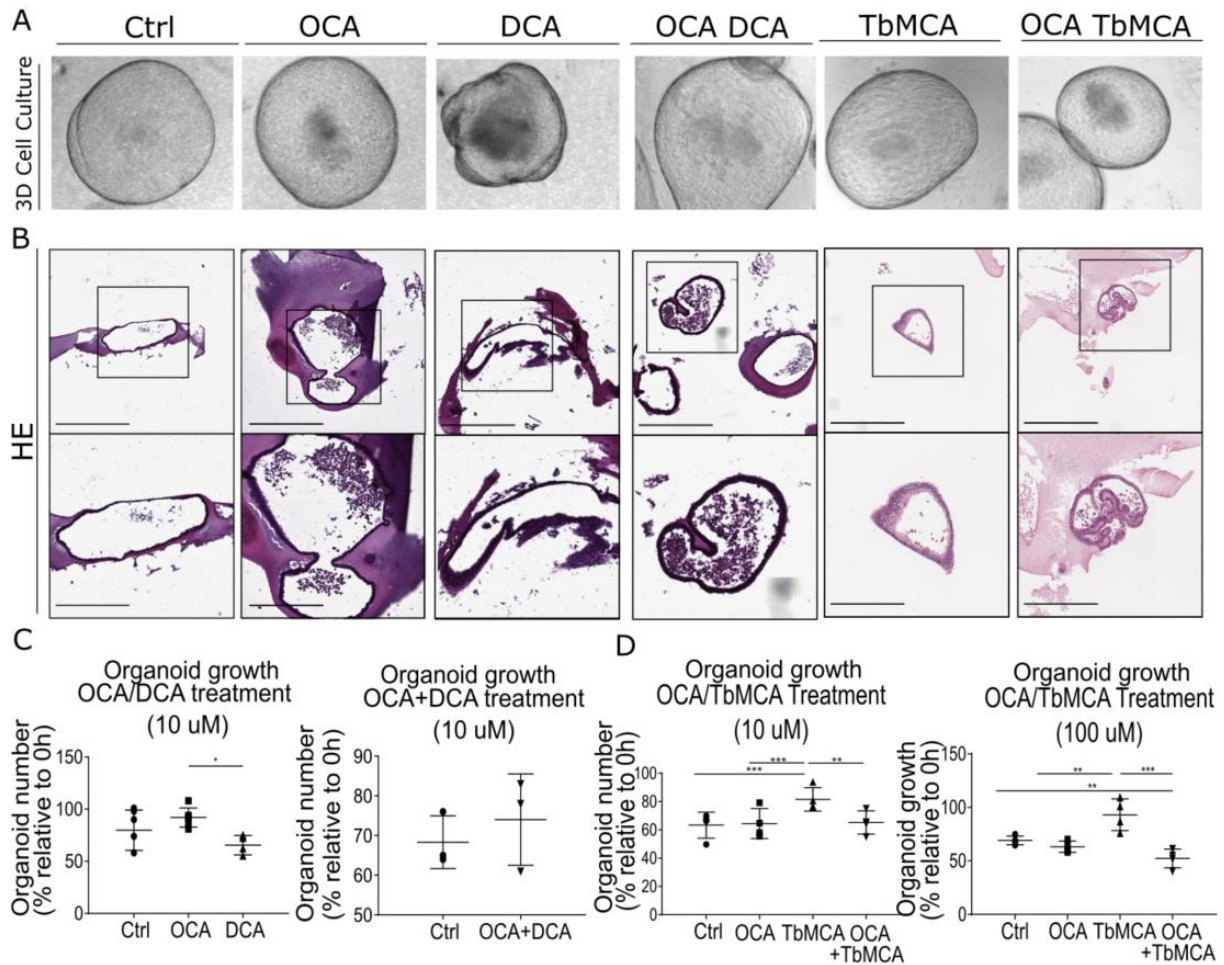


Figure 29: OCA treatment ameliorates the damage induced by BA in L2-IL1B BE Organoids Organoids were treated with 10 μ M OCA, DCA or OCA and DCA; or with 10 μ M or 100 μ M OCA, T β MCA or OCA+T β MCA in the media for 72 h **(A)** Representative pictures of 3D cell culture treated with 10 μ M of component each after 72h of treatment are depicted. Dead cells are accumulating in the center of organoids treated with DCA and organoids are deforming, while organoids treated with OCA+DCA are growing like controls in their size and shape. **(B)** Representative HE staining of paraffin embedded organoids treated with 10 μ M OCA, DCA or OCA and DCA; or with 10 μ M or 100 μ M OCA, T β MCA or OCA+T β MCA in the media for 72 h. **(C)** Number of organoids, depicted as percentage relative to timepoint 0 (0h) before treatment, after 72h treatment with 10 μ M OCA, 10 μ M DCA or 10 μ M OCA + 10 μ M DCA in the media compared to non-treated control organoids. Organoid numbers in samples treated with DCA were significantly decreased compared to organoid numbers in the samples treated with OCA, while OCA and DCA did not significantly differ from the control values (n=5; 72h OCA vs. DCA p=0.0103). The number of organoids treated with OCA and DCA does not develop different from the control group (n=3; 72h Ctrl vs OCA+DCA p=0.5020). **(D)** Number of organoids, depicted as percentage relative to timepoint 0 (0h) before treatment, after treatment with 10 μ M or 100 μ M OCA, T β MCA or OCA+T β MCA in the media for 72 h. Organoid numbers in the samples treated with 10 μ M T β MCA are significantly higher than organoid numbers in the samples treated with 10 μ M OCA, OCA+T β MCA or control organoids. (n=4; Ctrl-T β MCA p=0.0006; OCA-T β MCA p=0.0009; OCA+T β MCA-T β MCA p=0.0013). Organoid numbers in the samples treated with 100 μ M T β MCA are significantly higher than organoid numbers in the samples treated with 100 μ M OCA, OCA+T β MCA or control organoids. (n=4; Ctrl-T β MCA p=0.0080; OCA-T β MCA p=0.0019; OCA+T β MCA-T β MCA p=0.0002). Data are presented as mean with SD. For statistical evaluation of **(C, D)**, unpaired two-tailed t-test was used for two treatment groups, ordinary one-way ANOVA with Tukey-test to correct for multiple comparisons was used for more than two treatment groups.

3.3.1.2. OCA Treatment Rescues the Pro-Proliferative Effect of the BA DCA and T β MCA on L2-IL1B Organoids

To further investigate the effect of OCA on the BA DCA and T β MCA on proliferation in organoid culture, immunohistochemistry for Ki67 was performed on paraffin sections of organoids from 12-month-old L2-IL1B mice with 10 μ M OCA, DCA or OCA + DCA or with 10 and 100 μ M OCA, T β MCA or OCA+T β MCA in the media for 72h (Fig.30 A). Treatment with DCA significantly increased the amount of proliferating cells compared to both Ctrl and OCA treated organoids, while addition of OCA to DCA treatment rescued this increase (Fig.30 B). In both 10 μ M and 100 μ M treatments with OCA, T β MCA and OCA+T β MCA, T β MCA significantly increased the amount of proliferating cells compared to both Ctrl and OCA treated organoids, while addition of OCA to DCA treatment again reduced the amount of proliferating cells (Fig.30 C). This effect only reached significance in 100 μ M treatments. For confirmation purposes, the percentage of proliferating cells in the organoid samples treated with OCA, T β MCA or OCA+T β MCA, was subsequently measured using the Invitrogen flow cytometry Click-iT EdU cell proliferation kit (Fig.30 D). While in the 10 μ M treated samples, the results mirrored the findings of the Ki67 IHC with additional significance in the reduction of proliferation by addition of OCA to T β MCA treatment, in 100 μ M treatments, while general trends also mirrored the findings from analysis of Ki67 expression, proliferation of all treated samples compared to controls decreased, potentially due to the unphysiologically high compound concentrations (Fig.30 D).

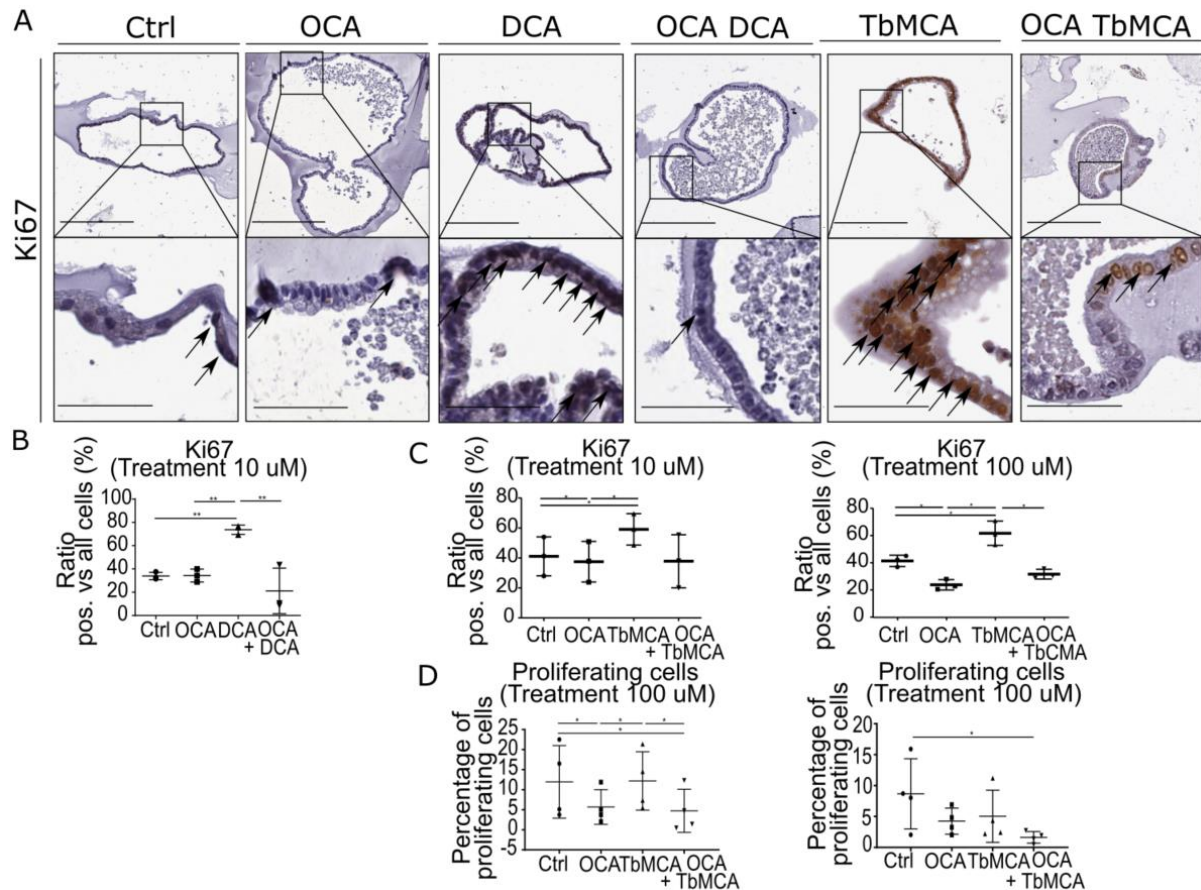


Figure 30: OCA treatment reduces proliferation induced by BA in L2-IL1B BE Organoids Organoids were treated with 10 μM OCA, DCA or OCA and DCA; or with 10 μM or 100 μM OCA, TβMCA or OCA+TβMCA in the media for 72 h. **(A)** Representative pictures of Ki67 immunohistochemistry of organoids treated with 10 μM of OCA, DCA; OCA+DCA, TβMCA or OCA+TβMCA or controls each after 72h of treatment. **(B)** Ki67 immunohistochemical analysis of organoids treated with OCA, DCA, OCA+DCA and controls to determine proliferation rates. Proliferation in DCA treated samples is significantly higher compared to Control, OCA, and OCA+DCA treated samples (n=3; Ctrl-DCA p=0.0090; OCA-DCA p=0.0095; OCA+DCA-DCA p=0.0022). The Proliferation rate was determined as the ratio of cells positively stained for Ki67 vs. all cells. **(C)** Ki67 immunohistochemical analysis of organoids treated with 10 μM or 100 μM OCA, TβMCA, OCA+TβMCA each and controls, TβMCA levels are increased compared to other treatments, while OCA treatment decreases proliferation compared to control (n=3; Ctrl – OCA p=0.00186; Ctrl – TβMCA p=0.0165; OCA – TβMCA p=0.0168). Ki67 immunohistochemical analysis of organoids treated with 100 μM of OCA, TβMCA, OCA+TβMCA each and Controls, TβMCA levels are increased compared to other treatments (n=3; Ctrl – OCA p=0.0439; Ctrl – TβMCA p=0.0485; OCA – TβMCA p=0.0438; TβMCA – OCA+TβMCA p=0.0379). The Proliferation rate was determined as the ratio of cells positively stained for Ki67 vs. all cells. **(D)** Proliferating cells measured with the Click IT FC Kit in organoids after treatment with 10 μM OCA, 10 μM TβMCA or 10 μM OCA and 10 μM TβMCA in the media for 72 h. The number of proliferating cells is significantly lower in OCA and OCA+TβMCA treated organoids compared to Control and TβMCA treated organoids (n=4; Ctrl – OCA p=0.0273; Ctrl -OCA+TβMCA p=0.0124; OCA-TβMCA p=0.0229; TβMCA-OCA+TβMCA p=0.0105). Proliferating cells measured with the Click IT FC Kit in organoids after treatment with 100 μM OCA, 100 μM TβMCA or 100 μM OCA and 100 μM TβMCA in the media for 72 h. The number of proliferating cells is significantly lower in OCA+TβMCA treated organoids compared to Control organoids. (n=4; Ctrl – OCA+TβMCA p=0.0320). Data are presented as mean with SD. For statistical evaluation of **(B-D)** ordinary one-way ANOVA with Tukey-test to correct for multiple comparisons was used.

3.3.1.3. OCA Treatment Rescues the Damaging Effect of the BA DCA on L2-IL1B Organoids

To further investigate the effect of OCA on the BA DCA and T β MCA on proliferation in organoid culture, immunohistochemistry for γ -H2AX was performed on paraffin sections of organoids from 12-month-old L2-IL1B mice with 10 μ M OCA, DCA or OCA + DCA or with 10 and 100 μ M OCA, T β MCA or OCA+T β MCA in the media for 72h (Fig.31 A). Treatment with DCA significantly increased the amount of γ -H2AX positive cells with DNA damage compared to Ctrl treated organoids, while addition of OCA to DCA treatment rescued this increase (Fig.31 B). In both 10 μ M and 100 μ M treatments with OCA, T β MCA and OCA+T β MCA, the amount of cells expressing γ -H2AX did not differ between groups. To confirm these results, levels of 8-hydroxy 2 deoxyguanosine (8'OHDG), a molecule produced and secreted by cells upon oxidative DNA damage were measured in the media of the treated organoids via ELISA (Fig.31 D). 8'OHDG levels in treated samples were normalized to untreated controls. 8'OHDG levels increased in the media of DCA compared to OCA treated organoids, while addition of OCA to DCA treatment again decreased 8'OHDG levels significantly. T β MCA and OCA+T β MCA treatment did not change 8'OHDG levels in the media. These results replicated and thus confirmed the findings from analysis of γ -H2AX expression.

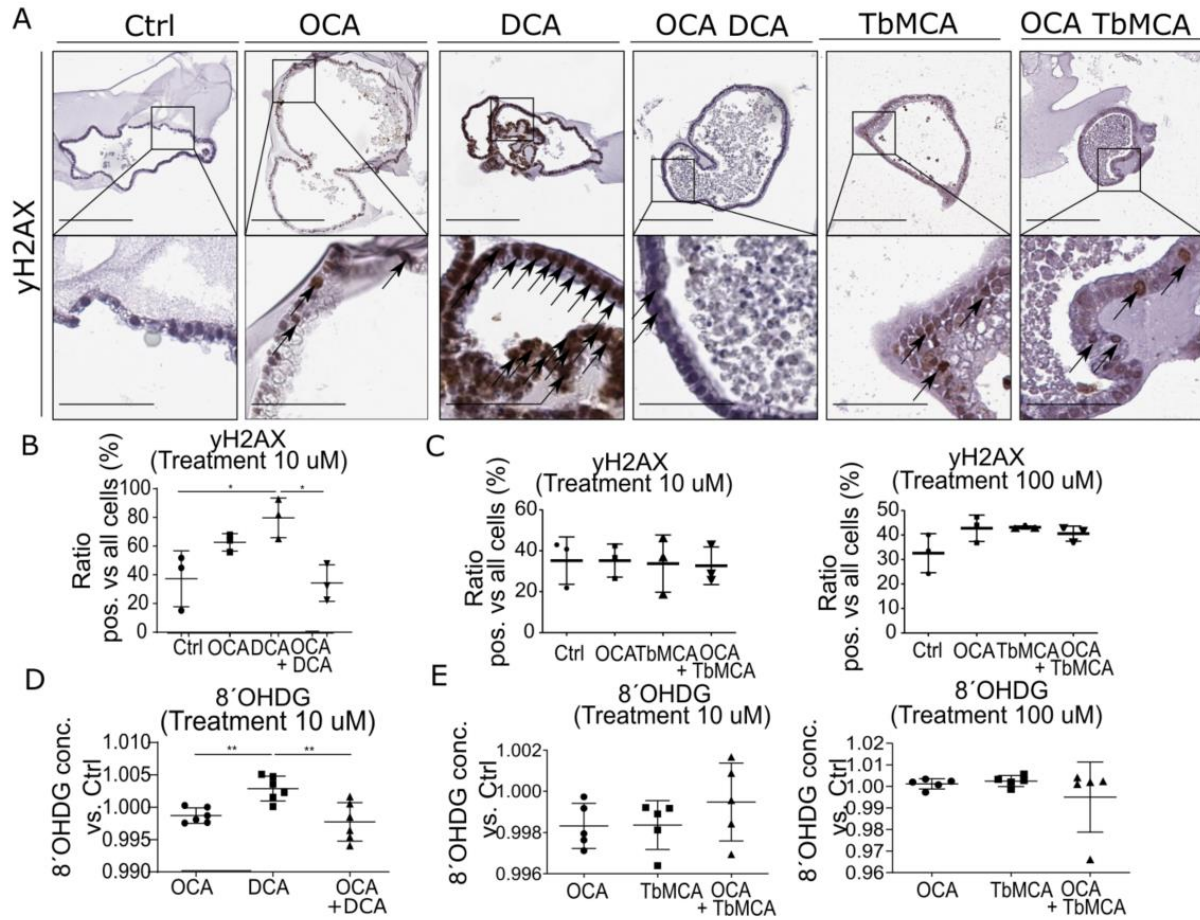


Figure 31: OCA treatment reduces DNA Damage induced by cytotoxic DCA in L2-IL1B BE Organoids
 Organoids were treated with 10 μ M OCA, DCA or OCA and DCA; or with 10 μ M or 100 μ M OCA, T β MCA or OCA+T β MCA in the media for 72 h. **(A)** Representative pictures of γ -H2AX immunohistochemistry of organoids treated with 10 μ M of OCA, DCA; OCA+DCA, T β MCA or OCA+T β MCA or controls each after 72h of treatment. **(B)** γ -H2AX immunohistochemical analysis of organoids treated with OCA, DCA, OCA+DCA and controls to determine DNA damage. DNA damage in DCA treated samples is significantly higher compared to Control and OCA+DCA treated samples (n=3; Ctrl-DCA p=0.0399; OCA+DCA- DCA p=0.0301). The rate of DNA damage was determined as the ratio of cells positively stained for γ -H2AX vs. all cells. **(C)** γ -H2AX immunohistochemical analysis to determine DNA damage in 10 μ M and 100 μ M treated OCA, T β MCA and OCA+T β MCA treated samples normalized to controls shows no significant differences between treatments (n=3; p \geq 0.05). The rate of DNA damage was determined as the ratio of cells positively stained for γ -H2AX vs. all cells. **(D)** 8'OHdG ELISA to determine cellular damage in OCA, DCA and OCA+DCA treated samples normalized to controls shows increased damage in conditioned media of DCA treated organoids compared to both OCA and OCA+DCA (n=6; OCA-DCA p=0.0086; OCA+DCA- DCA p=0.0041). **(E)** 8'OHdG ELISA to determine cellular damage in 10 μ M and 100 μ M treated OCA, T β MCA and OCA+T β MCA treated samples normalized to controls shows no significant differences of 8'OHdG in conditioned media between treatments (n=5; p \geq 0.05). Data are presented as mean with SD. For statistical evaluation of **(B-E)** ordinary one-way ANOVA with Tukey test to correct for multiple comparisons was used.

3.3.2. Treatment of a Cohort of L2-IL1B Mice Raised in NYC with CD, HFD or HFD+OCA

3.3.2.1. OCA Treatment Ameliorates the Dysplastic Phenotype in L2-IL1B HFD Mice

Upon showing treatment efficacy of OCA in 3D organoid culture *in vitro*, two L2-IL1B mouse cohorts were treated with HFD in combination with OCA *in vivo*. The intervention groups of the first mouse cohort were treated with CD, HFD or HFD+OCA from 2 to 6 or 9 months of age in NYC. Mice were sacrificed at 6 and 9 months of age to evaluate disease progression by analyzing the phenotype histologically. HE staining of sections of the FFPE stomach tissue blocks of all mice was prepared for histologic scoring. A previously developed scoring system adapted to the L2-IL1B mouse model was applied^{270,271}. Evaluation of HE staining (Fig.32 A) showed, that at 9 months of age, HFD treatment significantly increased dysplasia scores, while OCA treatment in L2-IL1B mice fed HFD trended to decrease dysplasia scores (Fig.32 E). inflammation and metaplasia scores, goblet cell ratio and the amount of mucus producing PAS positive cells did not differ significantly between groups (Fig. 32 B-D, F).

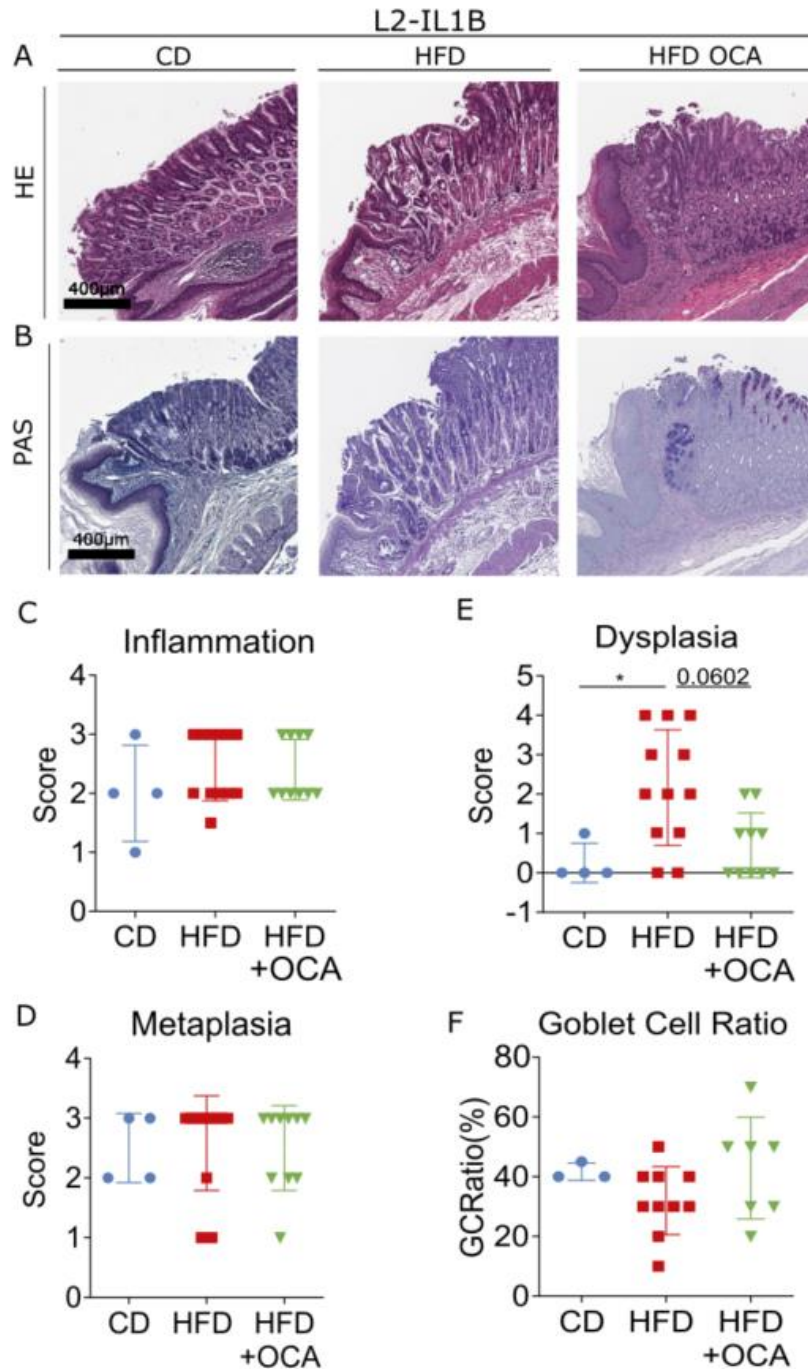


Figure 32: HFD increases the dysplastic phenotype in L2-IL1B mice, while OCA treatment in L2-IL1B mice fed HFD ameliorates the dysplastic phenotype. (A) Representative pictures of HE staining of 9-month-old L2-IL1B mice treated with CD, HFD or HFD+OCA. (B) Representative pictures of PAS staining of 9-month-old L2-IL1B mice treated with CD, HFD or HFD+OCA. (C) Inflammation and (D) Metaplasia scores do not differ significantly between treatment groups. (E) Dysplasia scores in 9-month-old L2-IL1B HFD+OCA diet mice are significantly increased in HFD compared to CD and trending to be lower in HFD+OCA compared to HFD treated mice (n=4-12; CD-HFD p=0.0422; HFD-HFD+OCA p=0.0602). (F) Goblet cell ratio is not differing significantly between treatment groups. Data are depicted as mean with SD. For statistical evaluation of (C-F) Kruskal-Wallis test with Dunn's test to correct for multiple comparisons was used.

3.3.2.2. OCA Treatment Causes Increased FXR Expression in Small Intestinal Tissue of L2-IL1B HFD Mice

FXR expression was evaluated via quantitative real time-PCR (qRT-PCR) in the small intestinal (SI), colon, and cardia tissue of L2-IL1B mice fed HFD and HFD+OCA. relative gene expression of FXR increased significantly in SI tissue upon OCA treatment (Fig.33 B), while expression did not differ significantly between groups in cardia (Fig.33 B) and colon (Fig.33 C) tissue.

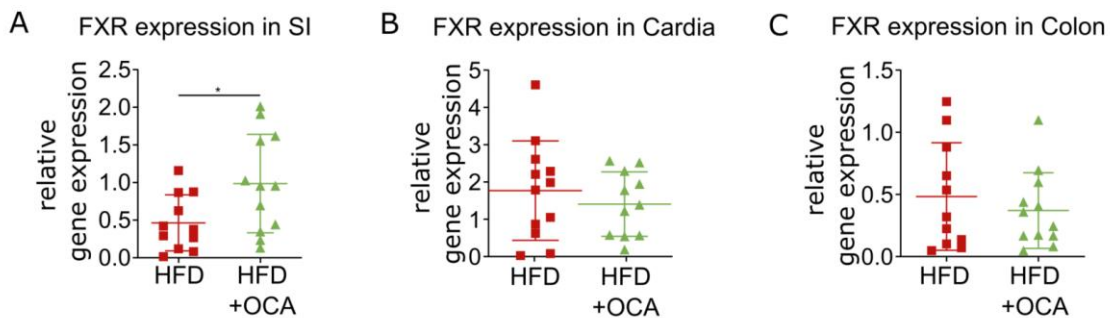


Figure 33: FXR expression is significantly increasing in small intestinal (SI) tissue of L2-IL1B mice upon OCA treatment Relative gene expression of FXR in (A) Small Intestine (SI), (B) Cardia and (C) Colon of 6-9-month-old L2-IL1B HFD and HFD+OCA mice, normalized to control (HFD n=9-12; HFD+OCA n=9-12). FXR gene expression is significantly higher in OCA treated compared to HFD only mice in small intestinal tissue ($p=0.0305$; HFD n=11; HFD+OCA n=9). Data are presented as mean with SD; relative gene expression is determined from $2^{-\Delta\Delta CT}$. For statistical evaluation unpaired two-tailed t-tests were used.

3.3.2.3. OCA Treatment Decreases Proliferation in L2-IL1B Mice

We assessed proliferation rates in L2-IL1B mice fed CD, HFD and HFD+OCA via Ki67 IHC (Fig. 34 A). Interestingly, in this cohort, proliferation decreased significantly in HFD compared to CD mice, in contrast to findings in previous studies (Fig. 34 B)²⁷⁰. OCA treatment in mice fed HFD further decreased the amount of Ki67 positive cells (Fig. 34 B). These results matched our previous *in vitro* treatment results and other studies showing that vice versa, antagonism or loss of FXR expression leads to increased proliferation *in vitro*²⁷⁶⁻²⁷⁸.

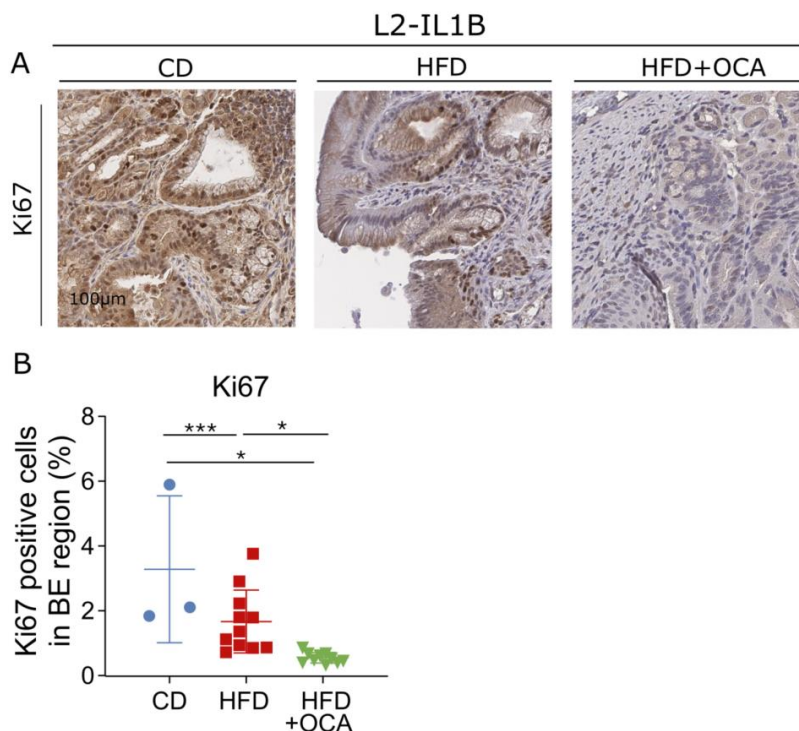


Figure 34: OCA treatment in L2-IL1B mice fed HFD significantly decreases proliferation analyzed by Ki67 compared to CD and HFD (A) Representative pictures of Ki67 immunohistochemistry of 9-month-old L2-IL1B mice treated with CD, HFD or HFD+OCA. **(B)** Ki67 immunohistochemistry for evaluation of proliferation showed significantly decreasing proliferation rates from CD to HFD and to HFD+OCA ($n=4-12$; CD-HFD $p=0.0481$; CD-HFD+OCA $p=0.0010$; HFD-HFD+OCA $p=0.0400$). Data are presented as mean with SD. For statistical evaluation of **(B)** ordinary one-way ANOVA with Tukey-test to correct for multiple comparisons was used.

3.3.2.4. OCA treatment does not Decrease DNA Damage in L2-IL1B Mice Fed HFD

To assess the amount of cells with DNA damage in L2-IL1B mice fed HFD and HFD+OCA in comparison to CD treated mice, we analyzed immunohistochemistry for γ -H2AX (Fig. 35 A). We did not find DNA damage to be significantly different between treatment groups (Fig. 35 B).

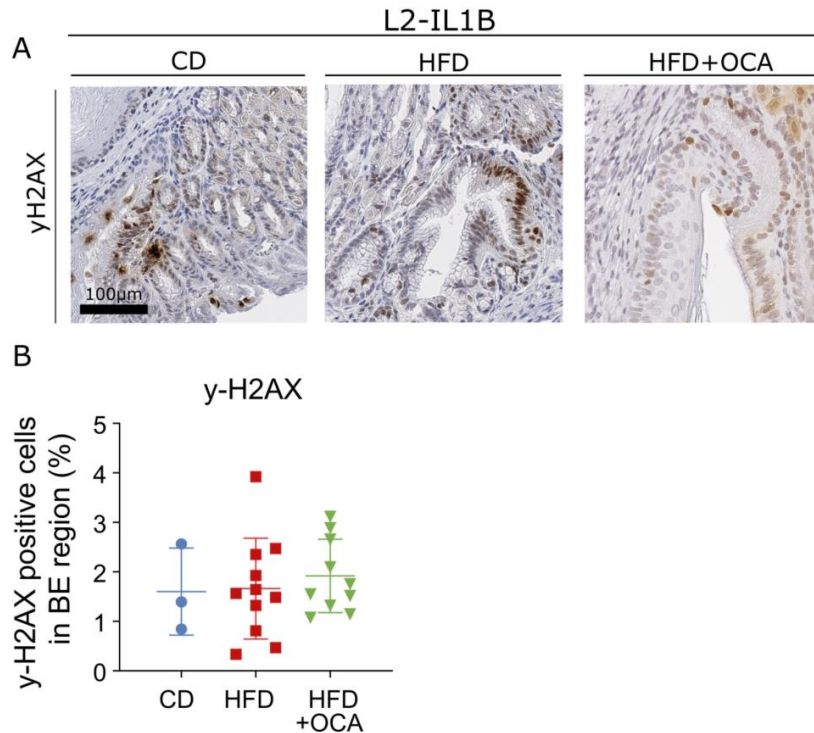


Figure 35: OCA treatment in L2-IL1B mice fed HFD does not reduce DNA damage compared to CD and HFD (A) Representative pictures of γ -H2AX immunohistochemistry of 9-month-old L2-IL1B mice treated with CD, HFD or HFD+OCA. (B) γ -H2AX immunohistochemistry for evaluation of DNA Damage shows no difference between intervention groups. Data are presented as mean with SD. For statistical evaluation of (B) ordinary one-way ANOVA with Tukey test to correct for multiple comparisons was used.

3.3.2.5. OCA treatment Decreases the Amount of Lgr5+ Stem Cells Elevated by HFD in L2-IL-1B Mice

It was shown that inhibition of FXR increased proliferation of Lgr5 cancer stem cells in intestinal cancer²¹⁸. In the L2-IL1B model, we observed FXR and Lgr5 coexpression in epithelial cells and detected an increase of Lgr5 stem cells in mice with FXR knockout. Hence, we suspected FXR dependent regulation of Lgr5 stem cell numbers in our mouse model. To examine the effect of FXR activation by OCA treatment on Lgr5 stem cell numbers, we performed and analyzed in-situ hybridization for Lgr5 and FXR on serial sections of PFPE slides of 9-month-old L2-IL1B mice fed CD, HFD or HFD+OCA (Fig.36 A, B). The total number of Lgr5 positive cells and Lgr5 expression on FXR positive cells significantly increased with HFD treatment. OCA treatment in HFD rescued this effect and significantly decreased Lgr5 positive cell number and Lgr5 expression on FXR positive cells (Fig, 36 C, E). Also, the number of FXR positive cells decreased in mice fed HFD, while it again increased in mice fed HFD+OCA but the effect did not reach significance (Fig.36 D, F)

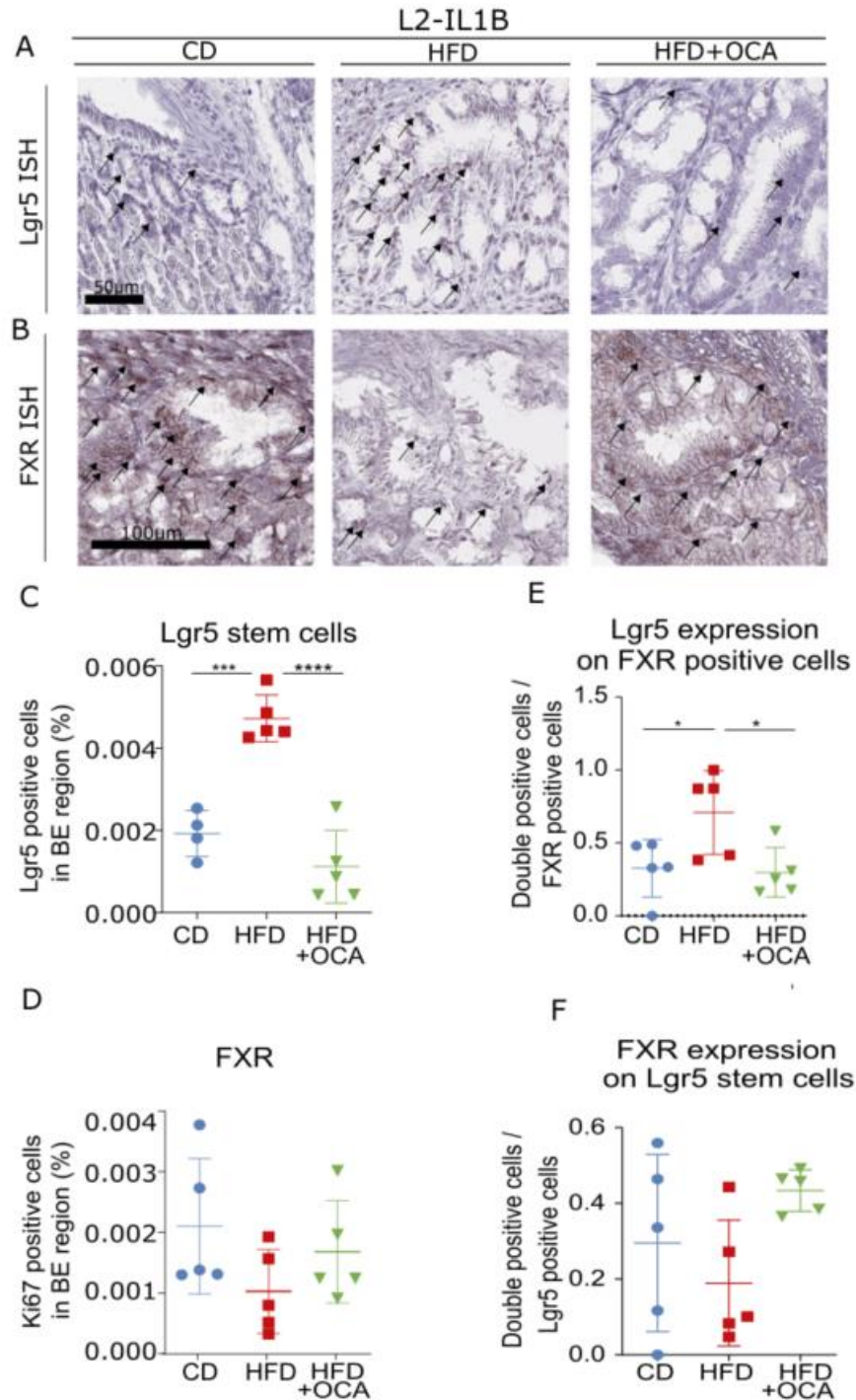


Figure 36: Lgr5 stem cell numbers are decreasing in L2-IL1B HFD mice upon treatment with OCA. Lgr5 and FXR ISH in BE tissue of L2-IL1B mice fed CD, HFD or HFD+OCA shows increasing Lgr5 stem cell numbers in HFD compared to CD, while OCA treatment in HFD mice rescues the phenotype. **(A)** Representative pictures of Lgr5 ISH of 9-month-old L2-IL1B mice treated with CD, HFD or HFD+OCA. **(B)** Representative pictures of FXR ISH of 9-month-old L2-IL1B mice treated with CD, HFD or HFD+OCA. **(C)** Lgr5 stem cell numbers are significantly increased in HFD vs CD mice and significantly decreased in HFD+OCA compared to HFD treated mice (n=4-5; CD-HFD p=0.0002; HFD-HFD+OCA p<0.0001). **(D)** FXR positive cell numbers are not significantly changed between treatment groups **(E)** Lgr5 expression on FXR positive cells is significantly elevated in HFD compared to CD and again significantly downregulated in HFD+OCA treated mice (n=5; CD-HFD p=0.0470; HFD-HFD+OCA p=0.0331). **(F)** FXR expression on Lgr5 positive stem cells is not significantly changed between treatment groups. Data are presented as mean with SD. For statistical evaluation of **(C-F)** ordinary one-way ANOVA with Tukey-test to correct for multiple comparisons was used.

3.3.2.6. Expression of TGR5 in L2-IL1B Mice does not Change Between Intervention Groups

To examine potential compensation of signaling by upregulation of TGR5 expression upon treatment with CD, HFD or HFD+OCA, we assessed TGR5 levels in the SCJ tissue of the different treatment cohorts by analyzing IHC for TGR5 (Fig. 37). TGR5 was broadly expressed in the tissue of all intervention groups. We could therefore exclude the possibility of compensation of the dietary effects via deregulation of TGR5 expression.

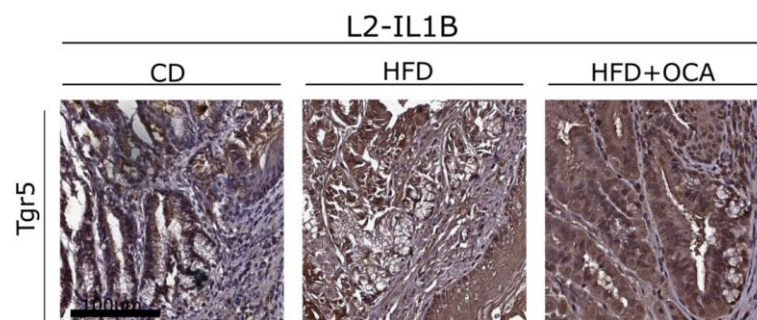


Figure 37: Expression of the BA receptor Tgr5 does not change between intervention groups Representative pictures of Tgr5 immunohistochemistry of 9-month-old L2-IL1B mice treated with CD, HFD or HFD+OCA.

3.3.2.7. OCA Treatment Changes the Gut Metabolome of L2-IL1B Mice fed HFD

Previous results showed FXR knockout and HFD treatment to change the BA pool and to mostly increase BA levels in L2-IL1B mice. To elucidate the effect of OCA treatment on BA levels in mice fed HFD, we performed targeted metabolomic analyses of the stool of the first L2-IL1B mouse cohort fed CD, HFD or HFD OCA.

3.3.2.8. OCA Treatment Causes a Reduction of Fecal BA Levels in L2-IL1B Mice Fed HFD

After showing a distinct change of the gut metabolome between L2-IL1B mice fed HFD compared to CD, we performed targeted metabolomic analyses for BA in the stool comparing mice fed CD, HFD and HFD+OCA treated mice. The ratio of fecal secondary to primary BA (Fig.38 A) and total secondary BA levels (Fig.38 B) decreased in L2-IL1B mice fed HFD+OCA compared to HFD mice. While levels of cholenic acid-3,12-diol, 3-DHCA, CDCA and TCDCA as well as UCA, UDCA, 7-ketolithocholic acid (7-KLCA) and γ MCA increased in HFD+OCA mice, levels of cholic acid-7- α -3-one, allocholic acid (ACA), 12-KLCA and most importantly of the cytotoxic BA DCA and its conjugate TDCA significantly decreased (Fig.38 C). Analyzing the data via PLS-DA we did not find a distinct spacial distribution but still a relatively clear separation between the clusters of the different intervention groups (Fig.38 D). A heatmap of the bile acid levels of all mice fed CD, HFD or HFD+OCA showed that, with few exemptions, levels of LCA and DCA and their derivatives, which build the secondary BA pool were increased with HFD compared to CD and were decreased in mice fed HFD+OCA (Fig.38 E). Analysis of important features by PLS-DA, displayed as VIP scores showed the main BA responsible for separation between groups, as well as the mean levels between groups. This graph showed cholic acid-7- α -3-one, TCDCA and γ MCA to be the three main separators of groups. While CA-3-one was specifically elevated in CD mice, both other BA were elevated in HFD+OCA mice. Cytotoxic DCA was distinctly elevated in HFD mice and UDCA was elevated in HFD+OCA mice compared to other groups (Fig.38 F).

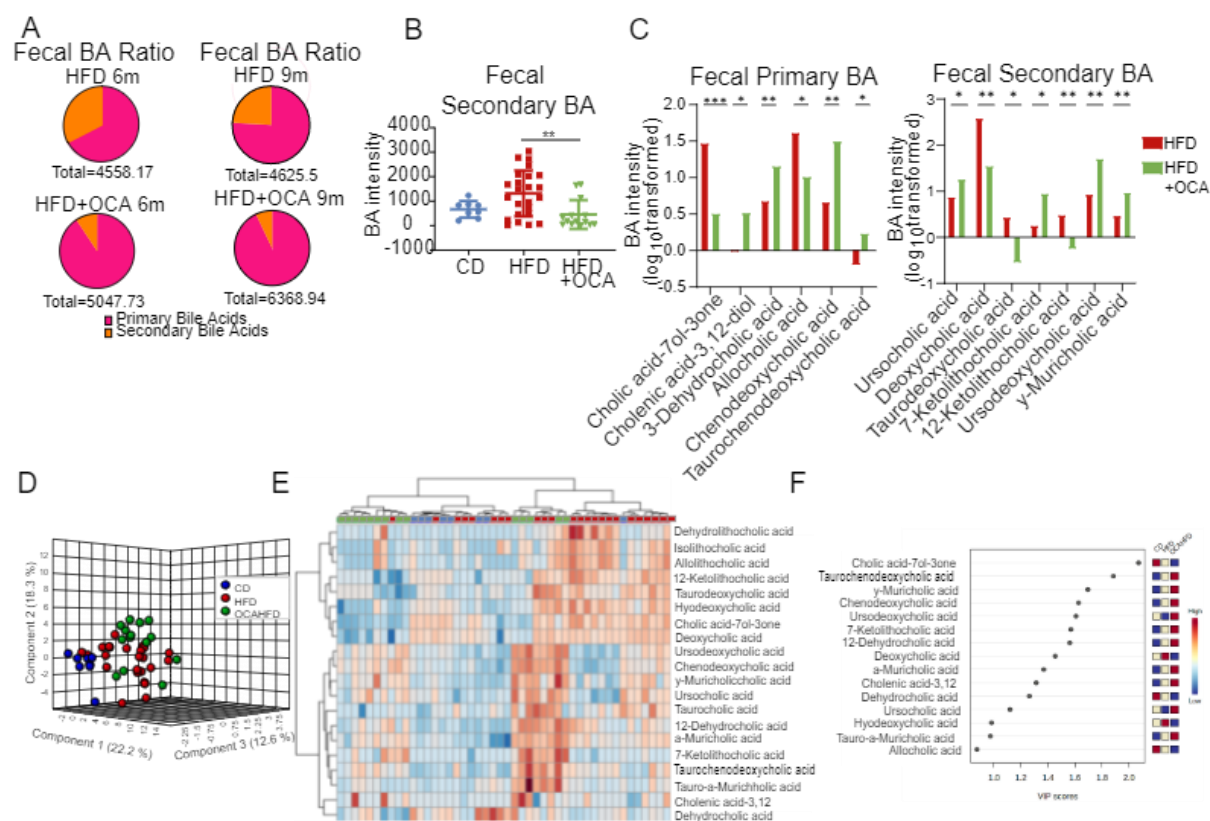


Figure 38: OCA treatment changes the fecal bile acid profile in L2-IL1B mice fed HFD (A) Pie charts showing primary compared to secondary BA levels as well as total BA levels in 6- and 9-month-old L2-IL1B mice fed HFD or HFD+OCA. **(B)** Combined fecal secondary BA levels are significantly lower in L2-IL1B mice fed HFD+OCA compared to HFD (L2-IL1B mice with combined ages of 6 and 9 months, CD n=8, HFD n=24, HFD+OCA n=14 HFD vs HFD+OCA p=0.0052) **(C)** Fecal primary and secondary BA significantly changed between 6-9m old HFD and HFD+OCA treated L2-IL1B mice (primary BA: cholic acid-7- α -3one p<0.0001; chenolic acid-3,12-diol p= 0.0168; 3-dehydrocholic acid p= 0.0049; allocholic acid p= 0.0165; chenodeoxycholic acid p=0.0016; secondary BA: ursolic acid p=0.0202; deoxycholic acid p=0.0054; taurodeoxycholic acid p=0.0248; 7-ketolithocholic acid p=0.0466; 12-ketolithocholic acid p=0.0071; ursodeoxycholic acid p=0.0021; γ -muricholic acid p=0.0070). **(D)** Partial least squares discriminant analysis (PLS-DA) of fecal BA profiles in L2-IL1B mice fed CD HFD and HFD+OCA (mice of all timepoints combined; CD n=8; HFD n=23; HFD+OCA n=14). **(E)** Clustering of murine fecal samples and fecal BAs in L2-IL1B mice fed CD, HFD or HFD+OCA shown as heatmap. Displayed are the top 20 BAs ranked by t-test (euclidean distance measure, ward clustering algorithm). **(F)** Important features identified by PLS-DA. The colored boxes on the right indicate the relative concentrations of the corresponding metabolite in each group under study. The VIP (variable's importance in projection) score of a feature indicates its importance as variable for distinction between groups. It is calculated as a weighted sum of the squared correlations between the PLS-DA components and the original variable, with the weights corresponding to the percentage variation explained by the PLS-DA component in the model. For statistical evaluation, ordinary one-way ANOVA with Tukey test to correct for multiple comparisons was used. **(C-G)** Data are presented as mean. For statistical evaluation of (C, D), unpaired two-tailed t-tests were used to compare BA levels between the two treatment groups.

3.3.2.9. OCA Treatment Changes Levels of Potentially BA metabolizing Cecal Microbiota in L2-IL1B mice fed HFD

The cecal and fecal microbiome of 6- and 9-month-old mice from the mouse cohort fed CD, HFD or HFD+OCA in NYC was analyzed via 16S-sequencing to assess changes in gut microbiota, especially of those with potential BA metabolizing capacities between groups. Significant separation of the microbial profiles characterized by beta-diversity was only detected in 6-month-old L2-IL1B mice on intervention diets in both cecum and feces (Figure 39, 41) In the cecum, relative abundance of the class of *Clostridia*, the only bacterial class with proven BA 7 α -dehydroxylation capacities was significantly increased in 6-month-old HFD compared to CD and HFD+OCA mice (Fig. 40 A). The relative abundance of the phylum *Firmicutes* dropped in 6-month-old HFD and HFD+OCA mice compared to CD mice and again increased in 9-month-old HFD+OCA mice (Fig. 40 B). The abundance of the phylum of *Bacteroidetes* increased in HFD+OCA, but interestingly also in 6-month-old HFD mice compared to CD mice (Fig. 40 C). Abundance of the family *Clostridiaceae 1* was only abundant in 6-month-old HFD and in 6- and 9-month-old HFD+OCA mice with higher abundance in HFD+OCA mice (Fig. 40 D). Abundance of the family *Ruminococcaceae* significantly decreased in 6-month-old HFD+OCA compared to CD and HFD mice (Fig. 40 E). The family *Lachnospiraceae* was significantly more abundant in 6-month-old HFD compared to CD and HFD+OCA mice (Fig. 40 F). The genus *Clostridium cluster IV* was only abundant in CD and HFD but missing in HFD+OCA mice (Fig. 40 G). The genus *Clostridium sensu stricto* was only present in 6-month-old HFD and in 6- and 9-month-old HFD+OCA mice with higher abundance in HFD+OCA mice (Fig. 40 H). The genus *Clostridium cluster XIVa* was significantly lower abundant in 9-month-old CD compared to 9-month-old HFD and 6-month-old CD mice (Fig. 40 I). The genus *Clostridium cluster XVIII* was not present in 9-month-old mice and only present in low levels in 6-month-old HFD mice, while abundance was significantly higher in 9-month-old CD and in HFD+OCA mice (Fig. 40 J). Figure 40 K shows correlation of cecal microbiota with potential BA metabolizing capacities with disease scores. *Clostridia*, *Firmicutes* and *Ruminococcaceae*, which were all most abundant in HFD compared to CD and HFD+OCA mice were all positively correlated with dysplasia scores and negatively correlated with the ratio of goblet cells (GC). On genus level, no correlation between dysplasia scores and the different genera of *Clostridia* was detected, with exception of the genus *Clostridium sensu stricto*, which was most abundant in HFD+OCA mice and negatively correlated with disease scores.

In the stool of the mice, while microbial richness stayed constant in L2-IL1B mice fed CD and HFD+OCA, richness dropped significantly in HFD mice between 6 and 9 months of age. Interestingly, microbial richness increased in 6-month-old HFD compared to CD mice (Fig. 42 A). The phylum *Firmicutes* was most abundant in the stool of 6-month-old CD and 9-month-old HFD+OCA mice (Fig. 42 B), while the phylum *Bacteroidaceae* was most abundant in both 6- and 9-month-old HFD+OCA mice (Fig. 42 C). Also, the family *Clostridiaceae 1* was most abundant in HFD+OCA mice (Fig. 42 D). The family *Ruminococcaceae* was most abundant in 6-month-old HFD mice compared to other groups (Fig. 42 E). The family *Lactobacillaceae* was not present in 6-month-old CD mice and was most abundant in 6- and 9-month-old HFD mice compared to CD and HFD+OCA mice (Fig. 42 F). The genus *Clostridium cluster IV* was not detectable at all in HFD+OCA mice (Fig. 42 G), while the genus *Clostridium sensu stricto* was only present in 6-month-old HFD and in HFD+OCA mice with highest abundance in HFD+OCA mice (Fig. 42 H). Also, the genus *Clostridium cluster XIVa* significantly increased in abundance in 9-month-old HFD+OCA compared to HFD mice (Fig. 42 I). *Clostridium cluster XVIII* was not present or with only very low abundance in HFD mice, while its abundance was comparatively higher in 9-month-old CD and HFD+OCA mice (Fig. 42 J).

The family of *Peptostreptococcaceae*, which was not differentially abundant between groups in the cecum was most abundant in 9-month-old HFD+OCA mice (Fig. 42 K). Figure 42 L shows correlation of cecal microbiota with potential BA metabolizing capacities with disease scores. *Clostridia* were positively correlated with disease scores, but abundance of the phylum was not as clearly differently abundant between groups as in the cecum. *Ruminococcaceae*, *Lactobacillaceae* and unknown *Ruminococcaceae*, which were most abundant in HFD mice were all positively correlated with dysplasia scores. On genus level, no correlation between dysplasia scores and the different genera of *Clostridia* was detected, with exception of the genus *Clostridium cluster XIVa* which was negatively correlated with disease scores and most abundant in HFD+OCA mice. Even though no strong conclusions can be drawn on the genus level, these results link disease severity in L2-IL1B mice to higher abundance of BA modulating bacteria in HFD mice.

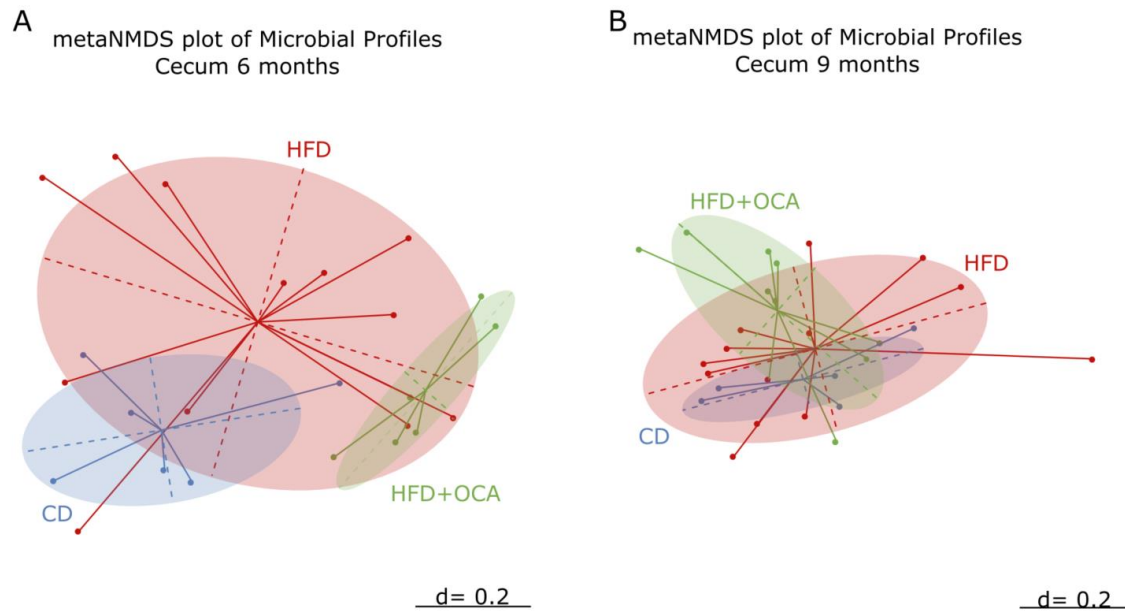


Figure 39: Beta diversity comparison for cecal microbial profiles: meta-Normalized Multidimensional Scaling (metaNMDS) plots of feces from 6- and 9-month-old L2-IL1B mice fed CD, HFD or HFD+OCA (A) Significant separation of study groups (cecum of 6-month-old L2-IL1B mice fed CD, HFD or HFD+OCA) in terms of bacterial community composition was detected ($p=0.002$). **(B)** No significant separation of study groups (cecum of 9-month-old L2-IL1B mice fed CD, HFD or HFD+OCA) in terms of bacterial community composition was detected ($p=0.289$). Permutational Multivariate Analysis of Variance (PERMANOVA) test was used for statistical comparison. The microbiota phylogenetic distances were evaluated through the generalized UniFrac distance. Each point represents the microbiota composition of one sample.

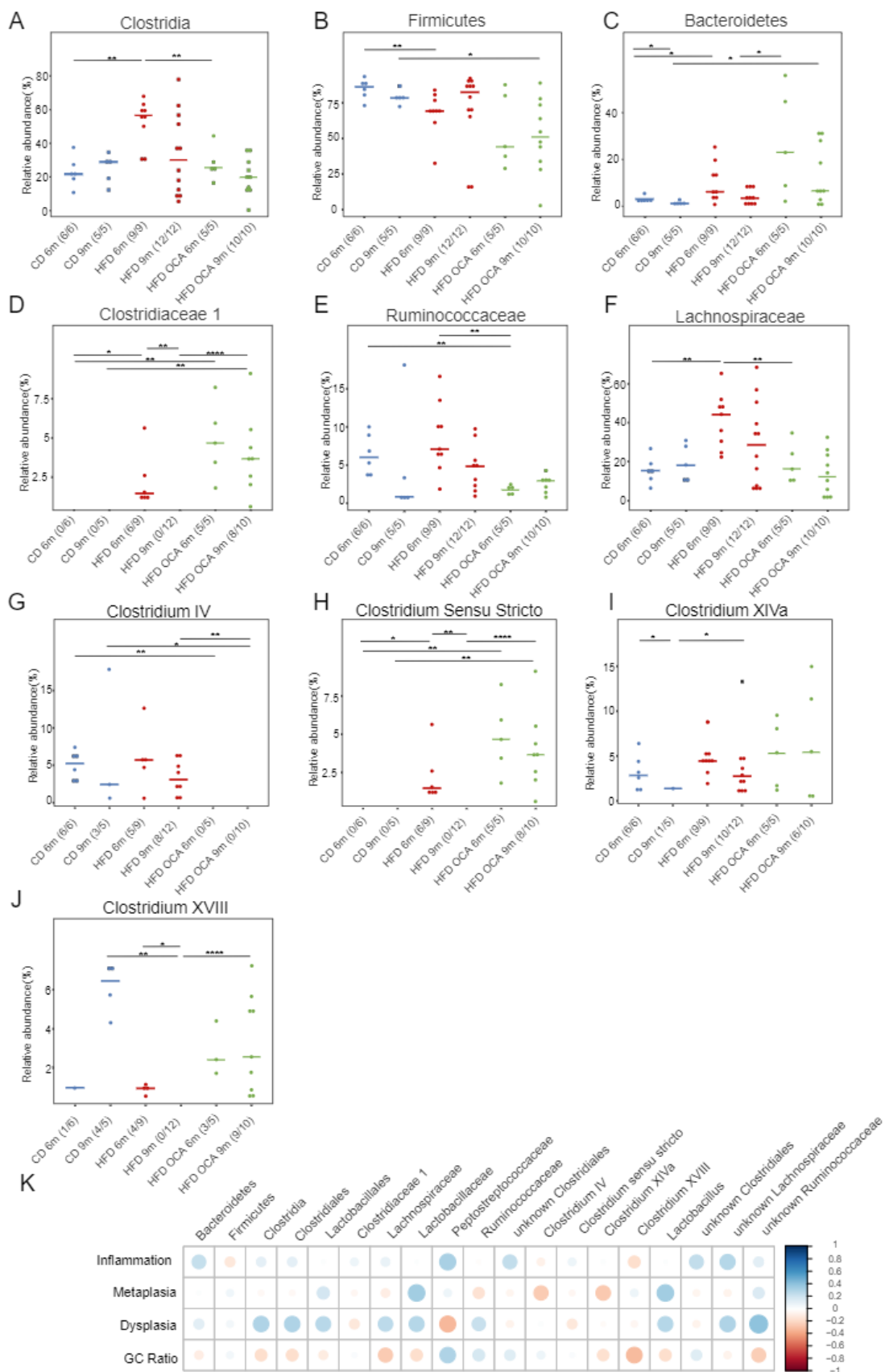


Figure 40: OCA treatment changes the BA metabolizing microbial profile in the cecum of L2-IL1B mice fed HFD Representation of the cecal relative abundance (%) of bacterial families with bile acid metabolizing capacities between L2-IL1B mice fed CD, HFD or HFD+OCA at 6m and 9m of age. Only relevant significant changes are shown. **(A)** The class of Clostridia is significantly enriched in abundance in 6m old HFD mice compared to CD and HFD+OCA (HFD6m – CD6m, $p=0.0016$; HFD6m – HFD+OCA6m $p=0.0040$). **(B)** The phylum Firmicutes decreases in abundance in 6m old HFD compared to CD mice and in 9m old HFD+OCA compared to CD mice (CD6m –

HFD6m $p=0.0076$; CD9m – HFD+OCA9m $p=0.0400$). **(C)** The phylum bacteroides is significantly higher abundant in 6-month-old HFD and HFD+OCA compared to CD mice. The relative abundance drops between 6 and 9m in CD and HFD+OCA mice (CD6m – CD9m $p=0.0303$; CD6m – HFD6m $p=0.0256$; CD9m – HFD+OCA9m $p=0.0400$; HFD+OCA6m – HFD+OCA9m $p=0.0400$). **(D)** The family Clostridiaceae 1 are only abundant in 6m old HFD and 6m and 9m old HFD+OCA mice (CD6m – HFD6m $p=0.0278$; CD6m – HFD+OCA6m $p=0.0022$; CD9m – HFD+OCA9m $p=0.0070$; HFD9m – HFD+OCA9m $p=0.0001$; HFD6m – HFD9m $p=0.0015$). **(E)** The family of Ruminococcaceae is significantly decreasing in abundance in 6m old HFD+OCA mice compared to CD and HFD mice (CD6m – HFD+OCA6m $p=0.0043$; HFD6m – HFD+OCA6m $p=0.0040$). **(F)** The family of Lachnospiraceae is significantly enriched in abundance in 6m old HFD mice compared to CD and HFD+OCA (CD6m – HFD6m $p=0.0016$; CD9m – HFD6m $p=0.0120$). **(G)** The genus Clostridium cluster IV is only abundant in CD and HFD mice (CD6m – HFD+OCA6m $p=0.0022$; CD9m – HFD+OCA9m $p=0.0220$; HFD9m – HFD+OCA9m $p=0.0017$). **(H)** The genus Clostridium sensu stricto is only abundant in 6m old HFD and in 6m and 9m old HFD+OCA mice (CD6m – HFD6m $p=0.0278$; CD6m – HFD+OCA6m $p=0.0022$; CD9m – HFD+OCA9m $p=0.0070$; HFD9m – HFD+OCA9m $p=0.0001$; HFD6m – HFD9m $p=0.0015$). **(I)** Abundance of the genus Clostridium cluster XIVa is increased in 9m old HFD vs CD mice ($p=0.0276$) and decreased in 9m vs 6m CD mice ($p=0.0152$) **(J)** The genus Clostridium cluster XVIII is significantly higher abundant in 9m old CD and HFD+OCA compared to HFD mice (CD9m – HFD9m $p=0.0021$; HFD9m – HFD+OCA9m $p=0.0000$) and is not present in 9m old HFD mice. (HFD6m – HFD9m $p=0.0211$) **(K)** Correlation analysis between the abundance of bacterial families with bile acid metabolizing capacities in all treatment groups versus inflammation, metaplasia and dysplasia scores as well as goblet cell (GC) ratio. Correlation analyses were performed using the Rhea pipeline for 16S-sequencing data. Clostridia, lactobacillales, Ruminococcaceae and unknown Lachnospiraceae are the main microbial groups positively correlated with dysplasia scores. For **(A-J)** relative abundances of microbiota are represented with mean. For statistical analysis, pairwise Wilcoxon rank sum test or fisher's exact test, if appropriate, were used.

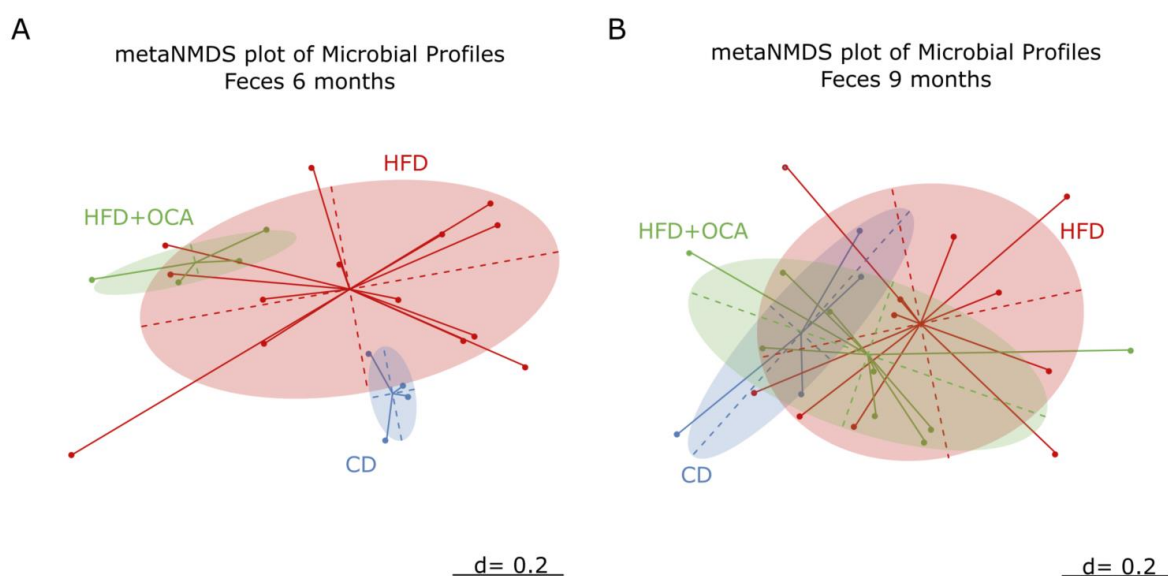


Figure 41: Beta diversity comparison for fecal microbial profiles: meta-Normalized Multidimensional Scaling (metaNMDS) plots of feces from 6- and 9-month-old L2-IL1B mice fed CD, HFD or HFD+OCA (A) Significant separation of study groups (feces of 6-month-old L2-IL1B mice fed CD, HFD or HFD+OCA) in terms of bacterial community composition was detected ($p=0.002$). **(B)** No significant separation of study groups (feces of 9-month-old L2-IL1B mice fed CD, HFD or HFD+OCA) in terms of bacterial community composition was detected ($p=0.214$). Permutational Multivariate Analysis of Variance (PERMANOVA) test was used for statistical comparison. The microbiota phylogenetic distances were evaluated through the generalized UniFrac distance. Each point represents the microbiota composition of one sample.

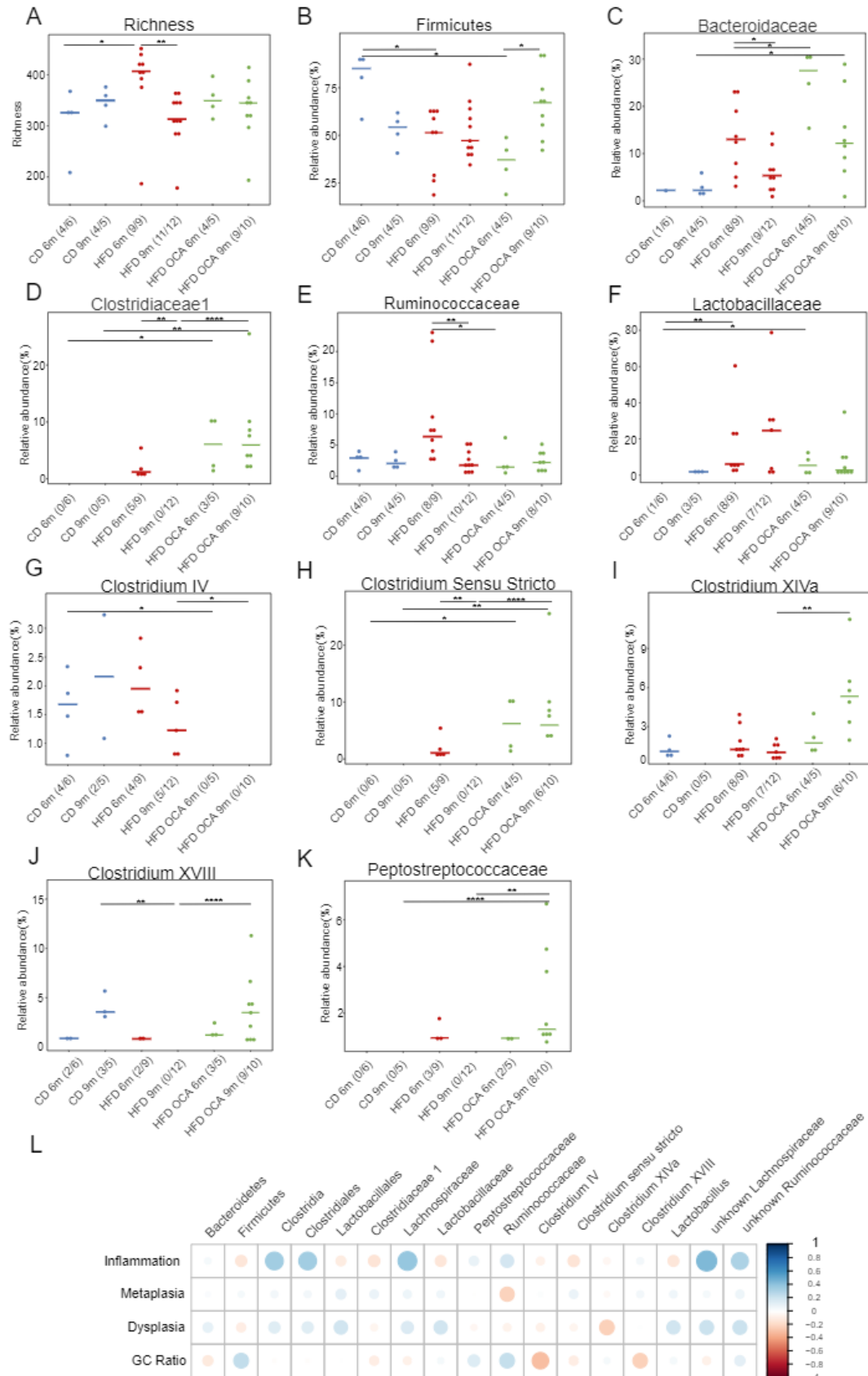


Figure 42: OCA treatment changes the BA metabolizing microbial profile in the feces of L2-IL1B mice fed HFD Representation of the fecal richness and relative abundance (%) of bacterial families with bile acid metabolizing capacities between L2-IL1B mice fed CD, HFD or HFD+OCA at 6m and 9m of age. Only relevant significant changes are shown. **(A)** Richness increases in the feces of 6m old HFD compared to CD mice ($p=0.0336$). While the richness in both CD and HFD+OCA diet stays constant between 6m and 9m old mice, richness significantly decreases within the HFD cohort (HFD6m – HFD9m $p=0.0016$). **(B)** The relative abundance of the

phylum Firmicutes decreases in both 6m old HFD and HFD+OCA mice compared to CD mice and increases in 9m compared to 6m old HFD+OCA mice. **(C)**The relative abundance of the family Bacteroidaceae significantly increases in 6m old HFD+OCA compared to HFD and in 9m old HFD+OCA compared to CD mice (CD9m – HFD+OCA9m $p=0.0485$; HFD6m – HFD+OCA6m $p=0.0283$), while the abundance decreases in HFD mice from 6 to 9 months of age ($p=0.0464$). **(D)** The family Clostridiaceae 1 are only abundant in 6m old HFD and 6m and 9m old HFD+OCA mice (CD6m – HFD+OCA6m $p=0.0286$; CD9m – HFD+OCA9m $p=0.0070$; HFD – HFD+OCA9m $p=0.0001$; HFD6m – HFD9m $p=0.0081$). **(E)** The relative abundance of the family of Ruminococcaceae decreases in both 9m HFD and 6m HFD+OCA mice compared to 6m HFD mice (HFD6m –HFD9m $p=0.0044$; HFD6m – HFD+OCA6m $p=0.0485$). **(F)**The family of Lactobacillaceae is significantly higher abundant in 6m old HFD and HFD+OCA compared to CD mice (CD6m –HFD6m $p=0.0070$; CD6m – HFD+OCA6m $p=0.0286$). **(G)**The genus Clostridium cluster IV is only abundant in CD and HFD mice (CD6m – HFD+OCA6m $p=0.0286$; HFD9m – HFD+OCA9m $p=0.0379$). **(H)**The genus Clostridium sensu stricto is significantly higher abundant compared to 6 and 9m old CD mice and compared to 9m old HFD mice (CD6m – HFD+OCA6m $p=0.0286$; CD9m – HFD+OCA9m $p=0.0070$; HFD9m –HFD+OCA9m $p=0.0001$). Abundance drops in HFD mice from 6 to 9 months of age ($p=0.0081$). **(I)** The Clostridium cluster XIV is significantly more abundant in 9m old HFD+OCA mice compared to HFD mice ($p=0.0023$). **(J)**The genus Clostridium XVIII is only abundant in 6m old HFD and in 6m and 9m old HFD+OCA mice (CD9m – HFD9m $p=0.0088$; HFD9m – HFD+OCA9m $p=0.0000$). **(K)**The genus Peptostreptococcaceae is only abundant in 6m old HFD and in 6m and 9m old HFD+OCA mice (CD9m –HFD+OCA9m $p=0.0070$; HFD9m – HFD+OCA9m $p=0.0001$). **(L)** Correlation analysis between the abundance of bacterial families with bile acid metabolizing capacities in all treatment groups versus inflammation, metaplasia, and dysplasia scores as well as goblet cell (GC) ratio. Correlation analyses were performed using the Rhea pipeline for 16S-sequencing data. Clostridia, Lactobacillales and Lachnospiraceae and unknown Ruminococcaceae are the main microbial groups positively correlated with dysplasia scores. For **(A-K)** relative abundances of microbiota are represented with mean. For statistical analysis, pairwise Wilcoxon rank sum test or fisher's exact test, if appropriate, were used.

3.3.2.10. Disease Severity is Linked to BA Modulating Bacterial Strains Correlating with Taurine Conjugated BA and Secondary BA Levels

Having shown a correlation between BA modulating bacterial communities and disease severity, in the following we correlated the levels of BA with the abundance of bacterial genera in the feces of the mice (Fig.43). The different genera of *Clostridia* correlated positively with a variety of different BA. *Clostridium cluster IV*, which was not present in HFD+OCA mice correlated positively with allocholic acid, lithocholic acid, and most importantly DCA levels. *Clostridium sensu stricto*, which was most abundant in HFD+OCA mice negatively correlated with disease progression on the other hand correlated negatively with DCA, TCA and TDCA levels. *Clostridium cluster XI* correlated positively with mainly secondary BA. *Clostridium cluster XIVa*, which was most abundant in HFD+OCA mice compared to other groups, correlated negatively with all taurine conjugated BA, with the exception of TLCA, while *Clostridium cluster XIVb* correlated positively mainly with LCA derivatives. *Clostridium cluster XVIII*, which was less abundant in HFD mice compared to both CD and HFD+OCA mice, showed positive correlations with different primary BA, LCA derivatives and UCA as well as UDCA. Of *Lachnospiraceae* and *Ruminococcaceae*, on genus level only the unknown genera, which were positively associated with dysplasia scores could be correlated to BA levels. The genera correlated negatively with most BA, with few exceptions. The genus *unknown Lachnospiraceae* correlated positively with ACA, LCA and TLCA, while the genus of *unknown Ruminococcaceae* correlated positively with different LCA derivatives.

The correlation between microbial strains, BA levels in the gut and disease severity presented as a highly complex interaction network. In conclusion, potentially BA modulating strains which were enriched in HFD+OCA seemed to negatively correlate mainly with taurine conjugated BA and DCA derivatives and positive with LCA derivatives as well as UDCA, while they were negatively correlated with disease severity. Strains abundant in HFD correlated positively with DCA and partially with LCAs. The unknown genera of *Lachnospiraceae* and *Ruminococcaceae*, which only potentially harbor BA modulating strains correlated positively with LCA derivatives and with disease progression.

3.3.2.11. OCA Treatment Causes a Reduction of BA Levels in the Serum of L2-IL1B Mice Fed HFD

We detected positive correlations between HFD, disease severity, BA metabolizing gut bacteria and fecal, mainly taurine conjugated and secondary BA levels, which were partially rescued by additional treatment with OCA. We analyzed serum and tissue BA levels of the mice in order to clarify if the diet dependent shift in the fecal microbiota and BA pool was reflected systemically. We could not detect a reduction of the secondary BA ratio in the serum of HFD+OCA compared to HFD mice (Fig.44 A). Total secondary BA levels were significantly reduced in both HFD and HFD+OCA mice compared to CD mice (Fig.44 B). Subsequently we assessed detailed changes of primary and secondary BA levels between HFD and HFD+OCA mice. Assessing primary BA levels, we found CA derivatives and ACA to be decreased and TCDCA and MCAs to be enriched in HFD+OCA compared to HFD mice. Assessing secondary BA levels, we found DCA, TDCA and 6-KLCA to be significantly less abundant in HFD+OCA mice, while UDCA and TUDCA levels increased (Fig.44 C). PLS-DA analysis showed similar tendencies between the intervention groups as seen in fecal BA analysis (Fig.44 D). In a clustered heatmap of the BA levels of the individual mice, we found a relatively clear separate clustering of the different cohorts. In HFD+OCA mice, significant reduction of a cluster of BA including DCA, TCA and TDCA was detected, while another cluster of BA, including UDCA, TUDCA and taurine conjugated primary BA was enriched in HFD+OCA mice (Fig.44 E). Analysis of important features by PLS-DA, displayed as VIP scores showed these BA to also be mainly responsible for separation between groups (Fig.44 F). In the small intestinal, colon and BE tissue, almost all BA levels decreased significantly in HFD+OCA mice compared to HFD mice (Fig.44 G-I), with the exception of DHCA in the small intestine (Fig.44 G) and TLCA as well as 6-KLCA in the colon. Secondary BA were the only BA differently abundant between groups in the colon (Fig.44 H). A detailed view of BA levels changing between intervention groups in the tissues is shown in the supplement (Supplementary Fig.7 A-C). Most interestingly levels of DCA and its derivatives were reduced in all three tissues. In the BE tissue both TCA and TDCA levels were significantly reduced (Fig.44 I), with TDCA levels being reduced also in colon tissue (Fig.44 H). Analysis of combined, primary, and secondary BA levels in BE tissue shows an increase of BA levels in BE tissue in HFD compared to CD mice, and again a reduction in HFD+OCA mice, but the effect fails to reach significance (Supplementary Fig.7 D). Altogether, these results indicate a role of BA of the classical BA synthesis pathway and mainly of its secondary BA DCA in disease progression, with a reduction of these BA by treatment with OCA.

treated L2-IL1B mice in colon. No significantly changed primary BA could be detected. (secondary BA: deoxycholic acid $p=0.0497$; glycodeoxycholic acid $p=0.0144$; taurodeoxycholic acid $p=0.0321$; isodeoxycholic acid $p=0.0139$; tauroolithocholic acid $p=0.0478$; 6-ketolithocholic acid $p=0.0258$). **(I)** Primary and secondary BA significantly changed between 6-9m old HFD and HFD+OCA treated L2-IL1B mice in small intestine (primary BA: taurocholic acid $p=0.0009$; secondary BA: taurodeoxycholic acid $p=0.0040$). **(B)** Data are presented as mean with SD. For statistical evaluation, ordinary one-way ANOVA with Tukey test to correct for multiple comparisons was used. **(C-I)** Data are presented as mean. For statistical evaluation of **(C, G-I)**, unpaired two-tailed t-tests were used to compare BA levels between the two treatment groups.

3.3.3. Treatment of a Second Cohort of L2-IL1B mice Raised in Munich with CD, CD+OCA, HFD or HFD+OCA

3.3.3.1. OCA Treatment does not Reduce Macroscopic Tumor Size or Coverage in L2-IL1B mice fed CD or HFD

A second cohort of L2-IL1B mice was treated with CD, CD+OCA, HFD or HFD+OCA in the diet from 2 to 6 or 9 months of age at Klinikum Rechts der Isar, TUM. After euthanasia at 6 or 9 months of age, pictures were taken from the opened and cleaned stomach and the percentage and size of tumors covering the SCJ were determined (Fig.45 A; Supplementary Fig.8 A). Tumor percentage and size did not differ between intervention groups, neither at 6 (Supplementary Fig.8 B, C) not at 9 months of age (Fig.45 B, C).

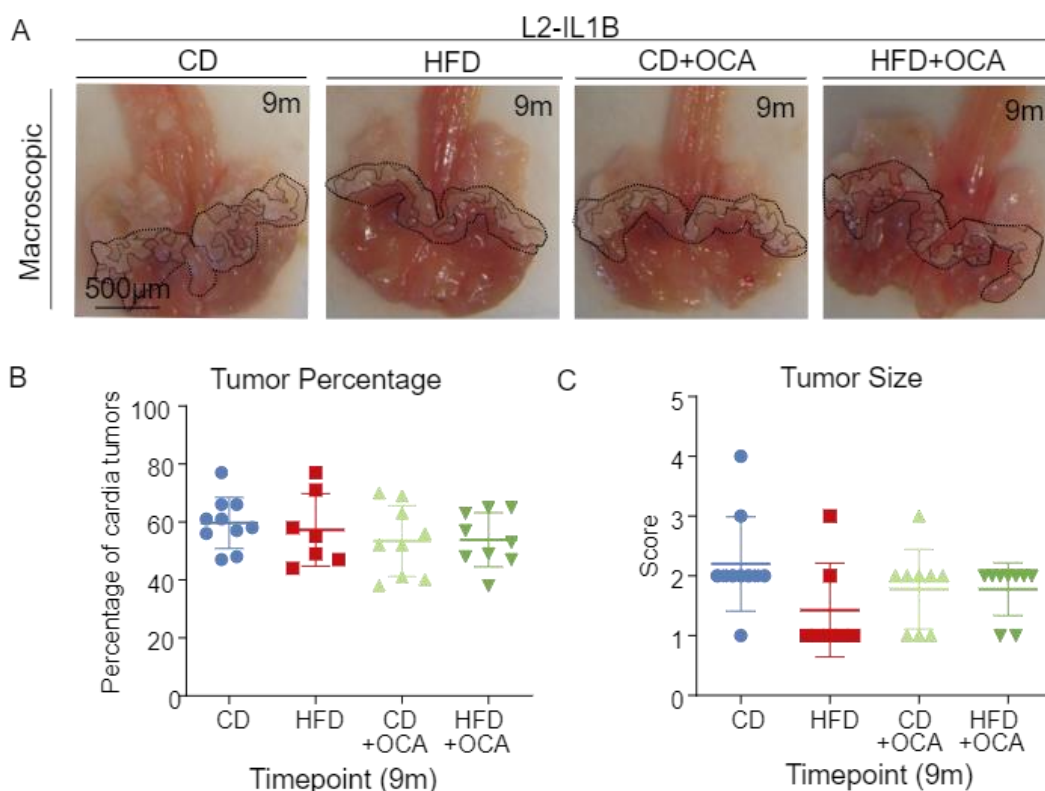


Figure 45: Macroscopic scores do not differ between treatment groups in L2-IL1B mice treated with CD or HFD with or without OCA (A) Representative macroscopic image of the SCJ region of L2-IL1B mice fed CD, HFD, CD+OCA or HFD+OCA at 9 months of age, with the SCJ and tumor nodes in the SCJ being outlined **(B)** Tumor percentage and **(C)** Tumor size of 9-month-old L2-IL1B mice are not differing significantly between treatment groups. Data are presented as mean with SD. For statistical evaluation of **(B, C)** ordinary one-way ANOVA with Tukey-test to correct for multiple comparisons was used.

3.3.3.2. OCA Treatment Ameliorates the Dysplastic Phenotype of L2-IL1B Mice Fed HFD

HE and PAS-stained sections of FFPE stomach tissue of all mice was prepared for histologic scoring. A previously developed scoring system adapted to the L2-IL1B mouse model was applied^{270,271}. Evaluation of these HE sections and of PAS-stained sections (Fig.46 A, B) showed, that at 9 months of age, OCA treatment in HFD mice significantly decreased dysplasia scores (Fig.46 E). Inflammation and metaplasia scores did not differ significantly between groups (Fig. 46 C, D), but GC ratio was significantly elevated in HFD+OCA mice compared to the other intervention groups (Fig.46 F). These results were reflected also in the 6-month-old mice (Supplementary Fig. 9).

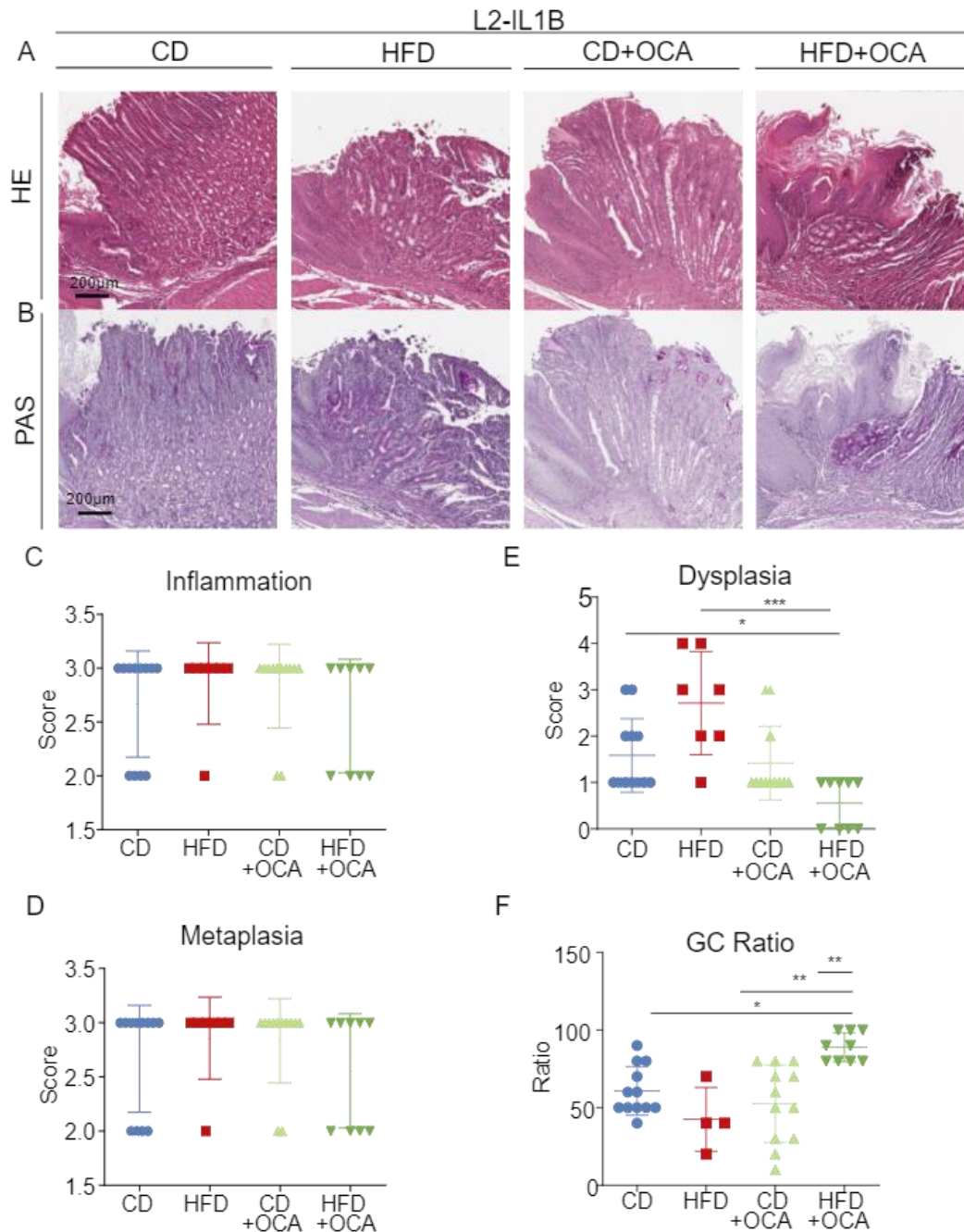


Figure 46: OCA treatment in L2-IL1B mice fed HFD ameliorates the dysplastic phenotype and increases differentiation represented by goblet cell (GC) ratio. (A) Representative pictures of HE staining of 9-month-old L2-IL1B mice treated with CD, HFD, CD+OCA or HFD+OCA. **(B)** Representative pictures of PAS staining of 9-month-old L2-IL1B mice treated with CD, HFD, CD+OCA or HFD+OCA. **(C)** Inflammation and **(D)** Metaplasia scores do not differ significantly between treatment groups. **(E)** Dysplasia scores in 9-month-old L2-IL1B HFD+OCA diet mice are significantly lower compared to CD and HFD treated mice (n=4-12; CD-HFD+OCA p=0.0427; HFD-HFD+OCA p=0.0002). **(F)** Goblet cell ratio is significantly higher in HFD+OCA treated mice compared to all other groups (n=4-12; CD-HFD+OCA p=0.0089; HFD-HFD+OCA p=0.0012; CD+OCA-HFD+OCA p=0.0006). Data are depicted as mean with SD. For statistical evaluation of **(C-F)** Kruskal-Wallis test with Dunn's test to correct for multiple comparisons was used.

3.3.3.3. OCA Treatment Changes the Gut Metabolome of L2-IL1B Mice Fed CD and HFD

Purpose of raising a second cohort of L2-IL1B mice was mainly to verify the microbiome and metabolome associated results from the first mouse cohort, as especially the microbiome is highly sensitive to the environment and location an organism is raised in²⁸⁷. We also aimed to further elucidate the effect of OCA on the microbiome and metabolome of CD treated mice, as the highly purified CD was shown to already aggravate the phenotype compared to chow diet, most probably due to the purification but also an increased energy content compared to chow (chow= 14MJ/kg; CD= 15.3MJ/kg; HFD 19.7MJ/kg).

Cecal and fecal material from mouse cohorts treated with CD or HFD with or without OCA (6 or 9 months of age) underwent untargeted metabolomic analyses via reverse phase (RP) chromatography and hydrophilic interaction chromatography (HILIC) in negative and positive ionization mode. Obeticholic acid was detected in the cecal content of both CD+OCA and HFD+OCA treated 6- and 9-month-old mice with both RP chromatography (Fig.47 A, B; CD+OCA Fig.48 A, C; HFD+OCA Fig.49 A, C) and HILIC (CD+OCA Fig.50 A, C; HFD+OCA Fig.51 A, C) in negative ionization mode. In the fecal content, OCA could not be detected, proving reuptake of OCA in the gut.

In the cecum, comparing CD to CD+OCA, BA were almost solely enriched in mice treated with CD in both RP chromatography (Fig.48 A-D) and HILIC (Fig.50 A-D). Besides OCA, mainly CDCA and glycochenodeoxycholic acid (GCDCA), GCA and DCA and its derivatives were enriched in CD compared to CD+OCA mice (Fig.48; Fig.50). In HFD compared to HFD+OCA mice, we found CA derivatives to be enriched in HFD (Fig.49; Fig.51) and 1b-hydroxycholeic acid to be enriched in HFD+OCA (Fig.49 B).

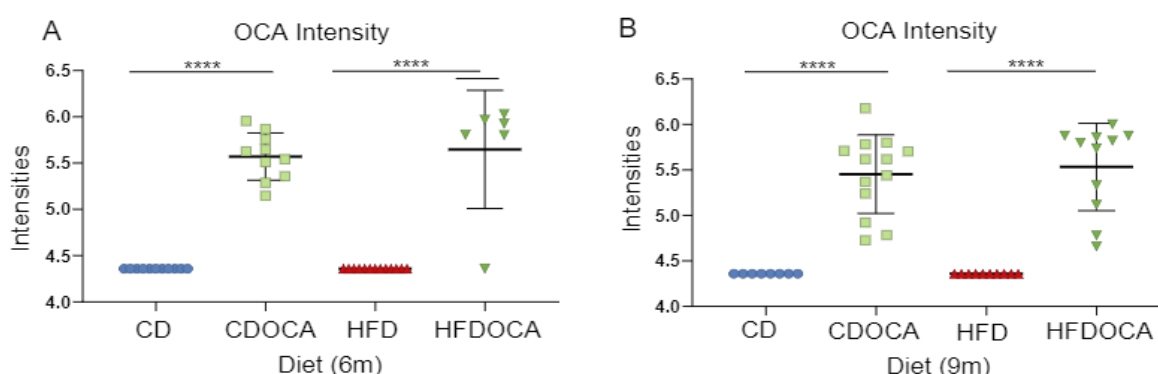


Figure 47: Obeticholic acid levels in the cecum of OCA treated L2-IL1B mice on CD and HFD mice are significantly elevated compared to untreated mice Data were extracted from untargeted analysis of the cecal content of the mice via reverse phase (RP) chromatography. Similar results are found when evaluating HILIC based analysis, while in the feces of the mice OCA could not be detected, therefore proving treatment efficacy. **(A)** OCA intensities in 6-month-old L2-IL1B mice fed CD, CD+OCA, HFD or HFD+OCA shows highly significant enrichment of OCA in OCA treated mice ($p < 0.0001$) **(B)** OCA intensities in 9-month-old L2-IL1B mice fed CD, CD+OCA, HFD or HFD+OCA shows highly significant enrichment of OCA in OCA treated mice ($p < 0.0001$)

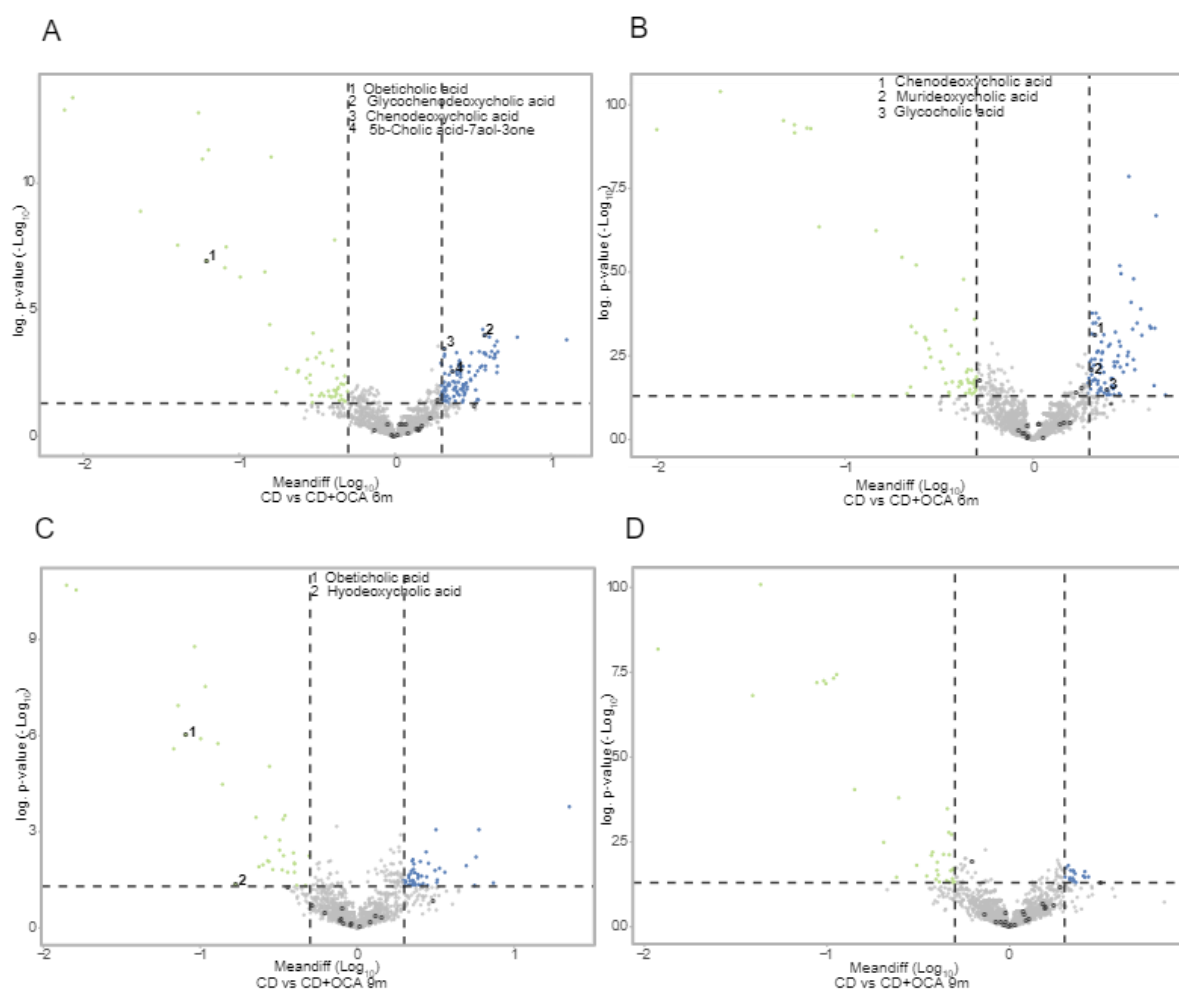


Figure 48: Untargeted metabolomic analysis of cecal content from mice fed CD vs CD+OCA via RP chromatography. For untargeted metabolomic analysis, reversed phase chromatography (RP) was performed in the positive and negative ionization mode. Data is depicted as volcano plots showing metabolites enriched in CD vs CD+OCA fed mice at 6 and 9 months of age, with significantly enriched metabolites ($p \leq 0.05$, Fold Change ≥ 2 ; equals p-value $\log_{10} \geq 1.3$; Meandiff. $\log_{10} \geq 0.3$) being highlighted in green if enriched in CD+OCA and in blue if enriched in CD. Detected bile acid derivatives are marked with circles, significantly enriched BA are numbered. **(A)** Significantly enriched BA in 6m L2-IL1B mice fed CD vs CD+OCA, reverse phase chromatography in neg. ionization mode. Enrichment in CD+OCA: obeticholic acid; enrichment in CD: glycochenodeoxycholic acid, chenodeoxycholic acid, 5b-cholic acid-7 α ol-3-one. **(B)** Significantly enriched BA in 6m L2-IL1B mice fed CD, reverse phase chromatography in pos. ionization mode: chenodeoxycholic acid, murideoxycholic acid, glycocholic acid. **(C)** Significantly enriched BA in 9m L2-IL1B mice fed CD+OCA, reverse phase chromatography in neg. ionization mode: obeticholic acid, hyodeoxycholic acid **(D)** In 9m old L2-IL1B mice fed CD vs CD+OCA, no significantly enriched BA were found via reverse phase chromatography in pos. ionization mode.

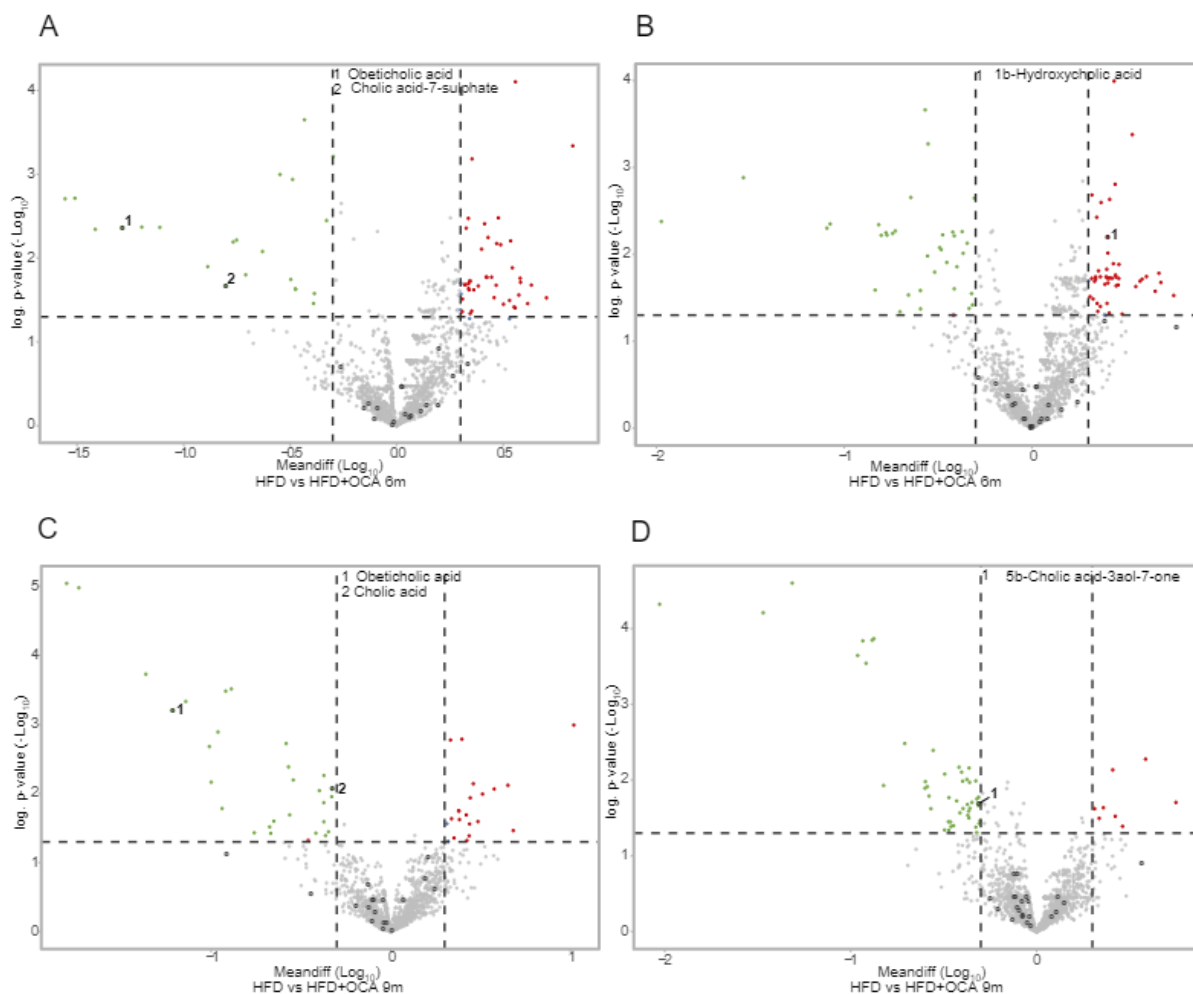


Figure 49: Untargeted metabolomic analysis of cecal content from mice fed HFD vs HFD+OCA via RP chromatography. For untargeted metabolomic analysis, reversed phase chromatography (RP) was performed in the positive and negative ionization mode. Data is depicted as volcano plots showing metabolites enriched in HFD vs HFD+OCA fed mice at 6 and 9 months of age, with significantly enriched metabolites ($p \leq 0.05$, Fold Change ≥ 2 ; equals p-value $\log_{10} \geq 1.3$; Meandiff. $\log_{10} \geq 0.3$) being highlighted in green if enriched in HFD+OCA and in red if enriched in HFD. Detected bile acid derivatives are marked with circles, significantly enriched BA are numbered. **(A)** Significantly enriched BA in 6m L2-IL1B mice fed HFD+OCA, reverse phase chromatography in neg. ionization mode: obeticholic acid, cholic acid-7-sulphate. **(B)** Significantly enriched BA in 6m L2-IL1B mice fed HFD, reverse phase chromatography in pos. ionization mode: 1b-hydroxycholic acid. **(C)** Significantly enriched BA in 9m L2-IL1B mice fed HFD+OCA, reverse phase chromatography in neg. ionization mode: obeticholic acid, cholic acid **(D)** Significantly enriched BA in 9m L2-IL1B mice fed HFD+OCA, reverse phase chromatography in pos. ionization mode: 5b-cholic acid-3a-ol-7-one.

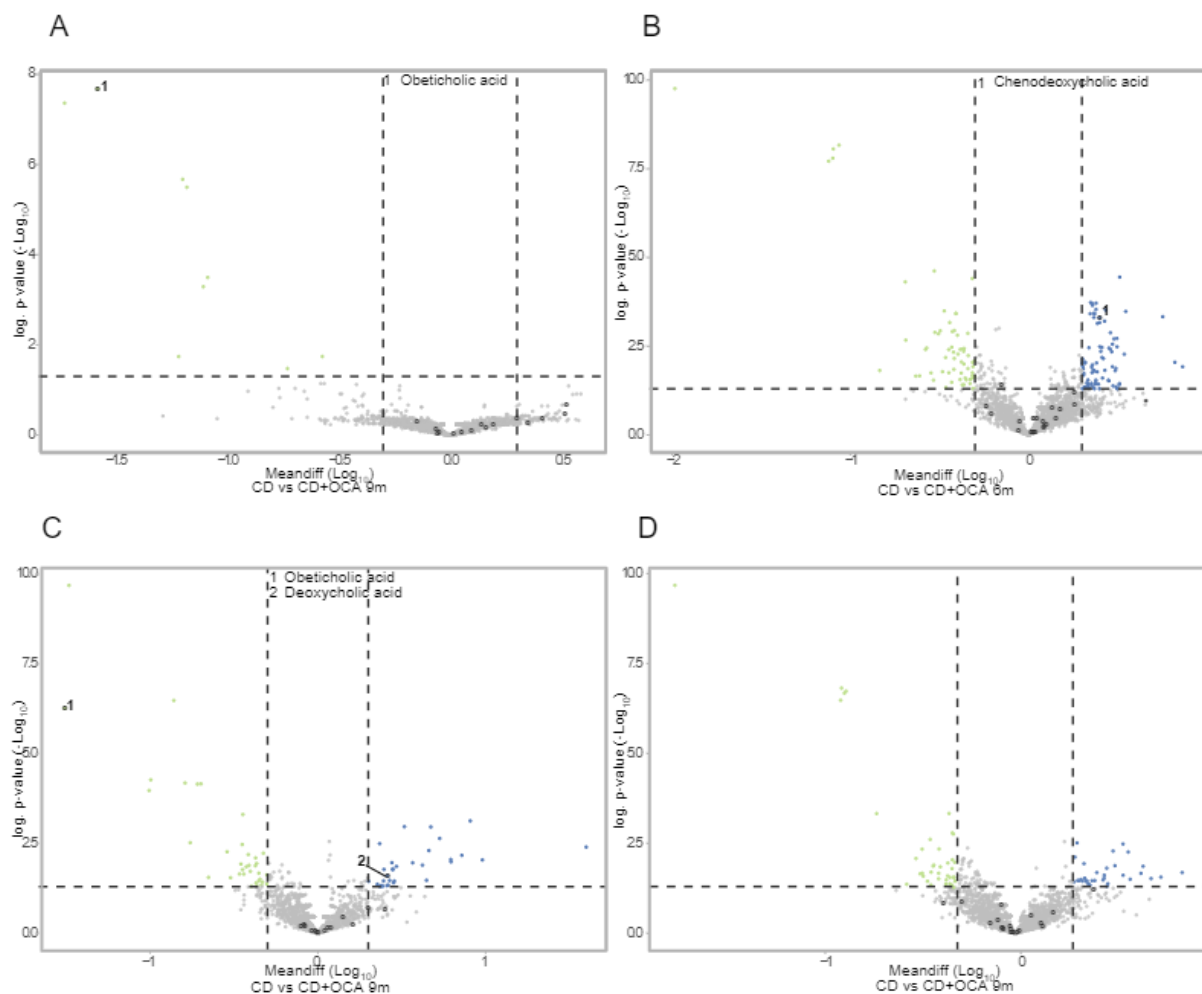


Figure 50: Untargeted metabolomic analysis of cecal content from mice fed CD vs CD+OCA via HILIC. For untargeted metabolomic analysis, hydrophilic interaction chromatography (HILIC) was performed in the positive and negative ionization mode. Data is depicted as volcano plots showing metabolites enriched in CD vs CD+OCA fed mice at 6 and 9 months of age, with significantly enriched metabolites ($p \leq 0.05$, Fold Change ≥ 2 ; equals p -value $\log_{10} \geq 1.3$; Meandiff. $\log_{10} \geq 0.3$) being highlighted in green if enriched in CD+OCA and in blue if enriched in CD. Detected bile acid derivatives are marked with circles, significantly enriched BA are numbered. **(A)** In 6m L2-IL1B mice fed CD+OCA, in hydrophilic interaction chromatography in neg. ionization mode obeticholic acid is detected to be significantly enriched. **(B)** In 6m L2-IL1B mice fed CD, in hydrophilic interaction chromatography in pos. ionization mode chenodeoxycholic acid is detected to be significantly enriched. **(C)** Significantly enriched BA in 9m L2-IL1B mice fed CD+OCA, hydrophilic interaction chromatography in neg. ionization mode: obeticholic acid, deoxycholic acid **(D)** In 9m old L2-IL1B mice fed CD vs CD+OCA, no significantly enriched BA were found via hydrophilic interaction chromatography in pos. ionization mode.

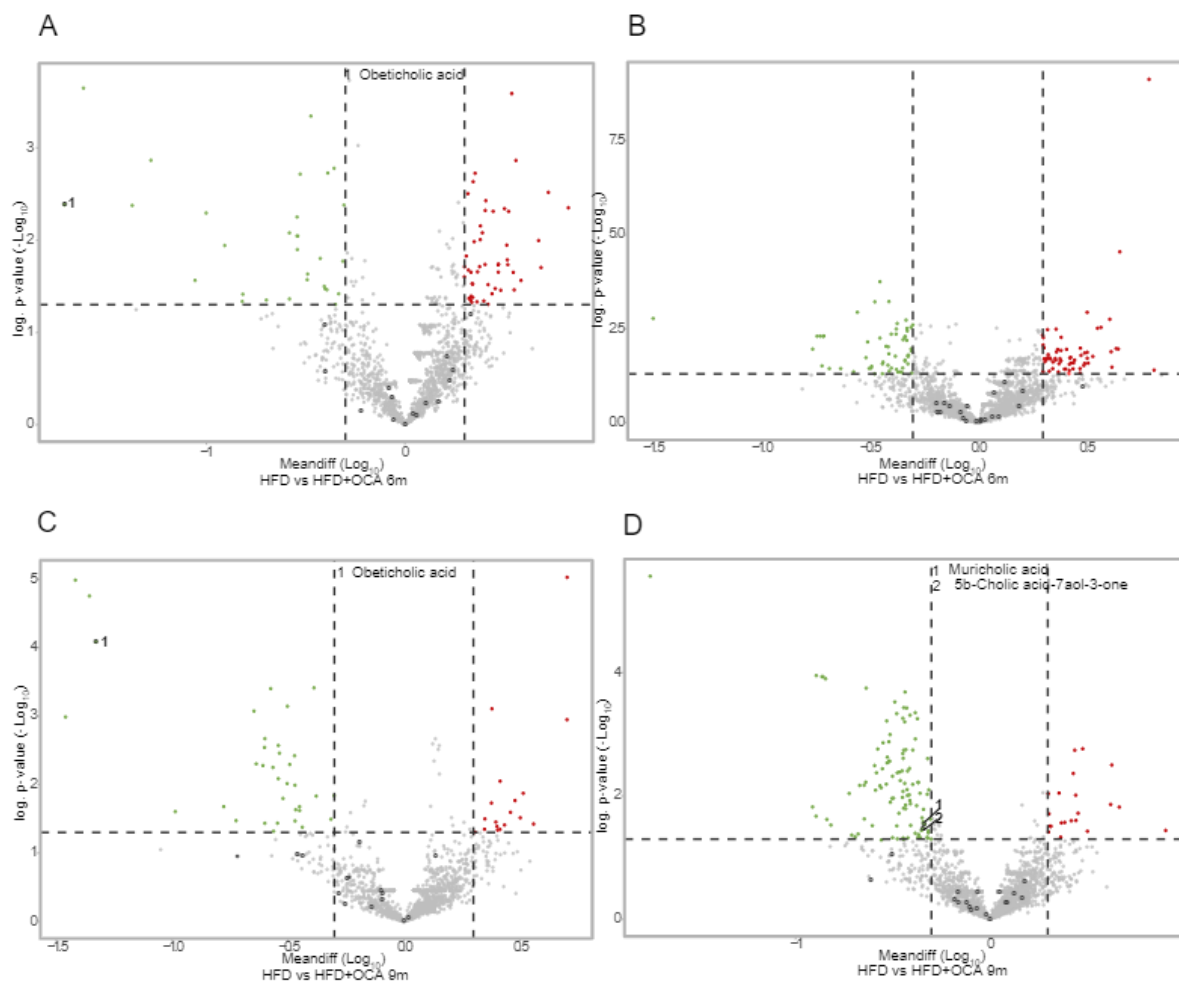


Figure 51: Untargeted metabolomic analysis of cecal content from mice fed HFD vs HFD+OCA via HILIC. For untargeted metabolomic analysis, hydrophilic interaction chromatography (HILIC) was performed in the positive and negative ionization mode. Data is depicted as volcano plots showing metabolites enriched in HFD vs HFD+OCA fed mice at 6 and 9 months of age, with significantly enriched metabolites ($p \leq 0.05$, Fold Change ≥ 2 ; equals p -value $\log_{10} \geq 1.3$; Meandiff. $\log_{10} \geq 0.3$) being highlighted in green if enriched in HFD+OCA and in red if enriched in HFD. Detected bile acid derivatives are marked with circles, significantly enriched BA are numbered. **(A)** In 6m L2-IL1B mice fed HFD+OCA, in hydrophilic interaction chromatography in neg. ionization mode obeticholic acid is detected to be significantly enriched. **(B)** In 6m L2-IL1B mice fed HFD, no significantly enriched BA were found via hydrophilic interaction chromatography in pos. ionization mode. **(C)** In 9m L2-IL1B mice fed HFD+OCA, in hydrophilic interaction chromatography in neg. ionization mode obeticholic acid is detected to be significantly enriched. **(D)** Significantly enriched BA in 9m L2-IL1B mice fed HFD+OCA, hydrophilic interaction chromatography in pos. ionization mode: muricholic acid, 5b-cholic acid-7aol-3-one.

In the fecal content, comparing CD to CD+OCA, BA were also solely enriched in mice treated with CD in HILIC (Fig.52 A-D). While OCA could not be detected anymore, taurine-conjugated BA, CA and its derivatives, CDCA, 7-KLCA and DCA derivatives but also UDCA were enriched in CD mice (Fig.52 A-D).

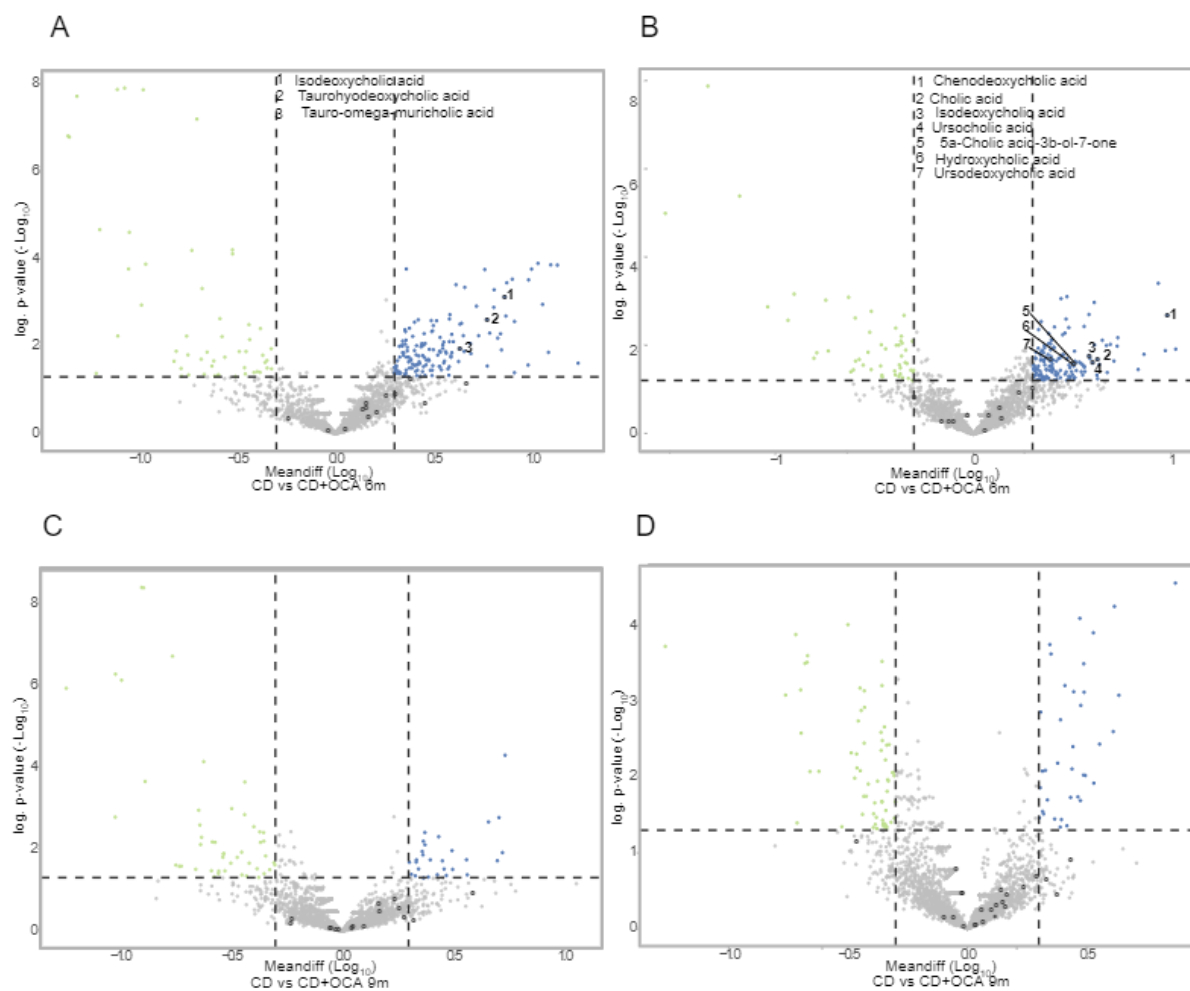


Figure 52: Untargeted metabolomic analysis of fecal content from mice fed CD vs CD+OCA via HILIC. For untargeted metabolomic analysis, hydrophilic interaction chromatography (HILIC) was performed in the positive and negative ionization mode. Data is depicted as volcano plots showing metabolites enriched in CD vs CD+OCA fed mice at 6 and 9 months of age, with significantly enriched metabolites ($p \leq 0.05$, Fold Change ≥ 2 ; equals p -value $\log_{10} \geq 1.3$; Meandiff. $\log_{10} \geq 0.3$) being highlighted in green if enriched in CD+OCA and in blue if enriched in CD. Detected bile acid derivatives are marked with circles, significantly enriched BA are numbered. Bile acids are significantly enriched in CD. **(A)** Significantly enriched BA in 6m L2-IL1B mice fed CD, hydrophilic interaction chromatography in neg. ionization mode: isoleoxycholic acid, taurohyodeoxycholic acid, tauro-omega-muricholic acid **(B)** Significantly enriched BA in 6m L2-IL1B mice fed CD, hydrophilic interaction chromatography in pos. ionization mode: chenodeoxycholic acid, cholic acid, isoleoxycholic acid, ursocholic acid, 5a-cholic acid-3b-ol-7-one, hydroxycholic acid, ursodeoxycholic acid **(C)** No significantly enriched BA could be detected in 9m L2-IL1B mice fed HFD, hydrophilic interaction chromatography in neg. ionization mode. **(D)** No significantly enriched BA could be detected in 9m L2-IL1B mice fed HFD hydrophilic interaction chromatography in pos. ionization mode.

In the feces of HFD mice, we found ALCA to be enriched in HFD and GCDCA to be enriched in HFD+OCA (Fig.53 A). As for the fecal content only HILIC but not RP chromatography – which is more optimal for detection of BA – was performed, potential additional enriched BA could not be detected to draw more refined conclusions especially in HFD mice. The results indicate that in this mouse cohort, treatment with OCA has a strong effect on BA levels in CD and a less pronounced effect in HFD.

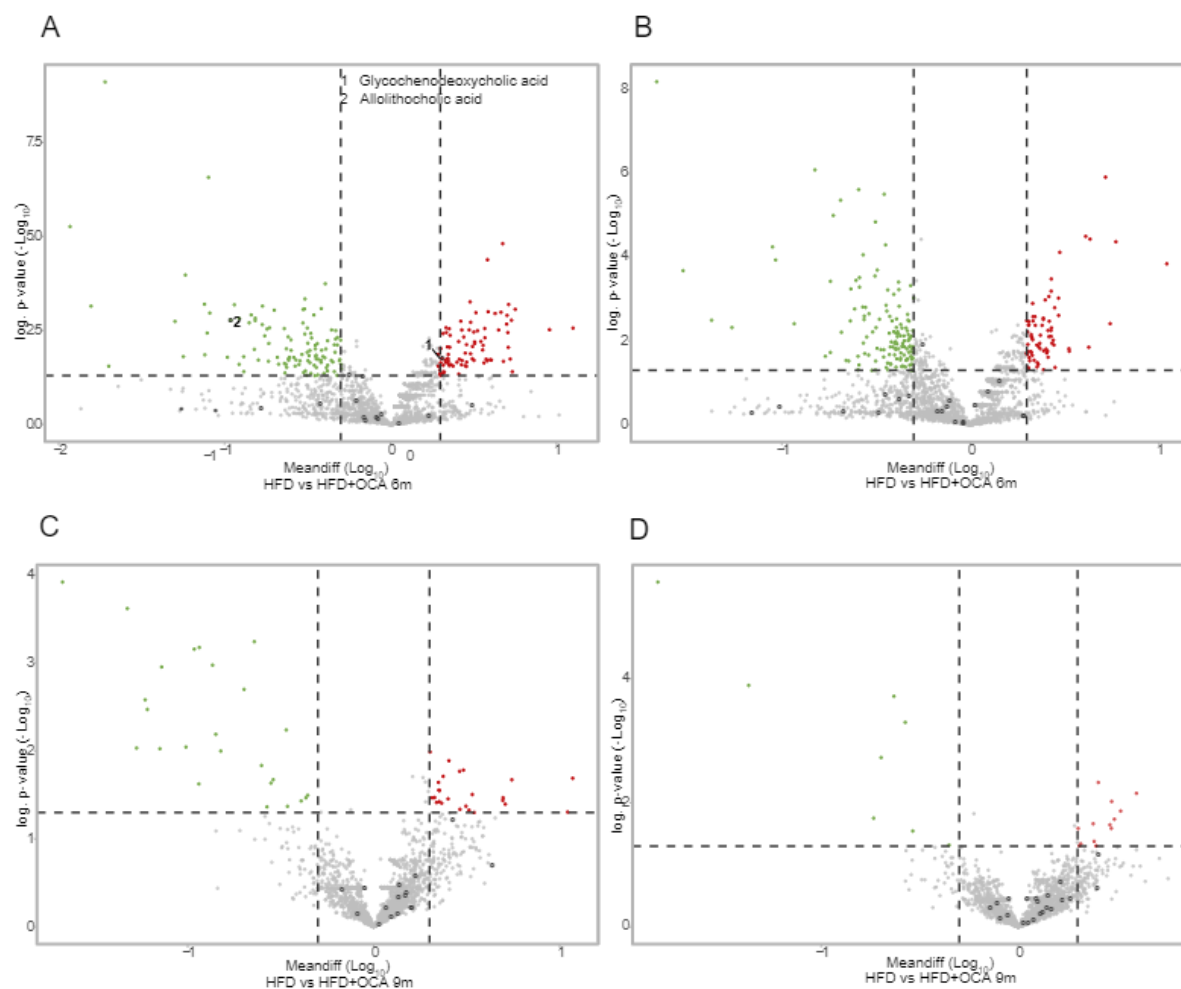


Figure 53: Untargeted metabolomic analysis of fecal content from mice fed HFD vs HFD+OCA via HILIC. For untargeted metabolomic analysis, hydrophilic interaction chromatography (HILIC) was performed in the positive and negative ionization mode. Data is depicted as volcano plots showing metabolites enriched in HFD vs HFD+OCA fed mice at 6 and 9 months of age, with significantly enriched metabolites ($p \leq 0.05$, Fold Change ≥ 2 ; equals p -value $\log_{10} \geq 1.3$; Meandiff. $\log_{10} \geq 0.3$) being highlighted in green if enriched in HFD+OCA and in red if enriched in HFD. Detected bile acid derivatives are marked with circles, significantly enriched BA are numbered. **(A)** Significantly enriched BA in 6-month-old L2-IL1B mice fed HFD vs HFD+OCA, hydrophilic interaction chromatography in neg. ionization mode. Enriched in HFD: glycochenodeoxycholic acid, enriched in HFD+OCA: allolithocholic acid **(B)** No significantly enriched BA could be detected in 6-month-old L2-IL1B mice fed CD, hydrophilic interaction chromatography in pos. ionization mode. **(C)** No significantly enriched BA could be detected in 9-month-old L2-IL1B mice fed HFD, hydrophilic interaction chromatography in neg. ionization mode. **(D)** No significantly enriched BA could be detected in 9-month-old L2-IL1B mice fed HFD hydrophilic interaction chromatography in pos. ionization mode.

3.3.3.4. OCA Treatment Changes the Gut BA Pool of L2-IL1B Mice Fed CD and HFD

After showing a distinct change of the gut metabolome between L2-IL1B mice fed CD and HFD with or without OCA treatment, targeted metabolomic analyses for BA in the cecal and fecal content of the mice provided more information on BA levels between intervention groups. While in the cecum the primary to secondary BA ratio did not change neither in CD nor HFD mice upon treatment with OCA (Supplementary Fig. 10 A, B), against our expectations we found total secondary BA levels to increase in HFD+OCA mice compared to the other intervention groups (Supplementary Fig. 10 C). We further analyzed the change of single cecal BA levels in CD and HFD mice with and without OCA treatment. In CD+OCA compared to CD mice, we found CA-7-ol-3one, CDCA, TCA, DCA and its glycine and taurine conjugates as well as 7,12-DKLCA to be significantly decreased (Fig.54 A). When comparing HFD+OCA to HFD mice, we found an increase in α MCA, a decrease in β MCA acid and increases in both 7- and 12-KLCA (Fig.54 B).

Analyzing the data via PLS-DA we found a relatively clear separation between the clusters of CD and CD+OCA (Fig.54 C), as well as between HFD and HFD+OCA (Fig.54 F). Heatmap and clustering analysis of the bile acid levels of all mice fed CD or CD+OCA showed that, with few exemptions, most BA, especially taurine conjugated and secondary BA were less abundant in CD+OCA compared to CD mice (Fig.54 D). DCA derivatives and CDCA were also the main separators between CD and CD+OCA according to analysis of important features by PLS-DA, displayed as VIP scores (Fig.54 E). Analysis of HFD compared to HFD+OCA mice showed that, in this mouse cohort, HFD+OCA mice clustered between two different clusters of HFD treated mice (Fig.54 G). While BA levels in one cluster of HFD mice were generally relatively low abundant, they were elevated in the other cluster of HFD mice. Also, we found four mice, three of them HFD+OCA and one of them HFD treated, to have generally enriched BA levels compared to all other mice. When comparing HFD and HFD+OCA mice with neither very low nor very high general BA levels, we found enrichment of LCAs in HFD+OCA mice. This finding was mirrored in the analysis of important features by PLS-DA, displayed as VIP scores, showing high abundance of LCA in HFD+OCA mice to be the main separator between groups (Fig.54 H). In this cohort, we also found higher levels of CDCA and MCA but also UDCA and their different conjugates to be enriched in HFD+OCA compared to HFD mice (Fig.54 H).

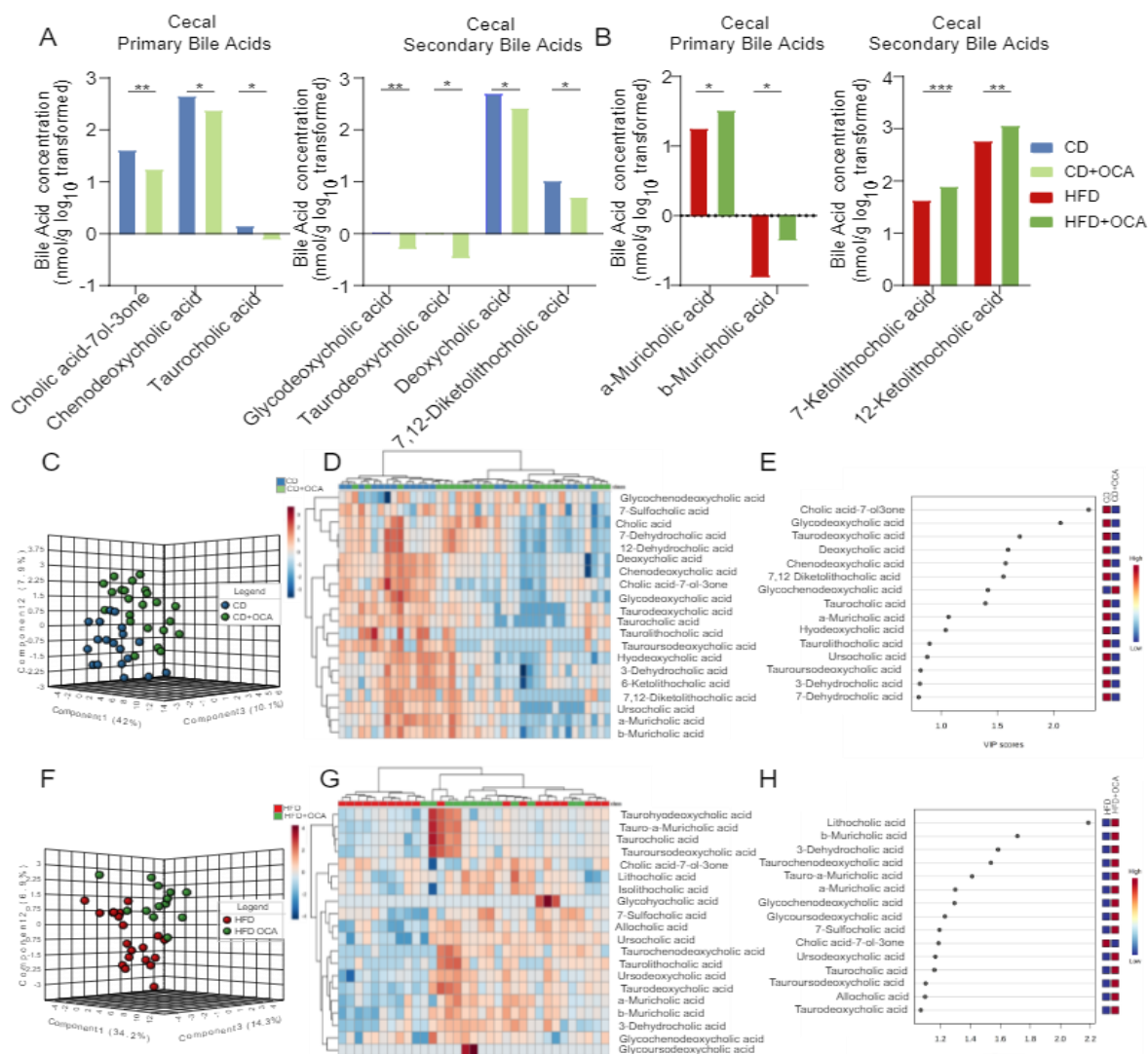


Figure 54: OCA treatment changes the cecal bile acid profile in L2-IL1B mice fed CD or HFD (A) Cecal primary and secondary BA significantly changed between 6-9m old CD and CD+OCA treated L2-IL1B mice (primary BA: cholic acid-7- α -3one $p=0.0020$; chenodeoxycholic acid $p=0.0277$; taurocholic acid $p=0.0312$; secondary BA: glycodeoxycholic acid $p=0.0048$; taurodeoxycholic acid $p=0.0140$; deoxycholic acid $p=0.0217$) **(B)** Cecal primary and secondary BA significantly changed between 6-9m old HFD and HFD+OCA treated L2-IL1B mice (primary BA: a-muricholic acid $p=0.0160$; b-muricholic acid $p=0.0287$; secondary BA: 7-Ketolithocholic acid $p=0.0006$; 12-Ketolithocholic acid $p=0.00538$) **(C)** Partial least squares discriminant analysis (PLS-DA) of fecal BA profiles in L2-IL1B mice fed CD or CD+OCA (mice of all timepoints combined; CD $n=19$; CD+OCA $n=23$). **(D)** Clustering of murine fecal samples and fecal BAs in L2-IL1B mice fed CD or CD+OCA shown as heatmap. Displayed are the top 20 BAs ranked by t-test (euclidean distance measure, ward clustering algorithm). **(E)** Important features identified by PLS-DA. The colored boxes on the right indicate the relative concentrations of the corresponding metabolite in each group under study. The VIP (variable's importance in projection) score of a feature indicates its importance as variable for distinction between groups. It is calculated as a weighted sum of the squared correlations between the PLS-DA components and the original variable, with the weights corresponding to the percentage variation explained by the PLS-DA component in the model. The plot shows most BA, including chenodeoxycholic acid, DCA and their derivatives to be increased in CD compared to CD+OCA, while protective UDCA is decreased in CD and increased in CD+OCA treated mice. **(F)** Partial least squares discriminant analysis (PLS-DA) of fecal BA profiles in L2-IL1B mice fed HFD or HFD+OCA (mice of all timepoints combined; HFD $n=20$; HFD+OCA $n=13$). **(G)** Clustering of murine fecal samples and fecal BAs in L2-IL1B mice fed HFD or HFD+OCA shown as heatmap. Displayed are the top 20 BAs ranked by t-test (euclidean distance measure, ward clustering algorithm). **(H)** Important features identified by PLS-DA. The colored boxes on the right indicate the relative concentrations of the corresponding metabolite in each group under study. The VIP (variable's importance in projection) score of a feature indicates its importance as variable for distinction between groups. It is calculated as a weighted sum of the squared correlations between the PLS-DA components and the original variable, with the weights corresponding to the percentage variation explained by the PLS-DA component in the model. The plot shows most BA but Cholic acid-7- α -3one to be increased in HFD+OCA compared to HFD, with Lithocholic acid being the most important BA in discrimination between HFD and HFD+OCA, while DCA was not significantly increased in HFD+OCA compared to HFD **(A, B)** Data are presented as mean. For statistical evaluation of **(A, B)**, unpaired two-tailed t-tests were used to compare BA levels between the two treatment groups. **(C-H)** Data are presented as mean.

In the feces of the mice, besides minor changes between OCA treated and untreated mice, we found a reduction in the ratio of secondary BA levels in 6-month-old HFD+OCA compared to HFD mice (Supplementary Fig. 11 A, B). Also, in the feces of the mice we found total secondary BA levels to increase in HFD+OCA mice compared to CD mice while BA levels in CD+OCA were significantly lower compared to both HFD and HFD+OCA mice (Supplementary Fig. 10 C). We further analyzed the change of single fecal BA levels in CD and HFD mice with and without OCA treatment. In CD+OCA compared to CD mice, similar to the cecal content we found CA, CDCA, CA-7-ol-3one, DCA and its glycine and taurine conjugates but also DHCAs, sulfocholic acid, α MCA and UCA to be significantly reduced (Fig.55 A). In HFD+OCA compared to HFD mice, we found CA-7-ol-3one to be decreased and ILCA to be elevated (Fig.55 B). Analyzing the data via PLS-DA we found a relatively clear separation between the clusters of CD and CD+OCA (Fig.55 C), as well as between HFD and HFD+OCA (Fig.55 F). Heatmap and clustering analysis of the BA levels of all mice fed CD or CD+OCA showed that, with few exemptions, most BA, especially taurine conjugated and secondary BA were less abundant in CD+OCA compared to CD mice (Fig.55 D). DCA derivatives, CDCA and CA were also the main separators between CD and CD+OCA according to analysis of important features by PLS-DA, displayed as VIP scores (Fig.55 E). Heatmap and clustering analysis of HFD compared to HFD+OCA mice showed that, in this mouse cohort, HFD+OCA mice clustered in three different clusters between two different clusters of HFD treated mice (Fig.55 G). While BA levels in one cluster of HFD and one cluster of HFD+OCA mice were generally relatively low abundant, they were elevated in two other clusters of HFD+OCA and HFD mice. When not considering three mice with extremely high general BA levels, we found enrichment of taurine conjugated and DCA levels in HFD compared to HFD+OCA mice (Fig.55 G). Analysis of important features by PLS-DA, displayed as VIP scores, showed high abundance of CA-7-ol-3one in HFD and of TLCA, GCA, glyoursodeoxycholic acid (GUDCA) and ILCA in HFD+OCA to be the main separators between groups (Fig.55 H). As already suspected after untargeted metabolomic analysis, these results indicate that in this mouse cohort, treatment with OCA had a strong effect on BA levels in CD, comparable to the findings in HFD+OCA compared to HFD in the first mouse cohort. The less pronounced effect in HFD in the second mouse cohort might have arisen from the subset of HFD mice in which total BA levels were relatively low. Also in this cohort, while secondary BA, especially DCA and its derivatives and taurine-conjugated BA were decreased by OCA in CD mice, we see a different pattern in HFD mice. In these mice, mainly ursodeoxycholic acid and its derivatives, glycine conjugated primary BA and partially lithocholic acids are elevated. As OCA still reduces dysplasia scores in HFD mice, it is plausible that not only the reduction of the more cytotoxic DCA and taurine conjugated BA, but also the enrichment of UDCAs, primary BA in general and especially glycine conjugated BA are important players in phenotypic amelioration.

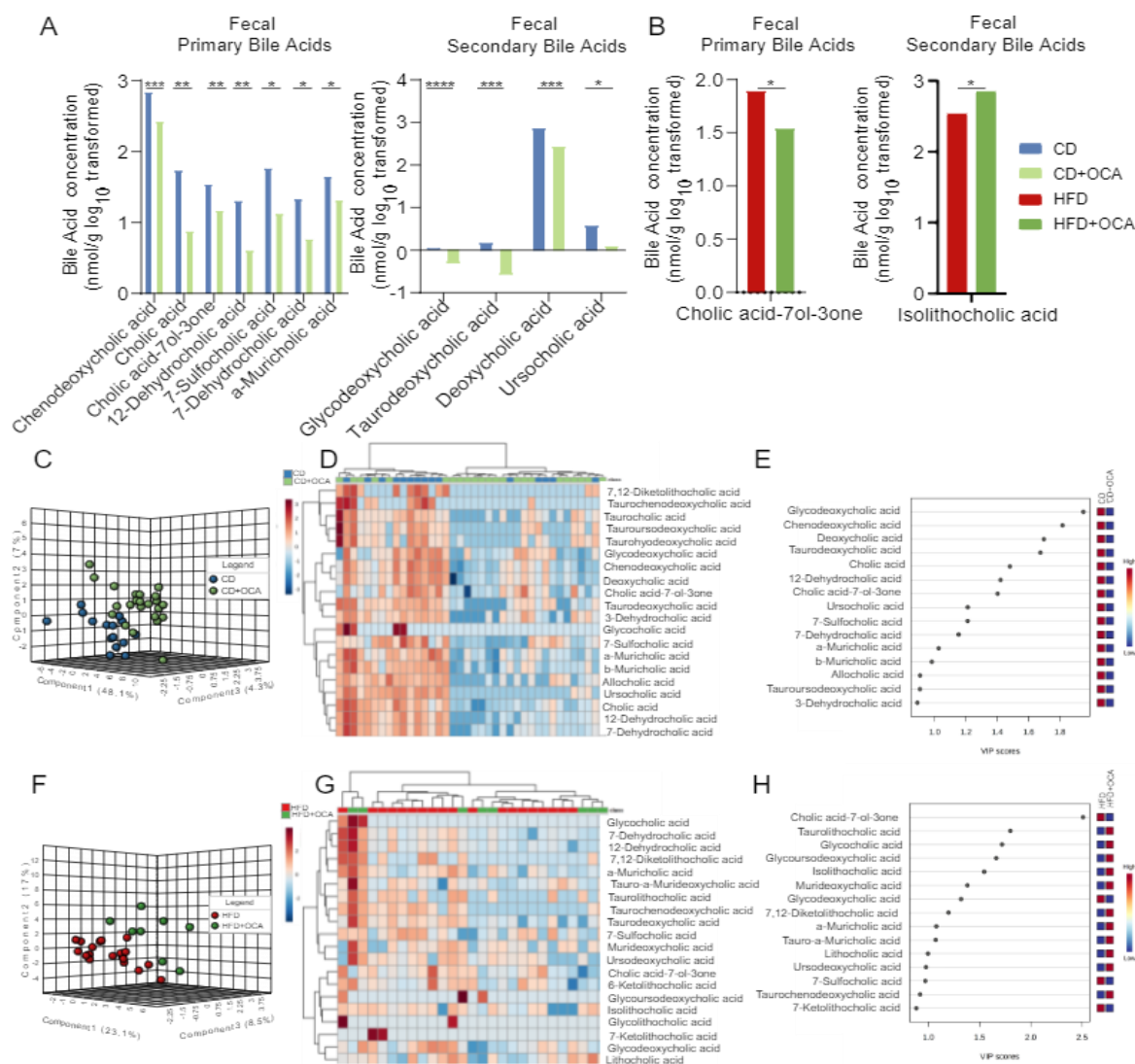


Figure 55: OCA treatment changes the fecal bile acid profile in L2-IL1B mice fed CD or HFD (A) Fecal primary and secondary BA significantly changed between 6-9m old CD and CD+OCA treated L2-IL1B mice (primary BA: chenodeoxycholic acid $p=0.0003$; cholic acid $p=0.0023$; cholic acid-7-ol-3one $p=0.0054$; 12-dehydrocholic acid $p=0.0082$; 7-sulfocholic acid $p=0.0181$; 7-dehydrocholic acid $p=0.0258$; a-muricholic acid $p=0.0497$; secondary BA: glycodeoxycholic acid $p\leq 0.0001$; taurodeoxycholic acid $p=0.0002$; deoxycholic acid $p=0.0004$; ursocholic acid $p=0.0179$) **(B)** Fecal primary BA significantly changed between 6-9m old HFD and HFD+OCA treated L2-IL1B mice (primary BA: cholic acid-7-ol-3one $p=0.0171$; secondary BA: isolithocholic acid $p=0.0337$) **(C)** Partial least squares discriminant analysis (PLS-DA) of fecal BA profiles in L2-IL1B mice fed CD or CD+OCA (mice of all timepoints combined; CD $n=15$; CD+OCA $n=23$). **(D)** Clustering of murine fecal samples and fecal BAs in L2-IL1B mice fed CD or CD+OCA shown as heatmap. Displayed are the top 20 BAs ranked by t-test (euclidean distance measure, ward clustering algorithm). **(E)** Important features identified by PLS-DA. The colored boxes on the right indicate the relative concentrations of the corresponding metabolite in each group under study. The VIP (variable's importance in projection) score of a feature indicates its importance as variable for distinction between groups. It is calculated as a weighted sum of the squared correlations between the PLS-DA components and the original variable, with the weights corresponding to the percentage variation explained by the PLS-DA component in the model. The plot shows most BA, including cholic acid and DCA and its derivatives to be increased in CD compared to CD+OCA, while protective UDCA and LCA are decreased in CD and increased in CD+OCA treated mice. **(F)** Partial least squares discriminant analysis (PLS-DA) of fecal BA profiles in L2-IL1B mice fed HFD or HFD+OCA (mice of all timepoints combined; HFD $n=19$; HFD+OCA $n=8$). **(G)** Clustering of murine fecal samples and fecal BAs in L2-IL1B mice fed HFD or HFD+OCA shown as heatmap. Displayed are the top 20 BAs ranked by t-test (euclidean distance measure, ward clustering algorithm). **(H)** Important features identified by PLS-DA. The colored boxes on the right indicate the relative concentrations of the corresponding metabolite in each group under study. The VIP (variable's importance in projection) score of a feature indicates its importance as variable for distinction between groups. It is calculated as a weighted sum of the squared correlations between the PLS-DA components and the original variable, with the weights corresponding to the percentage variation explained by the PLS-DA component in the model. The plot shows most BA but cholic acid-7-ol3one, glycodeoxycholic acid, 7-sulfocholic acid and 7-ketolithocholic acid to be increased in HFD+OCA compared to HFD, with Lithocholic acid and its derivatives and glycine conjugated BA being the most important BA in discrimination between HFD and HFD+OCA, while DCA was

not significantly increased in HFD+OCA compared to HFD. **(A, B)** Data are presented as mean. For statistical evaluation of **(A, B)**, unpaired two-tailed t-tests were used to compare BA levels between the two treatment groups. **(C-H)** Data are presented as mean.

Expression of bile salt hydrolase (BSH), a microbial enzyme responsible for BA deconjugation was evaluated via quantitative Realtime-PCR (qRT-PCR) in the fecal content of L2-IL1B mice fed CD and HFD with and without OCA treatment. Relative gene expression of BSH decreased significantly in CD mice upon OCA treatment (Fig.56 A). While expression showed the same trend between HFD and HFD+OCA mice, the effect did not reach significance (Fig.56 B).

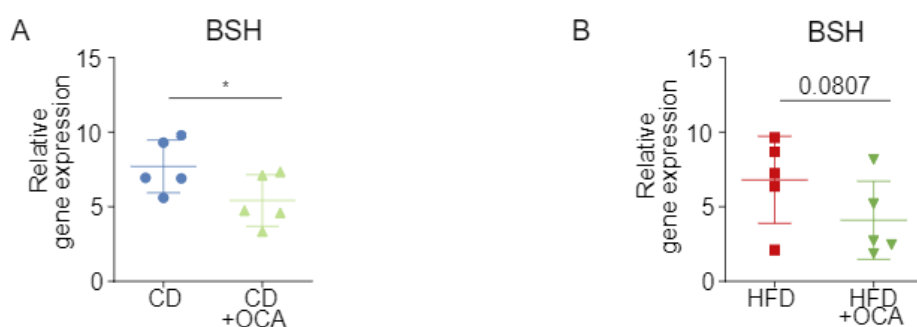


Figure 56: Fecal bile salt hydrolase (BSH) expression decreases in L2-IL1B mice fed CD or HFD upon treatment with OCA **(A)** Relative gene expression of the microbial bile acid deconjugating enzyme BSH in feces of L2-IL1B mice fed CD with or without OCA. In CD+OCA treated mice, BSH gene expression significantly decreases compared to CD mice ($p=0.0365$). **(B)** Relative gene expression of the microbial bile acid deconjugating enzyme BSH in feces of L2-IL1B mice fed HFD with or without OCA. In HFD+OCA treated mice, BSH gene expression trends to decrease compared to HFD mice ($p=0.0807$). **(A, B)** Data are presented as mean with SD, relative gene expression is determined from $2^{-\Delta\Delta CT}$. For statistical evaluation unpaired two-tailed t-tests were used.

3.3.3.5. OCA Treatment Changes Levels of Potentially BA Metabolizing Gut Microbiota in L2-IL1B Mice Fed CD and HFD

The cecal and fecal microbiome of 6- and 9-month-old mice from the mouse cohort fed CD, or HFD with or without OCA treatment was analyzed via 16S-sequencing to assess changes in gut microbiota, especially of those with potential BA metabolizing capacities between groups. Both cecal and fecal samples separated significantly between groups at 6 and 9 months of age (Fig.57; Fig.58) Of note, there were only two data points available for the fecal samples in the 6-month-old HFD+OCA group, thus potentially perturbing the meaningfulness of the results for this group (Fig.58 A). In the cecum, effective richness was higher in both CD+OCA and HFD+OCA mice compared to HFD mice (Fig.59 A). The relative abundance of the phylum *Firmicutes* did not change between CD and CD+OCA mice, was highest in 6-month-old HFD mice and reduced significantly in 9-month-old HFD and 6- and 9-month-old HFD+OCA mice (Fig.59 B). The family of *Bacteroidaceae* decreased in abundance between CD and CD+OCA mice, while they again increased in HFD+OCA mice (Fig.59 C). While the relative abundance of the class of *Clostridia* did not change significantly between CD and CD+OCA mice, abundance increased in 6-month-old HFD mice and decreased in 9-month-old HFD and 6- and 9-month-old HFD+OCA mice (Fig.59 D). Relative abundance of the family of *Lachnospiraceae* similarly increased in 6-month-old HFD mice and decreased in 9-month-old HFD and 6- and 9-month-old HFD+OCA mice (Fig.59 E). Relative abundance of the family of *Desulfovibrionaceae* increased in HFD and HFD+OCA mice compared to the other intervention groups (Fig.59 F). Almost all bacterial strains in the family *Desulfovibrionaceae* are sulfur reducing. Especially the genus *Bilophila* was already shown to reduce the sulphated amino acid taurine, and to produce toxic hydrogen sulfide²⁸⁸. Figure 59 G shows correlation of cecal microbiota with potential BA metabolizing capacities with disease scores. Correlations were generally less pronounced compared to correlation analyses in the first mouse cohort. *Desulfovibrionaceae* which were more abundant in HFD and HFD+OCA mice compared to CD and CD+OCA mice and the genus *unknown Lachnospiraceae*, with its family *Lachnospiraceae* being most abundant in HFD mice were positively correlated with dysplasia scores. *Helicobacter* is not BA metabolizing but contains the species *H. Pylori*. *H. Pylori* was shown to correlate negatively with EAC while positively with gastric cancer in humans was negatively correlated with disease severity¹²⁰⁻¹²².

Analysis of the fecal content of CD and HFD with and without OCA treatment did only show few bacterial species to be differently abundant between intervention groups. None of the potentially BA metabolizing bacteria were differently abundant.

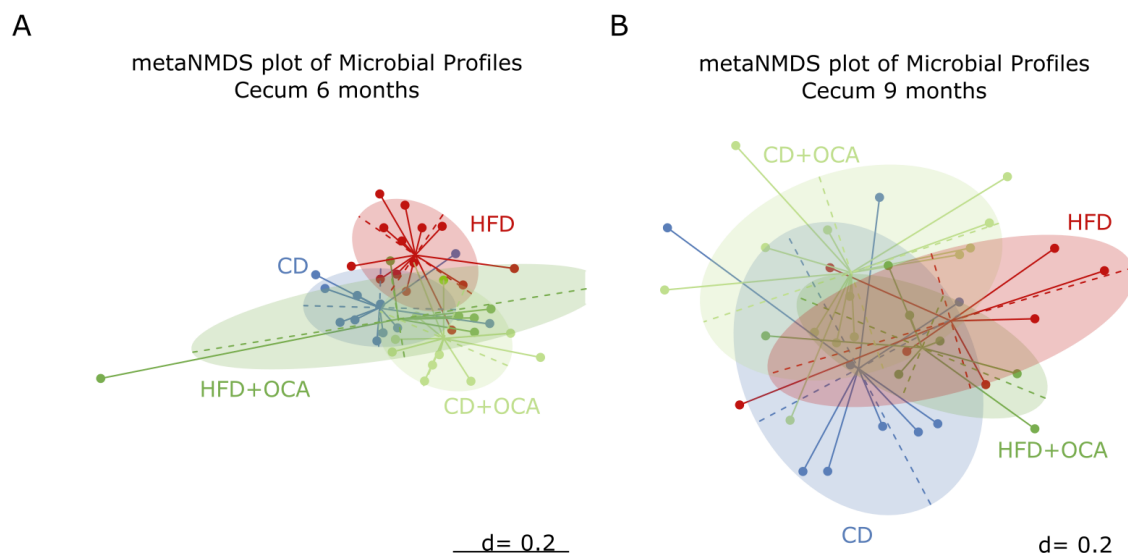


Figure 57: Beta diversity comparison for fecal microbial profiles: meta-Normalized Multidimensional Scaling (metaNMS) plots of feces from 6- and 9-month-old L2-IL1B mice fed CD, HFD, CD+OCA or HFD+OCA (A) Significant separation of study groups (cecum of 6-month-old L2-IL1B mice fed CD, HFD, CD+OCA or HFD+OCA) in terms of bacterial community composition was detected ($p=0.001$). (B) Significant separation of study groups (cecum of 9-month-old L2-IL1B mice fed CD, HFD, CD+OCA or HFD+OCA) in terms of bacterial community composition was detected ($p=0.002$). Permutational Multivariate Analysis of Variance (PERMANOVA) test was used for statistical comparison. The microbiota phylogenetic distances were evaluated through the generalized UniFrac distance. Each point represents the microbiota composition of one sample.

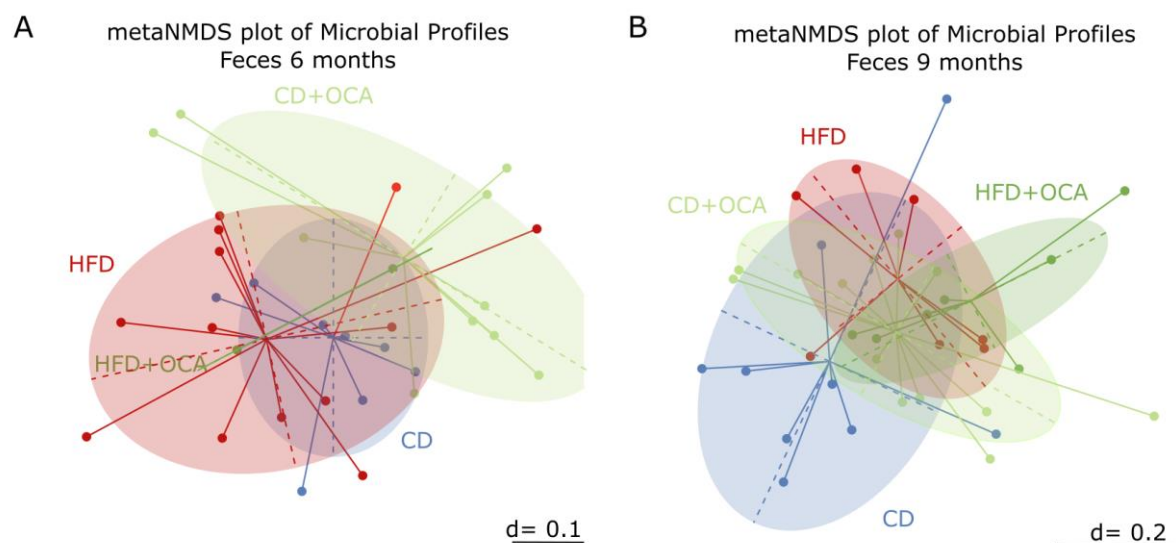


Figure 58: Beta diversity comparison for fecal microbial profiles: meta-Normalized Multidimensional Scaling (metaNMS) plots of feces from 6- and 9-month-old L2-IL1B mice fed CD, HFD, CD+OCA or HFD+OCA (A) Significant separation of study groups (feces of 6-month-old L2-IL1B mice fed CD, HFD, CD+OCA or HFD+OCA) in terms of bacterial community composition was detected ($p=0.001$). (B) Significant separation of study groups (feces of 9-month-old L2-IL1B mice fed CD, HFD, CD+OCA or HFD+OCA) in terms of bacterial community composition was detected ($p=0.001$). Permutational Multivariate Analysis of Variance (PERMANOVA) test was used for statistical comparison. The microbiota phylogenetic distances were evaluated through the generalized UniFrac distance. Each point represents the microbiota composition of one sample.

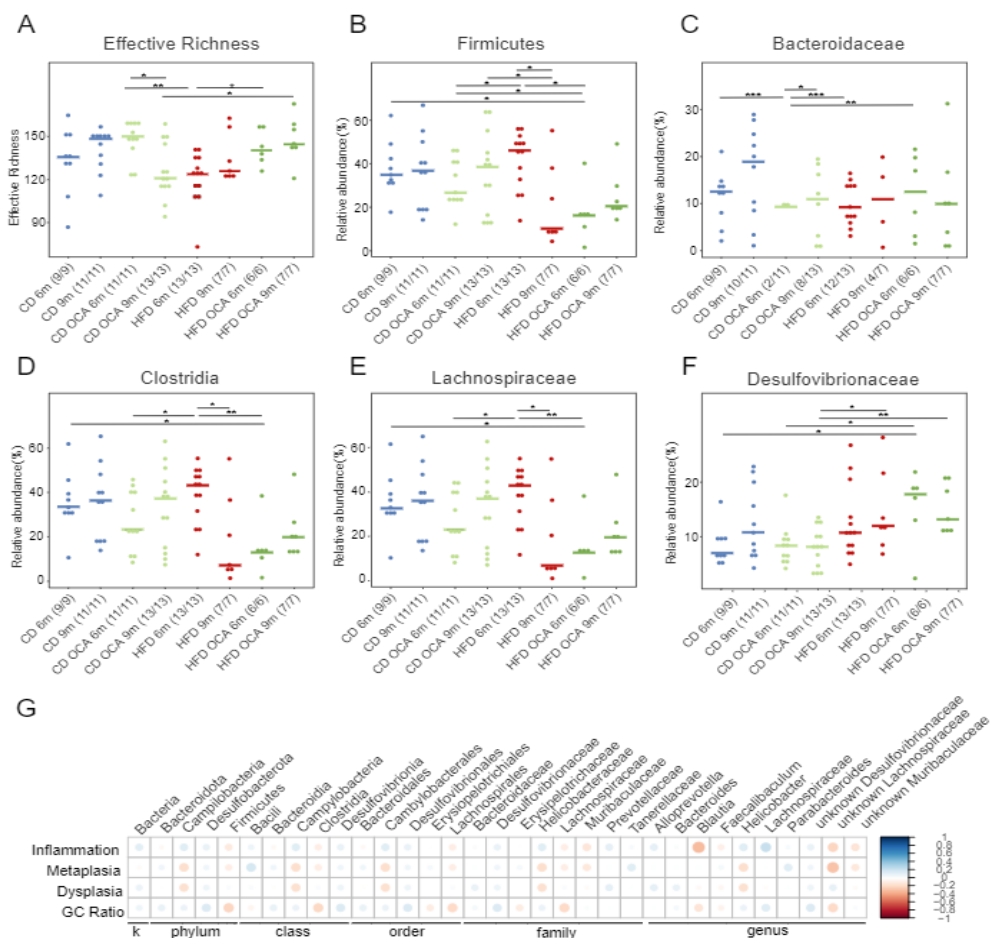


Figure 59: OCA treatment changes the BA metabolizing microbial profile in the cecum of L2-IL1B mice fed CD and HFD (A) Representation of the effective richness and cecal relative abundance (%) of bacterial families with bile acid metabolizing capacities between L2-IL1B mice fed CD, HFD or HFD+OCA at 6m and 9m of age. Effective richness is significantly lower in 6m old HFD compared to CD+OCA and HFD+OCA mice and increases in 9m old HFD+OCA compared to CD+OCA mice (CD+OCA6m – HFD6m $p=0.0010$; HFD6m – HFD+OCA6m $p=0.0177$; CD+OCA9m – HFD+OCA9m $p=0.0429$; CD+OCA6m – CD+OCA9m $p=0.0082$). **(B)** The relative abundance of the phylum Firmicutes is decreasing in 6m old HFD+OCA compared to CD, CD+OCA and HFD mice (CD6m – HFD+OCA6m $p=0.0120$; CD+OCA6m – HFD+OCA6m $p=0.0273$; HFD6m – HFD+OCA6m $p=0.0047$) and in 9m old CD+OCA compared to HFD mice (CD+OCA9m – HFD9m $p=0.0456$) while it increases in 6m old HFD compared to CD+OCA mice ($p=0.0301$). Abundance also drops in 9m old compared to 6m old HFD mice ($p=0.0236$). **(C)** The family of Bacteroidaceae significantly decreases in relative abundance in 6m old CD+OCA compared to CD mice ($p=0.0003$) and increases in 9m old CD+OCA, 6m old HFD and 6m old HFD+OCA mice compared to 6m old CD+OCA mice (CD+OCA6m – CD+OCA9m $p=0.0472$; CD+OCA6m – HFD6m $p=0.0005$; CD+OCA6m – HFD+OCA6m $p=0.0023$). **(D)** The relative abundance of the class of Clostridia is decreasing in 6m old HFD+OCA compared to CD and HFD mice (CD6m – HFD+OCA6m $p=0.0496$; HFD6m – HFD+OCA6m $p=0.0047$) while it increases in 6m old HFD compared to CD+OCA mice ($p=0.0301$). Abundance also drops in 9m old compared to 6m old HFD mice ($p=0.0236$). **(E)** The relative abundance of the family of Lachnospiraceae is decreasing in 6m old HFD+OCA compared to CD and HFD mice (CD6m – HFD+OCA6m $p=0.0360$; HFD6m – HFD+OCA6m $p=0.0047$) while it increases in 6m old HFD compared to CD+OCA mice ($p=0.0352$). Abundance also drops in 9m old compared to 6m old HFD mice ($p=0.0236$). **(F)** Relative abundance of the family of Desulfovibrionaceae is increasing in 6m old HFD+OCA compared to CD and CD+OCA mice (CD6m – HFD+OCA6m $p=0.0496$; CD+OCA6m – HFD+OCA6m $p=0.0477$) and in 9m old HFD and HFD+OCA compared to CD+OCA mice. (CD+OCA9m – HFD9m $p=0.0346$; CD+OCA9m – HFD+OCA9m $p=0.0008$). **(G)** Correlation analysis between the abundance of bacterial families with bile acid metabolizing capacities versus inflammation, metaplasia, and dysplasia scores as well as goblet cell (GC) ratio. Correlation analyses were performed using the Rhea pipeline for analysis of 16S-sequencing data. The class desulfovibrionaceae, the genus *Alloprevotella* (- class Prevotellaceae) and unknown Lachnospiraceae are positively correlated with dysplasia scores, while the family Helicobacteraceae with the genus *Helicobacter*. (family Helicobacteraceae, order Campylobacteriales, class Campylobacteria, phylum Campylobacteria) is negatively correlated with metaplasia and dysplasia but positively correlated with inflammation scores. In this model, Clostridia did not show a significant correlation with dysplasia scores. For **(A-F)** relative abundances of microbiota are represented with mean. For statistical analysis, pairwise Wilcoxon rank sum test or fisher's exact test, if appropriate, were used.

3.3.3.6. Potentially BA Metabolizing Gut Microbiota are Linked to BA Levels

Having shown a correlation between BA modulating bacterial communities and OCA treatment, although detecting less pronounced effects on disease severity, in the following we correlated the levels of BA with the abundance of bacterial genera in the cecum (Fig.60) and feces (Fig.61) of the mice. In the cecum, we found positive correlations of the class of *Clostridia* with CDCA, muricholic acids, DCA, LCA, and KLCA acids but also with UDCA while negative correlations were detected with GCA and some of the taurine-conjugated BA. The family of *Lachnospiraceae* correlated weakly positively with α MCA and γ MCA, LCA and some of its derivatives and negatively with the primary BA CA and CDCA and their conjugates. Interestingly, *Desulfovibrionaceae* were not found to be positively correlated with taurine conjugated BA. In the correlation analyses of the fecal microbiota with BA levels (Fig.61), we found positive correlations of the class of *Clostridia* and the family of *Lachnospiraceae* with most BA. Interestingly, the family of *Desulfovibrionaceae* correlated negatively with taurine conjugated BA and positively with glycine conjugated BA.

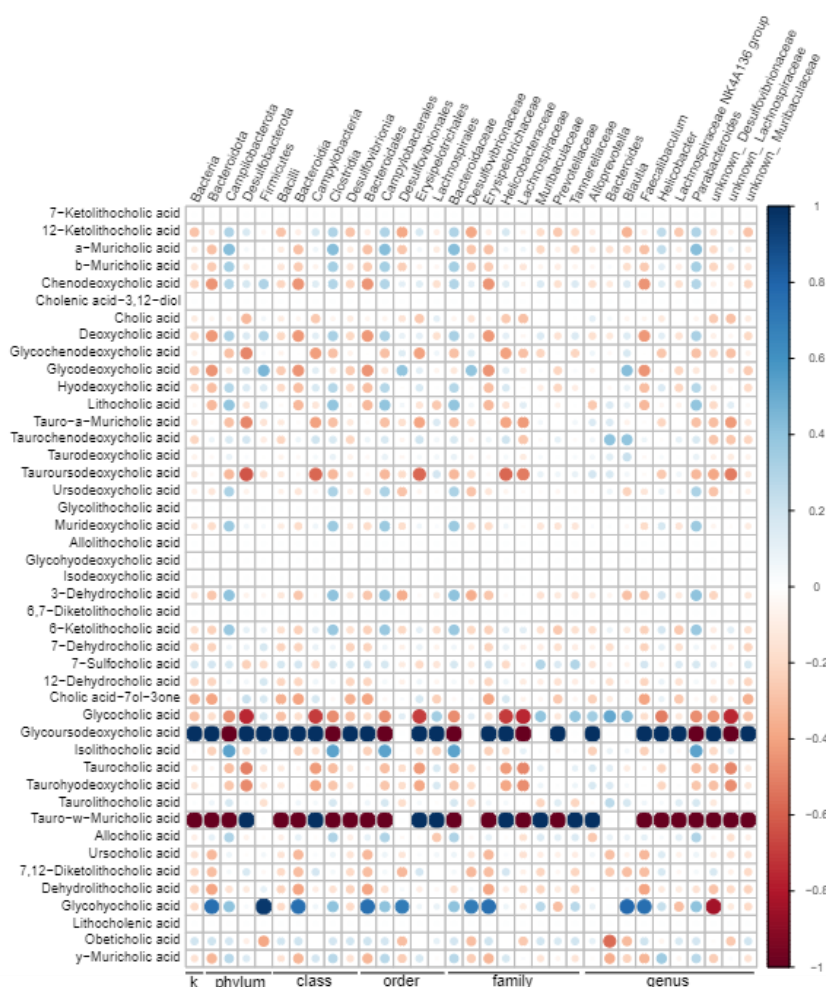


Figure 60: Correlation of the relative abundance of bacteria from kingdom (k) to genus level in the cecum of L2-IL1B mice fed CD, CD+OCA, HFD and HFD+OCA with cecal BA levels. Correlation analyses were performed using the Rhea pipeline for 16S-sequencing data.

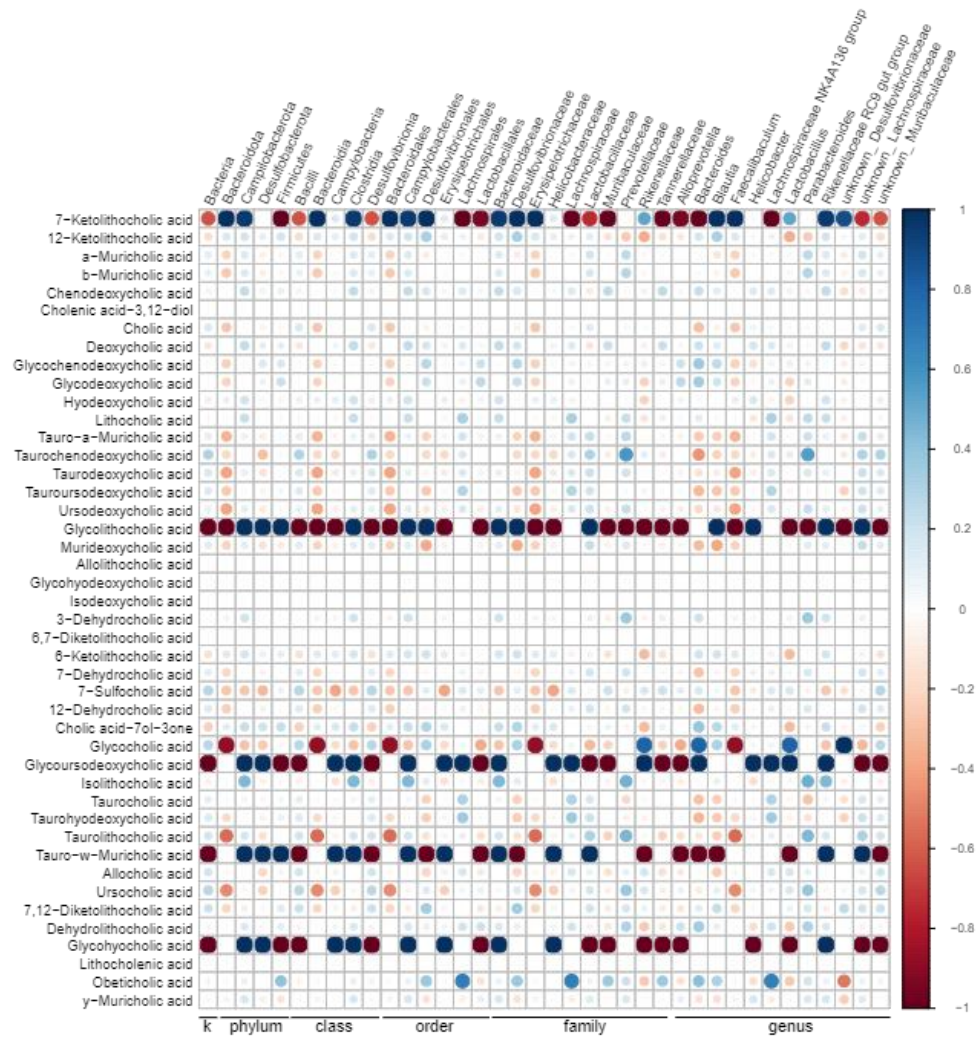


Figure 61: Correlation of the relative abundance of bacteria from kingdom (k) to genus level in the stool of L2-IL1B mice fed CD, CD+OCA, HFD and HFD+OCA with fecal BA levels. Correlation analyses were performed using the Rhea pipeline for 16S-sequencing data.

3.3.3.7. OCA Treatment Ameliorates Side Effects of HFD in Digestive Organs

To examine potential effects of OCA on different organs, tissues with FXR expression (liver, kidney, intestines) and the lung were stained by HE staining and examined for changes in morphology (Fig.62 A). Lung tissue was included, as some mice showed signs of lung infection. We later found lung infections to be cohort and strain independent but associated to the mouse room. Livers of mice treated with HFD showed hepatocyte ballooning and increased lipid deposition, which could be rescued by treatment with OCA. We also found OCA treatment to increase colon crypt length in HFD mice (Fig.62 B). Increasing colon crypt length might be a result of less damage through production of secondary BA, as deconjugated BA undergo bacterial driven 7α -dehydroxylation in the colon²⁰³.

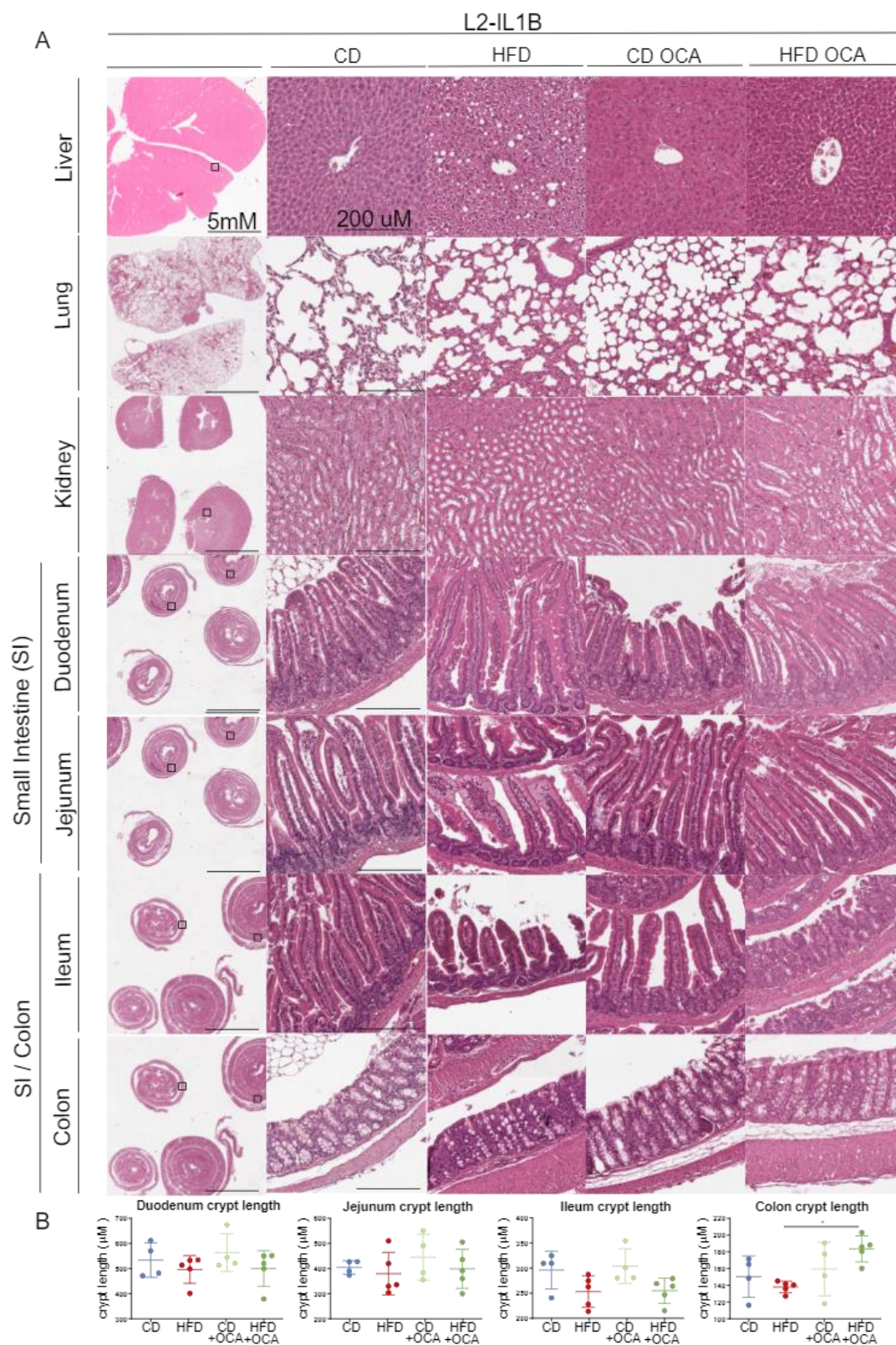


Figure 62: The influence of OCA treatment on tissue morphology of CD or HFD fed mice in respective organs (A) Tissue morphology of CD, HFD, and CD and HFD cohorts treated with OCA in 9-month-old L2-IL1B mice. Depicted are tissues with FXR expression (liver, kidney, intestines) and lung. Lung was included as some mice showed signs of lung infection, which was excluded to be strain or treatment specific but confirmed to be mouse room associated. Livers in mice treated with HFD showed hepatocyte ballooning and increased lipid deposition, which could be rescued by treatment with OCA. Colon crypt length decreased in HFD treated mice, which could also be rescued by OCA treatment. (B) Crypt length in μm in all intestinal compartments. OCA treatment rescues shortening of colonic crypts in L2-IL1B mice fed HFD ($p=0.0177$). ($n=4$). For (B) data are presented as mean + SD; For statistical evaluation, ordinary one-way ANOVA with Tukey-correction was performed.

3.3.3.8. OCA Treatment Decreases Neutrophil Infiltration in the Cardia of HFD Mice and Increases the Abundance of NK and NKT Cells

To evaluate potential effects of OCA treatment on the immune profile in 6- or 9-month-old L2-IL1B mice on CD or HFD, flow cytometry analysis for two panels of myeloid and t-cells were performed. Flow cytometry for immune cell analysis was performed on esophagus, cardia, rest of stomach, liver, small intestinal and colon tissue, and blood of the mice. OCA did not have a strong impact on the immune profile of the mice. Relevant changes between 9-month-old L2-IL1B mice fed HFD compared to HFD+OCA are shown in Fig. 63. Quantification of neutrophils in the cardia region of HFD compared to HFD+OCA mice (Fig.63 A) showed a significant decrease of neutrophils in mice treated with OCA (Fig.63 B). Quantification of NK cells in the cardia region of HFD compared to HFD+OCA mice (Fig.63 C) showed a significant increase of NK cells in mice treated with OCA (Fig.63 D). Quantification of activated NKT cells in the blood of HFD compared to HFD+OCA mice (Fig.63 E) showed a significant increase of activated NKT cells in mice treated with OCA (Fig.63 F).

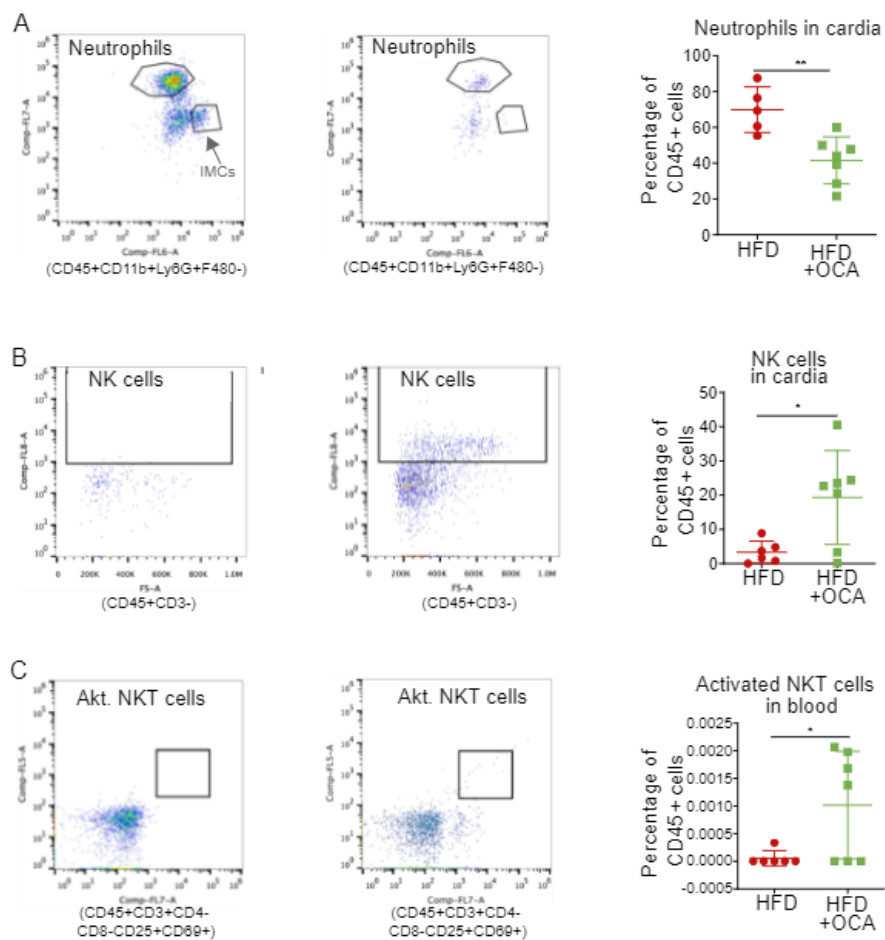


Figure 63: OCA treatment decreases neutrophil infiltration in the cardia and increases cardia NK and blood NKT cell levels. Quantification of flow cytometry analysis of tissue and blood samples of 9-month-old L2-IL1B mice treated with CD or HFD with or without OCA revealed few changes between immune cell populations (n=6-7). Relevant changes between HFD and HFD+OCA mice are depicted. **(A)** Representative gating for quantification of neutrophils in the cardia region of L2-IL1B mice fed HFD or HFD+OCA. **(B)** The percentage of neutrophils decreases significantly in cardia tissue of HFD+OCA compared to HFD mice (p=0.0039). **(C)** Representative gating for quantification of NK cells in the cardia region of L2-IL1B mice fed HFD or HFD+OCA. **(D)** The percentage of NK cells increases significantly in cardia tissue of HFD+OCA compared to HFD mice (p=0.0180). **(E)** Representative gating for quantification of activated (CD25+CD69+) NKT cells in the blood of L2-IL1B mice fed HFD or HFD+OCA. **(F)** The percentage of activated (CD25+CD69+) NKT cells increases significantly in the blood of HFD+OCA compared to HFD mice (p=0.0368). Graphs **(B, D, F)** show the percentage of gated cells compared to CD45+ cells. Values are depicted as mean with SD. For statistical analysis, unpaired, two-tailed t-tests were performed.

3.4. Assessment of the Microbiome and Bile Acid Profile in Patients with BE, Dysplastic BE and EAC

3.4.1. The BA Pool in the Stool of Patients Shifts with the Disease State

Targeted metabolomic analyses of single BA in the stool of control patients undergoing endoscopy, BE, dysplasia and EAC patients showed a shift of the BA profile with disease state. In the clustering analyses, samples from dysplasia patients were excluded due to low sample size and thus limited informative value.

Analyzing the data via PLS-DA we found no clear separation between the clusters of control, BE and EAC patients, but while the BA profile of some of the diseased patients clustered with control patients, in both BE and EAC state the profile of some patients clustered separately (Fig.64 A). Heatmap and clustering analysis of the mean bile acid levels of all control, BE and EAC patients showed a distinct shift between BA levels in the different disease states (Fig.64 B). While GCA, GDCA, 7-DHCA acid and UCA reduced with disease progression, DCA, LCA, and CA-7-ol-3one levels increased in BE compared to control patients and again decreased in EAC patients. DHLCA and 12-KLCA levels increased with disease progression. Cholenic acid-3-12-diol, CDCA and its glycine and taurine conjugates, TDCA, and TCA and also ACA, 7-sulfocholic acid, and UDCA were strongly elevated in EAC patients compared to both BE and Ctrl patients. Analysis of important features by PLS-DA, displayed as VIP scores, showed high abundance of 7-sulfocholic acid and TCA in EAC and of DCA in BE to be the main separators between groups (Fig.64 C).

The enrichment of distinct BA in different disease states indicates different roles of BA during disease onset and progression, with DCA seeming to be the main driving BA in onset of disease. The enrichment of bile acids of the classical synthesis pathway – CDCA and DCA – but also of taurine conjugated bile acids and of CA-7-ol-3one correlates with the findings in the mouse cohorts.

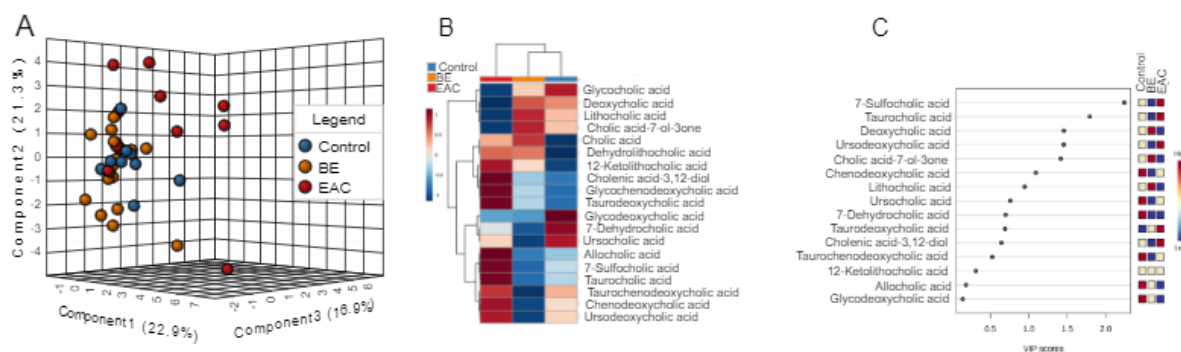


Figure 64: The human fecal BA profile changes in BE and EAC compared to control patients (A) Partial least squares discriminant analysis (PLS-DA) of BA profiles in the stool of human Control, BE and EAC patients (Control n=9; BE n=18; EAC n=11). BE and EAC patient samples are partially clustering differently than of the control samples, indicating a shift between the fecal BA pool between control and diseased patients. **(B)** Clustering of the mean stool BA levels in human control, BE and EAC patients shown as heatmap. Displayed are the top 20 BAs ranked by t-test (euclidean distance measure, ward clustering algorithm). The heatmap shows distinct BA profiles for all three patient groups. **(C)** Important features for distinction of groups identified by PLS-DA. The colored boxes on the right indicate the relative concentrations of the corresponding metabolite in each group under study. The VIP (variable's importance in projection) score of a feature indicates its importance as variable for distinction between groups. It is calculated as a weighted sum of the squared correlations between the PLS-DA components and the original variable, with the weights corresponding to the percentage variation explained by the PLS-DA component in the model. The plot indicates 7-sulfocholic acid, taurocholic acid and deoxycholic acid to be the three main distinguishing BA between groups, while the concentrations of 7-sulfocholic acid and taurocholic acid are highest in EAC compared to the other groups, and deoxycholic acid is highest in BE compared to the other groups.

Expression of the microbial BA deconjugating enzyme bile salt hydrolase (BSH) was analyzed via quantitative Realtime-PCR (qRT-PCR) in the stool of patients with different disease states. Relative gene expression of BSH increased and correlated significantly with severity of the disease (Fig.65 A, B).

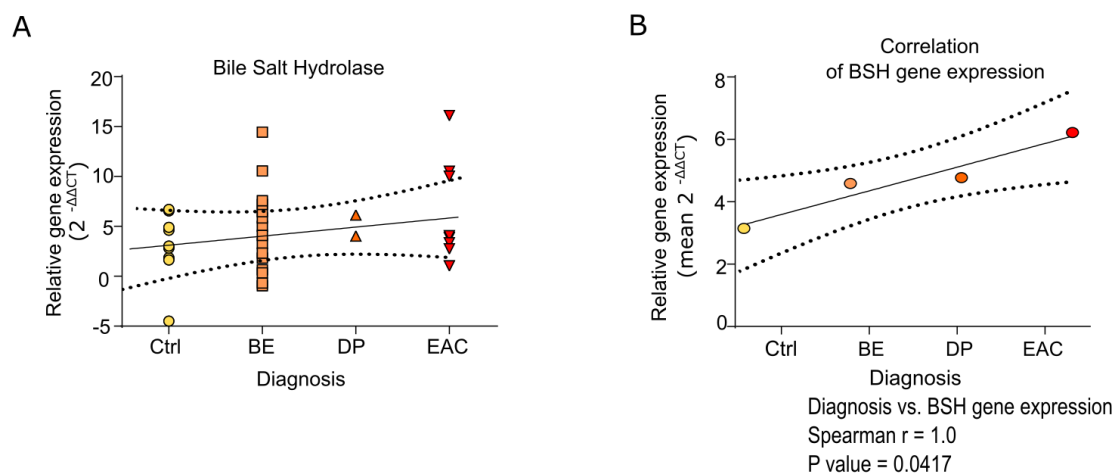


Figure 65: Bacterial bile salt hydrolase (BSH) expression in the stool of human patients increases with disease severity (A) Relative gene expression of the microbial bile acid deconjugating enzyme BSH in stool of human control, BE, dysplasia (DP) and EAC patients. Relative gene expression is depicted as $2^{-\Delta\Delta CT}$ and increases with diagnosis. **(B)** Spearman correlation analysis of the mean BSH gene expression in the stool of human control, BE, dysplasia (DP) and EAC patients shows a significant correlation between relative gene expression and diagnosis ($p=0.0417$).

3.4.1. The BA Pool in the Serum of Patients Shifts with the Disease State

To further elucidate the role of the shifted BA pool in the stool of the patients, and to verify a potential systemic effect of the shifted BA pool on disease progression, we analyzed targeted metabolomic analyses of single BA in the serum of control patients undergoing endoscopy, BE, dysplasia and EAC patients. Comparing single BA levels in the serum of BE and EAC to control patients, we found elevated levels of TUDCA in both patient groups (Fig.66 A, B). Analyzing the data via PLS-DA we found no clear separation between the clusters of control, BE and EAC patients (Fig.66 C). Heatmap and clustering analysis of the mean bile acid levels of all control, BE and EAC patients still showed a distinct shift between BA levels in the different disease states (Fig.66 D). GCA, similar to stool analyses, but also ILCA and 7,12-DKLCA levels were elevated in control patients. Similar to stool analyses, DCA and LCA, but also ACA, LCA, 7- and 12-KLCA levels increased in BE compared to control patients and again decreased in EAC patients. CA-7-ol-3one, TUDCA, DHLCA, GDCA, UDCA and cholenic acid-3-12-diol levels were elevated in both BE and EAC and GUDCA, TCDCA, DHCA, 7-sulfocholic acid, TDCA and GCDCA levels were strongly enriched in EAC compared to control and BE patients. Analysis of important features by PLS-DA, displayed as VIP scores, showed high abundance of TCDCA in EAC and of ACA and LCA in BE to be the main separators between groups (Fig.66 E). Also elevated levels of taurodeoxycholic acid in EAC and DCA in BE contributed to group separation. When comparing bile acid levels between control and all diseased patients we found TUCA and TDCA levels to be significantly enriched with disease (Fig.66 F). When comparing BE to dysplasia and EAC patients we found TCDCA and GUDCA to be enriched in dysplasia and EAC (Fig.66 G). Altogether, depending on the groups selected for comparison we found different BA to be significantly regulated between groups. Consistently, BA in the serum of patients were upregulated in correlation with severity of the disease state. The majority of BA found to be enriched in disease was found to be taurine conjugated and synthesized via the classical BA synthesis pathway, with CDCA and DCA being its main BA. Although the results were not as clear as in the murine experiments due to the given higher complexity of influencing factors in patients and the comparatively low sample number, these results reflect the findings in the murine analyses. Taurine conjugated BA and BA of the classical synthesis pathway, especially DCA derivatives are elevated in stool and serum of patients with increasing disease severity similar to findings in L2-IL1B mice treated with HFD. These results are consistently indicating a role of the axis of diet, BA metabolizing microbiome and gut and especially serum BA levels on disease onset and progression in BE and EAC.

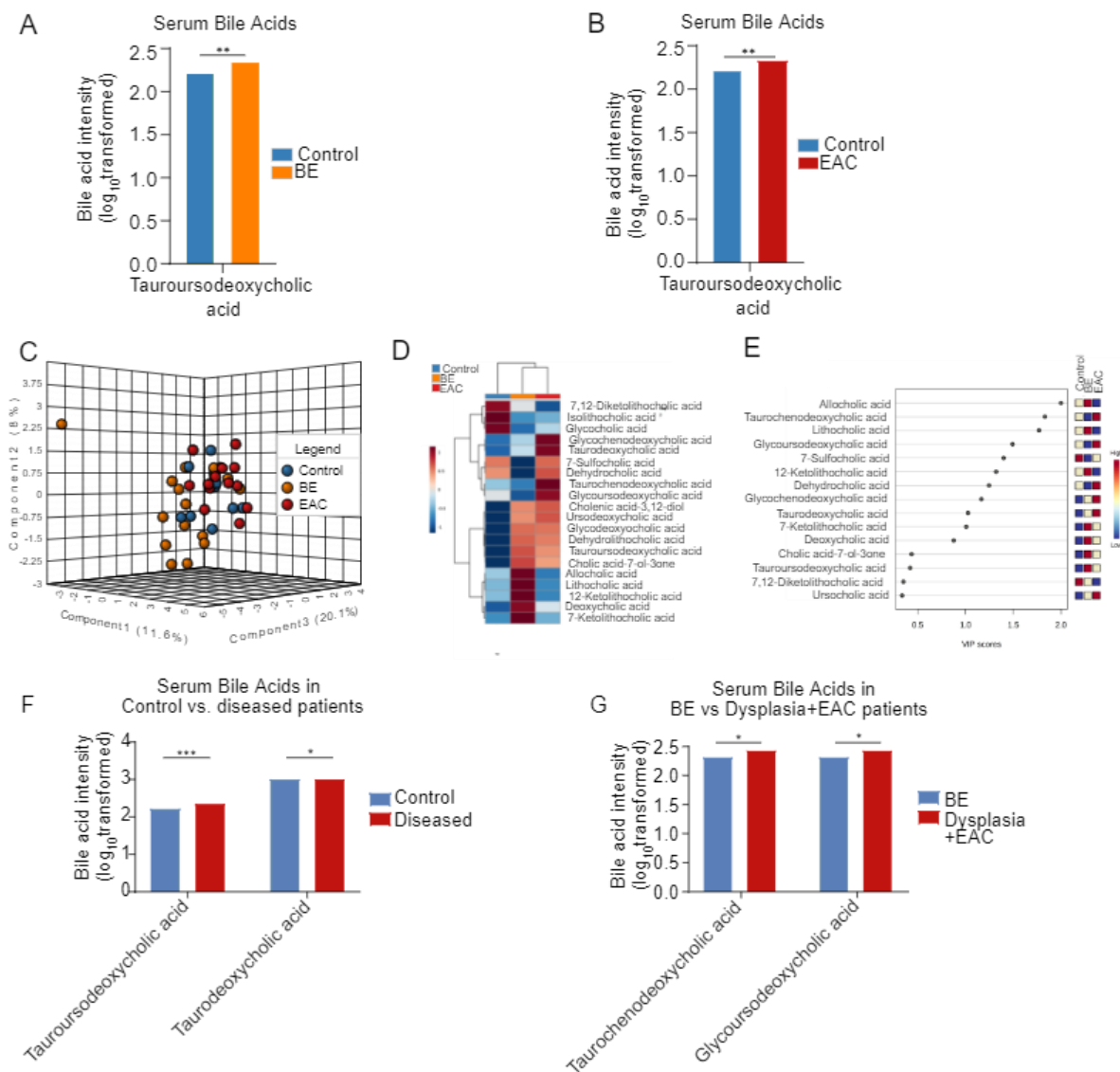


Figure 66: The human serum BA profile changes in diseased (BE, dysplasia, EAC) compared to control patients Bile acid levels in the serum of human control, BE, dysplasia and EAC patients were measured via targeted BA analysis (control n=10; BE n=16; dysplasia n=5; EAC n=14) **(A)** Tauroursodeoxycholic acid levels are significantly increased the serum of BE compared to control patients ($p=0.0044$). **(B)** Tauroursodeoxycholic acid levels are significantly increased the serum of EAC compared to control patients ($p=0.0075$). **(C)** Partial least squares discriminant analysis (PLS-DA) of BA profiles in the serum of human control, BE and EAC patients. While no definitive clusters are formed, BE patient samples are partially clustering differently than the control samples. **(D)** Clustering of the mean stool BA levels in human control, BE and EAC patients shown as heatmap. Displayed are the top 20 BAs ranked by t-test (euclidean distance measure, ward clustering algorithm). The heatmap shows distinct BA profiles for all three patient groups, with increased BA levels in the BE and EAC patients compared to the control group. **(E)** Important features for distinction of groups identified by PLS-DA. The colored boxes on the right indicate the relative concentrations of the corresponding metabolite in each group under study. The VIP (variable's importance in projection) score of a feature indicates its importance as variable for distinction between groups. It is calculated as a weighted sum of the squared correlations between the PLS-DA components and the original variable, with the weights corresponding to the percentage variation explained by the PLS-DA component in the model. The plot indicates allocholic acid, taurochenodeoxycholic acid and lithocholic acid to be the be the three main distinguishing BA between groups. While allocholic and lithocholic acid levels are highest in BE patients, taurochenodeoxycholic levels are highest in EAC patients. **(F)** Tauroursodeoxycholic acid and taurodeoxycholic acid levels are both significantly increased in the serum of diseased versus control patients (diseased – BE, dysplasia, EAC patients). **(G)** Taurochenodeoxycholic acid and glycoursodeoxycholic acid levels are both significantly increased in the serum of dysplasia and EAC versus control patients.

3.4.2. BA Metabolizing Bacteria Levels in the Stool of Patients do not Change with Disease Progression

The microbiome from stool samples of the patients was analyzed via 16S-sequencing to assess changes in gut microbiota, especially of those with potential BA metabolizing capacities between groups. No major changes between bile acid metabolizing bacteria could be detected. Relative abundance of the genus *Akkermansia*, was found to be reduced in diseased (BE, dysplasia and EAC) compared to control patients (Fig.67 A). *Akkermansia* is a mucin degrading bacterial species which is important for intestinal homeostasis and metabolic as well as immune functions. It is also thought to prevent colonization of the gut and its mucus layer with pathogenic bacteria, thus playing a role in maintaining the intestinal barrier²⁸⁹. Also, the relative abundance of the genera *Ruminococcus* and unknown *Ruminococcaceae* was found to be decreased in BE compared to DP and EAC patients (Fig.67 B, C). Correlation analysis of bacterial species with control and diseased patients does not show enrichment of BA metabolizing bacteria neither in control nor in diseased patients.

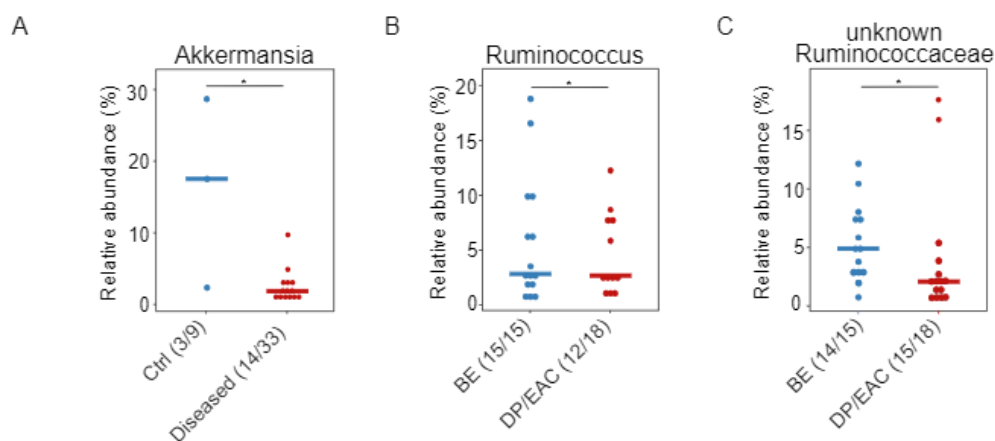


Figure 67: The gut microbial profile in human patients with focus on BA metabolizing bacteria. Mucus protective *Akkermansia* are decreased in abundance in diseased patients, while potentially BA modulating *Ruminococcaceae* are more abundant in BE than in dysplasia (DP) and EAC patients in the stool microbiome (A) Levels of the genus *Akkermansia* are significantly decreased in abundance in patients with BE, dysplasia and EAC (diseased) compared to control patients. (B) Levels of the genera *ruminococcus* and (C) unknown *Ruminococcaceae* are significantly decreased in abundance in dysplasia and EAC compared to BE patients (*ruminococcus* $p=0.0213$; unknown *Ruminococcaceae* $p=0.0328$). For (A-C) relative abundances of microbiota are represented with mean. For statistical analysis, pairwise Wilcoxon rank sum test or fisher's exact test, if appropriate, were used.

3.4.3. Disease Severity in Patients Correlates Positively with Potentially BA Metabolizing Gut Microbiota and BA Levels

Although no BA metabolizing bacteria were specifically regulated between groups, we correlated bacterial abundance with disease progression and BA levels in the stool of patients. Figure 68 shows the correlation analysis for fecal microbiota on the genus level, a detailed correlation analysis between all fecal microbiota from kingdom to genus level is shown in Supplementary Fig. 12. Of note, the genus *Akkermansia* correlates strongly negatively with disease severity, while the genera *Blautia*, *Clostridium cluster IV* and *Clostridium cluster XVIII*, which most probably harbor BA metabolization capacities all correlate positively with disease progression. While *Blautia* and *Clostridium cluster IV* are correlating positively with the majority of fecal BA, *Clostridium cluster XVII* correlates positively mainly with TCDCA. The genus of unknown *Clostridiales* correlates negatively with all BA. Interestingly also the genera *Ruminococcus* and *unknown Ruminococcaceae*, which were lower abundant in diseased compared to control patients correlate negatively with almost all BA. Only *Ruminococcus* is positively correlated with TDCA and TCA which are associated with higher disease state but also with UDCA which is elevated in both EAC and control patients and 7-DHCA which is elevated in control patients.

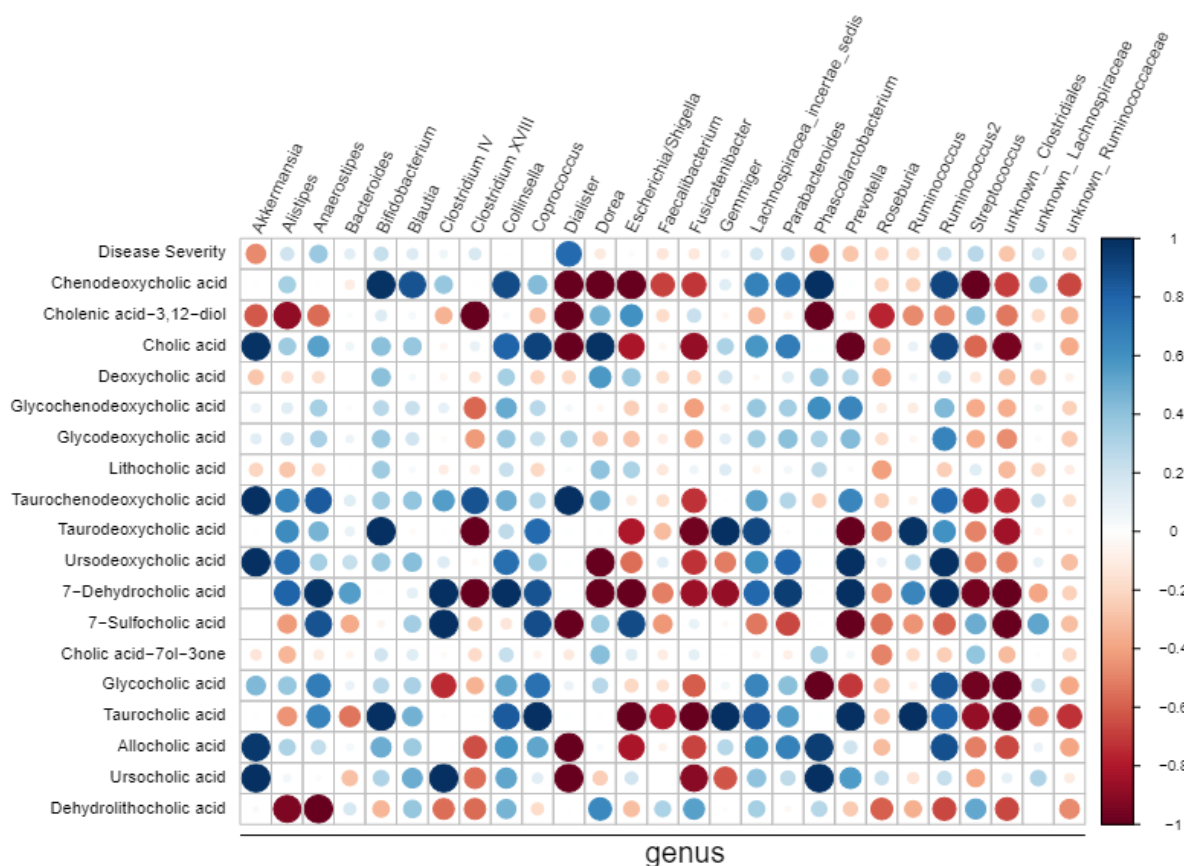


Figure 68: Correlation of the relative abundance of bacteria genera in the stool of human patients with disease severity and fecal BA levels. Correlation analyses were performed using the Rhea pipeline for 16S-sequencing data. Disease severity was evaluated by transferring the different diagnoses into numerical disease scores (Control = 0; BE = 1; dysplasia = 2; EAC = 3)

3.4.4. BA Metabolizing Bacteria Levels Extracted From Patient Biopsies Increase With Disease Progression

The microbiome from specimen of BE tissue of the patients was analyzed via 16S-sequencing to assess changes in colonization of microbiota, especially of those with potential BA metabolizing capacities between groups. Interestingly, in BE tissue we can detect bacterial strains with BA metabolizing capacities to be enriched in correlation with increasing disease severity. While relative abundance of the phylum *Firmicutes* was significantly higher in dysplasia and EAC compared to BE patients (Fig. 69 A), relative abundance of the class *Clostridia* increased gradually with disease progression from control to BE, dysplasia and to EAC (Fig. 69 B). Relative abundances of the families *Lachnospiraceae*, *Ruminococcaceae*, *unknown Clostridiales* and *unknown Lachnospiraceae* also increased with disease progression (Fig.69 C-F).

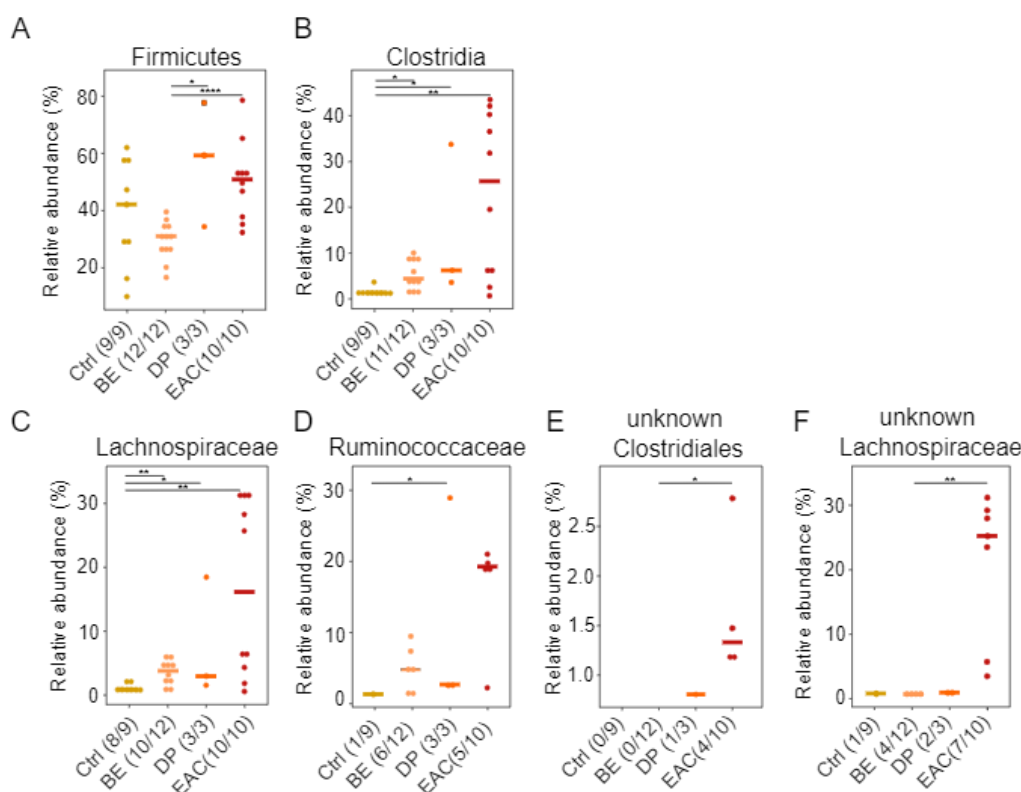
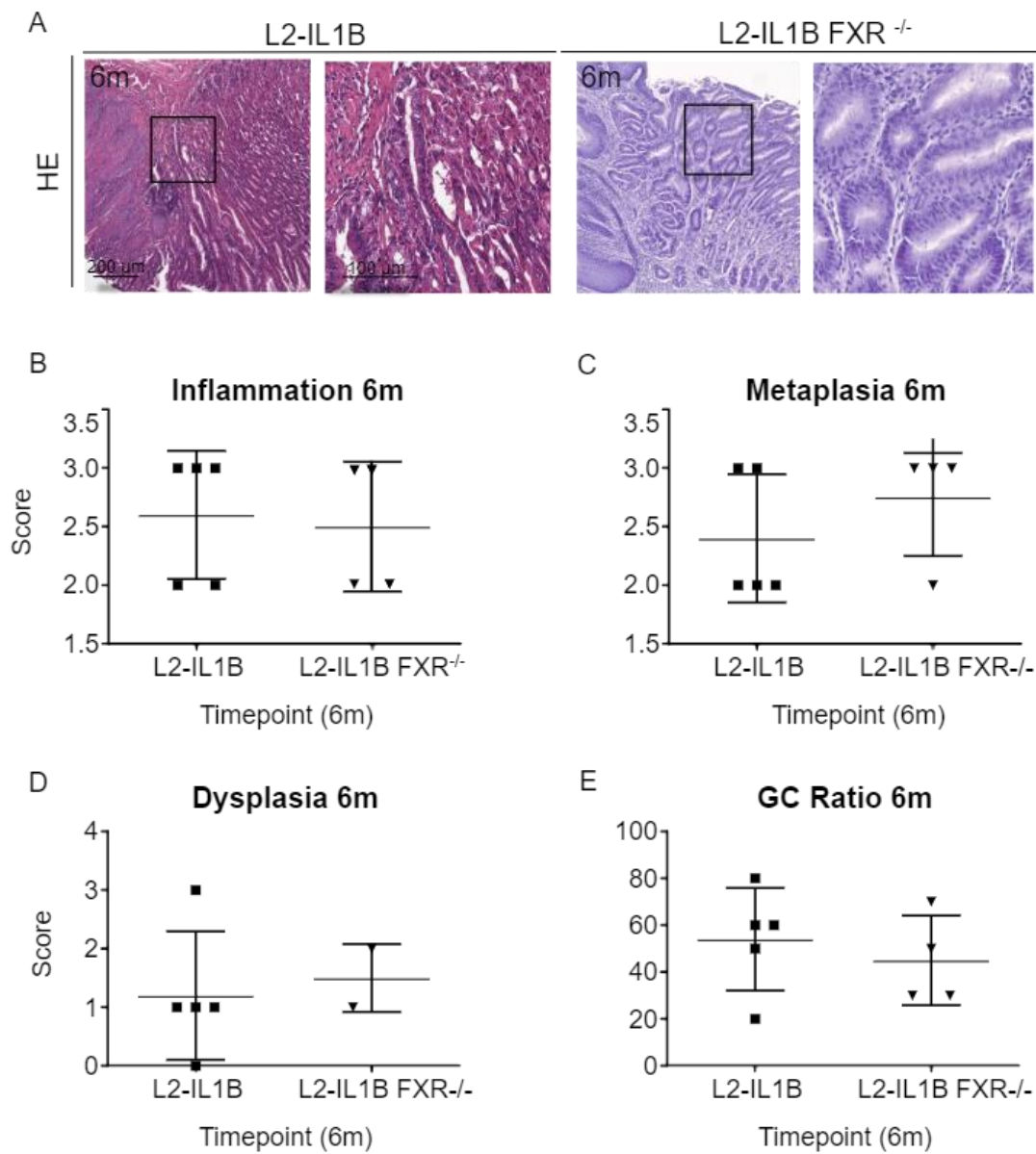
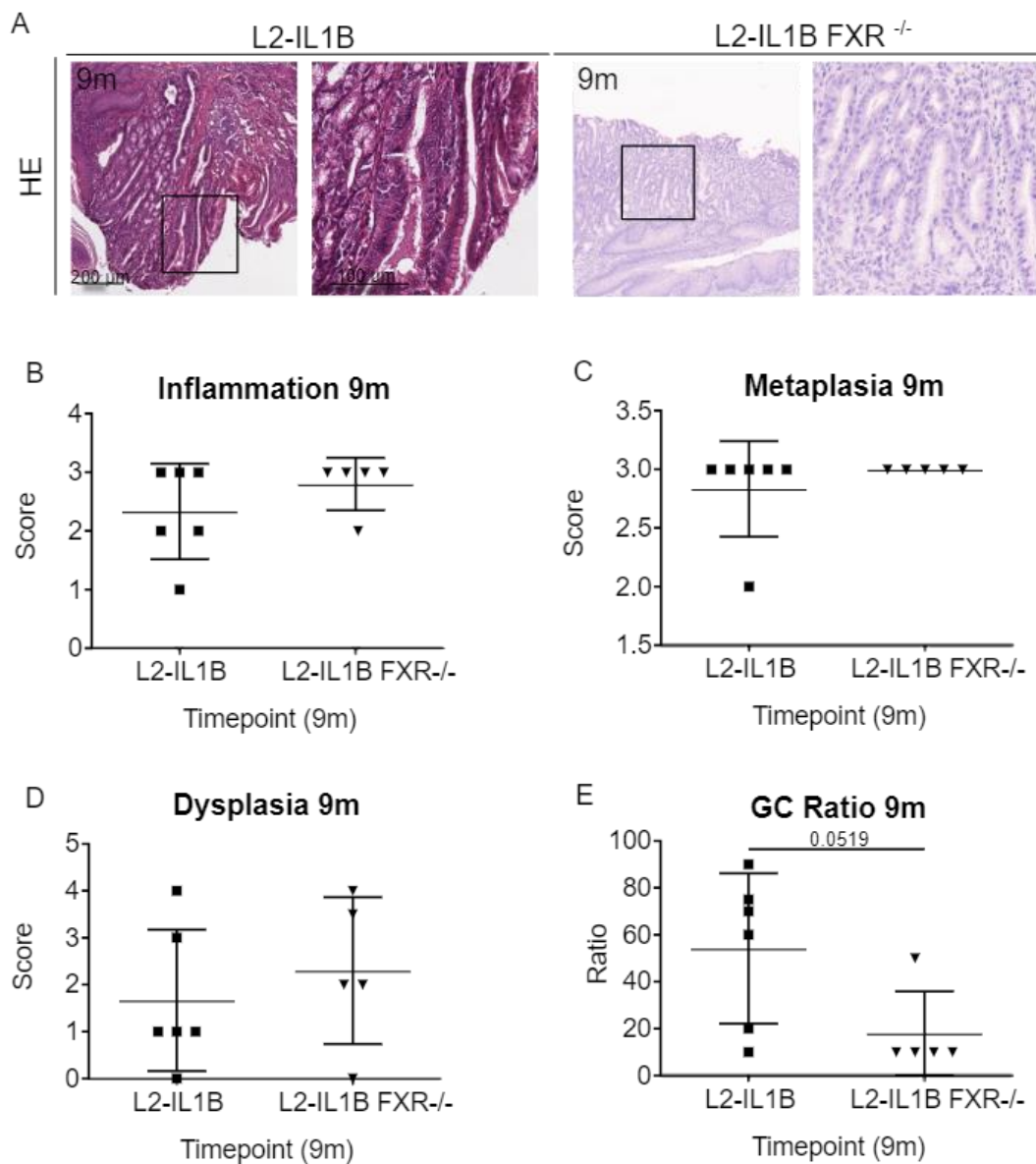


Figure 69: Bacterial groups with potential BA modulating capacities are increasing in abundance in correlation with disease severity in the esophageal microbiome (A) Relative abundance of the phylum Firmicutes are significantly increasing in dysplasia and EAC patients compared to BE patients (BE-DP $p=0.0484$; BE-EAC $p=0.0001$). (B) Relative abundance of the class Clostridia is significantly increased in BE, DP and EAC patients compared to control patients (Ctrl-BE $p=0.0125$; Ctrl-DP $p=0.0182$; Ctrl-EAC $p=0.0030$). (C) Relative abundance of the family Lachnospiraceae is significantly increased in BE, DP and EAC patients compared to control patients (Ctrl-BE $p=0.0062$; Ctrl-DP $p=0.0242$; Ctrl-EAC $p=0.0031$). (D) Relative abundance of the family Ruminococcaceae is significantly increased in DP compared to control patients ($p=0.0182$). (E) The genus of unknown Clostridiales is only abundant in the tissue of DP and EAC patients. Relative abundance of the genus unknown Clostridiales is significantly increased in EAC compared to BE patients ($p=0.0287$). (F) Relative abundance of the genus unknown Lachnospiraceae is significantly increased in EAC compared to BE patients ($p=0.0198$). For (A-D) relative abundances of microbiota are represented with mean. For statistical analysis, pairwise Wilcoxon rank sum test or fisher's exact test, if appropriate, were used.

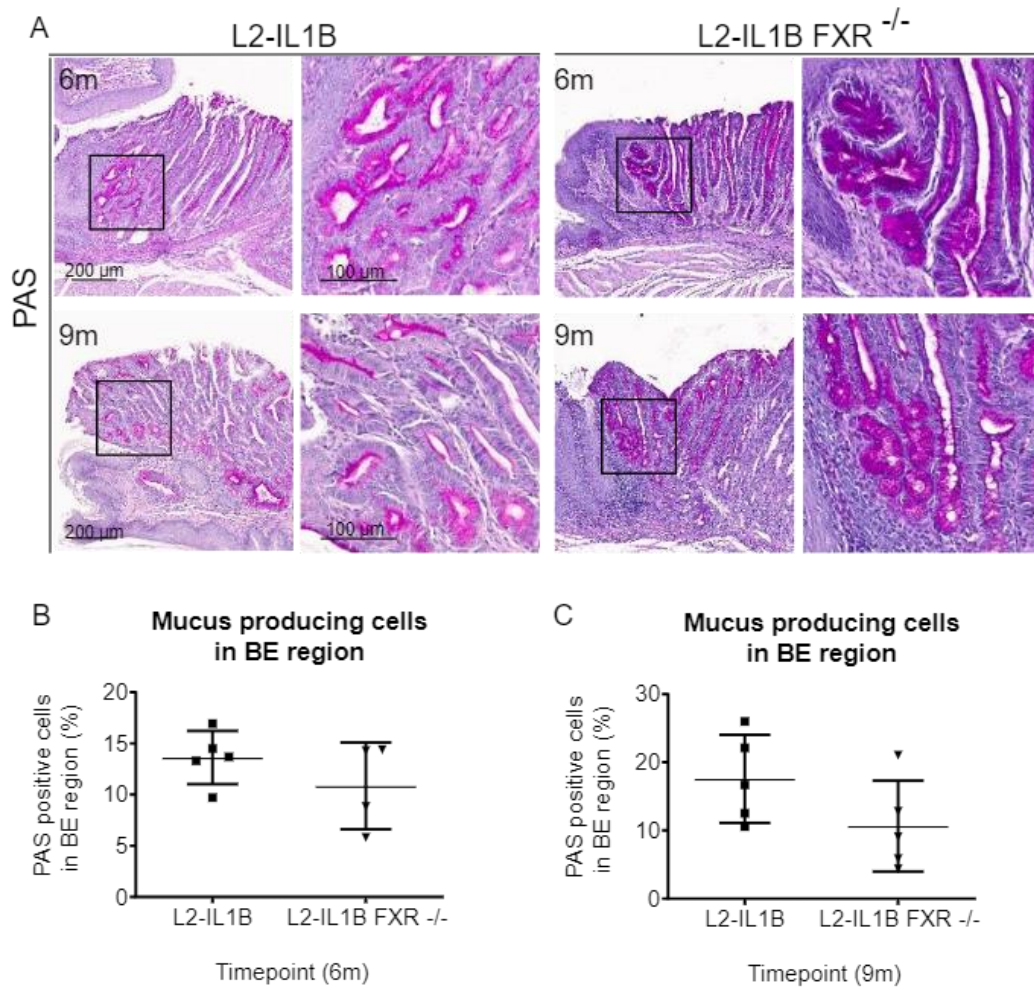
4. Supplementary Figures



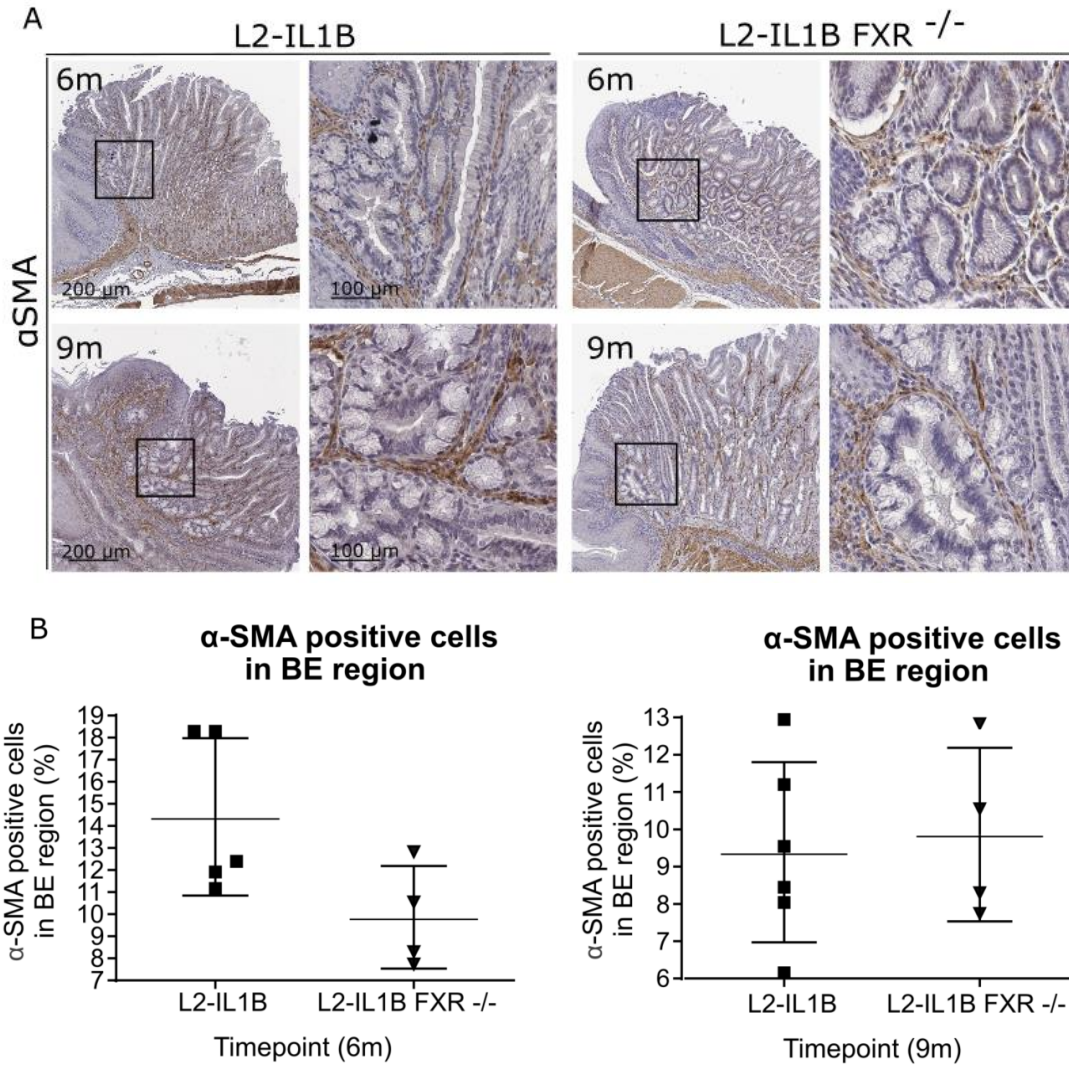
Supplementary Fig. 1: Histological scores are not changing significantly between L2-IL1B and L2-IL1B-FXR^{-/-} mice at 6 months of age (A) Representative Hematoxylin & Eosin (HE) staining of cardia tissue of L2-IL1B and L2-IL1B-FXR^{-/-} mice at 6months of age. Bars 200 and 100 μ M. **(B)** Inflammation **(C)** Metaplasia and **(D)** Dysplasia scores as well as **(E)** Goblet cell ratio in 6-month-old L2-IL1B-FXR^{-/-} mice. Scores are not differing significantly between L2-IL1B and L2-IL1B-FXR^{-/-} mice. Data are presented as mean with SD. For statistical evaluation of **(B-D)** unpaired two-tailed t-tests were used.



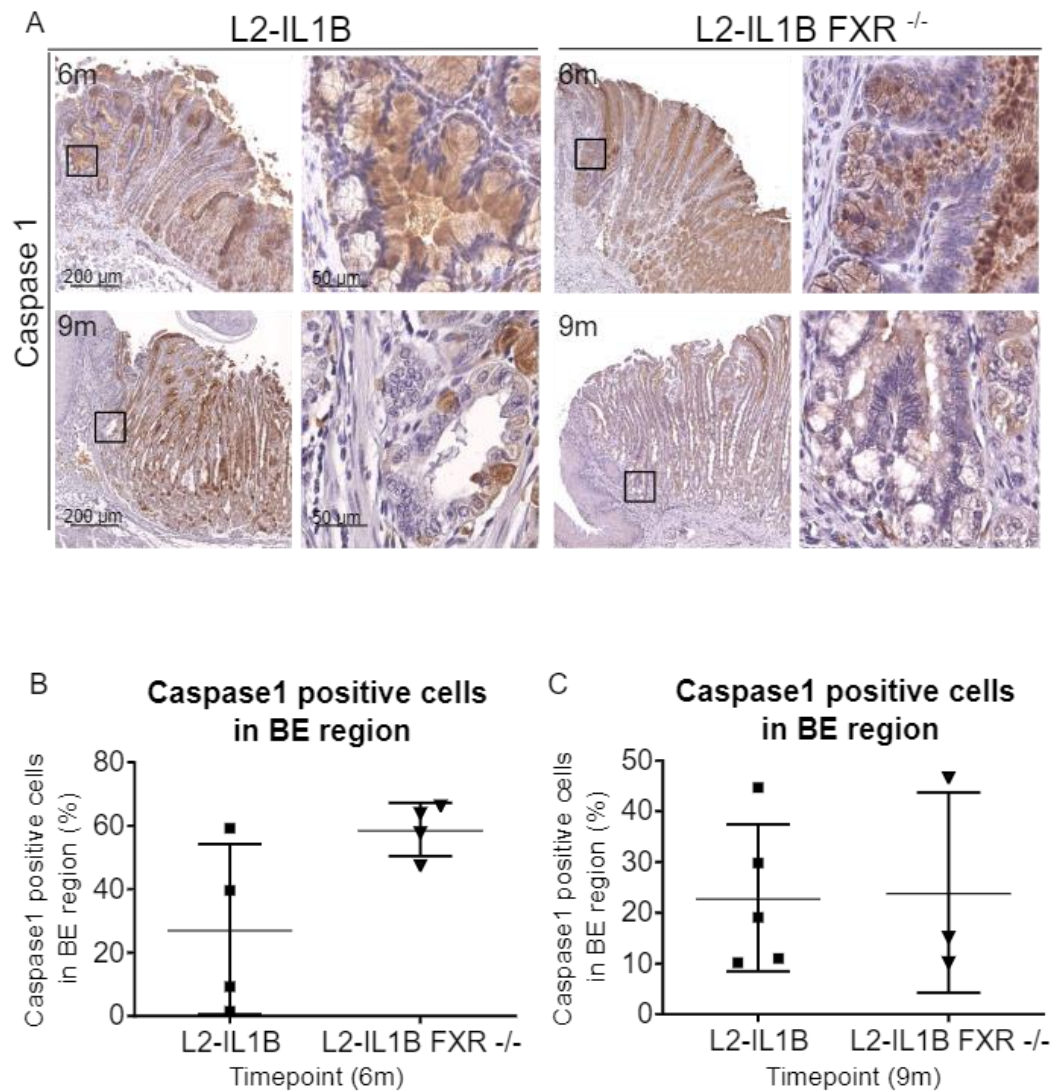
Supplementary Fig. 2: Histological scores are not changing significantly between L2-IL1B and L2-IL1B-FXR^{-/-} mice at 9 months of age (A) Representative Hematoxylin & Eosin (HE) staining of cardia tissue of L2-IL1B and L2-IL1B-FXR^{-/-} mice at 9 months of age. Bars 200 and 100 μ M. **(B)** Inflammation **(C)** Metaplasia and **(D)** Dysplasia scores as well as **(E)** Goblet cell ratio in 9-month-old L2-IL1B-FXR^{-/-} mice. Scores are not differing significantly between L2-IL1B and L2-IL1B-FXR^{-/-} mice. Data are presented as mean with SD. For statistical evaluation of **(B-D)** unpaired two-tailed t-tests were used.



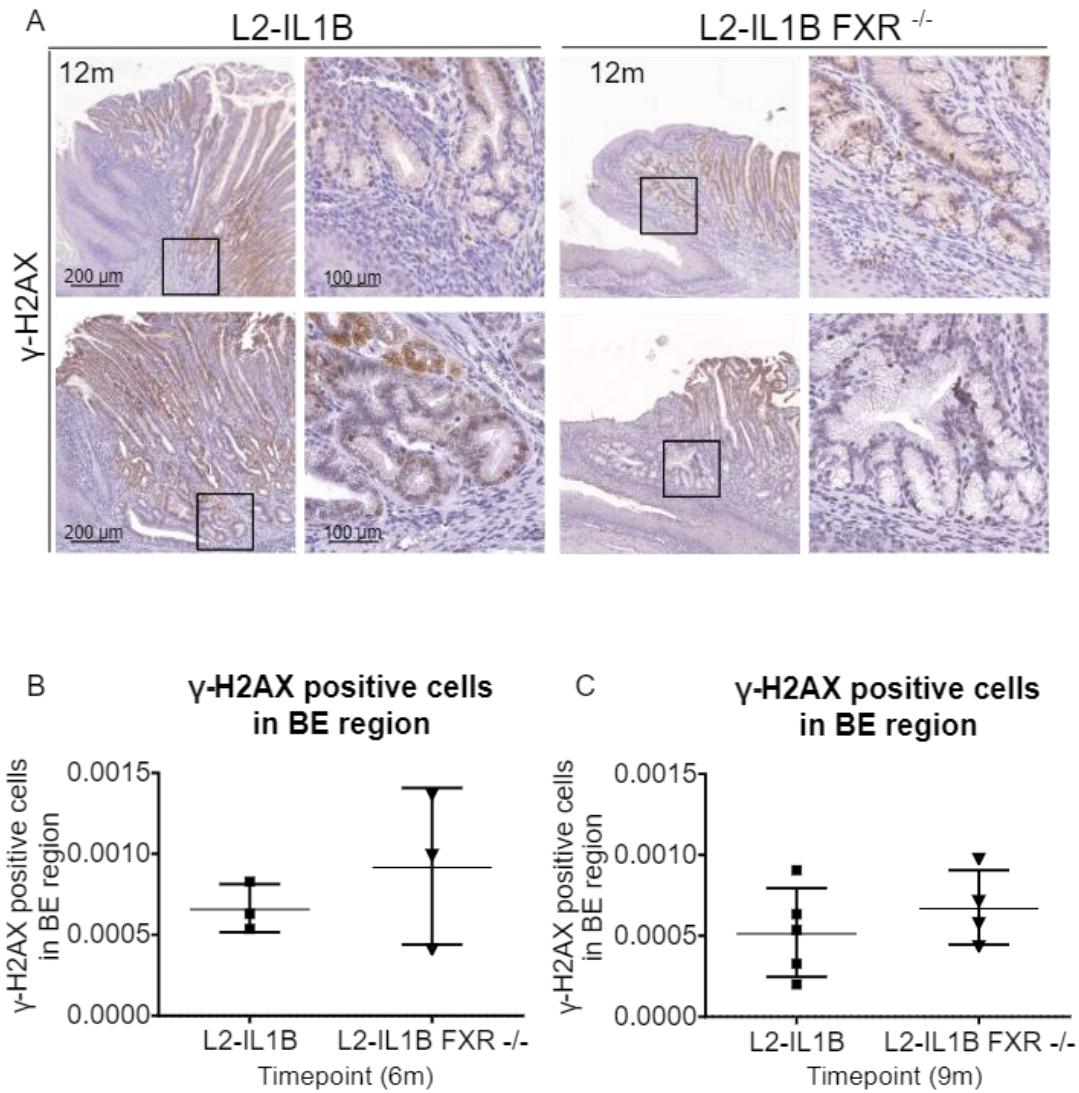
Supplementary Fig. 3: The amount of PAS positive mucus producing cells is not changing significantly between L2-IL1B and L2-IL1B-FXR^{-/-} mice at 6 and 9 months of age (A) Representative Periodic Acid-Schiff (PAS) staining of cardia tissue of L2-IL1B and L2-IL1B-FXR^{-/-} mice at 6 and 9 months. Bars 100 μ m. The amount of PAS positive mucus producing Goblet-like cells does not significantly differ between groups at 6m (B) or 9m (C) of age. Data are presented as mean with SD. For statistical evaluation of (B, C) unpaired two-tailed t-tests were used.



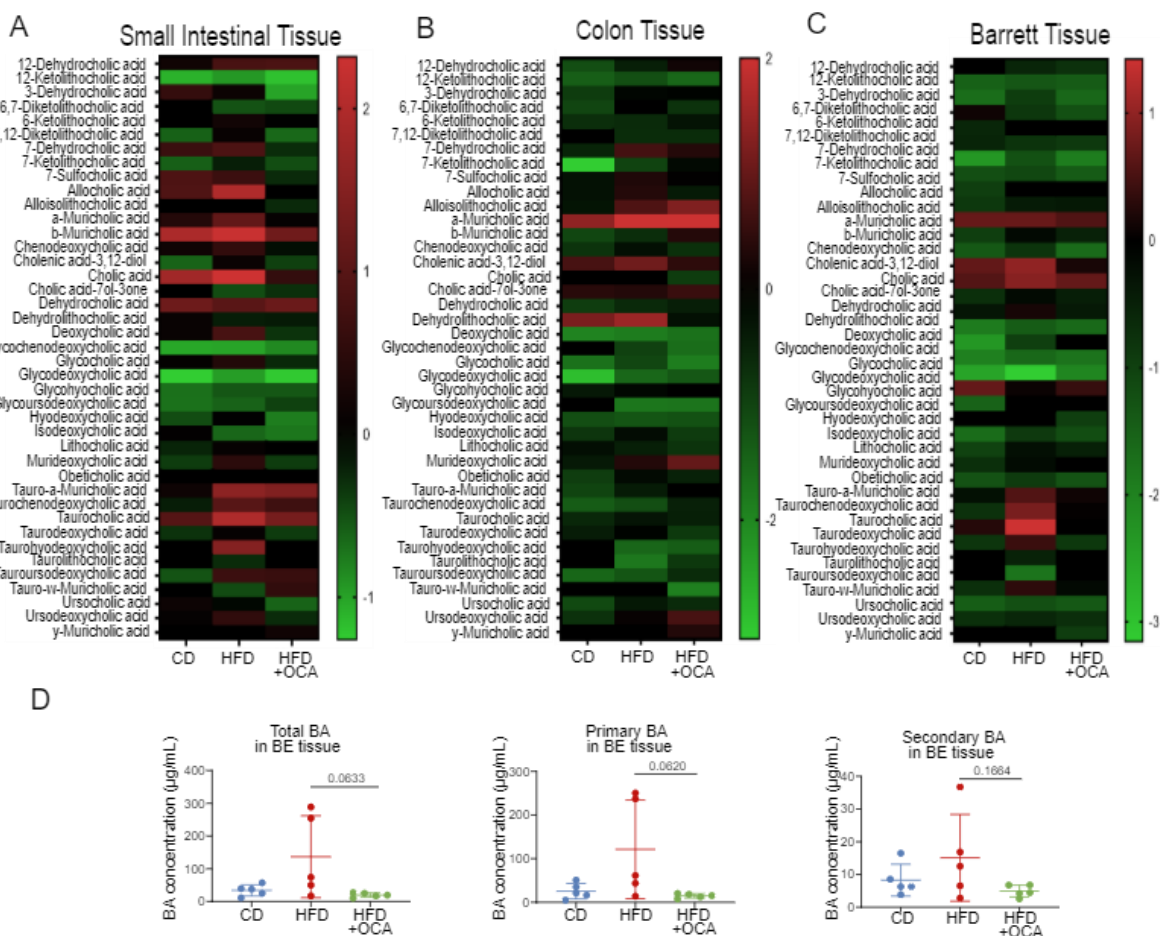
Supplementary Fig. 4: The amount of αSMA positive cells is not changing significantly between L2-IL1B and L2-IL1B-FXR^{-/-} mice at 6 and 9 months of age (A) Representative αSMA immunohistochemistry of cardia tissue of L2-IL1B and L2-IL1B-FXR^{-/-} mice at 6 and 9 months. Bars 200 μM and 100 μM. **(B)** The amount of αSMA positive cells does not differ significantly between L2-IL1B and L2-IL1B-FXR^{-/-} mice at 6 and 9 months of age. Data are presented as mean with SD. For statistical evaluation of **(B, C)** unpaired two-tailed t-tests were used.



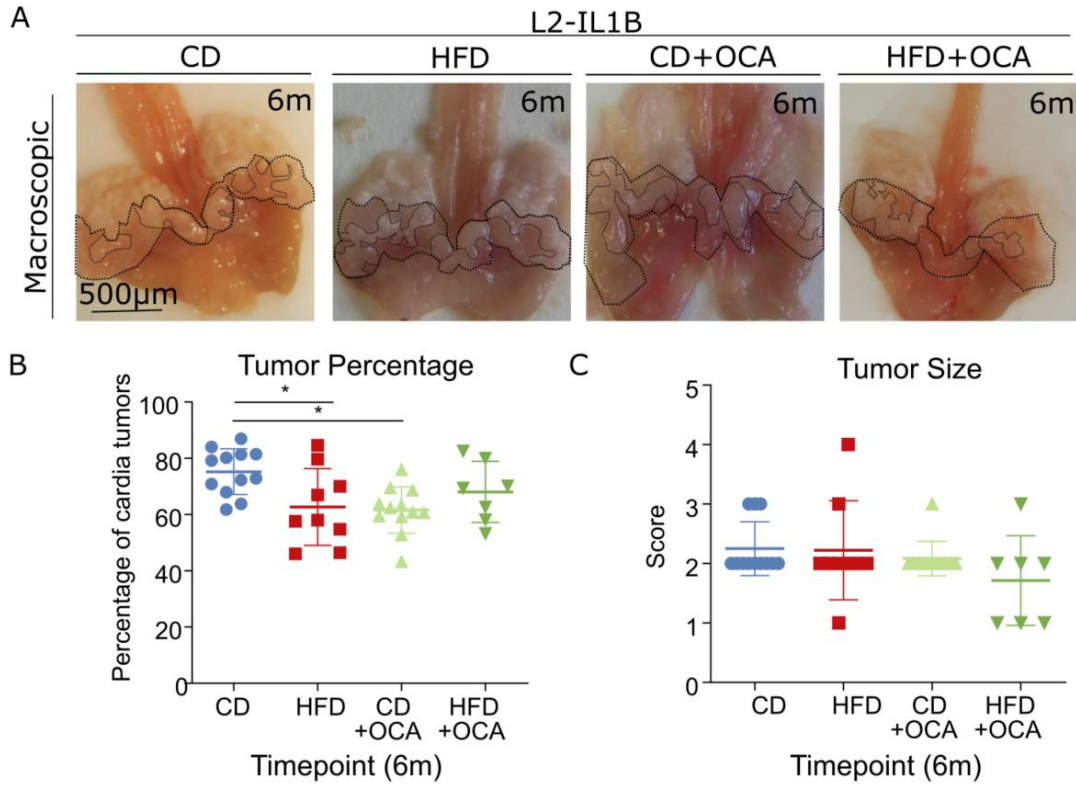
Supplementary Fig. 5: The amount of Caspase1 positive cells is not changing significantly between L2-IL1B and L2-IL1B-FXR^{-/-} mice at 6 and 9 months of age (A) Representative Caspase1 immunohistochemistry of cardia tissue of L2-IL1B and L2-IL1B-FXR^{-/-} mice at 6 and 9 months. Bars 200 μ M and 50 μ M. **(B)** The amount of Caspase1 positive cells does not differ significantly between L2-IL1B and L2-IL1B-FXR^{-/-} mice at 6 and 9 months of age. Data are presented as mean with SD. For statistical evaluation of **(B, C)** unpaired two-tailed t-tests were used.



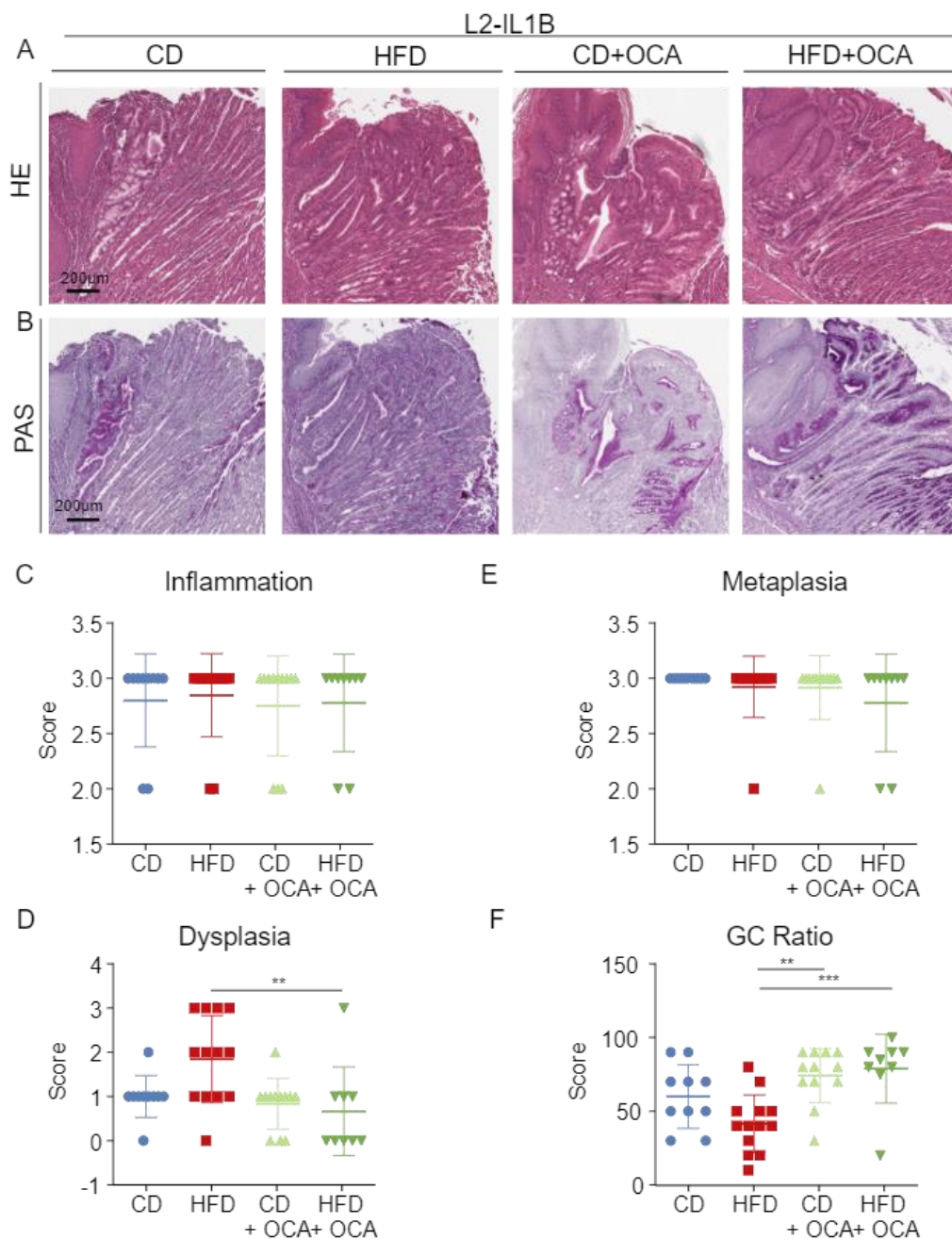
Supplementary Fig. 6: The amount of γ -H2AX positive cells is not changing significantly between L2-IL1B and L2-IL1B-FXR^{-/-} mice at 6 and 9 months of age (A) Representative γ -H2AX immunohistochemistry of cardia tissue of L2-IL1B and L2-IL1B-FXR^{-/-} mice at 6 and 9 months. Bars 200 μ m and 100 μ m. **(B)** The amount of γ -H2AX positive cells does not differ significantly between L2-IL1B and L2-IL1B-FXR^{-/-} mice at 6 and 9 months of age. Data are presented as mean with SD. For statistical evaluation of **(B, C)** unpaired two-tailed t-tests were used.



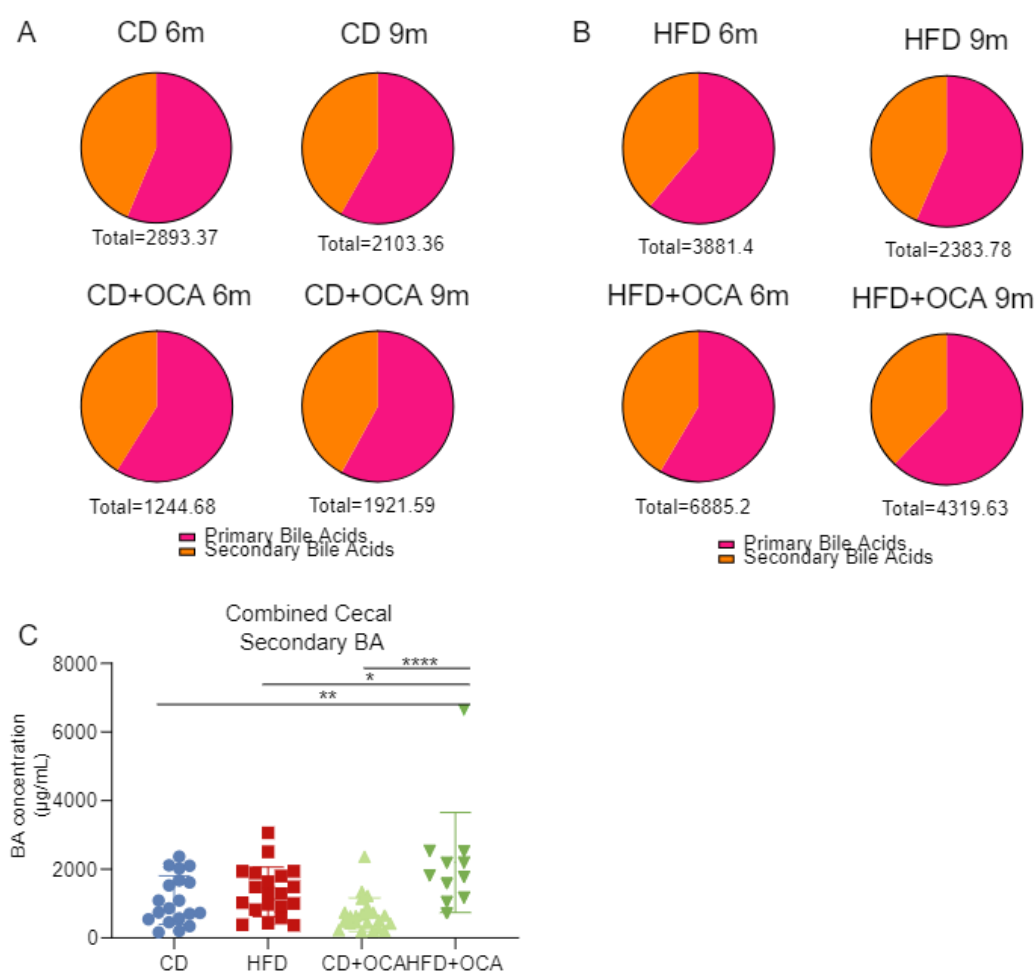
Supplementary Fig. 7: Bile Acid concentrations in Small Intestinal, Colon and BE tissue (A) Heatmap showing log₁₀ transformed bile acid concentrations (µg/mL) in the small intestinal tissue of 6-month-old L2-IL1B mice fed CD, HFD or HFD+OCA (n=5). The heatmap shows increased bile acid levels in mice fed HFD compared to CD with levels again decreased upon treatment with HFD+OCA. **(B)** Heatmap showing log₁₀ transformed bile acid concentrations (µg/mL) in the colon tissue of 6-month-old L2-IL1B mice fed CD, HFD or HFD+OCA (n=5). The heatmap shows increased bile acid levels, especially of DCA, glycine conjugated BA and single taurine conjugated BA in mice fed HFD compared to CD with levels mainly again decreased upon treatment with HFD+OCA. By contrast, mainly levels of LCA and UDCA levels are increased in HFD+OCA compared to CD and HFD treated mice. **(C)** Heatmap showing log₁₀ transformed bile acid concentrations (µg/mL) in the BE tissue of 6-month-old L2-IL1B mice fed CD, HFD or HFD+OCA (n=5). The heatmap shows increased bile acid levels in mice fed HFD compared to CD with levels again decreased upon treatment with HFD+OCA. **(D)** Analysis of combined primary, secondary and total bile acid concentrations (µg/mL) in BE show a trend to reduced overall bile acid levels in HFD+OCA compared to HFD treated mice (n=4; primary BA p=0.0620; secondary BA p=0.1664; total BA p=0.0633)



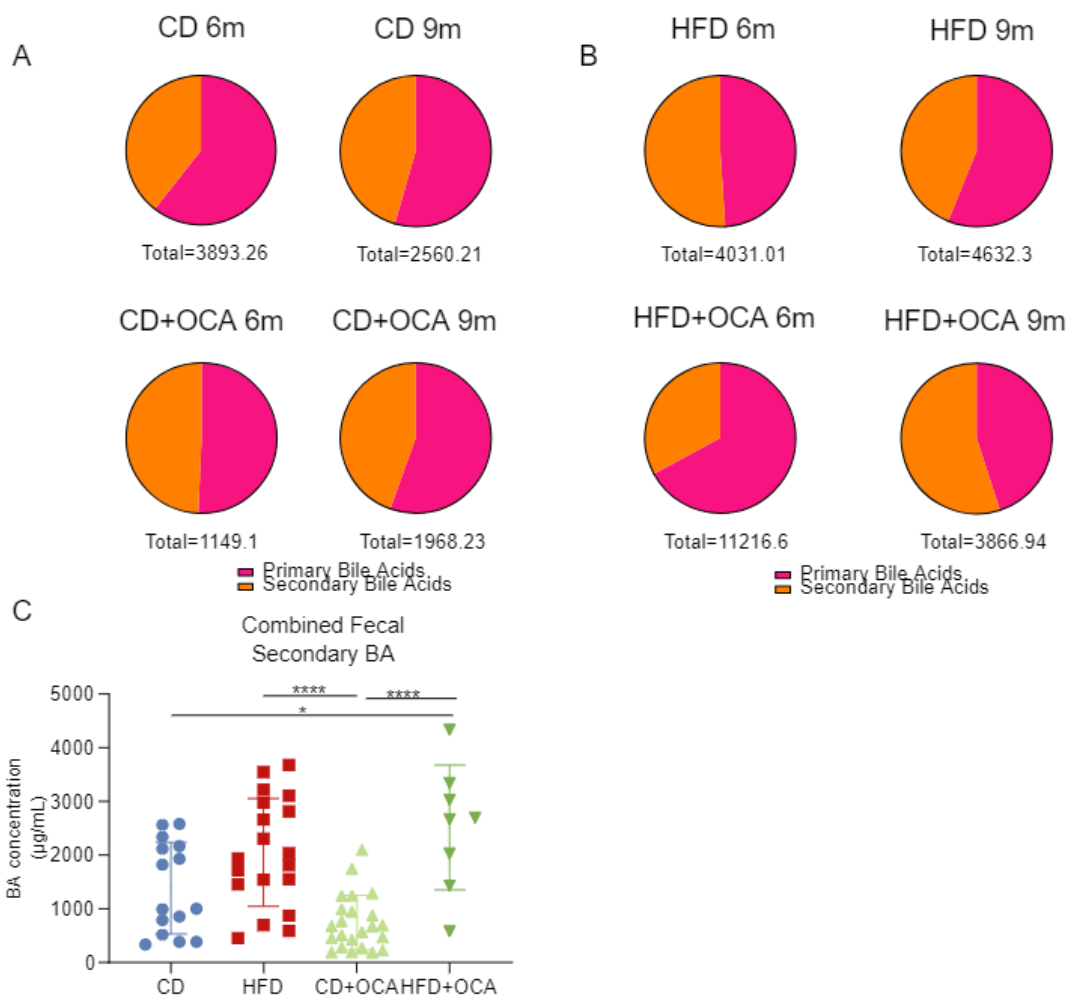
Supplementary Fig. 8: The macroscopic tumor percentage in the SCJ of L2-IL1B mice at 6 months of age is decreasing significantly in mice fed HFD and CD+OCA compared to CD (A) Representative macroscopic image of the SCJ region of L2-IL1B mice fed CD, HFD, CD+OCA or HFD+OCA at 6 months of age, with the SCJ and tumor nodes in the SCJ being outlined **(B)** Tumor percentage and **(C)** Tumor size of 6-month-old L2-IL1B mice is decreasing significantly in mice fed HFD and CD+OCA compared to CD. Data are presented as mean with SD. For statistical evaluation of **(B, C)** ordinary one-way ANOVA with Tukey-test to correct for multiple comparisons was used.



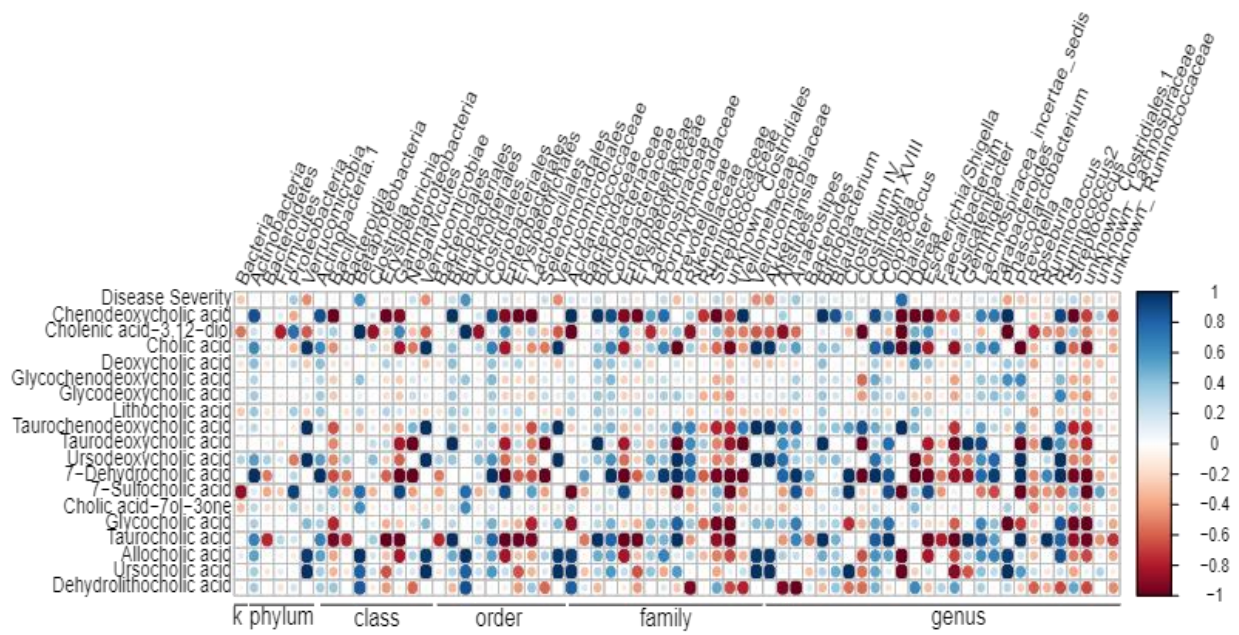
Supplementary Fig. 9: OCA treatment decreases dysplasia scores and increases the goblet cell (GC) ratio in 6m old L2-IL1B mice fed HFD (A) Representative Hematoxylin & Eosin (HE) staining of cardia tissue of L2-IL1B mice fed CD or HFD with or without OCA at 6months of age. Bars 200 μM. (B) Representative Periodic Acid-Schiff (PAS) staining of cardia tissue of L2-IL1B mice fed CD or HFD with or without OCA at 6 months of age. Bars 200 μM. (C) Inflammation (D) Metaplasia and (E) Dysplasia scores as well as (F) Goblet cell ratio in 6-month-old L2-IL1B mice on CD, HFD, CD+OCA or HFD+OCA. While Inflammation and Metaplasia scores are not differing significantly between groups, Dysplasia scores of HFD+OCA mouse cohort are significantly lower compared to the HFD cohort ($p=0.0086$). The goblet cell ratios of both CD+OCA and HFD+OCA mouse cohorts are significantly higher compared to the HFD cohort (HFD vs. CD+OCA $p=0.0016$; HFD vs. HFD+OCA $p=0.0008$). Data are presented as mean with SD. For statistical evaluation of the Inflammation, Metaplasia and Dysplasia scores (C-E) Kruskal-Wallis test was used, for analysis of the Goblet cell ratio (F), ordinary one-way ANOVA was used.



Supplementary Fig. 10: OCA treatment in L2-IL1B mice fed CD or HFD does not change cecal primary to secondary BA ratios (A) Pie charts showing primary compared to secondary BA levels as well as total BA levels in 6- and 9-month-old L2-IL1B mice fed CD, HFD, CD+OCA or HFD+OCA. Ratios are not changing between groups. **(B)** Combined fecal secondary BA levels are significantly lower in L2-IL1B mice fed CD, CD+OCA and HFD compared to HFD+OCA (L2-IL1B mice with combined ages of 6 and 9 months, CD n=19, CD+OCA n=23, HFD n=20, HFD+OCA n=13 CD vs. HFD p=0.0116; CD+OCA vs HFD+OCA p≤0.0001; HFD vs HFD+OCA p=0.0260; CD vs HFD+OCA p=0.0027) **(A-B)** Data are represented as mean. **(C)** Data are represented as mean with SD. For statistical evaluation of **(C)** ordinary one-way ANOVA with Tukey-test to correct for multiple comparisons was used.



Supplementary Fig. 11: OCA treatment in L2-IL1B mice fed CD or HFD does not change fecal primary to secondary BA ratios (A) Pie charts showing primary compared to secondary BA levels as well as total BA levels in 6- and 9-month-old L2-IL1B mice fed CD, HFD, CD+OCA or HFD+OCA. While in 6m old HFD+OCA mice secondary BA are decreasing compared to primary BA, this effect was not apparent in 9m old mice. **(B)** Combined fecal secondary BA levels are significantly lower in L2-IL1B mice fed CD and CD+OCA compared to HFD+OCA and in CD+OCA compared to HFD (L2-IL1B mice with combined ages of 6 and 9 months, CD n=15, CD+OCA n=23, HFD n=19, HFD+OCA n=8; CD+OCA vs HFD+OCA $p \leq 0.0001$; HFD vs HFD+OCA $p \leq 0.0001$; CD vs HFD+OCA $p = 0.0172$) **(A-B)** Data are represented as mean. **(C)** Data are represented as mean with SD. For statistical evaluation of **(C)** ordinary one-way ANOVA with Tukey-test to correct for multiple comparisons was used.



Supplementary Fig. 12: Correlation Fecal Microbiome targeted BA metabolome

5. Discussion

Esophageal cancer is a highly aggressive malignancy with poor prognosis and low overall survival rates⁶⁴, and is listed as one of the deadliest types of cancer since several decades⁶⁰⁻⁶³. Most esophageal cancers are characterized as either ESCC or as EAC, with EAC being the main type of esophageal cancer in western and westernized countries. EAC incidence is increasing steadily in western countries, has exceeded that of ESCC in the past decades, and is predicted to further increase in the next years^{104-107,111}. Risk factors for EAC include smoking, obesity and GERD triggering BE^{65,67,72-74}.

BE is the most relevant precursor lesion of EAC, and patients diagnosed with BE have a 30-50x increased risk to develop EAC compared to those without BE⁴⁸⁻⁵⁴. It was shown that GERD, the main risk factor for BE has more severe tissue damaging effects if the refluxed gastric juice contains bile acids from gastro-duodenal content³⁶⁻³⁸. Treatment of cells *in vitro* and in a mouse model *in vivo* with excess bile acids promoted disease progression^{82,244}. Souza et al. (2009) showed that the damaging effect of BA on BE is not only conveyed via reflux, since cellular alterations preceded reflux mediated tissue damage⁴⁴. These findings support the concept that bile acid exposure, triggers inflammatory signaling and cytokine secretion rather than causing direct tissue erosion via the reflux.

Risk of progression from BE to EAC correlates with increasing obesity incidence and intake of western-style diet yet understanding the interaction between diet and mechanisms resulting in disease progression remains challenging. Dietary intake high in fat, as in western diet, leading to obesity in humans causes gut BA levels to increase and the gut microbiome to shift²⁸⁴⁻²⁸⁶. Our group showed that HFD changes the gut microbiome and inflammatory environment in the L2-IL1B mouse model, leading to massively increased tumor development²⁷⁰. Dietary intake, the gut microbiome and the bile acid pool are mutually dependent on each other. A diet high in fat favors production of lipid solubilizing BA while high BA concentrations favor growth of bile tolerant microbes, and gut bacteria which metabolize primary to secondary BAs for energy production.

In this study, using the L2-IL1B mouse model we investigated the protective role of the BA receptor FXR on disease progression and analyzed the diet dependent BA metabolizing gut microbiome in correlation with BA levels in the gut, serum, intestinal, and BE tissue. To transfer the findings and research to a translational stage, we also evaluated the gut and tissue microbiome as well as gut and serum BA levels in relation to disease progression from BE to EAC.

5.1. The Protective Role of FXR Expression on the Phenotype in the L2-IL1B Mouse Model

It is assumed that bile acids damage the esophageal tissue and create an inflammatory microenvironment which then promotes tumorigenesis^{47,82,242,264}. Furthermore, different studies in different GI diseases show more severe damage through microbiome metabolized secondary BAs^{290,291}. In accordance with previous studies, we found FXR, a nuclear BA receptor central to primary BA transport, de novo BA synthesis, metabolic and inflammatory BA signaling^{217,219,240}, to be expressed in BE of patients and L2-IL1B mice^{265,266}, while its expression was lost over time with tumor progression, pointing to a protective effect^{267,268}.

FXR is normally expressed in the small intestine and the liver where it is involved in maintaining homeostasis of the BA pool and signaling. The function of FXR expression in other tissues is not completely clear yet leads to the impression that FXR is also involved in other signaling pathways. Besides BA signaling, FXR activation was already shown to lead to inhibition of fibrosis²¹⁴, intestinal tumorigenesis²¹⁵, hepatic tumor cell proliferation, dedifferentiation and migration²¹⁶, inhibition of inflammatory signaling²¹⁷, inhibition of cancer stem cell proliferation, and cellular damage in CRC²¹⁸.

FXR is primarily activated by primary BA, and TMCAs as well as UDCA are natural antagonists of the receptor^{203,209}. Upon activation FXR regulates the expression of downstream targets, and inhibits primary bile acid synthesis via a negative feedback loop involving downregulation of *Cyp7A1* and *Cyp8B1* gene expression, mainly reducing production of bile acid synthesis via the classical synthesis pathway^{203,204}.

5.1.1. The Impact of FXR Knockout on Disease Development on Cellular Level

The function of FXR expression in the development of BE and EAC was further investigated by inducing a full body knockout of FXR on the background of the L2-IL1B mouse model by crossing L2-IL1B transgenic mice with FXR^{-/-} mice (L2-IL1B-FXR^{-/-}). Elimination of FXR in L2-IL1B mice caused aggravation of the dysplastic phenotype and tumor formation with decreased differentiation represented by goblet cells in cohorts of L2-IL1B-FXR^{-/-} mice compared to age matched L2-IL1B mice. Loss of FXR led to increased immune responsiveness characterized by inflammasome activation by caspase 1 and fibroblast infiltration as well as increased DNA damage represented by γ -H2AX positive cells in the metaplastic region, and less protective mucus production. The promoting impact of loss of FXR on inflammation and tissue reorganization in response to inflammation was already previously shown²⁹².

FXR knockout also fostered the formation of a tumor promoting microenvironment with enrichment of tissue reorganization pathways, protumorigenic signaling pathways such as Kras and loss of p53 signaling and of genes involved in developmental pathways such as Wnt, Hedgehog and Notch signaling. Wnt, Hedgehog and Notch signaling are important in normal tissue structure development and embryogenesis and are often activated/deregulated during carcinogenesis in multiple cancer types. Especially concerning Notch signaling we only recently found activation of this signaling pathway to be an important player in the development of BE and it's progression to EAC²⁷¹. As expected, we also found advanced cancer gene sets but also a gene set involved in cholesterol homeostasis, - with cholesterol being important for BA synthesis^{11,30,31} - to be enriched in L2-IL1B-FXR^{-/-} mice.

LGR5 stem cell numbers in the BE tissue of L2-IL1B-FXR^{-/-} mice were also increasing. Co-expression of Lgr5 and FXR in the BE region of L2-IL1B mice together with detected enrichment of stem cell signaling pathways upon loss of FXR pointed to a direct impact of FXR on Lgr5 progenitor cells. This finding correlated with previous reports of FXR regulated Lgr5 cancer stem cell proliferation in CRC²¹⁸. Potential compensation of BA signaling by upregulation of TGR5 expression upon loss of FXR could be excluded, as we did not find changes in TGR5 expression in BE.

Altogether, our results correlate with previous findings of FXR activation inhibiting tumor progression, cancer stem cell proliferation, cellular damage and inflammatory signaling.

5.1.2. The Impact of FXR Knockout on the BA Pool, with Possible Implications for Disease Progression

Investigation of serum BA levels through untargeted and targeted metabolomics showed enrichment of TCA and DHCA, and decrease in LCA, HDCA and UDCA levels induced by FXR knockout in L2-IL1B mice.

Microarray expression data of the tumor showed a significant decrease of *Cyp27A1* gene expression, together with an increase in *Cyp7B1* gene expression in tumor tissue of L2-IL1B-FXR^{-/-} compared to L2-IL1B mice. *Cyp7B1* overexpression potentially resulted from a feedback loop upon loss of *Cyp27A1*. *Cyp27A1* and *Cyp7B1* are the main enzymes involved in the alternative bile acid synthesis pathway leading to production of CDCA and its secondary bile acid LCA, with *Cyp27A1* being the rate limiting enzyme in the synthesis process and *Cyp7B1* being downstream of *Cyp27A1*²⁰²⁻²⁰⁴.

Loss of FXR activity might thus lead to an inhibition of the alternative BA synthesis pathway with reduction of CDCA and LCA levels. A resulting shift towards the classical bile acid synthesis pathway would lead to higher production of CA, the toxic secondary BA DCA²³⁰, and their conjugates. Decreasing LCA levels and increasing TCA levels in the serum of L2-IL1B mice correlated with these findings and thus gave evidence for the plausibility of the hypothesis.

Generally, a shift from secondary to primary BA was detected, and both LCA and UDCA, which were previously shown to be rather beneficial, having anti-inflammatory effects and protective effects against DCA induced damage^{293,294}, were decreased. Also, the primary BA TCA has the potential to stimulate taurine deconjugation by gut microbiota, leading to production of both toxic hydrogen sulfide (H₂S) and DCA²⁹⁵.

It was previously shown that FXR activation could ameliorate the phenotype in a mouse model for CRC, amongst others by shifting the BA pool. Besides its tumor-promoting effects at the cellular level, the shift of the BA pool with increasing levels of potentially toxic TCA and decreasing levels of beneficial LCA and UDCA upon knockout of FXR might also have an impact on disease progression, especially as we could show systemic distribution of reabsorbed BA in the serum of the mice. In general, expression and activation of FXR in L2-IL1B mice seems to have protective effects, with loss of FXR promoting disease progression on the cellular level in correlation with a shift of the serum BA pool towards the classical BA synthesis pathway and more toxic BA, which could damage the tissue after their distribution via the serum.

5.2. HFD Treatment Leads To Increasing Numbers of BA Metabolizing Bacteria and of BA Levels in the L2-IL1B Mouse Model

Risk of progression from BE to EAC correlates with increasing obesity incidence and intake of western-style diet. Our group showed that feeding of L2-IL1B mice with HFD leads to accelerated tumor development in correlation with changes in the gut microbiome and the systemic inflammatory environment²⁷⁰. Yet the exact mechanisms underlying acceleration of disease progression through a diet high in fat are not clear.

What is known is that dietary intake high in fat causes gut BA levels to increase²⁸⁴⁻²⁸⁶. Bile acids are secreted from the gallbladder upon food consumption to support digestion of fat and lipid soluble substances^{11,30,31}. It was shown that reflux containing BA from gastro-duodenal content as well as treatment of BE cells *in vitro* and mice *in vivo* had damaging effects on the cells and promoted disease^{36-38,244}. Especially DCA, the most cytotoxic secondary and thus microbiome metabolized BA was shown to trigger inflammation and apoptosis resistance in BE and EAC via activation of ROS/NF- κ B signaling^{82,236,245}. To investigate if the tumor promoting effect of HFD on L2-IL1B mice might be conveyed by changes in the bile acid pool, we performed additional analyses on the L2-IL1B mouse cohort fed HFD, in which we found accelerated tumor development²⁷⁰.

5.2.1. The Gut Microbiome and Metabolome in Response to HFD

We could show primary, secondary, and total BA levels to be significantly increased in HFD mice compared to chow diet mice from our previously published paper²⁷⁰. In untargeted metabolomic analyses of cecal and fecal samples of an additional cohort of L2-IL1B mice fed HFD compared to CD, we could find enrichment of BA almost solely in HFD mice. Enrichment of MCAs and LCAs predominated but we also found hydroxycholeic acid, DHCA, IDCA and CDCA to be enriched in HFD mice. The only BA which could be detected to be enriched in CD mice were GCA and 3-DHCA. Interestingly we also found palmitic acid, the main FA compound of the HFD to be enriched in HFD mice, confirming enrichment of dietary components of the HFD in the metabolome.

Generally, MCA, taurine-conjugated BA, and secondary BA were shown to be the main BA responsible for the shift of the BA pool in HFD compared to chow and CD mice. Secondary BA which were metabolized from primary BA by gut bacteria were shown to have damaging effects in different diseases of the GI tract²²⁶. Secondary BA and taurine-conjugated BA were previously shown to also be associated with erosive esophagitis and BE in patients²⁹⁰, with influx of taurine-conjugated BA provoking symptoms in more patients than acidic reflux alone²⁹⁶. Secondary BA are metabolized by gut microbiota in the colon and are partially reabsorbed into the serum via the intestinal epithelium. Interestingly, the effect of BA on BE might not only be conveyed via reflux causing tissue damage, but also via signaling independent from reflux⁴⁴. Together with the fact that rodents are not capable of gastric and gastro-duodenal reflux, these findings support a more comprehensive concept of bile acid exposure triggering systemic effects rather than solely inducing direct tissue damage and erosion in the esophagus via reflux.

Regarding the fecal microbiome, we found a decrease in *Bacteroidota* and an increase in *Firmicutes* as often seen in studies on HFD or obesity¹⁹⁵. The class *Clostridia*, the families *Ruminococcaceae* and *Peptostreptococcaceae*, and also the genus *Blautia*, which are all involved in BA metabolism were more abundant in mice fed HFD compared to CD. The only bacterial strains with confirmed 7 α -dehydroxylation capacity have been identified in the classes *Clostridium* and *Eubacterium*^{203,206}. Only recently, members of the families *Ruminococcaceae*, *Lachnospiraceae* and *Peptostreptococcaceae* were predicted to also have strains with 7 α -dehydroxylation properties²⁰⁷. Also *Blautia* were already addressed as 7 α -dehydroxyating bacterium²⁹⁷. Increase of these bacterial groups might thus explain the shift towards secondary BA in HFD mice. Additionally, certain subordinates of the class *Clostridia* and the families *Ruminococcaceae* and *Peptostreptococcaceae* harbor HSDHs, enzymes capable of bacterial metabolism processes responsible for dehydrogenation, oxidation,

reduction, or epimerization of the BA, thus capable of inducing further changes in the fecal BA pool²⁰⁶.

Correlation analyses between bacterial groups and disease scores showed that *Clostridia*, but also the families of *Peptostreptococcaceae* and *Lachnospiraceae* and the genus *Blautia* positively correlated with dysplasia scores, while the family of *Ruminococcaceae* negatively correlated with dysplasia scores. None of the BA modulating genera in the family *Ruminococcaceae* could be identified to be regulated between disease groups or to be correlated with disease progression, indicating that other genera of the *Ruminococcaceae* family might be responsible for this correlation.

The findings of mainly positive correlation of BA metabolizing bacterial groups with disease progression and the increasing levels of taurine-conjugated and secondary BA in HFD mice substantiate the hypothesis that the shifted microbiome, producing increased levels of damaging BA might have an impact on accelerated disease progression in HFD mice. We propose the systemically distributed BA to promote disease progression via their damaging effect on the epithelial cells in the BE region.

5.2.2. The Serum and Tissue Metabolome in Response to HFD

Targeted BA analyses of the previously published mouse cohort showed that, in the serum of L2-IL1B mice fed HFD vs CD, enrichment, mainly of MCA and taurine-conjugated BA in all mice and of secondary BA with more pronounced effects in male mice could be detected, similar to the shift in gut BA levels. When correlating serum BA levels with dysplasia scores and inversely with goblet cell ratio as measure for differentiation, we found levels of DCA, the most cytotoxic secondary BA to be strongly correlated with disease severity.

Targeted BA analysis in the tissue of L2-IL1B mice showed that, in small intestinal tissue, DHCA levels were lower in HFD compared to CD mice; in accordance with the findings in untargeted metabolomic analysis, in which 3-DHCA was enriched in 6-month-old CD mice. The BA enriched in HFD were mainly taurine-conjugated BA and BA of the classical BA synthesis pathway involving DCA. In the colon tissue, the levels of all detected BA were significantly increasing in HFD compared to CD fed mice. Almost all BA enriched in colon tissue in response to HFD were deconjugated, as bacterial BA deconjugation in the intestine takes place before the fecal content reaches the colon.

Interestingly, we could also prove presence of BA in the BE tissue, and found significant enrichment of all BA in HFD compared to CD fed mice, again especially of taurine-conjugated BA and BA of the classical BA synthesis pathway including DCA derivatives. Interestingly the FXR antagonizing BAs α MCA, and the taurine conjugate of UDCA were enriched in both intestinal and BE tissue upon consumption of HFD^{189,298}, which correlates with the findings of loss of FXR during tumorigenesis. Most of the BA detected to be enriched in BE tissue were also enriched in small intestinal or colon tissue, where BA are absorbed from the gut and translocate into the serum, indicating systemic distribution of the reabsorbed BA into the BE tissue.

In general, our data confirm reuptake of BA via intestinal tissue and show systemic distribution of BA via blood circulation, with potential transport towards distal tissues. As blood from cardiac puncture was used for serum preparation it is not possible that the BA might only be present in the blood during enterohepatic circulation between gut and liver. Also, the BA found in serum and tissue of the examined mice reflected changes found by analyses of cecal content and feces.

These findings further substantiate the hypothesis that the shifted microbiome, producing increased levels of more damaging taurine-conjugated and secondary BA, including DCA, might have an impact on accelerated disease progression in HFD mice. Taurine-conjugation of BA encourages 7α -dehydroxylation of BA, and cleaved taurine can be metabolized by gut

bacteria producing cytotoxic H₂S^{295,299}. The effect of the BA on disease progression might be conveyed by systemic distribution via the serum towards distal tissues such as the SCJ.

Additionally, these findings correlate with the previous findings of FXR expression acting protective in BE. While FXR is not expressed in normal tissue, expression increases in BE due to activation by BA and is lost after progression to EAC. While FXR is mainly activated by primary BA, thus acting protectively against tissue damage and CSC proliferation, a diet-dependent shift of the BA pool towards taurine-conjugated and secondary BA and an increase in FXR antagonizing BA might lead to increased tissue damage on one hand, and on the other hand cause loss of FXR expression and thus loss of its protective effects in the tissue during carcinogenesis. These findings might be the first findings to potentially directly link dietary intake and gut microbiome composition to BA signaling triggering disease progression in an animal model of BE and EAC.

5.3. Treatment of L2-IL1B Mice Fed CD or HFD with OCA Shifts the BA Metabolizing Microbiome and BA Pool, Reduces Levels of Specific BA, and Acts Protective on Disease Progression

Diet-related obesity is an important risk factor for EAC^{282,283}. Taken together, our previous research findings showed that HFD increases BA metabolizing gut bacteria as well as gut, serum, and tissue BA levels with a shift towards secondary, taurine conjugated and potentially more FXR inhibiting BA. We also showed a protective function of FXR in BE tissue, with loss of FXR being observed in EAC patients and FXR knockout in mice promoting disease progression.

These findings indicated that the diet-shifted BA-pool has a damaging effect on epithelial cells in the BE region, which is not only conveyed via reflux, but also via systemic distribution in the blood. Certain BA, predominantly primary BA seem to stimulate FXR activation in the BE tissue, which induces downstream pathways that protect from BA mediated damage. A diet dependent shift of the gut microbiome and thus the BA pool towards more damaging and FXR antagonizing BA, as seen in HFD treated mice, during carcinogenesis might lead to loss of protective FXR activity in both gut and BE in combination with increased cellular damage.

We thus suspected treatment of L2-IL1B HFD mice with an FXR agonist to act protectively on diet-induced disease progression and performed treatment of L2-IL1B organoids and mice with the semi-synthetic, highly selective FXR agonist OCA to evaluate our hypothesis.

5.3.1. The Impact of OCA Treatment on Disease Development on Cellular Level

To examine the potentially ameliorating effect of an FXR agonist on disease progression, we first studied the effect of OCA on L2-IL1B mouse derived BE organoids in combination with BA treatment. OCA treatment had a protective function in L2-IL1B organoids treated with the highly cytotoxic BA DCA and the FXR antagonizing BA T β MCA. OCA effectively reduced cellular damage induced by DCA, and increased proliferation induced by both DCA and T β MCA. After confirmation of the treatment efficacy of OCA in 3D organoid culture, we treated two different cohorts of mice with OCA. The first cohort was treated with CD, HFD or HFD+OCA, while the second cohort was treated with CD, CD+OCA, HFD or HFD+OCA.

In L2-IL1B mice fed HFD, OCA induced differentiation and decreased proliferation and Lgr5 stem cell numbers in the metaplastic tissue and ameliorated the dysplastic phenotype in both treatment cohorts. OCA also significantly reduced expression of Lgr5 on FXR positive cells, thus substantiating our hypothesis of a direct regulation of Lgr5 via FXR, as previously also theorized by Fu et al. 2019²¹⁸. Potential compensation of BA signaling by upregulation of TGR5 expression upon treatment with OCA could be excluded, as we did not find changes in TGR5 expression in BE.

OCA treatment did not change FXR expression in the cardia region or the colon, but increased FXR expression in small intestinal tissue, where the majority of primary BA is reabsorbed. It was previously reported that OCA treatment in humans and mice led to reduced BA concentrations and increased abundance of probiotic microbiota in the small intestine, with protection of the probiotic microbiota from BA mediated growth inhibition³⁰⁰. Interestingly, in this study, microbial changes were specifically detected in the small intestinal, but not the fecal microbiome of OCA treated mice. This finding is consistent with our analyses, in which we detected a stronger impact of OCA on the cecal compared to the fecal microbiome, with significant changes in the fecal microbiome in only one of our two treatment cohorts.

Another study also reported beneficial effects of OCA treatment on intestinal integrity, leading to restoration of the epithelial barrier function along with reduced bacterial translocation and a reduction of inflammation characterized by immune cell infiltration and cytokine release in a rat model for liver cirrhosis³⁰¹. Also, in the treatment study of L2-IL1B mice, we could find restoration of colon crypt length and reduction of serum BA levels in HFD mice upon treatment with OCA, thus indicating a similar effect of OCA treatment in our mouse cohorts.

5.3.2. The Impact of OCA Treatment on the Microbiome and BA Profile in L2-IL1B HFD Mice in Context with other Systemic Effects

In the first mouse cohort fed CD, HFD or HFD+OCA, we found OCA to decrease the ratio of fecal secondary to primary BA, and to decrease total secondary BA levels in the stool of HFD mice. Especially DCA and TDCA acid levels, which were found to be increased in the stool of L2-IL1B mice fed HFD compared to CD and chow mice before, with additional increase of TDCA in BE tissue, were decreased by treatment with OCA. The increase of TCDCA with the parallel decrease of TDCA might indicate a shift back to less production of secondary from primary BA.

Clustering analysis showed that secondary BA levels were increased in HFD compared to CD and again decreased in HFD+OCA mice. While CA-7-ol-3-one and γ MCA were the main separators of the BA profile between groups, we also found cytotoxic DCA distinctly elevated in HFD mice and UDCA elevated in HFD+OCA mice compared to other groups. While UDCA was shown to inhibit FXR in obesity, it is generally seen as FXR activating BA and was also shown to have protective effects against DCA induced damage and against cytokine release and inflammation in a DSS-induced colitis model^{293,294}. Thus, in combination with FXR activation by OCA treatment, UDCA might also exert beneficial functions in L2-IL1B mice. Altogether these results showed a reduction of secondary BA levels, especially of cytotoxic DCA and TDCA in the stool of HFD+OCA compared to HFD mice, while on the other hand protective UDCA levels were elevated.

Analyzing the cecal microbiome of the mouse cohort, relative abundance of the phylum *Firmicutes* decreased, while abundance of *Bacteroidetes* increased in HFD+OCA mice compared to CD and HFD mice. The class of *Clostridia*, the only bacterial class with proven BA 7-dehydroxylation capacities was significantly decreased in 6-month-old CD and HFD+OCA compared to HFD mice^{203,206}. Also, the abundance of *Ruminococcaceae*, *Lachnospiraceae* and *Clostridium cluster IV* decreased in HFD+OCA compared to HFD mice, while *Clostridiaceae 1*, *Clostridium sensu stricto* and *Clostridium cluster XVIII* were more abundant. Especially strains of the *Clostridium cluster IV* were already shown to express bile acid-inducible (*bai*) operon encoding enzymes, that are key players in 7 α -dehydroxylation²⁸¹, thus indicating reduced secondary BA production in HFD+OCA treated mice. *Clostridium cluster XIVa*, which also expresses *bai* operon encoding enzymes was higher abundant in HFD compared to CD mice²⁸¹, indicating increased secondary BA metabolism upon treatment with HFD. According to our expectations *Clostridia*, *Firmicutes* and *Ruminococcaceae*, which were all highest abundant in HFD mice and proven or predicted to have 7-dehydroxylation capacities^{203,206,207}, were all positively correlated with dysplasia scores and negatively correlated with the

ratio of goblet cells (GC), correlating with the findings from metabolome analysis. Analyzing the fecal microbiome of the mouse cohort, microbial richness as a marker for microbial stability and health dropped significantly in HFD mice between 6 and 9 months of age. Findings closely resembled the findings from the analysis of the cecal content but were comparatively less pronounced.

Additionally, we found the family *Peptostreptococcaceae* to be more abundant in HFD+OCA mice compared to other groups. Disease correlations were less pronounced than in the cecal analysis, yet *Clostridia*, *Lachnospiraceae*, *Lactobacillaceae*, and *Ruminococcaceae* were all still negatively correlated with dysplasia scores and mainly positively correlated with the GC ratio, while *Peptostreptococcaceae* were negatively correlated with dysplasia scores. As only few strains of the family *Peptostreptococcaceae* were predicted to exert 7 α -dehydroxylation, this finding might not be related to BA metabolism²⁰⁷. These results correlate with our previous findings and our hypothesis that stimulation of FXR via OCA treatment could shift the BA pool in correlation with BA-metabolizing microbiota. Altogether, OCA treatment in HFD mice ameliorated disease severity in correlation with a reduction in BA metabolizing bacteria and secondary BA, especially of DCA and TDCA.

In the second cohort of L2-IL1B mice fed CD, CD+OCA, HFD or HFD+OCA, we performed untargeted and targeted metabolome and microbiome analyses to validate and extend the findings from the first treatment cohort. In untargeted metabolomic analyses of cecal content and feces we found OCA to be present in cecum but not the feces of the mice, therefore proving uptake and metabolization of OCA in the gut. In untargeted analyses of the cecum and feces BA, were almost exclusively upregulated in CD compared to CD+OCA mice. Results in the HFD cohort were less pronounced compared to the first treatment cohort, but we found CA, CA-7-sulphate, GCDCA and 7-KLCA to be enriched in HFD. In targeted BA analyses we found CA and DCA conjugates and CDCA and 7,12-DKLCA to be significantly decreased in the cecum of CD+OCA compared to CD mice. In HFD+OCA mice, we found increases in MCAs and LCA derivatives and a decrease in β MCA compared to HFD mice. In the feces, we detected an increase of secondary BA levels in HFD+OCA mice compared to HFD mice, while BA levels were lowest in CD+OCA mice. Single BA analyses showed similar effects as detected in the cecum. Reduced BSH activity in the gut of OCA treated CD and HFD mice indicated reduced deconjugation of primary BA by fecal bacteria^{30,205}. Deconjugation of BA is necessary before primary to secondary BA conversion can take place.

Microbiome analyses showed that in the cecum of the mice, OCA treatment in HFD mice increased richness compared to HFD. The *Firmicutes* to *Bacteroidetes* ratio, of which increases are associated with obesity decreased in HFD+OCA mice¹⁹³⁻¹⁹⁵. Also, the

abundance of BA metabolizing bacteria, represented by *Clostridia* and *Lachnospiraceae* decreased in HFD+OCA mice while the abundance of *Desulfovibrionaceae* increased. Almost all bacterial strains in the family *Desulfovibrionaceae* are sulfur reducing. Especially the genus *Bilophila* was already shown to reduce the sulphated amino acid taurine- and to produce toxic hydrogen sulfide²⁸⁸. Direct correlations of bacterial abundance with disease progression were less pronounced compared to the first treatment cohort. In the feces of the mice, we did not find significant changes in BA metabolizing bacterial groups, the availability of only two samples in the 6-month HFD+OCA group might have been additionally problematic for proper analyses. Also, in general we found almost no changes in bacteria with the different diets in the feces of the mice. As changes in the cecum were clearly detectable, this might indicate problems with the quality of 16S-sequencing results.

As already suspected after untargeted metabolomic analysis, these results indicate that in this mouse cohort, treatment with OCA had a strong effect on BA levels in CD, comparable to the findings in HFD+OCA compared to HFD in the first mouse cohort. The less pronounced effect in HFD in the second mouse cohort might have arisen from a subset of HFD mice in which total BA levels were relatively low.

Also, in this cohort while BA of the classical BA synthesis pathway leading to production of DCA and secondary BA, especially DCA and its derivatives but also taurine-conjugated BA were decreased by OCA in CD mice, we see a different pattern in HFD mice. In these mice, mainly UDCA and its derivatives, glycine conjugated primary BA and partially lithocholic acids are elevated. The increase in *Desulfovibrionaceae* might explain the lower abundance of taurine conjugated BA in most of the HFD+OCA mice, although they produce toxic H₂S. As OCA reduces dysplasia scores in both CD and HFD mice, it is plausible that not only the reduction of the more cytotoxic DCA and taurine conjugated BA, but also the enrichment of UDCA, and primary BA, especially glycine conjugated BA are important players in phenotypic amelioration in the L2-IL1B mouse model via their effect on BE cells. It was shown that both UDCA and LCA inhibited epithelial cytokine release and protected against inflammation in a mouse model of DSS-induced colitis²⁹⁴. Together, these findings fit into context with the fact that DCA was shown to promote inflammation^{236,237,245}, and to be cytotoxic in general and genotoxic to esophageal cells³⁰², while UDCA was ranging among the least toxic BA²³⁰, and both LCA and UDCA were shown to have beneficial effects²⁹⁴.

In general, in gastrointestinal tumor models especially secondary bile acids and accumulating toxic bile acids, mainly CA, TCA, DCA and TDCA promote carcinogenesis²⁴⁰⁻²⁴². Most importantly, in the BE tissue of the L2-IL1B HFD mice, levels of TCA and TDCA, both taurine-conjugated BA of the classical synthesis pathway reduced upon treatment with OCA. DCA

evidently also causes dysbiosis in the gut which further promotes intestinal carcinogenesis²²⁹. In addition, while CA, CDCA, DCA and its glycine and taurine conjugates were shown to increase intestinal permeability, UDCA did not^{234,235}.

OCA treatment was shown to increase abundance of probiotic microbiota in the gut and to promote intestinal barrier function and reduce bacterial translocation and inflammation^{300,301}. Reflecting these functions, we could show increased FXR expression in small intestinal tissue and restoration of crypt length in the colon of L2-IL1B HFD mice upon treatment with OCA. This finding together with our findings of shifting gut microbial bacteria indicates that OCA treatment potentially has similar beneficial effects on gut health in the L2-IL1B mouse model. Analyzing gut barrier integrity in HFD compared to HFD+OCA mice would thus be of interest in the future.

Analyzing immune cell levels in different organs of L2-IL1B mice fed HFD or HFD+OCA, we found a decrease of neutrophil infiltration in the cardia region of L2-IL1B mice, and an increase of NK cells in the cardia and activated NKT cells in the blood. Briefly, Neutrophils are seen as first defense mechanism promoting acute inflammation upon invasion of pathogens³⁰³, while NK and NKT cells were shown to kill tumor cells and shape the antitumor immune response via different modes of action^{304,305}.

It was previously demonstrated that immune cells such as macrophages, dendritic cells and NKT cells express FXR²⁹², and while the exact effect of OCA on immune cell levels and their activity in L2-IL1B mice is not entirely clear, our results indicate that activation of FXR by OCA treatment might reduce the systemic inflammatory phenotype of the mice that was shown to be massively aggravated in HFD treated L2-IL1B mice²⁷⁰. FXR knockout mice have been previously shown to develop severe inflammatory responses in disease models of intestinal damage and inflammation due to effects of FXR signaling on immune cell levels, inflammasome activation and control of immune cell – tissue interactions²⁹². Hence, the speculation of a reduction of systemic inflammation by OCA seems plausible. It would be highly interesting to perform additional experiments on L2-IL1B-FXR^{-/-}, HFD and HFD+OCA treated mice to better understand the exact effects of BA and OCA induced FXR signaling on the immune phenotype in L2-IL1B mice.

In summary, our findings, in correlation with previous findings on the different functions of the bile acids on cellular level or in other gastrointestinal diseases, show a general reduction of BA levels and indicate a detoxification of the BA pool in L2-IL1B HFD mice upon treatment with OCA, and a beneficial effect of OCA on the BA-metabolizing gut microbiome and intestinal homeostasis.

FXR knockout shifts the BA pool towards production of BA via the classical BA synthesis pathway, potentially by downregulation of the expression of Cyp27A1, the rate limiting enzyme for the alternative BA signaling pathway²⁰²⁻²⁰⁴, leading to enrichment of CA and DCA. Fittingly, FXR activation by OCA shifts the BA pool towards BA of the alternative BA synthesis pathway, ultimately leading to decreasing levels of DCA and enrichment of less toxic LCA but also of UDCA.

OCA treatment further leads to decreased abundance of BA metabolizing bacteria, most likely due to its activation of FXR with subsequent repression of de-novo BA generation and hence less substrate availability. OCA thus leads to lower BA levels in general and especially less toxic BA in the serum and tissue of the mice. The reduction of BA and activation of FXR by OCA might additionally reduce systemic inflammation in L2-IL1B HFD mice. Reduced inflammation in combination with reduced BA levels and microbial shifts upon OCA treatment might again have beneficial effects on gut health and barrier function and thus reduced translocation of metabolites via the intestinal barrier.

We thus propose that activation of FXR signaling by OCA treatment in L2-IL1B mice on HFD has different points of action in the gut, in BE tissue but also systemically, altogether leading to an amelioration of the dysplastic phenotype.

5.4. The BA Profile of Patients Shifts with Disease Progression, with Specific BA Increasing with Higher Disease Stage

The findings from our analyses of the different L2-IL1B based mouse cohorts with FXR knockout, CD and HFD feeding and OCA treatment in CD and HFD mice showed a diet-dependent increase of systemic BA levels in correlation with gut microbial shifts and with disease progression. We also found BA signaling to play an important role in microbial and BA pool homeostasis and on BA mediated disease progression in the L2-IL1B mouse model.

An effect of BA exposure on inflammation and cellular signaling in epithelial cells that precedes epithelial damage by the reflux was already previously suggested^{43,44}. We thus wondered whether elevated BA levels could also be distributed and affect the BE tissue independent of additional chronic reflux.

In our model we found BA levels not only elevated in the gut but also in the serum of the mice, which, supporting this hypothesis do not have reflux. We also found enrichment of BA in BE, which were reabsorbed into the serum via the intestinal tissue, indicating systemic distribution of reabsorbed BA via the serum towards distal tissues. To evaluate our hypothesis that BA, in addition to reflux, might support disease progression also via systemic distribution, we reanalyzed data and performed additional analyses on a subcohort of patients from a previously published human study cohort²⁴⁶. We reanalyzed microbial data based on zOTUs, with a focus on BA metabolizing bacteria, and performed targeted metabolomic BA analyses in both stool and serum of the patients.

5.4.1. The BA Profile in the Stool of Patients Shifts With Increasing Disease Severity in Correlation with an Increased Potential of Microbial Secondary BA Synthesis

In the stool of the patients, comparing the composition of the BA pool between groups, we found disease state specific shifts of the BA pool. In the patients' stool, we found an increase of secondary BA levels in BE compared to control patients, indicating a role of secondary BA in disease progression. Especially TDCA but also levels of the primary BA TCA, TCDCA and GCDCA increased with disease progression. Also, relative gene expression of BSH increased and correlated significantly with severity of the disease, indicating increased BA deconjugation as first step of secondary BA production in the gut. Nevertheless, we could not detect disease associated changes of single BA-metabolizing bacterial groups in the stool of the patients. We found a significant decrease in the abundance of *Akkermansia*, which is important for gut health and intestinal mucus barrier integrity in diseased compared to control patients²⁸⁹. *Akkermansia* is a commensal mucus degrading bacterial strain that colonizes the gut mucus and defends its niche against colonization with pathogenic mucus degrading bacteria, thus maintaining mucus barrier integrity and homeostasis. Decreasing levels of this bacterial species were also found in obese and type-2-diabetes mice, while its presence was shown to have beneficial effects on the host metabolic profile¹⁹⁸. Decreasing *Akkermansia* levels could be indicating increased colonization with pathogens and increased permeability of the gut barrier function in diseased patients, leading to increasing translocation of bacteria and metabolites, including BA.

5.4.2. The BA Profile in the Serum of Patients Shows Distinct Shifts Towards Taurine-Conjugated and Secondary BA in Correlation with Disease Progression, in Association with Enrichment of Potentially BA-Metabolizing Bacteria in the Esophagus

Analyzing the serum of patients, we could detect efficient reabsorption of BA into the blood. The fact that we are able to find BA distributed by the serum indicates a systemic effect of BA on distal tissues, that is independent of chronic reflux. When comparing serum BA of patients with different disease states, we found significant increases of the single BA TUDCA, TDCA, TCDCA and GUDCA with increasing disease severity. In general, we found primarily taurine conjugated BA, DCA and UDCA to be upregulated in the serum of patients correlating with accelerated disease progression, similar to the tendencies in the stool BA pool. These observations correlate with our hypothesis that malignant progression from BE to EAC might be triggered by a shift towards more cytotoxic DCA and taurine-conjugates which can be metabolized to produce toxic H₂S.

TCA, DCA and TDCA which were all enriched in the serum of more severely diseased patients were previously shown to promote carcinogenesis in models of gastrointestinal cancers²⁴⁰⁻²⁴². The enrichment of distinct BA in different disease states indicates different roles of BA during disease onset and progression, with DCA seeming to be the main driving BA in onset of disease. The enrichment of bile acids of the classical synthesis pathway –CA and DCA – but also of taurine conjugated bile acids and of CA-7- α -3one correlates with the findings in the HFD fed mouse cohorts. An increase in BA metabolizing bacteria at the esophageal tissue in correlation with the shift towards taurine-conjugated BA might indicate additional metabolization of BA in the esophagus. Upon loss of FXR activity in BE tissue due to a shift towards secondary BA, also its protective functions against BA mediated cellular damage in the tissue are lost, thus leading to increased effects of cellular damage by toxic BA.

In summary, although we were unable to map changes in single BA metabolizing bacteria in the stool to disease progression in patients, we found BSH expression as marker for secondary BA production potential by the gut microbiome. We also found taurine-conjugated BA and especially CA, CDCA and DCA conjugates to be elevated in the serum correlating with worsened disease states. These findings further substantiate our hypothesis that systemically distributed BA, especially taurine-conjugated BA and DCA conjugates might effect disease progression in BE and EAC independent from direct reflux induced effects.

5.5. Conclusion

Previous studies hypothesized that BA exert their toxic functions mainly as free acids soluble only at a pH of 3-6, which is reached in gastric juices upon acid suppression³⁰⁶. This theory conflicts with studies reporting that acid suppression significantly decreases gastroduodenal reflux and thus likely bile acid exposure to the esophagus³⁰⁷, and excludes efficacy of BA mediated damage in patients without acid suppressors. Consistent with our findings, different conjugated BAs and DCA as secondary BA exerted their damaging function also at neutral pH in a study on esophageal cell lines. They did not increase acid mediated damage in acidified media, leading to the question how BA mediated DNA damage might be correlated with acidic reflux³⁰⁸. Additionally, esophageal damage in the development of BE is not primarily caused by direct effects of acidic gastro-duodenal reflux, but via a cytokine and immune mediated injury^{38,44} consistent with previous findings of elevated cytokine levels in the L2-IL1B mouse model^{270,271}. We found that activation of FXR signaling by OCA might have a beneficial effect on the inflammatory phenotype in L2-IL1B mice fed HFD. Additional analyses to explain the specific effects of BA and FXR signaling on the immune phenotype would be of high interest.

Interestingly, bile acid transporters are expressed in BE and lost in EAC, similarly to the expression of FXR³⁰⁹. Active BA transport through the cell and the protective intracellular effects of elevated FXR expression in the tissue could be one explanation of how esophageal epithelial cells react to direct BA exposure. Loss of FXR expression would correlate with increasing DNA damage and mutational capacities supporting malignant transformation. As FXR is mainly activated by primary BA, a shift in the BA pool towards secondary, taurine-conjugated, and generally less FXR activating BA due to shifted dietary intake could lead to loss of FXR expression. Loss of the protective effects of FXR and increased damaging, inflammatory and pro-proliferative effects of secondary and taurine-conjugated BA in the tissue presumably cumulate in promotion of carcinogenesis. Our serum BA analysis showed a correlation between FXR activity, serum BA levels and disease progression in mice. Given that mice lack gastroduodenal reflux this clearly points to a systemic effect of circulating BAs on FXR expression in the metaplastic tissue. Vice versa, activation of FXR via OCA is able to change BA metabolism and the BA pool systemically.

In summary, a diet high in fat and energy changes the microbiome and increases BA levels, which in turn leads to modifications in BA metabolism in the gut. HFD in L2-IL1B mice increases BA levels, especially of more damaging secondary and taurine-conjugated BA in the stool, in the intestinal tissues and serum, with a correlation of serum DCA and disease severity. These findings are proving effective transition of increased amounts of secondary BA into the blood stream, that consequently lead to increased levels of BA in BE tissue, similar to previously demonstrated findings in the portal vein and liver²²⁶. Loss of FXR with onset of

tumorigenesis results in a dysfunctional cellular response to BA induced cell stress in the epithelial (stem)cells leading to a tumor-promoting microenvironment, characterized by dedifferentiation, stem cell expansion, DNA damage and increased inflammatory responsiveness. Metabolomic analyses suggest a feedback loop where the loss of FXR further inhibits alternative BA production and promotes classical BA synthesis, leading to increased cytotoxic DCA and its conjugates. Treatment with OCA ameliorates the dysplastic phenotype, reduces BA levels, and leads to a detoxification of the BA pool together with potential beneficial effects on gut health and the inflammatory phenotype. In patients, metabolomic analysis of the blood serum also revealed a systemic increase of secondary BAs, mainly of cytotoxic DCA derivatives and of taurine-conjugated BA with disease progression. In conclusion, these data provide a novel concept on how the tightly interrelated diet-microbiome-metabolome axis influences tumorigenesis at a distant location.

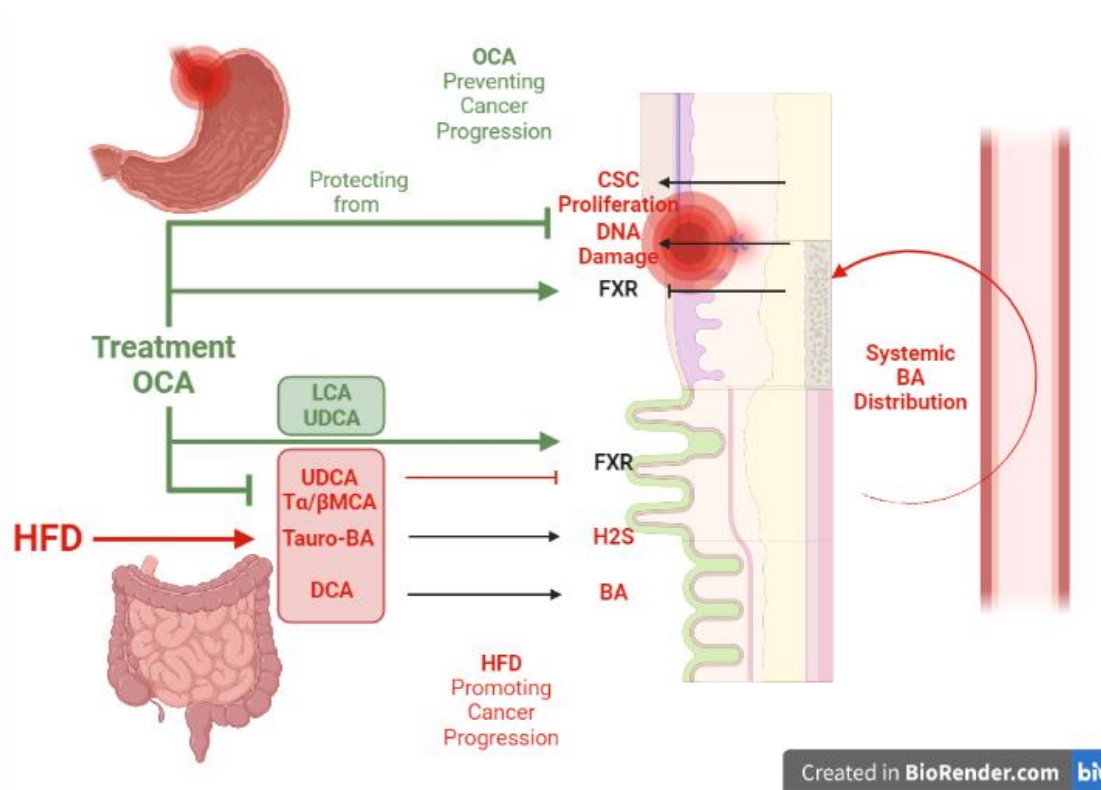


Figure 70: Schematic graphical overview over the effects of Diet and OCA treatment on Disease Progression from BE to EAC (Created with BioRender.com)

5.6. Limitations

Certainly, the performed studies can only provide a limited insight in diet induced shifts of the microbiome and metabolome on disease progression, as the interaction between dietary components, the abundance of gut microbial bacteria and resulting changes in BA metabolization are part of a highly complex and interactive network. Due to evolving analysis, sequencing, and computational techniques, we are now able to perform sequencing of bacterial species and mass spectrometry of the metabolome of all different samples, but the scientific world has only begun to analyze, evaluate and categorize findings in both of these fields. Until today, we have a very limited knowledge about which bacterial strains are capable of BA metabolization, and especially the additional metabolization potential that lies in bacterial interaction networks remains elusive. This thesis addresses the overarching scientific question of how dietary intake can change the microbiome and metabolome with a focus on BA metabolization and signaling and although we found evidence proving the existence of a diet-microbiome-metabolome axis influencing disease progression amongst others via changing the systemic BA pool, the complexity and novelty of the field leaves room for evaluation of our findings in more detail. Also, analysis of cohorts with bigger sample sizes would be of interest to further evaluate our findings, as both mouse cohort sizes and the number of patients per group ranged between $n=5-18$. Upscaling, especially of analyses in patients might provide more valuable insight in the applicability of our hypothesis to a broad spectrum of patients.

5.7. Future Perspectives

Our findings revealed how a diet–microbiome–metabolome axis, with focus on BA metabolization and signaling, might influence esophageal carcinogenesis in a genetic mouse model of BE (L2-IL1B) and in patients. Feeding of a HFD increased the presence of BA-metabolizing bacterial communities in the gut and of systemic BA levels in the mice in correlation with accelerated disease progression, while activation of FXR by treatment with OCA reduced BA levels and the dysplastic phenotype of the mouse model. Increasing serum BA levels in patients in correlation with disease progression fit into the context with findings of the mouse model. Yet the complexity of this study leaves room for further investigation of our findings in detail and on a greater scale.

Currently, patient acquisition and sample collection in the BarretNET study is ongoing and provides the potential for microbial and metabolomic analysis in a bigger patient cohort. Additionally, further in-depth evaluation of the untargeted metabolomic data from both the mouse and human studies will be performed to search for additional metabolomic anomalies between groups aside from enriched BA levels.

5.7.1. Impact of Environmental Factors on Inflammation and Progenitor Cells in the L2-IL1B Mouse Model

In addition to the promotion of the phenotype via diet affected BA levels and signaling, we found evidence for a direct effect of BA signaling via FXR on the inflammatory phenotype and Lgr5 stem cell proliferation. Previous studies on the L2-IL1B mouse model showed that HFD increases the inflammatory phenotype in correlation with promoted disease progression²⁷⁰, while anti-inflammatory medication has beneficial effects on disease progression³¹⁰, and Notch signaling promotes disease progression via regulation of inflammatory signaling and progenitor cell differentiation²⁷¹. These findings together with the results of this study indicate that the inflammatory phenotype and its effects on the stem cell niche are highly important for disease progression in BE. Currently, a study to examine detailed interactions between environmental triggers such as circulating BA and their effects on systemic inflammation and signaling in progenitor cells in the BE epithelium is planned.

5.7.2. A Fructose Enriched Diet Study to Examine the Effects of Excessive Consumption of Sweeteners on L2-IL1B Mice

In combination with previous findings from Münch et al.²⁷⁰ we showed that a diet rich in fat massively accelerates disease progression in L2-IL1B mice by increasing systemic inflammation and BA levels. Excessive fat consumption is one of the components of so called western diet, that promotes obesity, which became endemic in the western world and is a risk factor for BE and EAC. Excessive consumption of sweeteners such as high fructose corn sirup in sweets and beverages is also a component of western diet. To examine if a high fructose diet has similar effects as a HFD on the L2-IL1B mouse model, currently, a high fructose diet intervention study is performed in the laboratory. This study involves evaluation of the phenotype and gene expression, microbiome and metabolome analysis similar to the HFD study. Results are expected soon.

5.7.3. A Fiber Enriched Diet Study to Examine Potential Beneficial Effects of Dietary Intervention on Disease Progression in L2-IL1B Mice

In addition to analyzing the effects of components of western diet on the L2-IL1B mouse model, we are also planning to analyze, whether a diet enriched in fiber and potentially beneficial fatty acids could have beneficial effects on disease progression in the L2-IL1B mouse model. Currently, a high fiber diet intervention study with supplementation of the omega-3 fatty acid docosahexaenoic acid or the omega-6 fatty acid arachidonic acid is planned in collaboration with another laboratory, involving evaluation of the phenotype and gene expression, microbiome and metabolome analysis similar to this study.

5.7.4. Summary of Future Perspectives

The findings of this study showed a complex interaction between environmental triggers, metabolic changes, genetic drivers, and recruitment of the immune system in onset and progression of BE. The findings of how dietary intake might affect disease progression and signaling on both systemic and cellular level in combination with the ongoing and future studies have the potential to provide a more comprehensive understanding of how the environment triggers BE and EAC and might lead to a change in thinking regarding disease prevention strategies for this disease. A more holistic view on disease prevention in human patients in the future could potentially involve addition of nutritional advice and individual counseling to improve a healthy and active lifestyle of the patients to existing strategies.

6. References

1. Su, A., Parker, C.H. & Conklin, J.L. Esophageal anatomy and physiology. in *Clinical and Basic Neurogastroenterology and Motility* 79-88 (Elsevier, 2020).
2. Chaudhry, S.R. & Bordoni, B. Anatomy, Thorax, Esophagus. in *StatPearls [Internet]* (StatPearls Publishing, 2019).
3. Kuo, B. & Urma, D. Esophagus-anatomy and development. *GI Motility online* (2006).
4. Feldman, M., Friedman, L.S. & Brandt, L.J. *Sleisenger and Fordtran's gastrointestinal and liver disease E-book: pathophysiology, diagnosis, management*, (Elsevier Health Sciences, 2015).
5. Brasseur, J.G., Nicosia, M.A., Pal, A. & Miller, L.S. Function of longitudinal vs circular muscle fibers in esophageal peristalsis, deduced with mathematical modeling. *World journal of gastroenterology: WJG* **13**, 1335 (2007).
6. Rosen, R.D. & Winters, R. Physiology, Lower Esophageal Sphincter. in *StatPearls [Internet]* (StatPearls Publishing, 2020).
7. Lang, I.M. & Shaker, R. Anatomy and physiology of the upper esophageal sphincter. *The American journal of medicine* **103**, 50S-55S (1997).
8. Zaninotto, G., DeMeester, T.R., Schwizer, W., Johansson, K.-E. & Cheng, S.-C. The lower esophageal sphincter in health and disease. *The American journal of surgery* **155**, 104-111 (1988).
9. Mittal, R. Motor function of the pharynx, esophagus, and its sphincters. in *Colloquium Series on Integrated Systems Physiology: From Molecule to Function*, Vol. 3 1-84 (Morgan & Claypool Life Sciences, 2011).
10. Bajwa, S.A. & Kasi, A. Physiology, Esophagus. (2019).
11. Tortora, G.J. & Derrickson, B.H. *Principles of anatomy and physiology*, (John Wiley & Sons, 2018).
12. Wellcome, M.O. *Gastrointestinal Physiology*, (Springer, 2018).
13. Csendes, A., *et al.* Location of the lower oesophageal sphincter and the squamous columnar mucosal junction in 109 healthy controls and 778 patients with different degrees of endoscopic oesophagitis. *Gut* **34**, 21-27 (1993).
14. Delattre, J.-F., Avisse, C., Marcus, C. & Flament, J.-B. Functional anatomy of the gastroesophageal junction. *Surgical Clinics of North America* **80**, 241-260 (2000).
15. Adler, D.G. & Romero, Y. Primary esophageal motility disorders. in *Mayo Clinic Proceedings*, Vol. 76 195-200 (Elsevier, 2001).
16. Garman, K.S., Orlando, R.C. & Chen, X. experimental models for Barrett's esophagus and esophageal adenocarcinoma. *American Journal of Physiology-Gastrointestinal and Liver Physiology* **302**, G1231-G1243 (2012).
17. Greaves, P. *Histopathology of preclinical toxicity studies: interpretation and relevance in drug safety evaluation*, (Academic Press, 2011).
18. Gärtner, K. The forestomach of rats and mice, an effective device supporting digestive metabolism in muridae. *Journal of Experimental Animal Science* **42**, 1-20 (2002).
19. Hogben, C.A.M., Schanker, L.S., Tocco, D.J. & Brodie, B.B. Absorption of drugs from the stomach. II. The human. *Journal of pharmacology and experimental therapeutics* **120**, 540-545 (1957).
20. Lim, R.T., *et al.* First-pass metabolism of ethanol is predominantly gastric. *Alcoholism: Clinical and Experimental Research* **17**, 1337-1344 (1993).
21. Chvasta, T.E. & Cooke, A.R. Emptying and absorption of caffeine from the human stomach. *Gastroenterology* **61**, 838-843 (1971).

22. Chung, K.W. & Chung, H.M. *Gross anatomy*, (Lippincott Williams & Wilkins, 2008).
23. Fisher, R. & Cohen, S. Physiological characteristics of the human pyloric sphincter. *Gastroenterology* **64**, 67-75 (1973).
24. Fisher, R.S., Lipshutz, W. & Cohen, S. The hormonal regulation of pyloric sphincter function. *The Journal of Clinical Investigation* **52**, 1289-1296 (1973).
25. Schiff, E.R., Small, N.C. & Dietschy, J.M. Characterization of the kinetics of the passive and active transport mechanisms for bile acid absorption in the small intestine and colon of the rat. *The Journal of clinical investigation* **51**, 1351-1362 (1972).
26. Booth, C. & Mollin, D. The site of absorption of vitamin B12 in man. *Lancet* **1**, 18-21 (1959).
27. Azzouz, L.L. & Sharma, S. Physiology, large intestine. *StatPearls [Internet]* (2020).
28. Moran Jr, E. Anatomy, microbes, and fiber: Small versus large intestine. *Journal of Applied Poultry Research* **15**, 154-160 (2006).
29. Rui, L. Energy metabolism in the liver. *Comprehensive physiology* **4**, 177-197 (2011).
30. Chiang, J.Y. & Ferrell, J.M. Bile acid metabolism in liver pathobiology. *Gene Expression The Journal of Liver Research* **18**, 71-87 (2018).
31. Coleman, R. Biochemistry of bile secretion. *Biochemical Journal* **244**, 249-261 (1987).
32. Kahrilas, P.J., Bredenoord, A.J., Carlson, D.A. & Pandolfino, J.E. Advances in management of esophageal motility disorders. *Clinical Gastroenterology and Hepatology* **16**, 1692-1700 (2018).
33. Richter, J.E. & Rubenstein, J.H. Presentation and epidemiology of gastroesophageal reflux disease. *Gastroenterology* **154**, 267-276 (2018).
34. Tack, J. & Pandolfino, J.E. Pathophysiology of gastroesophageal reflux disease. *Gastroenterology* **154**, 277-288 (2018).
35. Ness-Jensen, E., Hveem, K., El-Serag, H. & Lagergren, J. Lifestyle intervention in gastroesophageal reflux disease. *Clinical gastroenterology and hepatology* **14**, 175-182. e173 (2016).
36. Kauer, W., *et al.* Mixed reflux of gastric and duodenal juices is more harmful to the esophagus than gastric juice alone. The need for surgical therapy re-emphasized. *Annals of surgery* **222**, 525 (1995).
37. McQuaid, K., Laine, L., Fennerty, M., Souza, R. & Spechler, S. Systematic review: the role of bile acids in the pathogenesis of gastro-oesophageal reflux disease and related neoplasia. *Alimentary pharmacology & therapeutics* **34**, 146-165 (2011).
38. Oh, D.S., *et al.* The impact of reflux composition on mucosal injury and esophageal function. *Journal of Gastrointestinal Surgery* **10**, 787-797 (2006).
39. Schlottmann, F., Dreifuss, N.H. & Patti, M.G. Obesity and esophageal cancer: GERD, Barrett's esophagus, and molecular carcinogenic pathways. *Expert review of gastroenterology & hepatology*, 1-9 (2020).
40. Shaheen, N. & Ransohoff, D.F. Gastroesophageal reflux, Barrett esophagus, and esophageal cancer: scientific review. *Jama* **287**, 1972-1981 (2002).
41. Winters Jr, C., *et al.* Barrett's esophagus: a prevalent, occult complication of gastroesophageal reflux disease. *Gastroenterology* **92**, 118-124 (1987).
42. Spechler, S.J. Carcinogenesis at the gastroesophageal junction: free radicals at the frontier. *Gastroenterology* **122**, 1518-1520 (2002).
43. Souza, R.F. Reflux esophagitis and its role in the pathogenesis of Barrett's metaplasia. *Journal of gastroenterology* **52**, 767-776 (2017).

44. Souza, R.F., *et al.* Gastroesophageal reflux might cause esophagitis through a cytokine-mediated mechanism rather than caustic acid injury. *Gastroenterology* **137**, 1776-1784 (2009).
45. Souza, R.F. From reflux esophagitis to esophageal adenocarcinoma. *Digestive diseases* **34**, 483-490 (2016).
46. Elinav, E., *et al.* Inflammation-induced cancer: crosstalk between tumours, immune cells and microorganisms. *Nature reviews. Cancer* **13**, 759 (2013).
47. Abdel-Latif, M.M., Duggan, S., Reynolds, J.V. & Kelleher, D. Inflammation and esophageal carcinogenesis. *Current opinion in pharmacology* **9**, 396-404 (2009).
48. Spechler, S.J., Fitzgerald, R.C., Prasad, G.A. & Wang, K.K. History, molecular mechanisms, and endoscopic treatment of Barrett's esophagus. *Gastroenterology* **138**, 854-869 (2010).
49. Hvid-Jensen, F., Pedersen, L., Drewes, A.M., Sørensen, H.T. & Funch-Jensen, P. Incidence of adenocarcinoma among patients with Barrett's esophagus. *New England Journal of Medicine* **365**, 1375-1383 (2011).
50. Sikkema, M., De Jonge, P.J., Steyerberg, E.W. & Kuipers, E.J. Risk of esophageal adenocarcinoma and mortality in patients with Barrett's esophagus: a systematic review and meta-analysis. *Clinical gastroenterology and hepatology* **8**, 235-244 (2010).
51. Bhat, S., *et al.* Risk of malignant progression in Barrett's esophagus patients: results from a large population-based study. *Journal of the National Cancer Institute* **103**, 1049-1057 (2011).
52. Dulai, G.S., Guha, S., Kahn, K.L., Gornbein, J. & Weinstein, W.M. Preoperative prevalence of Barrett's esophagus in esophageal adenocarcinoma: a systematic review. *Gastroenterology* **122**, 26-33 (2002).
53. Ruol, A., *et al.* Intestinal metaplasia is the probable common precursor of adenocarcinoma in Barrett esophagus and adenocarcinoma of the gastric cardia. *Cancer* **88**, 2520-2528 (2000).
54. Rustgi, A.K. & El-Serag, H.B. Esophageal carcinoma. *The New England journal of medicine* **371**, 2499-2509 (2014).
55. Xian, W., Ho, K.Y., Crum, C.P. & McKeon, F. Cellular origin of Barrett's esophagus: controversy and therapeutic implications. *Gastroenterology* **142**, 1424-1430 (2012).
56. Spechler, S.J. & Goyal, R.K. Barrett's esophagus. *New England Journal of Medicine* **315**, 362-371 (1986).
57. Shaheen, N.J., Falk, G.W., Iyer, P.G. & Gerson, L.B. ACG clinical guideline: diagnosis and management of Barrett's esophagus. *The American journal of gastroenterology* **111**, 30-50 (2016).
58. Pouw, R.E., *et al.* Efficacy of radiofrequency ablation combined with endoscopic resection for Barrett's esophagus with early neoplasia. *Clinical gastroenterology and hepatology* **8**, 23-29 (2010).
59. Phoa, K.N., *et al.* Radiofrequency ablation vs endoscopic surveillance for patients with Barrett esophagus and low-grade dysplasia: a randomized clinical trial. *Jama* **311**, 1209-1217 (2014).
60. Jemal, A., *et al.* Cancer statistics, 2003. *CA: a cancer journal for clinicians* **53**, 5-26 (2003).
61. Pisani, P., Parkin, D.M., Bray, F. & Ferlay, J. Estimates of the worldwide mortality from 25 cancers in 1990. *International journal of cancer* **83**, 18-29 (1999).
62. Ferlay, J., *et al.* Estimates of worldwide burden of cancer in 2008: GLOBOCAN 2008. *International journal of cancer* **127**, 2893-2917 (2010).

63. Jemal, A., *et al.* Cancer statistics, 2009. *CA: a cancer journal for clinicians* **59**, 225-249 (2009).
64. Siegel, R.L., Miller, K.D. & Jemal, A. Cancer statistics, 2019. *CA: a cancer journal for clinicians* **69**, 7-34 (2019).
65. Jemal, A., Center, M.M., DeSantis, C. & Ward, E.M. Global patterns of cancer incidence and mortality rates and trends. *Cancer Epidemiology and Prevention Biomarkers* **19**, 1893-1907 (2010).
66. Jemal, A., *et al.* Global cancer statistics. *CA: a cancer journal for clinicians* **61**, 69-90 (2011).
67. Engel, L.S., *et al.* Population attributable risks of esophageal and gastric cancers. *Journal of the National Cancer Institute* **95**, 1404-1413 (2003).
68. Islami, F., *et al.* High-temperature beverages and foods and esophageal cancer risk—A systematic review. *International journal of cancer* **125**, 491-524 (2009).
69. Tran, G.D., *et al.* Prospective study of risk factors for esophageal and gastric cancers in the Linxian general population trial cohort in China. *International journal of cancer* **113**, 456-463 (2005).
70. Islami, F., *et al.* Epidemiologic features of upper gastrointestinal tract cancers in Northeastern Iran. *British journal of cancer* **90**, 1402-1406 (2004).
71. Castellsagué, X., *et al.* Independent and joint effects of tobacco smoking and alcohol drinking on the risk of esophageal cancer in men and women. *International journal of cancer* **82**, 657-664 (1999).
72. Veugeliers, P., Porter, G., Guernsey, D. & Casson, A. Obesity and lifestyle risk factors for gastroesophageal reflux disease, Barrett esophagus and esophageal adenocarcinoma. *Diseases of the Esophagus* **19**, 321-328 (2006).
73. Camilleri, M., Malhi, H. & Acosta, A. Gastrointestinal complications of obesity. *Gastroenterology* **152**, 1656-1670 (2017).
74. Ryan, A.M., *et al.* Obesity, metabolic syndrome and esophageal adenocarcinoma: epidemiology, etiology and new targets. *Cancer epidemiology* **35**, 309-319 (2011).
75. Allison, P. & Johnstone, A. The oesophagus lined with gastric mucous membrane. *Thorax* **8**, 87 (1953).
76. Barrett, N. Chronic peptic ulcerz of the œophagus and ‘œsophagitis’. *British Journal of Surgery* **38**, 175-182 (1950).
77. Qumseya, B.J., *et al.* Disease Progression in Barrett’s Low-Grade Dysplasia With Radiofrequency Ablation Compared With Surveillance: Systematic Review and Meta-Analysis. *The American Journal of Gastroenterology* (2017).
78. Hamilton, S.R. & Yardley, J.H. Regeneration of cardiac type mucosa and acquisition of Barrett mucosa after esophagogastrostomy. *Gastroenterology* **72**, 669-675 (1977).
79. Chandrasoma, P. Controversies of the cardiac mucosa and Barrett's oesophagus. *Histopathology* **46**, 361-373 (2005).
80. O’Neil, A., Petersen, C.P., Choi, E., Engevik, A.C. & Goldenring, J.R. Unique cellular lineage composition of the first gland of the mouse gastric corpus. *Journal of Histochemistry & Cytochemistry* **65**, 47-58 (2017).
81. Lee, Y., *et al.* Gastrin stimulates a cholecystokinin-2-receptor-expressing cardia progenitor cell and promotes progression of Barrett's-like esophagus. *Oncotarget* **8**, 203 (2017).
82. Quante, M., *et al.* Bile acid and inflammation activate gastric cardia stem cells in a mouse model of Barrett-like metaplasia. *Cancer cell* **21**, 36-51 (2012).

83. Senoo, M., Pinto, F., Crum, C.P. & McKeon, F. p63 is essential for the proliferative potential of stem cells in stratified epithelia. *Cell* **129**, 523-536 (2007).
84. Wang, X., *et al.* Residual embryonic cells as precursors of a Barrett's-like metaplasia. *Cell* **145**, 1023-1035 (2011).
85. Gedert, H., Kiel, S., Heep, H.J., Gabbert, H.E. & Sarbia, M. The role of p63 and Δ Np63 (p40) protein expression and gene amplification in esophageal carcinogenesis. *Human pathology* **34**, 850-856 (2003).
86. Tosh, D. & Slack, J.M. How cells change their phenotype. *Nat Rev Mol Cell Biol* **3**, 187-194 (2002).
87. Yu, W.Y., Slack, J.M. & Tosh, D. Conversion of columnar to stratified squamous epithelium in the developing mouse oesophagus. *Dev Biol* **284**, 157-170 (2005).
88. Milano, F., *et al.* Bone morphogenetic protein 4 expressed in esophagitis induces a columnar phenotype in esophageal squamous cells. *Gastroenterology* **132**, 2412-2421 (2007).
89. Kong, J., Crissey, M.A., Funakoshi, S., Kreindler, J.L. & Lynch, J.P. Ectopic Cdx2 expression in murine esophagus models an intermediate stage in the emergence of Barrett's esophagus. *PloS one* **6**, e18280 (2011).
90. Barbera, M. & Fitzgerald, R.C. Cellular origin of Barrett's metaplasia and oesophageal stem cells. *Biochemical Society transactions* **38**, 370-373 (2010).
91. Coad, R.A., *et al.* On the histogenesis of Barrett's oesophagus and its associated squamous islands: a three-dimensional study of their morphological relationship with native oesophageal gland ducts. *The Journal of pathology* **206**, 388-394 (2005).
92. Gillen, P., Keeling, P., Byrne, P.J., West, A.B. & Hennessy, T.P. Experimental columnar metaplasia in the canine oesophagus. *The British journal of surgery* **75**, 113-115 (1988).
93. Miwa, K., *et al.* Reflux of duodenal or gastro-duodenal contents induces esophageal carcinoma in rats. *International journal of cancer* **67**, 269-274 (1996).
94. Leedham, S.J., *et al.* Individual crypt genetic heterogeneity and the origin of metaplastic glandular epithelium in human Barrett's oesophagus. *Gut* **57**, 1041-1048 (2008).
95. Owen, R.P., *et al.* Single cell RNA-seq reveals profound transcriptional similarity between Barrett's oesophagus and oesophageal submucosal glands. *Nat Commun* **9**, 4261 (2018).
96. Jiang, M., *et al.* Transitional basal cells at the squamous-columnar junction generate Barrett's oesophagus. *Nature* **550**, 529 (2017).
97. Houghton, J., *et al.* Gastric cancer originating from bone marrow-derived cells. *Science* **306**, 1568-1571 (2004).
98. Shi, Q., *et al.* Evidence for circulating bone marrow-derived endothelial cells. *Blood* **92**, 362-367 (1998).
99. Petersen, B.E., *et al.* Bone marrow as a potential source of hepatic oval cells. *Science* **284**, 1168-1170 (1999).
100. LaBarge, M.A. & Blau, H.M. Biological progression from adult bone marrow to mononucleate muscle stem cell to multinucleate muscle fiber in response to injury. *Cell* **111**, 589-601 (2002).
101. Krause, D.S., *et al.* Multi-organ, multi-lineage engraftment by a single bone marrow-derived stem cell. *Cell* **105**, 369-377 (2001).
102. Sarosi, G., *et al.* Bone marrow progenitor cells contribute to esophageal regeneration and metaplasia in a rat model of Barrett's esophagus. *Dis Esophagus* **21**, 43-50 (2008).

103. Hutchinson, L., *et al.* Human Barrett's adenocarcinoma of the esophagus, associated myofibroblasts, and endothelium can arise from bone marrow-derived cells after allogeneic stem cell transplant. *Stem cells and development* **20**, 11-17 (2011).
104. Haiyu, Z., *et al.* Incidence and Survival Changes in Patients with Esophageal Adenocarcinoma during 1984–2013. *BioMed research international* **2019**(2019).
105. Hur, C., *et al.* Trends in esophageal adenocarcinoma incidence and mortality. *Cancer* **119**, 1149-1158 (2013).
106. Matsuno, K., *et al.* Time trends in the incidence of esophageal adenocarcinoma, gastric adenocarcinoma, and superficial esophagogastric junction adenocarcinoma. *Journal of gastroenterology* **54**, 784-791 (2019).
107. Rantanen, T., Oksala, N. & Sand, J. Adenocarcinoma of the oesophagus and oesophagogastric junction: analysis of incidence and risk factors. *Anticancer Research* **36**, 2323-2329 (2016).
108. Islami, F., DeSantis, C.E. & Jemal, A. Incidence trends of esophageal and gastric cancer subtypes by race, ethnicity, and age in the United States, 1997–2014. *Clinical Gastroenterology and Hepatology* **17**, 429-439 (2019).
109. He, H., *et al.* Trends in the incidence and survival of patients with esophageal cancer: A SEER database analysis. *Thoracic Cancer* **11**, 1121-1128 (2020).
110. Nishi, T., Makuuchi, H., Ozawa, S., Shimada, H. & Chino, O. The present status and future of Barrett's esophageal adenocarcinoma in Japan. *Digestion* **99**, 185-190 (2019).
111. Arnold, M., Laversanne, M., Brown, L.M., Devesa, S.S. & Bray, F. Predicting the future burden of esophageal cancer by histological subtype: international trends in incidence up to 2030. *American Journal of Gastroenterology* **112**, 1247-1255 (2017).
112. McColl, K.E. What is causing the rising incidence of esophageal adenocarcinoma in the West and will it also happen in the East? *Journal of gastroenterology*, 1-5 (2019).
113. Ness-Jensen, E., Lindam, A., Lagergren, J. & Hveem, K. Changes in prevalence, incidence and spontaneous loss of gastro-oesophageal reflux symptoms: a prospective population-based cohort study, the HUNT study. *Gut* **61**, 1390-1397 (2012).
114. Peters, Y., *et al.* Incidence of progression of persistent nondysplastic Barrett's esophagus to malignancy. *Clinical Gastroenterology and Hepatology* **17**, 869-877. e865 (2019).
115. Desai, T.K., *et al.* The incidence of oesophageal adenocarcinoma in non-dysplastic Barrett's oesophagus: a meta-analysis. *Gut* **61**, 970-976 (2012).
116. Singh, S., *et al.* Incidence of esophageal adenocarcinoma in Barrett's esophagus with low-grade dysplasia: a systematic review and meta-analysis. *Gastrointestinal endoscopy* **79**, 897-909. e894 (2014).
117. Rastogi, A., *et al.* Incidence of esophageal adenocarcinoma in patients with Barrett's esophagus and high-grade dysplasia: a meta-analysis. *Gastrointestinal endoscopy* **67**, 394-398 (2008).
118. Cook, M.B., *et al.* Gastroesophageal reflux in relation to adenocarcinomas of the esophagus: a pooled analysis from the Barrett's and Esophageal Adenocarcinoma Consortium (BEACON). *PloS one* **9**, e103508 (2014).
119. Chow, W.-H., *et al.* The relation of gastroesophageal reflux disease and its treatment to adenocarcinomas of the esophagus and gastric cardia. *Jama* **274**, 474-477 (1995).
120. Islami, F. & Kamangar, F. Helicobacter pylori and esophageal cancer risk: a meta-analysis. *Cancer prevention research* **1**, 329-338 (2008).
121. Blaser, M.J. Disappearing microbiota: Helicobacter pylori protection against esophageal adenocarcinoma. *Cancer Prevention Research* **1**, 308-311 (2008).

122. Hooi, J.K., *et al.* Global prevalence of *Helicobacter pylori* infection: systematic review and meta-analysis. *Gastroenterology* **153**, 420-429 (2017).
123. Anderson, L.A., *et al.* Relationship between *Helicobacter pylori* infection and gastric atrophy and the stages of the oesophageal inflammation, metaplasia, adenocarcinoma sequence: results from the FINBAR case-control study. *Gut* **57**, 734-739 (2008).
124. Oksanen, A., *et al.* Atrophic gastritis and *Helicobacter pylori* infection in outpatients referred for gastroscopy. *Gut* **46**, 460-463 (2000).
125. Blaser, M.J. & Atherton, J.C. *Helicobacter pylori* persistence: biology and disease. *The Journal of clinical investigation* **113**, 321-333 (2004).
126. Locke III, G.R., Talley, N.J., Fett, S.L., Zinsmeister, A.R. & Melton III, L.J. Risk factors associated with symptoms of gastroesophageal reflux. *The American journal of medicine* **106**, 642-649 (1999).
127. Wajed, S.A., Streets, C.G., Bremner, C.G. & DeMeester, T.R. Elevated body mass disrupts the barrier to gastroesophageal reflux. *Archives of Surgery* **136**, 1014-1019 (2001).
128. Hampel, H., Abraham, N.S. & El-Serag, H.B. Meta-analysis: obesity and the risk for gastroesophageal reflux disease and its complications. *Annals of internal medicine* **143**, 199-211 (2005).
129. Nilsson, M., Johnsen, R., Ye, W., Hveem, K. & Lagergren, J. Obesity and estrogen as risk factors for gastroesophageal reflux symptoms. *Jama* **290**, 66-72 (2003).
130. Mayne, S.T. & Navarro, S.A. Diet, obesity and reflux in the etiology of adenocarcinomas of the esophagus and gastric cardia in humans. *The Journal of nutrition* **132**, 3467S-3470S (2002).
131. Festi, D., *et al.* Body weight, lifestyle, dietary habits and gastroesophageal reflux disease. *World journal of gastroenterology: WJG* **15**, 1690 (2009).
132. Kamat, P., Wen, S., Morris, J. & Anandasabapathy, S. Exploring the association between elevated body mass index and Barrett's esophagus: a systematic review and meta-analysis. *The Annals of thoracic surgery* **87**, 655-662 (2009).
133. Lagergren, J., Bergström, R. & Nyrén, O. Association between body mass and adenocarcinoma of the esophagus and gastric cardia. *Annals of internal medicine* **130**, 883-890 (1999).
134. Poutahidis, T., *et al.* Microbial reprogramming inhibits Western diet-associated obesity. *PloS one* **8**, e68596 (2013).
135. Bäckhed, F., Manchester, J.K., Semenkovich, C.F. & Gordon, J.I. Mechanisms underlying the resistance to diet-induced obesity in germ-free mice. *Proceedings of the National Academy of Sciences* **104**, 979-984 (2007).
136. Rockett, J., Larkin, K., Darnton, S., Morris, A. & Matthews, H. Five newly established oesophageal carcinoma cell lines: phenotypic and immunological characterization. *British journal of cancer* **75**, 258-263 (1997).
137. Kosoff, R.E., *et al.* Development and characterization of an organotypic model of Barrett's esophagus. *Journal of cellular physiology* **227**, 2654-2659 (2012).
138. Kalabis, J., *et al.* Isolation and characterization of mouse and human esophageal epithelial cells in 3D organotypic culture. *Nature protocols* **7**, 235 (2012).
139. Pastuła, A., *et al.* Three-dimensional gastrointestinal organoid culture in combination with nerves or fibroblasts: a method to characterize the gastrointestinal stem cell niche. *Stem cells international* **2016**(2016).
140. Selye, H. The experimental production of peptic haemorrhagic oesophagitis. *Canadian Medical Association journal* **39**, 447 (1938).

141. Omura, N., *et al.* Establishment of surgically induced chronic acid reflux esophagitis in rats. *Scandinavian journal of gastroenterology* **34**, 948-953 (1999).
142. Bremner, C., Lynch, V. & Ellis Jr, F. Barrett's esophagus: congenital or acquired? An experimental study of esophageal mucosal regeneration in the dog. *Surgery* **68**, 209-216 (1970).
143. Pera, M., *et al.* Influence of esophagojejunostomy on the induction of adenocarcinoma of the distal esophagus in Sprague-Dawley rats by subcutaneous injection of 2, 6-dimethylnitrosomorpholine. *Cancer research* **49**, 6803-6808 (1989).
144. Goldstein, S.R., *et al.* Development of esophageal metaplasia and adenocarcinoma in a rat surgical model without the use of a carcinogen. *Carcinogenesis* **18**, 2265-2270 (1997).
145. Chen, X., Ding, Y., Liu, C.-G., Mikhail, S. & Yang, C.S. Overexpression of glucose-regulated protein 94 (Grp94) in esophageal adenocarcinomas of a rat surgical model and humans. *Carcinogenesis* **23**, 123-130 (2002).
146. Levrat, M., Lambert, R. & Kirshbaum, G. Esophagitis produced by reflux of duodenal contents in rats. *The American journal of digestive diseases* **7**, 564-573 (1962).
147. Bulay, O. & Mirvish, S.S. Carcinogenesis in rat esophagus by intraperitoneal injection of different doses of methyl-n-amyl nitrosamine. *Cancer research* **39**, 3644-3646 (1979).
148. Clark, G.W., *et al.* Effect of gastroduodenal juice and dietary fat on the development of Barrett's esophagus and esophageal neoplasia: an experimental rat model. *Annals of surgical oncology* **1**, 252-261 (1994).
149. Goldstein, S.R., Yang, G.Y., Chen, X., Curtis, S.K. & Yang, C.S. Studies of iron deposits, inducible nitric oxide synthase and nitrotyrosine in a rat model for esophageal adenocarcinoma. *Carcinogenesis* **19**, 1445-1449 (1998).
150. Ellis Jr, F.H., Xu, X., Kulke, M.H., LoCicero III, J. & Loda, M. Malignant transformation of the esophageal mucosa is enhanced in p27 knockout mice. *The Journal of Thoracic and Cardiovascular Surgery* **122**, 809-814 (2001).
151. Pham, T.H., Genta, R.M., Spechler, S.J., Souza, R.F. & Wang, D.H. Development and characterization of a surgical mouse model of reflux esophagitis and Barrett's esophagus. *Journal of Gastrointestinal Surgery* **18**, 234-241 (2014).
152. Fein, M., *et al.* Loss of Function of Trp53, but Not Apc, Leads to the Development of Esophageal Adenocarcinoma in Mice with Jejunoesophageal Reflux. *Journal of Surgical Research* **83**, 48-55 (1999).
153. Crawford, S.E., *et al.* Thrombospondin-1 is a major activator of TGF- β 1 in vivo. *Cell* **93**, 1159-1170 (1998).
154. Armstrong, B. & Doll, R. Environmental factors and cancer incidence and mortality in different countries, with special reference to dietary practices. *International journal of cancer* **15**, 617-631 (1975).
155. Doll, R. & Peto, R. The causes of cancer: quantitative estimates of avoidable risks of cancer in the United States today. *JNCI: Journal of the National Cancer Institute* **66**, 1192-1308 (1981).
156. Alidadi, M., *et al.* The Effect of Caloric Restriction and Fasting on Cancer. in *Seminars in Cancer Biology* (Elsevier, 2020).
157. Calle, E.E., Rodriguez, C., Walker-Thurmond, K. & Thun, M.J. Overweight, obesity, and mortality from cancer in a prospectively studied cohort of US adults. *New England Journal of Medicine* **348**, 1625-1638 (2003).

158. Popkin, B.M. & Gordon-Larsen, P. The nutrition transition: worldwide obesity dynamics and their determinants. *International journal of obesity* **28**, S2-S9 (2004).
159. Cordain, L., *et al.* Origins and evolution of the Western diet: health implications for the 21st century. *The American journal of clinical nutrition* **81**, 341-354 (2005).
160. Patton, J.S. & Carey, M.C. Watching fat digestion. *Science* **204**, 145-148 (1979).
161. Lopez-Miranda, J., Williams, C. & Lairon, D. Dietary, physiological, genetic and pathological influences on postprandial lipid metabolism. *British Journal of Nutrition* **98**, 458-473 (2007).
162. Roberts, M.S., Magnusson, B.M., Burczynski, F.J. & Weiss, M. Enterohepatic circulation. *Clinical pharmacokinetics* **41**, 751-790 (2002).
163. Calle, E.E. & Thun, M.J. Obesity and cancer. *Oncogene* **23**, 6365-6378 (2004).
164. Tatsch, E., *et al.* Oxidative DNA damage is associated with inflammatory response, insulin resistance and microvascular complications in type 2 diabetes. *Mutation Research/Fundamental and Molecular Mechanisms of Mutagenesis* **782**, 17-22 (2015).
165. Barnea, M., Shamay, A., Stark, A.H. & Madar, Z. A high-fat diet has a tissue-specific effect on adiponectin and related enzyme expression. *Obesity* **14**, 2145-2153 (2006).
166. Barb, D., Pazaitou-Panayiotou, K. & Mantzoros, C.S. Adiponectin: a link between obesity and cancer. *Expert opinion on investigational drugs* **15**, 917-931 (2006).
167. Barb, D., Williams, C.J., Neuwirth, A.K. & Mantzoros, C.S. Adiponectin in relation to malignancies: a review of existing basic research and clinical evidence. *The American journal of clinical nutrition* **86**, 858S-866S (2007).
168. Wang, D., *et al.* Leptin regulates proliferation and apoptosis of colorectal carcinoma through PI3K/Akt/mTOR signalling pathway. *Journal of biosciences* **37**, 91-101 (2012).
169. Kim, K.-A., Gu, W., Lee, I.-A., Joh, E.-H. & Kim, D.-H. High fat diet-induced gut microbiota exacerbates inflammation and obesity in mice via the TLR4 signaling pathway. *PloS one* **7**, e47713 (2012).
170. Lee, Y.S., *et al.* Inflammation is necessary for long-term but not short-term high-fat diet-induced insulin resistance. *Diabetes* **60**, 2474-2483 (2011).
171. Harvey, A.E., Lashinger, L.M. & Hursting, S.D. The growing challenge of obesity and cancer: an inflammatory issue. *Annals of the New York Academy of Sciences* **1229**, 45-52 (2011).
172. Ibrahim, M.M. Subcutaneous and visceral adipose tissue: structural and functional differences. *Obesity reviews* **11**, 11-18 (2010).
173. Wisse, B.E. The inflammatory syndrome: the role of adipose tissue cytokines in metabolic disorders linked to obesity. *Journal of the American society of nephrology* **15**, 2792-2800 (2004).
174. Cani, P.D., *et al.* Changes in gut microbiota control metabolic endotoxemia-induced inflammation in high-fat diet-induced obesity and diabetes in mice. *Diabetes* **57**, 1470-1481 (2008).
175. Ridaura, V.K., *et al.* Gut microbiota from twins discordant for obesity modulate metabolism in mice. *Science* **341**(2013).
176. Peterson, J., *et al.* The NIH human microbiome project. *Genome research* **19**, 2317-2323 (2009).
177. Huttenhower, C., *et al.* Structure, function and diversity of the healthy human microbiome. *nature* **486**, 207 (2012).
178. Marchesi, J.R. & Ravel, J. The vocabulary of microbiome research: a proposal. (Springer, 2015).

179. Sartor, R.B. Microbial influences in inflammatory bowel diseases. *Gastroenterology* **134**, 577-594 (2008).
180. Jubelin, G., *et al.* Modulation of enterohaemorrhagic *Escherichia coli* survival and virulence in the human gastrointestinal tract. *Microorganisms* **6**, 115 (2018).
181. Sender, R., Fuchs, S. & Milo, R. Are we really vastly outnumbered? Revisiting the ratio of bacterial to host cells in humans. *Cell* **164**, 337-340 (2016).
182. Xu, H.-S., *et al.* Survival and viability of nonculturable *Escherichia coli* and *Vibrio cholerae* in the estuarine and marine environment. *Microbial ecology* **8**, 313-323 (1982).
183. Oliver, J.D. Recent findings on the viable but nonculturable state in pathogenic bacteria. *FEMS microbiology reviews* **34**, 415-425 (2010).
184. Stackebrandt, E. & GOEBEL, B.M. Taxonomic note: a place for DNA-DNA reassociation and 16S rRNA sequence analysis in the present species definition in bacteriology. *International journal of systematic and evolutionary microbiology* **44**, 846-849 (1994).
185. Duerkop, B.A., Vaishnav, S. & Hooper, L.V. Immune responses to the microbiota at the intestinal mucosal surface. *Immunity* **31**, 368-376 (2009).
186. Lawley, T.D. & Walker, A.W. Intestinal colonization resistance. *Immunology* **138**, 1-11 (2013).
187. Nieuwdorp, M., Gilijamse, P.W., Pai, N. & Kaplan, L.M. Role of the microbiome in energy regulation and metabolism. *Gastroenterology* **146**, 1525-1533 (2014).
188. Sonnenburg, J.L. & Bäckhed, F. Diet–microbiota interactions as moderators of human metabolism. *Nature* **535**, 56 (2016).
189. Sayin, S.I., *et al.* Gut microbiota regulates bile acid metabolism by reducing the levels of tauro-beta-muricholic acid, a naturally occurring FXR antagonist. *Cell metabolism* **17**, 225-235 (2013).
190. Ivanov, I.I., *et al.* Induction of intestinal Th17 cells by segmented filamentous bacteria. *Cell* **139**, 485-498 (2009).
191. Maynard, C.L., Elson, C.O., Hatton, R.D. & Weaver, C.T. Reciprocal interactions of the intestinal microbiota and immune system. *Nature* **489**, 231 (2012).
192. Atarashi, K., *et al.* T reg induction by a rationally selected mixture of *Clostridia* strains from the human microbiota. *Nature* **500**, 232 (2013).
193. Turnbaugh, P.J., *et al.* An obesity-associated gut microbiome with increased capacity for energy harvest. *nature* **444**, 1027 (2006).
194. Hildebrandt, M.A., *et al.* High-fat diet determines the composition of the murine gut microbiome independently of obesity. *Gastroenterology* **137**, 1716-1724. e1712 (2009).
195. Ley, R.E., Turnbaugh, P.J., Klein, S. & Gordon, J.I. Human gut microbes associated with obesity. *nature* **444**, 1022-1023 (2006).
196. Daniel, H., *et al.* High-fat diet alters gut microbiota physiology in mice. *The ISME journal* **8**, 295-308 (2014).
197. Walker, A., *et al.* Distinct signatures of host–microbial meta-metabolome and gut microbiome in two C57BL/6 strains under high-fat diet. *The ISME journal* **8**, 2380-2396 (2014).
198. Everard, A., *et al.* Cross-talk between *Akkermansia muciniphila* and intestinal epithelium controls diet-induced obesity. *Proceedings of the national academy of sciences* **110**, 9066-9071 (2013).

199. Neyrinck, A.M., *et al.* Dietary modulation of clostridial cluster XIVa gut bacteria (*Roseburia* spp.) by chitin–glucan fiber improves host metabolic alterations induced by high-fat diet in mice. *The Journal of nutritional biochemistry* **23**, 51-59 (2012).
200. de La Serre, C.B., *et al.* Propensity to high-fat diet-induced obesity in rats is associated with changes in the gut microbiota and gut inflammation. *American Journal of Physiology-Gastrointestinal and Liver Physiology* **299**, G440-G448 (2010).
201. Do, M.H., Lee, E., Oh, M.-J., Kim, Y. & Park, H.-Y. High-glucose or-fructose diet cause changes of the gut microbiota and metabolic disorders in mice without body weight change. *Nutrients* **10**, 761 (2018).
202. Chiang, J.Y. Regulation of bile acid synthesis: pathways, nuclear receptors, and mechanisms. *Journal of hepatology* **40**, 539-551 (2004).
203. Wahlström, A., Sayin, S.I., Marschall, H.-U. & Bäckhed, F. Intestinal crosstalk between bile acids and microbiota and its impact on host metabolism. *Cell metabolism* **24**, 41-50 (2016).
204. Russell, D.W. The enzymes, regulation, and genetics of bile acid synthesis. *Annual review of biochemistry* **72**, 137-174 (2003).
205. Begley, M., Hill, C. & Gahan, C.G. Bile salt hydrolase activity in probiotics. *Applied and environmental microbiology* **72**, 1729-1738 (2006).
206. Ridlon, J.M., Kang, D.-J. & Hylemon, P.B. Bile salt biotransformations by human intestinal bacteria. *Journal of lipid research* **47**, 241-259 (2006).
207. Vital, M., Rud, T., Rath, S., Pieper, D.H. & Schlüter, D. Diversity of bacteria exhibiting bile acid-inducible 7 α -dehydroxylation genes in the human gut. *Computational and structural biotechnology journal* **17**, 1016-1019 (2019).
208. van Nierop, F.S., *et al.* Clinical relevance of the bile acid receptor TGR5 in metabolism. *The lancet Diabetes & endocrinology* **5**, 224-233 (2017).
209. Wang, H., Chen, J., Hollister, K., Sowers, L.C. & Forman, B.M. Endogenous bile acids are ligands for the nuclear receptor FXR/BAR. *Molecular cell* **3**, 543-553 (1999).
210. Makishima, M., *et al.* Vitamin D receptor as an intestinal bile acid sensor. *Science* **296**, 1313-1316 (2002).
211. Chiang, J.Y. Bile acids: regulation of synthesis. *Journal of lipid research* **50**, 1955-1966 (2009).
212. Nakahara, M., *et al.* Ileal bile acid-binding protein, functionally associated with the farnesoid X receptor or the ileal bile acid transporter, regulates bile acid activity in the small intestine. *Journal of Biological Chemistry* **280**, 42283-42289 (2005).
213. Cipriani, S., Mencarelli, A., Palladino, G. & Fiorucci, S. FXR activation reverses insulin resistance and lipid abnormalities and protects against liver steatosis in Zucker (*fa/fa*) obese rats. *Journal of lipid research* **51**, 771-784 (2010).
214. Fiorucci, S., *et al.* Cross-talk between farnesoid-X-receptor (FXR) and peroxisome proliferator-activated receptor γ contributes to the antifibrotic activity of FXR ligands in rodent models of liver cirrhosis. *Journal of Pharmacology and Experimental Therapeutics* **315**, 58-68 (2005).
215. Modica, S., Murzilli, S., Salvatore, L., Schmidt, D.R. & Moschetta, A. Nuclear bile acid receptor FXR protects against intestinal tumorigenesis. *Cancer research* **68**, 9589-9594 (2008).
216. Lv, B., *et al.* FXR acts as a metastasis suppressor in intrahepatic cholangiocarcinoma by inhibiting IL-6-induced epithelial-mesenchymal transition. *Cellular Physiology and Biochemistry* **48**, 158-172 (2018).

217. Vavassori, P., Mencarelli, A., Renga, B., Distrutti, E. & Fiorucci, S. The bile acid receptor FXR is a modulator of intestinal innate immunity. *The Journal of Immunology* **183**, 6251-6261 (2009).
218. Fu, T., *et al.* FXR regulates intestinal cancer stem cell proliferation. *Cell* **176**, 1098-1112. e1018 (2019).
219. Wang, Y.-D., Chen, W.-D., Moore, D.D. & Huang, W. FXR: a metabolic regulator and cell protector. *Cell research* **18**, 1087-1095 (2008).
220. Markham, A. & Keam, S.J. Obeticholic acid: first global approval. *Drugs* **76**, 1221-1226 (2016).
221. Ridlon, J.M., Kang, D.J., Hylemon, P.B. & Bajaj, J.S. Bile acids and the gut microbiome. *Current opinion in gastroenterology* **30**, 332 (2014).
222. Reimer, R. & McBURNEY, M.I. Dietary fiber modulates intestinal proglucagon messenger ribonucleic acid and postprandial secretion of glucagon-like peptide-1 and insulin in rats. *Endocrinology* **137**, 3948-3956 (1996).
223. Kobayashi, M., *et al.* Prevention and treatment of obesity, insulin resistance, and diabetes by bile acid-binding resin. *Diabetes* **56**, 239-247 (2007).
224. Ma, H. & Patti, M.E. Bile acids, obesity, and the metabolic syndrome. *Best practice & research Clinical gastroenterology* **28**, 573-583 (2014).
225. Mouzaki, M., *et al.* Bile acids and dysbiosis in non-alcoholic fatty liver disease. *PloS one* **11**, e0151829 (2016).
226. Ma, C., *et al.* Gut microbiome-mediated bile acid metabolism regulates liver cancer via NKT cells. *Science* **360**(2018).
227. Hofmann, A.F. & Eckmann, L. How bile acids confer gut mucosal protection against bacteria. *Proceedings of the National Academy of Sciences* **103**, 4333-4334 (2006).
228. Gupta, B., *et al.* Western diet-induced increase in colonic bile acids compromises epithelial barrier in nonalcoholic steatohepatitis. *The FASEB Journal* **34**, 7089-7102 (2020).
229. Cao, H., *et al.* Secondary bile acid-induced dysbiosis promotes intestinal carcinogenesis. *International journal of cancer* **140**, 2545-2556 (2017).
230. Hofmann, A.F. The continuing importance of bile acids in liver and intestinal disease. *Archives of internal medicine* **159**, 2647-2658 (1999).
231. Poupon, R. Ursodeoxycholic acid and bile-acid mimetics as therapeutic agents for cholestatic liver diseases: an overview of their mechanisms of action. *Clinics and research in hepatology and gastroenterology* **36**, S3-S12 (2012).
232. Laurin, J., *et al.* Ursodeoxycholic acid or clofibrate in the treatment of non-alcohol-induced steatohepatitis: a pilot study. *Hepatology* **23**, 1464-1467 (1996).
233. Yao, J., *et al.* FXR agonist GW4064 alleviates endotoxin-induced hepatic inflammation by repressing macrophage activation. *World Journal of Gastroenterology: WJG* **20**, 14430 (2014).
234. Zhao, D. & Hirst, B.H. Bile salt-induced increases in duodenal brush-border membrane proton permeability, fluidity, and fragility. *Digestive diseases and sciences* **35**, 589-595 (1990).
235. Raimondi, F., *et al.* Bile acids modulate tight junction structure and barrier function of Caco-2 monolayers via EGFR activation. *American Journal of Physiology-Gastrointestinal and Liver Physiology* **294**, G906-G913 (2008).
236. Zhang, R., *et al.* Adiponectin modulates DCA-induced inflammation via the ROS/NF-kappa B signaling pathway in esophageal adenocarcinoma cells. *Digestive diseases and sciences* **59**, 89-97 (2014).

237. Lajczak-McGinley, N.K., *et al.* The secondary bile acids, ursodeoxycholic acid and lithocholic acid, protect against intestinal inflammation by inhibition of epithelial apoptosis. *Physiological reports* **8**, e14456 (2020).
238. Png, C.W., *et al.* Mucolytic Bacteria With Increased Prevalence in IBD Mucosa Augment In Vitro Utilization of Mucin by Other Bacteria. *American Journal of Gastroenterology* **105**, 2420-2428 (2010).
239. Van den Bossche, L., *et al.* Ursodeoxycholic acid and its taurine- or glycine-conjugated species reduce colitogenic dysbiosis and equally suppress experimental colitis in mice. *Applied and environmental microbiology* **83**(2017).
240. Ajouz, H., Mukherji, D. & Shamseddine, A. Secondary bile acids: an underrecognized cause of colon cancer. *World journal of surgical oncology* **12**, 1-5 (2014).
241. Lax, S., *et al.* Expression of the nuclear bile acid receptor/farnesoid X receptor is reduced in human colon carcinoma compared to nonneoplastic mucosa independent from site and may be associated with adverse prognosis. *International journal of cancer* **130**, 2232-2239 (2012).
242. Bernstein, H., Bernstein, C., Payne, C., Dvorakova, K. & Garewal, H. Bile acids as carcinogens in human gastrointestinal cancers. *Mutation Research/Reviews in Mutation Research* **589**, 47-65 (2005).
243. Yu, Q., Jiang, Z. & Zhang, L. Bile acid regulation: A novel therapeutic strategy in non-alcoholic fatty liver disease. *Pharmacology & therapeutics* **190**, 81-90 (2018).
244. Fang, D., *et al.* Barrett's esophagus: progression to adenocarcinoma and markers. *Annals of the New York Academy of Sciences* **1232**, 210-229 (2011).
245. Feng, C., *et al.* Diallyl disulfide suppresses the inflammation and apoptosis resistance induced by DCA through ROS and the NF- κ B signaling pathway in human barrett's epithelial cells. *Inflammation* **40**, 818-831 (2017).
246. Wiethaler, M., *et al.* BarrettNET—a prospective registry for risk estimation of patients with Barrett's esophagus to progress to adenocarcinoma. *Diseases of the Esophagus* **32**, doz024 (2019).
247. Quante, M., Abrams, J.A., Lee, Y. & Wang, T.C. Barrett esophagus: what a mouse model can teach us about human disease. *Cell Cycle* **11**, 4328-4338 (2012).
248. Sinal, C.J., *et al.* Targeted disruption of the nuclear receptor FXR/BAR impairs bile acid and lipid homeostasis. *Cell* **102**, 731-744 (2000).
249. Abramoff, M.D., Magalhães, P.J. & Ram, S.J. Image processing with ImageJ. *Biophotonics international* **11**, 36-42 (2004).
250. Godon, J.-J., Zumstein, E., Dabert, P., Habouzit, F. & Moletta, R. Molecular microbial diversity of an anaerobic digester as determined by small-subunit rDNA sequence analysis. *Applied and environmental microbiology* **63**, 2802-2813 (1997).
251. Klindworth, A., *et al.* Evaluation of general 16S ribosomal RNA gene PCR primers for classical and next-generation sequencing-based diversity studies. *Nucleic acids research* **41**, e1 (2013).
252. Lagkouravdos, I., *et al.* IMNGS: A comprehensive open resource of processed 16S rRNA microbial profiles for ecology and diversity studies. *Scientific reports* **6**, 33721 (2016).
253. Edgar, R.C. UPARSE: highly accurate OTU sequences from microbial amplicon reads. *Nat Methods* **10**, 996-998 (2013).
254. Edgar, R.C. Search and clustering orders of magnitude faster than BLAST. *Bioinformatics* **26**, 2460-2461 (2010).

255. Lagkouvardos, I., Fischer, S., Kumar, N. & Clavel, T. Rhea: a transparent and modular R pipeline for microbial profiling based on 16S rRNA gene amplicons. *PeerJ* **5**, e2836 (2017).
256. Team, R. RStudio: Integrated Development Environment for R. (RStudio, Inc., Boston, 2016).
257. R Core Development Team. R: A language and environment for statistical computing. (R Foundation for Statistical Computing, Vienna, 2018).
258. Goedhart, J. & Luijsterburg, M.S. VolcaNoseR is a web app for creating, exploring, labeling and sharing volcano plots. *Scientific reports* **10**, 1-5 (2020).
259. Chambers, M.C., *et al.* A cross-platform toolkit for mass spectrometry and proteomics. *Nature biotechnology* **30**, 918-920 (2012).
260. Smith, C.A., Want, E.J., O'Maille, G., Abagyan, R. & Siuzdak, G. XCMS: processing mass spectrometry data for metabolite profiling using nonlinear peak alignment, matching, and identification. *Analytical chemistry* **78**, 779-787 (2006).
261. Tautenhahn, R., Böttcher, C. & Neumann, S. Highly sensitive feature detection for high resolution LC/MS. *BMC bioinformatics* **9**, 1-16 (2008).
262. Benton, H.P., Want, E.J. & Ebbels, T.M. Correction of mass calibration gaps in liquid chromatography–mass spectrometry metabolomics data. *Bioinformatics (Oxford, England)* **26**, 2488-2489 (2010).
263. Xia, J., Sinelnikov, I.V., Han, B. & Wishart, D.S. MetaboAnalyst 3.0—making metabolomics more meaningful. *Nucleic acids research* **43**, W251-W257 (2015).
264. Zhang, F., *et al.* Duodenal reflux induces cyclooxygenase-2 in the esophageal mucosa of rats: evidence for involvement of bile acids. *Gastroenterology* **121**, 1391-1399 (2001).
265. Lefebvre, P., Cariou, B., Lien, F., Kuipers, F. & Staels, B. Role of bile acids and bile acid receptors in metabolic regulation. *Physiological reviews* **89**, 147-191 (2009).
266. Shaik, F.B., Prasad, D.V. & Narala, V.R. Role of farnesoid X receptor in inflammation and resolution. *Inflammation Research* **64**, 9-20 (2015).
267. De Gottardi, A., *et al.* Expression of the bile acid receptor FXR in Barrett's esophagus and enhancement of apoptosis by guggulsterone in vitro. *Molecular cancer* **5**, 48 (2006).
268. Capello, A., *et al.* Bile acid-stimulated expression of the farnesoid X receptor enhances the immune response in Barrett esophagus. *American Journal of Gastroenterology* **103**, 1510-1516 (2008).
269. Kim, S.M., *et al.* Prognostic biomarkers for esophageal adenocarcinoma identified by analysis of tumor transcriptome. *PloS one* **5**, e15074 (2010).
270. Munch, N., *et al.* High-fat Diet Accelerates Carcinogenesis in a Mouse Model of Barrett's Esophagus via IL8 and Alterations to the Gut Microbiome. *Gastroenterology in press*(2019).
271. Kunze, B., *et al.* Notch Signaling Mediates Differentiation in Barrett's Esophagus and Promotes Progression to Adenocarcinoma. *Gastroenterology* (2020).
272. Schellnegger, R., *et al.* Goblet Cell Ratio in Combination with Differentiation and Stem Cell Markers in Barrett Esophagus Allow Distinction of Patients with and without Esophageal Adenocarcinoma. *Cancer prevention research (Philadelphia, Pa.)* **10**, 55-66 (2017).
273. Rao, B., Malathi, N., Narashiman, S. & Rajan, S.T. Evaluation of myofibroblasts by expression of alpha smooth muscle actin: a marker in fibrosis, dysplasia and carcinoma. *Journal of clinical and diagnostic research: JCDR* **8**, ZC14 (2014).

274. Franchi, L., Eigenbrod, T., Muñoz-Planillo, R. & Nuñez, G. The inflammasome: a caspase-1-activation platform that regulates immune responses and disease pathogenesis. *Nature immunology* **10**, 241-247 (2009).
275. Inagaki, T., *et al.* Regulation of antibacterial defense in the small intestine by the nuclear bile acid receptor. *Proceedings of the National Academy of Sciences* **103**, 3920-3925 (2006).
276. Maran, R.R., *et al.* Farnesoid X receptor deficiency in mice leads to increased intestinal epithelial cell proliferation and tumor development. *Journal of Pharmacology and Experimental Therapeutics* **328**, 469-477 (2009).
277. Zhang, Y., *et al.* Downregulation of human farnesoid X receptor by miR-421 promotes proliferation and migration of hepatocellular carcinoma cells. *Molecular cancer research* **10**, 516-522 (2012).
278. Dossa, A.Y., *et al.* Bile acids regulate intestinal cell proliferation by modulating EGFR and FXR signaling. *American Journal of Physiology-Gastrointestinal and Liver Physiology* **310**, G81-G92 (2016).
279. Rizzo, G., *et al.* Functional characterization of the semisynthetic bile acid derivative INT-767, a dual farnesoid X receptor and TGR5 agonist. *Molecular pharmacology* **78**, 617-630 (2010).
280. Bardou, P., Mariette, J., Escudié, F., Djemiel, C. & Klopp, C. jvenn: an interactive Venn diagram viewer. *BMC bioinformatics* **15**, 1-7 (2014).
281. Ridlon, J.M., *et al.* The 'in vivo lifestyle' of bile acid 7 α -dehydroxylating bacteria: comparative genomics, metatranscriptomic, and bile acid metabolomics analysis of a defined microbial community in gnotobiotic mice. *Gut microbes* **11**, 381-404 (2020).
282. Huang, F.-L. & Yu, S.-J. Esophageal cancer: Risk factors, genetic association, and treatment. *Asian journal of surgery* **41**, 210-215 (2018).
283. Kubo, A., *et al.* Dietary patterns and the risk of Barrett's esophagus. *American journal of epidemiology* **167**, 839-846 (2008).
284. Reddy, B.S., *et al.* Effect of high-fat, high-beef diet and of mode of cooking of beef in the diet on fecal bacterial enzymes and fecal bile acids and neutral sterols. *The Journal of nutrition* **110**, 1880-1887 (1980).
285. Yokota, A., *et al.* Is bile acid a determinant of the gut microbiota on a high-fat diet? *Gut microbes* **3**, 455-459 (2012).
286. David, L.A., *et al.* Diet rapidly and reproducibly alters the human gut microbiome. *Nature* **505**, 559 (2014).
287. Yatsunenkov, T., *et al.* Human gut microbiome viewed across age and geography. *nature* **486**, 222-227 (2012).
288. Laue, H., Denger, K. & Cook, A.M. Taurine reduction in anaerobic respiration of *Bilophila wadsworthia* RZATAU. *Applied and environmental microbiology* **63**, 2016-2021 (1997).
289. Belzer, C. & De Vos, W.M. Microbes inside—from diversity to function: the case of *Akkermansia*. *The ISME journal* **6**, 1449-1458 (2012).
290. Nehra, D., Howell, P., Williams, C., Pye, J. & Beynon, J. Toxic bile acids in gastro-oesophageal reflux disease: influence of gastric acidity. *Gut* **44**, 598-602 (1999).
291. Bernstein, C., *et al.* Carcinogenicity of deoxycholate, a secondary bile acid. *Archives of toxicology* **85**, 863-871 (2011).
292. Fiorucci, S., Biagioli, M., Zampella, A. & Distrutti, E. Bile acids activated receptors regulate innate immunity. *Frontiers in immunology* **9**, 1853 (2018).

293. Im, E. & Martinez, J.D. Ursodeoxycholic acid (UDCA) can inhibit deoxycholic acid (DCA)-induced apoptosis via modulation of EGFR/Raf-1/ERK signaling in human colon cancer cells. *The Journal of nutrition* **134**, 483-486 (2004).
294. Ward, J.B., *et al.* Ursodeoxycholic acid and lithocholic acid exert anti-inflammatory actions in the colon. *American Journal of Physiology-Gastrointestinal and Liver Physiology* **312**, G550-G558 (2017).
295. Ridlon, J.M., Wolf, P.G. & Gaskins, H.R. Taurocholic acid metabolism by gut microbes and colon cancer. *Gut microbes* **7**, 201-215 (2016).
296. Bachir, G., Leigh-Collis, J., Wilson, P. & Pollak, E. Diagnosis of incipient reflux esophagitis: a new test. *Southern medical journal* **74**, 1072-1074 (1981).
297. Kakiyama, G., *et al.* Modulation of the fecal bile acid profile by gut microbiota in cirrhosis. *Journal of hepatology* **58**, 949-955 (2013).
298. Mueller, M., *et al.* Ursodeoxycholic acid exerts farnesoid X receptor-antagonistic effects on bile acid and lipid metabolism in morbid obesity. *Journal of hepatology* **62**, 1398-1404 (2015).
299. Van Eldere, J., Celis, P., De Pauw, G., Lesaffre, E. & Eysen, H. Tauroconjugation of cholic acid stimulates 7 alpha-dehydroxylation by fecal bacteria. *Applied and environmental microbiology* **62**, 656-661 (1996).
300. Friedman, E.S., *et al.* FXR-dependent modulation of the human small intestinal microbiome by the bile acid derivative obeticholic acid. *Gastroenterology* **155**, 1741-1752. e1745 (2018).
301. Úbeda, M., *et al.* Obeticholic acid reduces bacterial translocation and inhibits intestinal inflammation in cirrhotic rats. *Journal of hepatology* **64**, 1049-1057 (2016).
302. Jenkins, G.J., *et al.* Deoxycholic acid at neutral and acid pH, is genotoxic to oesophageal cells through the induction of ROS: the potential role of anti-oxidants in Barrett's oesophagus. *Carcinogenesis* **28**, 136-142 (2007).
303. Subramanian, P., Mitroulis, I., Hajishengallis, G. & Chavakis, T. Regulation of tissue infiltration by neutrophils: role of integrin $\alpha 3\beta 1$ and other factors. *Current opinion in hematology* **23**, 36 (2016).
304. Vitale, M., Cantoni, C., Pietra, G., Mingari, M.C. & Moretta, L. Effect of tumor cells and tumor microenvironment on NK-cell function. *European journal of immunology* **44**, 1582-1592 (2014).
305. Smyth, M.J., *et al.* Differential tumor surveillance by natural killer (NK) and NKT cells. *The Journal of experimental medicine* **191**, 661-668 (2000).
306. DeMeester, S.R. & DeMeester, T.R. Columnar mucosa and intestinal metaplasia of the esophagus: fifty years of controversy. *Annals of surgery* **231**, 303 (2000).
307. Stein, H., Kauer, W., Feussner, H. & Siewert, J. Bile reflux in benign and malignant Barrett's esophagus: effect of medical acid suppression and nissen fundoplication. *Journal of Gastrointestinal Surgery* **2**, 333-341 (1998).
308. Jolly, A., Wild, C. & Hardie, L. Acid and bile salts induce DNA damage in human oesophageal cell lines. *Mutagenesis* **19**, 319-324 (2004).
309. Dvorak, K., *et al.* Expression of bile acid transporting proteins in Barrett's esophagus and esophageal adenocarcinoma. *The American journal of gastroenterology* **104**, 302 (2009).
310. Baumeister, T., *et al.* Anti-inflammatory chemoprevention attenuates the phenotype in a mouse model of esophageal adenocarcinoma. *Carcinogenesis* (2021).

7. List of Abbreviations

Abbreviation	Detailed Name
12-DHCA	12-Dehydrocholic acid
12-KLCA	5 β -Cholic acid-3 α -ol-12-one 12- Ketolithocholic acid
3-DHCA	3-Dehydrocholic acid
6,7- DKLCA	5 β -Cholic acid-3 α -ol-6,7-dione
6-KLCA	5 β -Cholic acid-3 α -ol-6-one
7,12-DKLCA	5 β -Cholic acid-3 α -ol-7,12-dione
7-DHCA	7-Dehydrocholic acid
7-KLCA	5 β -Cholic acid-3 α -ol-7-one, 7-Ketolithocholic acid
7-SCA	Cholic acid-7-sulphate
8'OHDG	8-Hydroxy 2 Deoxyguanosine
ACA	Allocholic acid
ACC	Acyl-CoA Carboxylase
AKT	AKT serine/threonine kinase
ALCA	Allolithocholic acid
ALPI	Alkaline Phosphatase, Intestinal
AMPK	AMP Activated Protein Kinase
ANOVA	Analysis of Variance
ApCA	5 β -Cholen-24-oic acid-3 β -diol Apocholic acid
ASBT/IBAT/SLC10A2	Apical Sodium Dependent Bile Acid Transporter
BA	Bile Acid
bai	Bile Acid Inducible
BE	Barrett Esophagus
BMI	Body-Mass-Index
BSA	Bovine Serum Albumin
BSEP	Bile Salt Export Pump
BSH	Bile Salt Hydroxylase
CA	Cholic Acid
Ca-7ol3one	5 β -Cholic acid-7 α -ol-3-one
CCKBR	Cholecystokinin B Receptor

CD	Control Diet
CDCA	Chenodeoxycholic Acid
CDX2	Caudal Type Homeobox 2
CHREBP	Carbohydrate-Responsive Element Binding Protein
COX-2	Cyclooxygenase-2
CTGF	Connective Tissue Growth Factor
Cyp27A1	Cytochrome P450 Family 27 Subfamily A Member 1
Cyp7A1	cholesterol 7 α -hydroxylase
Cyp8B1	sterol 12 α -hydroxylase
DAB	3,3'-Diaminobenzidin
DCA	Deoxycholic Acid
DHCA	Dehydrocholic Acid
DHLCA	Dehydrolithocholic acid
DNA	Deoxyribonucleic acid
DSS	Dextran Sodium Sulfate
EAC	Esophageal Adenocarcinoma
EBV	Eppstein Barr Virus
EBV-L2 Promoter	Eppstein Barr Virus-L2 Promoter
EDTA	Ethylenediaminetetraacetic acid
EdU	5-Ethynyl-2'-Deoxyuridine
EGJAC	Adenocarcinoma of the Esophagogastric Junction
EGTA	Ethylene Glycol-Bis (β -aminoethyl ether)-N, N, N', N'-Tetraacetic Acid
EMT	Epithelial Mesenchymal Transition
ER	Endoplasmic Reticulum
ERK	Extracellular Signal-Regulated Kinase 1
ESCC	Esophageal Squamous Cell Carcinoma
FACS	Fluorescence Activated Cell Sorting
FAS	FAS cell surface death receptor
FASN	Fatty Acid Synthase
FBS	Fibroblast Growth Factor
FDA	Food and Drug Administration

FFPE	Formalin-Fixed Paraffin-Embedded
Fgf15	Fibroblast Growth Factor 15
Fgf19	Fibroblast Growth Factor 19
FMT	Fecal Microbiota Transplantation
FXR	Farnesoid-X-Receptor
GAPDH	Glyceraldehyde 3-phosphate dehydrogenase
GC	Goblet Cell
GCA	Glycocholic acid
GCDCA	Glycochenodeoxycholic acid
GDCA	Glycodeoxycholic acid
GEJ	Gastro-Esophageal Junction
GERD	Gastro-Esophageal Reflux Disease
GHCA	Glycohyocholic acid
GHCA	Glycohyodeoxycholic acid
GI	Gastro-Intestinal
GLCA	Glycolithocholic acid
GO	Gene Ontology
GPBAR1	G Protein Coupled Receptor 1
GSEA	Gene Set Enrichment Analysis
GUDCA	Glycoursodeoxycholic acid
HCA	Hyocholic Acid
HDCA	Hyodeoxycholic Acid
HE	Hematoxylin Eosin
HFCS	High Fructose Corn Syrup
HFD	High Fat Diet
HFrD	High Fructose Diet
HGD	High Grade Dysplasia
HILIC	Hydrophilic Interaction Chromatography
HPSF	High Purity Salt Free
HSDH	Hydroxysteroid Dehydrogenase
IBABP	Ileal Bile Acid Binding Protein

IBD	Inflammatory Bowel Disease
IDCA	Isoalloxycholic acid
IFN- γ	Interferon gamma
IGF1	Insulin Growth Factor 1
IHC	Immunohistochemistry
IL1B	Interleukin 1 Beta
IL2	Interleukin 2
IL6	Interleukin 6
ILCA	Isolithocholic acid
iNOS	Inducible Nitric Oxide Synthase
JNK	Janus-Kinase
KI67	Kiel-67 Antigen
Krt5	Keratin 5
Krt7	Keratin 7
LCA	Lithocholic Acid
LCenA	Lithocholenic acid
LES	Lower Esophageal Sphincter
LGD	Low Grade Dysplasia
LGR5	Leucine-rich repeat-containing G-protein coupled Receptor 5
LOD	Limit of Detection
LPS	Lipopolysaccharide
LRH-1	Liver Receptor Homolog 1
L-WRN	LWnt3A, R-spondin 3 and Noggin
MCA	Muricholic Acid
MCP-1	Monocyte Chemoattractant Protein 1
MDCA	Murideoxycholic Acid
MRI	Klinikum Rechts der Isar
mTOR	Mechanistic Target Of Rapamycin
NAFLD	Non-Alcoholic Fatty Liver Disease
NASH	Non-Alcoholic Steatohepatitis
NF- κ B	Nuclear Factor κ B

NTCP/SLC10A1	Na-Taurocholate Cotransporting Polypeptide
OCA	Obeticholic Acid
Ost- α /SLC51A	Organic Solute Transporter Alpha
Ost- β /SLC51B	Organic Solute Transporter beta
OTC	Organotypic Culture
OTU	Operational Taxonomic Unit
p63	Tumor Protein 63
PAS	Periodic-Acid-Schiff
PBC	Primary Biliary Cholangitis
PBS	Phosphate Buffered Saline
PCA	Principal Component Analysis
PCR	Polymerase Chain Reaction
PFA	Paraformaldehyde
PFPE	PAXgene-Fixed Paraffin-Embedded
PI3K	Phosphoinositid-3-Kinase
PLS	Partial Least Squares
PLS-DA	Partial Least Squares - Discriminant Analysis
PPAR γ	Peroxisome proliferator-activated receptor gamma
PPAR α	Peroxisome proliferator-activated receptor alpha
PSC	Primary Sclerosing Cholangitis
qRT-PCR	Quantitative Real Time PCR
RNA	Ribonucleic acid
ROS	Reactive Oxygen Species
RP	Reverse Phase
RT-PCR	Reverse Transcription Polymerase Chain Reaction
RXR	Retinoid-X-Receptor
SCFA	Short Chain Fatty Acids
SCJ	Squamous-Columnar Junction
SD	Standard Deviation
SHP	Small Heterodimer Partner
SPF	Specific Pathogen Free

SREBP	Sterol Response Element Binding Protein
STAT3	Signal Transducer and Activator of Transcription 3
TBS	Tris Buffered Saline
TCA	Taurocholic acid
TCDC	Taurochenodeoxycholic acid
TDCA	Taurodeoxycholic acid
TGR5	Takeda G Protein-Coupled Receptor
THBS1	Thrombospondin 1
THDCA	Taurohyodeoxycholic acid
TLCA	Taurolithocholic acid
TLR4	Toll Like Receptor 4
TNF- α	Tumor Necrosis Factor alpha
TUDCA	Tauroursodeoxycholic acid
TUM	Technische Universität München
T α MCA	Tauro- α -Muricholic acid
T β MCA	Tauro-beta-muricholic acid
T- ω -MCA	Tauro- ω -Muricholic acid
UCA	Ursocholic acid
UDCA	Ursodeoxycholic Acid
UES	Upper Esophageal Sphincter
VDR	Vitamin-D-Receptor
VEGF	Vascular Endothelial Growth Factor
VIP	Variable Importance in Projection
WD	Western Diet
WZW	Wissenschaftszentrum Weihenstephan
zOTU	Zero Radius Operational Taxonomic Unit
α MCA	α -Muricholic acid
α SMA	α -Smooth Muscle Actin
β MCA	β -Muricholic acid
γ -H2AX	phosphorylated form of histone H2A family member X
γ MCA	γ -Muricholic acid/Hyochoolic acid

8. Acknowledgements

First, I would like to express my gratitude to my supervisor Prof. Dr. Michael Quante, for giving me the opportunity to work in his group. I am very thankful for his guidance and his support concerning this work, but also the trust he put in me by involving me in the planning and implementation of several different projects in our lab, as well as by involving me in the development of several manuscripts. Besides for his support during my professional development, I am thankful his support in my personal development, especially for encouraging me to learn to be confident in myself and my work.

Furthermore, I am very grateful to Prof. Dr. Roland Schmid and Prof. Dr. Dirk Haller for the input and guidance they provided as members of my thesis advisory committee. I also want to convey my gratitude to Prof. Dr. Dirk Haller for having had the opportunity to be associated to the CRC1371. Being part of this research network was very inspiring and informative, and besides developing new research collaborations, also gave me the opportunity to meet many like-minded people and make new friends. I am also grateful to Prof. Dr. Timothy C. Wang, for giving me the opportunity to work in his laboratory at Columbia University for several weeks, and for his input and guidance regarding the different projects I have been working on. Getting to know his laboratory and the work atmosphere was deeply inspiring and I have greatly benefitted from the experience.

I am very much obliged to Dr. Amira Metwaly, who introduced me to the principles of microbiome sequencing and analysis and always provided me with input and support regarding my studies. Furthermore, I want to thank Dr. Karin Kleigrewe and Dr. Chen Meng for the constant support and guidance with my metabolome analyses. I never thought my project would take me so deep into these research fields. With your help, I have learned how to handle my data and get to know the most exciting facets of microbiome and metabolome research. I would also like to thank Dr. Ruppert Öllinger and Dr. Thomas Engleitner for helping me to perform various sequencing experiments for several different projects, all leading to the compilation of promising or published manuscripts.

I would also like to thank Dr. Jonas Ingermann, for all he taught me. I gained enormously from his great knowledge, his talent to teach and his critical eye on research. Special thanks also to Thorsten Neuss, who always took the time to provide help with any kind of problem, always had an open ear, and was always a great pleasure to exchange new favorite literature with. Furthermore, I feel deeply grateful for my colleague and friend Dr. Katrin Ciecieski, who always provided steadiness, support and encouragement during my work, my movement to Freiburg and during the writing of my thesis. I also want to convey my heartfelt gratitude to Julia

Strangmann, Akanksha Anand, and Julia Horstmann. I am extremely thankful for your friendship and support, and look back on four years of hard work, great experiences, and great teamwork. Thank you also to Andrea Proano-Vasco, for first being such a great, diligent, and inspiring student and now colleague and friend. I am convinced that you will carry forward the projects we started very successfully and hope you'll have a great time as doctoral candidate. I feel very grateful for being surrounded by so many great colleagues who became friends to me and thus want to thank Marcos, Donja, Lisa, Sabrina, Tatiana, and all other members of the laboratories in Munich for making work during the past four years so enjoyable.

Special thanks also go to my family and friends who have supported me throughout my studies and along my journey. I am very grateful to my family, especially my grandparents Helmut and Eleonore, who raised me and sparked my deep interest in learning, but also for their love, reassurance, and constant support throughout the years. I am also very grateful to my mother Kerstin and my brother Sebastian, to whom I am so much like. My energy, strong will and resilience that has carried me through so many phases of life, I have inherited from you. Being godmother to Laura and Max fills me with joy and love, but also with pride and gratitude for such a strong family bond. Thanks to my partner Thomas, my sister-in-law Nicole, and my stepfather Nicolas, for taking us all on since years and for bringing stability into our ambitious and volatile minds. Great thanks as well to my aunts and uncles Peter, Sabine, Maxi, Heinz, Christl, Eugen, my father Heinz, and my younger brother Lucas whom I all love dearly even though I might not talk about it that much. You all helped me to become the person I am today with your love and your support.

To my dearest friends Aylin, Lana, and Anna – I cannot express my gratitude for meeting you. Thank you for more than half of my life of friendship and support. You took me into your families like a sister, you have never left my side in all the years, and you helped me to become the strong, confident, and happy person I am today. I am thankful for having such good friends that are all so different and yet the same. Thank you also to Babsi, Carolin, Julia, Matthis, Andi, Xaver, Zora, Hannah, Lioba, Korbi, Laura, Christian, Sebastian, Martin, Carina, Sonja, Ruth, Matze, Ines, Totti, Armin, Steffy, Katrin, Andi, Marlene, Tom, Otto and Christl, my friends in Munich and in Utting – I am so deeply grateful for having such good friends that became my family over the time and I love every single one of you.

Last, I would like to thank you, Thomas, for your love, support and cheering me up. Thank you for understanding me and for not understanding me, for calming me down, for encouraging me, for making me feel loved and secure, for being my safe haven and my humorous best buddy in the past 7 years. I love you, and I am eager to see what the future holds for us.